N ° d'ordre: 40994

UNIVERSITÉ LILLE 1 SCIENCES ET TECHNOLOGIES

THÈSE

Présentée à

L'ÉCOLE DOCTORALE SCIENCES POUR L'INGÉNIEUR

Pour obtenir le titre de

DOCTEUR DE L'UNIVERSITE

Spécialité Micro et Nanotechnologies, Acoustique et Télécommunications

par

Jiaming GAO

Laboratoire sur puce pour caractérisation acoustique haute fréquence

Soutenue publiquement le 06 décembre 2012

Rapporteur	Mr. Yong CHEN	Professeur de l'Ecole Normale Supérieure, Paris
Rapporteur	Mr. Ayache BOUAKAZ	Directeur de recherche INSERM, Tours
Examinateur	Mr. Dominique REBIERE	Professeur de l'université de Bordeaux
Examinateur	Mr. Xingzhong ZHAO	Professeur, physics department of Wuhan university, china
Directeur de thèse	Mr. Bertrand NONGAILLARD	Professeur de l'Université de Valenciennes
Co-encadrant	Mr. Julien CARLIER	Maître de conférences de l'Université de Valenciennes
Co-encadrant	Mr. Pierre CAMPISTRON	Maître de conférences de l'Université de Valenciennes

Ph. D. Thesis

Lab-on-a-chip for high frequency acoustic characterization

Name	**Jiaming GAO**
Supervisors	**Prof. Bertrand NONGAILLARD**
	Prof. Xingzhong ZHAO
Co-supervisors	**Dr. Julien Carlier**
	Dr. Pierre CAMPISTRON
Date	**Dec. 06, 2012**

Abstract

This thesis presents an acoustofluidics platform for elastic characterization of biological samples using ultra high frequency (~1GHz) ultrasonic bulk acoustic waves (BAW).

Passive 45 ° mirror planes obtained by wet chemical etching can be used to control bulk acoustic wave to transmit in the directions parallel to the surface of the silicon wafer. Zinc oxide (ZnO) thin film transducers were deposited by radio frequency sputtering on the other side of the wafer, which act as emitter/receiver after aligned with the mirrors.

A microchannel fabricated using ICP technology was inserted between 45 °mirror and vertical mirrors to realize the real time biosensing applications. To validate the design and technology of the silicon and PDMS-based platform, the propagation of bulk acoustic waves through the microfluidic channel was studied. This lab-on–a-chip platform was used to characterize different concentrations of chemical solutions in the microfluidic channel and detect latex particles passing through the channel.

Moreover, with this design, a confocal cylindrical lens using ICP technology was integrated in the microsystem. The confocal lens controls the phase of acoustic waves for focusing which is used to characterize and detect biosamples (e.g. blood cells), especially on-line to evaluate the concentration of red blood cells.

Key words: ultra high frequency transducer; acoustical characterization; Lab -on –a- chip; microfluidics; bulk acoustic wave

Acknowledgement

First of all, I would like to express my thanks to the reviewers, Prof. Yong CHEN from l'Ecole Normale Supérieure, Paris and Ayache BOUAKAZ, Director of research from INSERM Tours, for their great contribution to review this dissertation. I have to thank also Pr Rebieres from Bordeaux University who accept to evaluate my Ph.D. work and to participate to the jury.

I have also to thank the IEMN laboratory and his director Pr L.Buchaillot to welcome me for this PHD.

I would like also to express my sincere thanks to my supervisors Professor Xingzhong ZHAO and Professor Bertrand NONGAILLARD for their invaluable advices and constant assistance. I have learned a lot from both of them who have helped me enrich and broaden my knowledge during past several years.

Then I would like to express my gratitude to my co-supervisors, Dr. Julien CARLIER and Pierre CAMPISTRON who have given me a lot of warm help and useful suggestions on the experimental and theoretical parts of my work.

I would also like to express my gratitude to all of you helped me in many ways. I have many discussions with Dr. Weijiang XU and Dr. Shishang GUO. I have got a lot of helps from Dr. Shengxiang WANG, Zhenkun CHEN, Zheng YUAN, Dr. Chang WU, and Dr. Xianglei HAN. I would like to thanks all the IEMN clean room staff for their constant technical support and all the members in MAMINA group of IEMN-DOAE and the prof. ZHAO's group. I appreciate the resources and environment of research in both groups.

Lastly, I would like to express my thanks to my parents for their everlasting love and my dear Yinger for all her love and patience.

Thanks again and best wishes for all of you.

Contents

General introduction

In the recent advances in the field of microelectromechanical (MEMS) system, microfluidics-based analysis systems are powerful tools which facilitate novel experiments and have many applications in chemical and biological systems, such as cell analysis and high-throughput biological screening. The use of small volumes of reagents, the increase in the sensitivity of these microfluidic components and the ability to perform numerous analyses in parallel have widely contributed to the wide interest in lab-on–a-chip. Various sensing technologies have been integrated in microfluidic systems (e.g. optics, RF, acoustics) making it possible to measure different physical properties. Over the last decades, these technologies have also been developed for the integration of actuators in microfluidic systems, including optical and magnetic tweezers, and electrical forces for manipulating small objects in aqueous solution. The latter application requires high electrical power.

In recent years, many efforts have been devoted to integrating acoustic techniques in microfluidic systems, such as sensing, mixing, manipulating and trapping. These applications are based mainly on the use of low frequency waves and/or surface acoustic waves. The interest of using BAW for biological applications has been demonstrated with the development of high frequency acoustic microscopy in this domain. It is well known that some pathology modify the elastic properties of biological cells. However, traditional acoustic microscopy is often a bulky, expensive or complex characterization method, which is hard to integrate for on-line elastic evaluation. In comparison with the acoustic sensing systems above, high frequency bulk acoustic waves (BAW) have potential applications for the detection of biochemical micro-objects and characterization of the elastic properties of biological cells (e.g. blood cells).

In our case, the aim was to integrate bulk acoustic wave sensors to carry out measurements in a microfluidic channel in order to evaluate the elastic properties of fluids and single biological cells.

In this thesis, we report a novel silicon-based high frequency (GHz range) bulk acoustic wave (BAW) sensing microsystem. BAWs have been generated using miniature piezoelectric transducers (thin zinc oxide films can be easily used to integrate low power, high frequency transducers) and guided using acoustical mirrors parallel to the surface of the silicon wafer. BAWs have been then transmitted through the microfluidic channel. Some components used in order to increase the spatial resolution and the sensitivity of the measurement technique such as cylindrical lenses have also been fabricated. Due to the non-contact nature and high resolution of acoustic waves in the field of classic scanning microscopy (a spatial resolution of one wavelength can be assumed, that is to say 1.5µm at a frequency of 1GHz), such microfluidics-based high frequency BAW platforms are suitable for non-destructive characterization and detection in microfluidic channels.

In the first chapter, various sensing technologies based on the microfluidic systems are reviewed. Optical and electrochemical methods have been widely used in the microfluidic

sensing system. For both types of systems, one of the major challenges in biological detection and clinical bioanalysis is the requirement of labeling, such as fluorescent markers, enzymes or quantum dots. For this reason, there is a high interest in developing label-free detection system. The acoustic wave based sensor devices can provide an answer. The current biomedical applications of the acoustic wave based devices are mainly classified into two types: BAW and SAW. The resonators method and delay lines method are presented.

In the second chapter, firstly we will present the background on acoustic waves. Then we study the elastic wave propagation in three different media. Later we will focus on the study of continuity conditions at the interface of two different materials (e.g. solid-air,) and we will turn to study the elastic wave motion in piezoelectric solid. Secondly, a difference of the acoustic impedances between two media in close contact leads to the reflection of the incident acoustic beam. This phenomenon can be widely reduced using the mechanical impedance matching. A common material for solid-liquid interface matching is the use of the anti-reflection layers of quarter wavelength. In the case of silicon wafer of silicon dioxide can easily be used in order to improve the losses of our system. At the same time, the silicon oxide coating layer between the solid media and gas media also play an important role in the acoustic wave reflection by an acoustic mirror. Finally we will evaluate the expected performances in different parts of our microsystem.

In the chapter three dedicated to the experimental fabrication of our system, the MEMS technology have been used to fabricate a novel silicon based microsystem with microfluidic channel, acoustic wave guiding components and thin film sensors. Radio-frequency sputtering technologies are chosen to fabricate ZnO / PZT high frequency piezoelectric transducer. The 45 ° mirror is etched with a mixture including isopropyl alcohol (IPA), Tetramethylammonium hydroxide (TMAH) and ammonium persulfate (AP) in order to obtain smooth mirror surface. The 45 ° mirror is used to guide the acoustic wave from the wafer thickness direction to a direction parallel to the surface of the wafer. Investigation of the microsystem properties was achieved to obtain the desired fabricated structures, some important parameters of deep Reactive-ion etching (RIE) fabrication process had been discussed; the surface roughness of the micro-structures is a key point for BAWs transmission, as well as the perpendicularity of the microchannel. Polydimethylsiloxane (PDMS) as the package material is used to assemble this microdevice.

Finally the last chapter of this thesis concerns the application of our silicon based microdevice for the detection of particles and elastic properties characterization. We used probe contact in the validation measurement, which is easily compatible with the vector network analyzer (VNA) measurements in our frequency range. The S_{ij} parameter measurement was based on a continuous wave using frequency sweeping. Then we used signal processing (inverse Fourier transform) to obtain the time domain echogram. The microdevice of original design was calibrated with deionized water (DIW). The transmitted and reflected acoustic waves have been investigated. Then the improvement of a pair of vertical mirrors has been performed to

increase the transmitted signal with respect to parasitic echoes of the microsystem. The improved microdevice has been calibrated with the DIW and potassium iodide solutions. The echograms of the transmitted acoustic wave have been discussed. Finally the confocal lenses have been integrated into the improved microdevice in order to give very first results about the characterization of the elastic properties of biological cells.

1 Introduction to Lab on a Chip system

The development of microfabrication technologies has enabled the integration of functional units for biochemical analysis onto miniaturized chips. In the recent years, lab-on-a-chip (LOC) has many applications in the biochemical and biomedical fields. Integrated microfluidic devices involve the large-scale integration of various microfluidic components, such as microvalves, micropumps, microfluidic mixers, and other elements to handle and control fluids at the microscale. They are frequently used for biological, chemical, and biomedical analysis. The optical and electrochemical methods have been widely used in the microfluidic sensing system. In both two types of systems, one of the greatest challenges in biological detection and clinical bioanalysis is the requirement of labeling, such as fluorescent markers, enzymes or quantum dots. For this reason, there is a high interest in developing label-free detection system. The acoustic wave based sensor devices can meet this requirement. The current biomedical applications of the acoustic wave based devices are mainly classified into two types: bulk acoustic wave (BAW) and surface acoustic wave (SAW). A great amount of microfluidic devices based on BAW or SAW mode have been used for biochemical sensing and detection. The basic principal of our microsystem is also introduced. Our microsystem is a highly integrated acoustofluidics platform. The ultra high frequency (~1GHz) ultrasonic bulk acoustic waves (BAW) and the transmission mode are used for elastic characterization of biological samples.

1.1 Microfluidics and Lab-on-a-Chip System

1.1.1 Historical aspects

In the 1950s, the invention of microtechnology realized integrated semiconductor structures for microelectronic chips. In the 1960s, the lithography-based technologies were soon applied in pressure sensor manufacturing as well. Next it was applied to pressure sensors, airbag sensors and other mechanically adaptable structures. The devices for fluid handling were developed, such as channels (capillary connections), mixers, valves, pumps and dosing devices. The first LOC analysis system was a gas chromatograph, developed in 1979 by S.C. Terry - Stanford University[1]. However, only at the end of the 1980s, and beginning of the 1990s, the LOC research started to seriously grow as a few research groups in Europe developed micropumps, flow sensors and the concepts for integrated fluid treatments for analysis systems[2]. These Micro Total Analysis System (μTAS) concepts demonstrated that development of standard bench-top instrumentation in a micro-scale could offer great versatility and extend the simple sensor functionality towards a complete integrated laboratory analysis[3].

A big interest in research and commercial interest came in the mid 1990's, when μTAS technologies turned out to provide interesting tooling for genomics applications, like capillary electrophoresis and DNA microarrays. A great deal of research has been devoted to the miniaturization of biochemical analysis systems, and many types of microdevices with integration of multi-analytical functions have been developed [4]. There is a demand not only for the integration of lab processes for analysis but also for the characteristic possibilities of individual components. Hence the term "Lab-on-a-Chip" was introduced.

Although the application of LOCs is still in the development, thousands of research spent a lot of time in different fields such as fluidic controlling (e.g. fluid transport, fluid mixing, microvalve and micropump), analysis (e.g. chemical analysis, medical diagnostics and cellomics) and synthetic chemistry (e.g. rapid screening and microreactors) within the last two decades. The research of further application in LOC systems is expected to extend towards downscaling of fluid handling structures by using nanotechnology. Sub-micrometer and nano-sized channels, single cell detection and analysis, and nano-sensors, might become feasible ways of interaction with biological species and large molecules.

1.1.2 Advantages and Applications

Most LOC fabrication processes are silicon based systems using fabrication techniques that grew out of integrated circuit (IC) fabrication technologies. Notable properties of silicon include its electrical conductivity and the wealth of techniques that have been developed for fabrication, surface treatment, and bonding[5].

Glass-based LOC system has the advantage that more is known about the demands for specific optical characteristics, bio- or chemical compatibility, lower production costs and faster prototyping. Many surface treatments exist for glass, and it has excellent thermal and optical properties. However, glass is more difficult to machine and designs based on glass need to adapt to the limited machining methods available[5].

Polymer based LOC systems are a more recent development and there exist many fabrication methods depending on the polymer used. polydimethylsiloxane (PDMS) is commonly used polymer in LOC systems. PDMS can be used with a surface patterned mask to create half of an LOC device which is sealed to a cover (e.g. glass slide). Many other manufacturing methods exist for polymers including embossing, lamination, injection molding, laser machining, as well as all of the tradition direct machining methods (e.g. drilling or milling) [6]. Furthermore the LOC field more and more exceeds the borders between lithography-based micro and nano technology.

LOC, the conventional biochemical processes, such as sample pretreatment, sample/reagent transport, mixing, reaction, separation, detection, and product collection, can be carried out automatically on a single cheap potable chip[7]. Microfluidics can be used in physical science for control systems, heat management and energy generation. They are the driving forces in microfluidic research, shown in Figure 1.1.

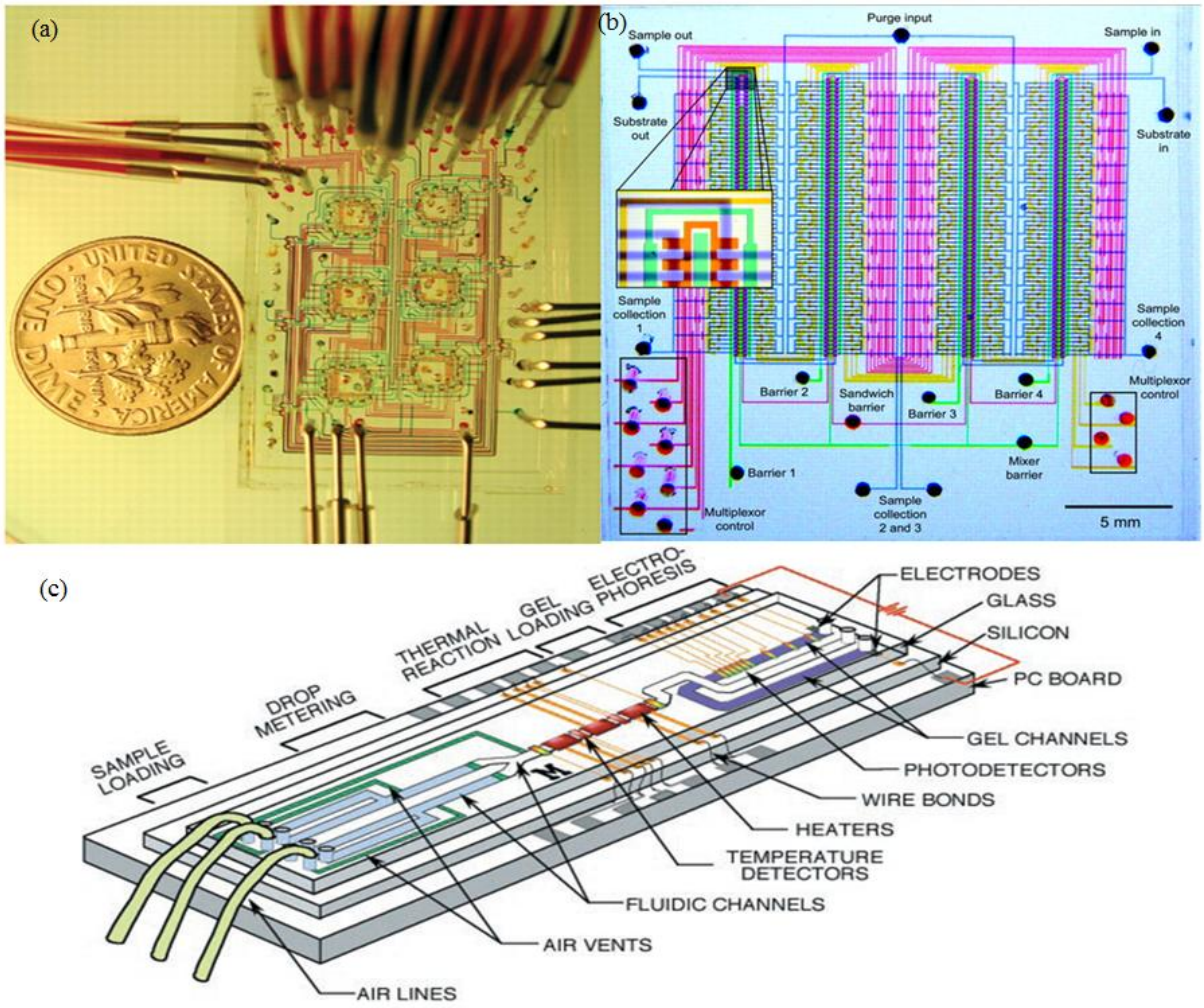

Figure 1.1 (a)Optical micrograph showing six microchemostats that operate in parallel on a single chip, (b) High integrated microfluidic chip containing micro-valve and micro-pump (c) Schematic of integrated device with two liquid samples and electrophoresis gel present [8].

Advancement of microfabrication technologies has enabled the integration of functional units for biochemical analysis onto miniaturized chips[9]. The realization of such a Lab-on-a-Chip (LOC) concept has been considered as the most important application of microfluidics. LOC systems provide analytical improvements associated with the minimized consumption of reagents, increased automation, short reaction time, and reduced manufacturing costs[10]. The demand of LOC systems has been growing rapidly due to its potentials on drug delivery, chemical analyses, point-of-care clinical devices, biowarfare and biochemical agent detection, high throughput screening, and water quality control[11]. Since LOC system aims miniaturization of a typical room-sized laboratory, major fluidic components for handling of analytical samples are similarly required including the pump, valve, mixer, concentrator, filter, sensor, etc. Thus, various types of microfluidic technologies are being widely investigated by

many researchers for the development of key LOC components[12].

LOCs may provide advantages such as[13][14]

a) Less fluid volumes consumption and lower reagents costs

b) Due to short diffusion distances and high surface to volume ratios, it can shorten analysis and response times

c) Good process control (e.g. thermal control for exothermic chemical reactions)

d) Compactness of the systems due to integration of much functionality and small volumes

e) Massive parallelization due to compactness, which allows high-throughtput analysis

f) Low fabrication costs, allowing cost-effective disposable chips, fabricated in mass production

g) Safer platform for chemical, radioactive or biological studies because of integration of functionality, smaller fluid volumes and stored energies

Some of the disadvantages of LOCs are[15]:

a) It is a developing technologies and therefore it is currently under research.

b) On the small scale some effects such as capillary forces, surface roughness will play an important role in the applications. This may make processes more complex in LOCs than in conventional lab equipment

c) The detection principles may not suitable for the miniaturized devices in a positive way which leads to low signal-to-noise ratios

d) Although the accuracies and precision of the microfabrication geometric are high, they are often rather poor in a relative way compared to precision engineering, for instance.

In the recent years, LOCs have many applications in the biochemical and biomedical fields[16]. Such as real-time polymerase chain reaction (PCR) for detection bacteria, viruses and cancers[17]; biochemical assays[18]; immunoassays for detection based on antigen-antibody reactions[19]; dielectrophoresis for detection of cancer cells and bacteria[20]; lab-on-a-chip for single cell analysis[21][22]; ion channel screening; testing the safety and efficacy of new drugs and manipulating soft matter particularly for confinement studies of colloids and cells.

1.2 Microfluidic Sensing Techniques

Integrated microfluidic devices involve the large-scale integration of various microfluidic components, such as microvalves, microchannels, micropumps, microfluidic mixers, and other elements to handle and control fluids at the microscale[13]. They are frequently used for biological, chemical, and biomedical analysis. Various detection methods exist in the field of

chemical, biological diagnosis, or analysis on microfluidic platforms.

Microfluidic sensing techniques can be categorized based on the physical forces employed into the optical methods, electromagnetic methods, and acoustical method. Among these methods, optical and electrochemical methods are the most frequently used due to their selectivity and sensitivity. Other than the above major methods, approaches such as nuclear magnetic resonance (NMR) spectroscopy, magnetoresistive, are also coupled to microfluidics for sensing application.

1.2.1 Optical Method

The integration of optical components and functions in a microfluidic platform enable to perform all the operations in a single device. Recent effort has focused on the term of micro-optical electromechanical systems (MOEMS)[23]. It drives the development of micro-optical technologies to replace bulky, large and expensive macroscopic optical systems. Typical optical detection methods comprise the direct detection by monitoring the light properties including absorbance [18,19], fluorescence[20,21] and chemiluminescent[24] (Figure 1.2). These methods usually involve techniques such as surface plasmon resonance (SPR) detection. interferometry, fiber optics and optical waveguides, Photonic crystals, optical cavity structures.

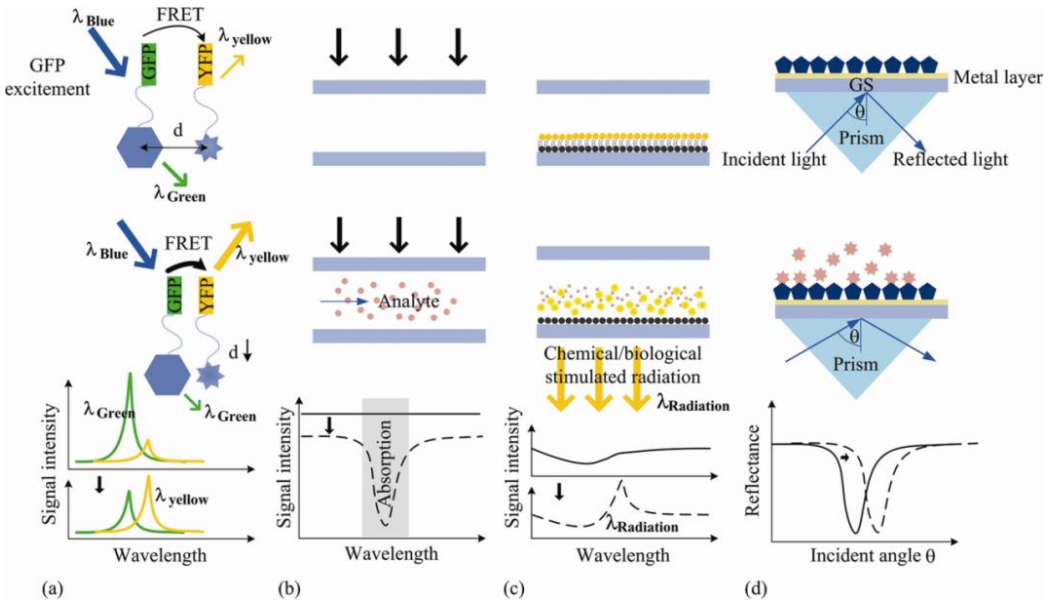

Figure 1.2 Typical optical methods. (a) fluorescence (in this case, fluorescent resonance energy transfer/FRET), (b) absorbance, (c) chemiluminescence, and (d) surface plasmon resonance-based optical detection methods. [25]

1.2.1.1 Absorbance

Absorbance detection is the most widely used detection method not only in common macro-structure sensing systems but also in the microfluidic devices. Peterson et al. [26]fabricated the device from a silicon substrate shown in Figure 1.3a. The device used nitrogen-doped SiO_2 (superior UV transmission) for waveguide fabrication in the absorbance mode at 254nm with a 750 μm long detection cell for on-chip electrophoretic separation. A 15 μm thick silicon layer and 6 μm thick silicon oxynitride layer was deposited and patterned. A 4 μm thick undoped silica cladding layer was deposited to complete the waveguide circuit. Balslev et al. [27] integrated liquid dye laser, waveguides, fluidic channels, measurement cuvettes, and photodiodes into the layer of SU-8 polymer which were embedded in the silicon substrate(Figure 1.3c).The emitted light of the dye laser at 576nm is directly coupled into five waveguides, that bring the light to five different locations along a fluidic channel for absorbance measurements.The transmitted portion of the light is collected at the other side of the cuvette, again by waveguides, and finally detected by the photodiodes.

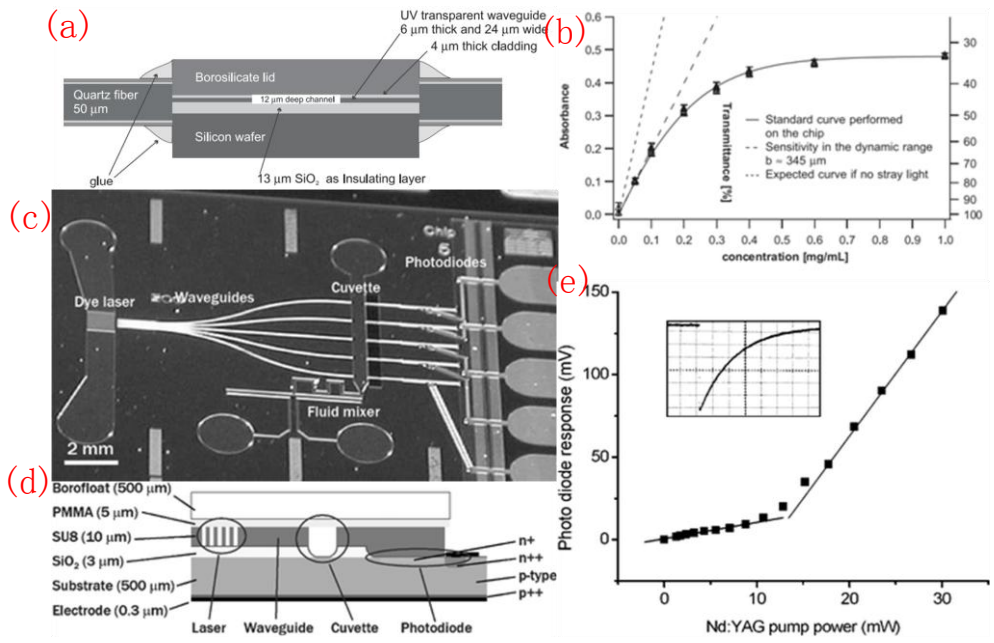

Figure 1.3 (a) Cross section of the separation device, (b)Standard curve for ketoprofen at λ=254nm performed on-chip[18], (c)Photograph of the lab-on-chip device with integrated microfluidic components. (d)Outline of the cross section of the lab-on-chip device. (e) Photodiode response as function of optical pump power of the laser pumping the on-chip dye laser. The inset shows the open circuit response from a photodiode to a single pump pulse[19].

1.2.1.2 Fluorescence

Hofmann et al. provide a device with150nm thick silicon nitride waveguides for evanescent field-based fluorescence excitation which is used to monitor antibody–antigen-binding events Figure 1.4[28]. The microfluidic channel network was used for continuous replenishment of the sample, thereby increasing the mass transport to the surface. Vertical confinement of the sample stream to the region close to the waveguide surface ensured low reagent consumption. High quality monolithically integrated optical long-pass filters are used in disposable diagnostic microchips [29]. The filters were prepared by incorporating dye molecules directly into the microfluidic chip, providing a fully integrated system that removes the usual need for discrete optical filters. The filters are robust in use, showing only slight degradation after extended illumination and negligible dye leaching after prolonged exposure to aqueous solutions.

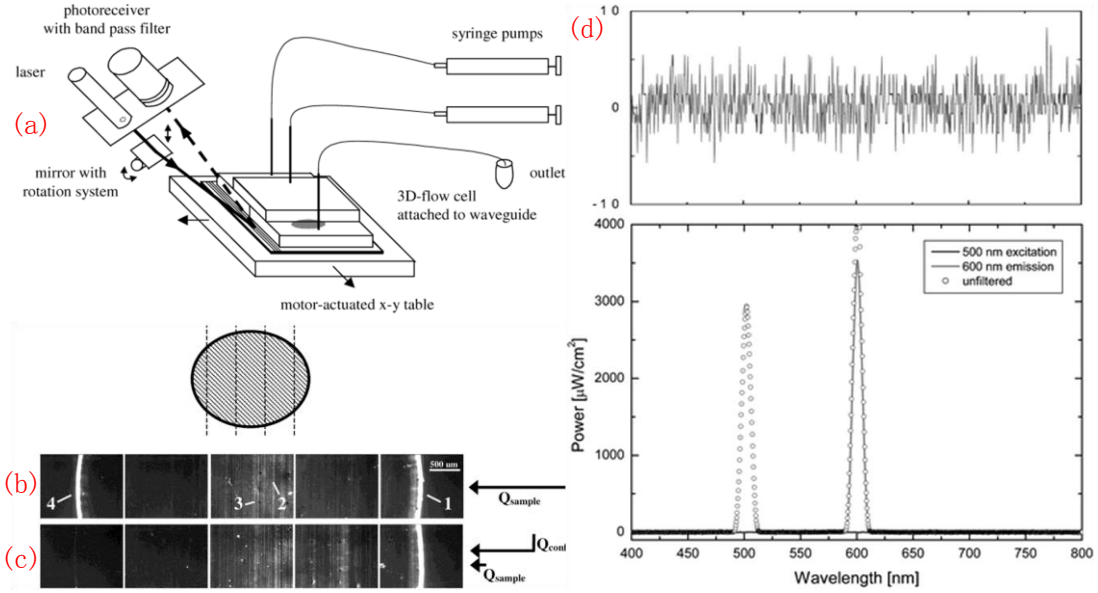

Figure 1.4 (a)Schematic of the sensor and microfluidic setup used to evaluate the flow confinement concept.[20] (b) Fluorescence micrographs of the sensing zones after immunoassay completion, (c) Fluorescence micrographs of the sensing zones after immunoassay completion (sample flow 6 µL/min + confinement flow 30 µL/min). (d) The blocking properties of a Sudan II filter, measured using the co-linear configuration.

1.2.1.3 Chemiluminescent

As shown in Figure 1.5a, a photodiode fabricated in the bottom of the channels etched in a silicon microchip has been reported [30]. All fluidic and electrical connections were placed on the backside of the wafer to facilitate easy sealing of the channels by anodic bonding of a Pyrex wafer. Since the devices were designed for chemiluminescent determination of glucose, the

channel network contained an enzyme reactor, a mixer, and a detection region. The emission light from the chemiluminescent reaction of hydrogen peroxide and luminol was determined on chip, with a detection limit for hydrogen peroxide of 5 μM. A microfluidic system has been fabricated to be a basic device for biochemical analyses, which contains three microfluidic functions: transport, mixing and detection in Figure 1.5c-e [31]. The electrochemiluminence(ECL) can be generated on the chip by applying a potential to the electrode, which can be enhanced by increasing the pH of the solution using the mixing mechanism. The detection limit of a nM order can be achieved.

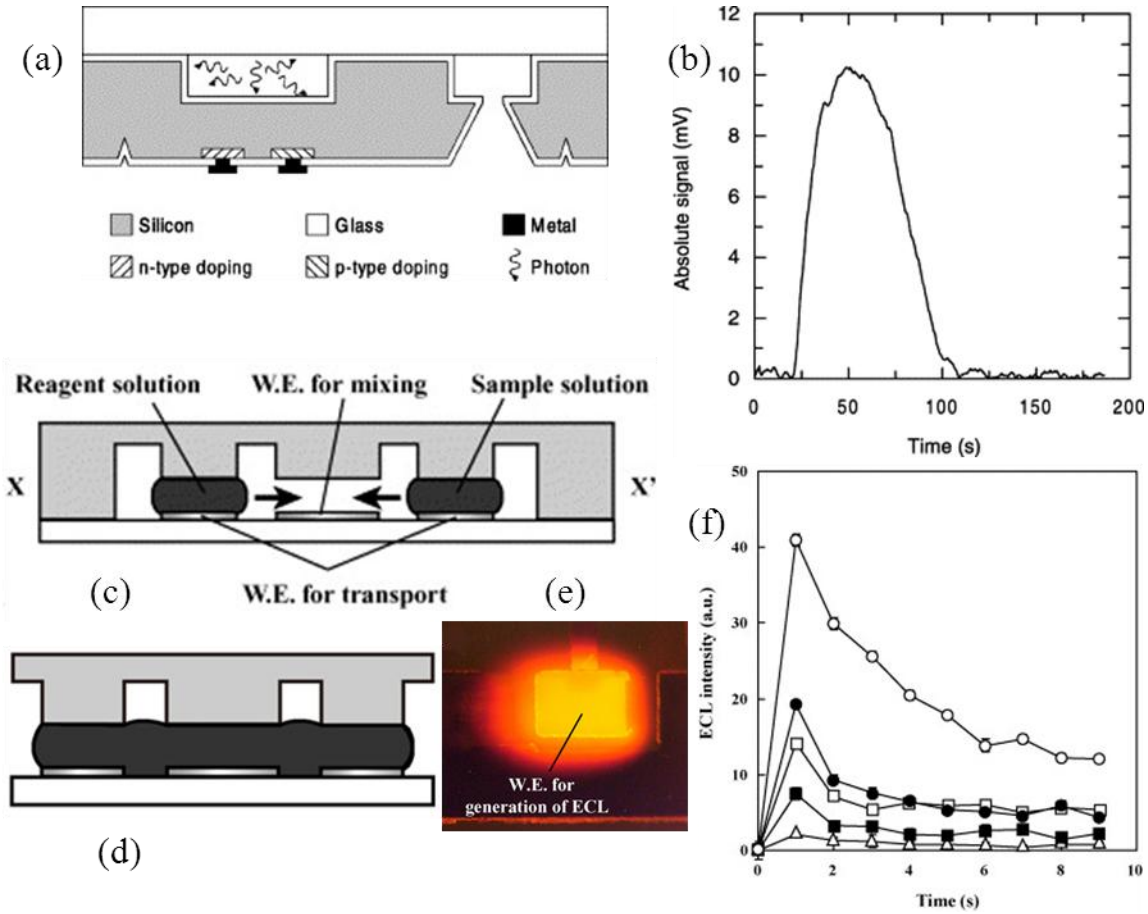

Figure 1.5 (a)Sketch of a cross-sectional view of the integrated system, (b) Example of a response of the system when a hydrogen peroxide sample is injected.(c-d) solutions mixed on the working electrode.(e) ECL is generated on the working electrode when a potential is applied (f) Time courses of the ECL intensity of the amino acids.

1.2.2 Electrochemical Method

Electrochemical measurements are based on electrical property modulations of the analyte species that undergo redox reactions, and are usually employed for the detection of the

electroactive species. Typically in electrochemistry, the reaction under investigation would either generate a measurable current (amperometric), a measurable potential or charge accumulation (potentiometric) or measurably alter the conductive properties of a medium (conductometric) between electrodes[32]. The principles of these methods are demonstrated in Figure 1.6. Amperometric detection is based on the measurement of the current between the working and counter electrode which is induced by a redox reaction at the working electrode. The conditions are chosen in such a way that the current is directly proportional to the concentration of a redox active species in the analyte solution. The electrical potential of the working electrode versus the measured solution is achieved by a separate reference electrode and is controlled by a potentiostat electronic system. Potentiometric devices measure the accumulation of a charge potential at the working electrode compared to the reference electrode in an electrochemical cell when zero or no significant current flows between them. In other words, potentiometry provides information about the ion activity in an electrochemical reaction[33]. For potentiometric measurements, the relationship between the concentration and the potential is governed by the Nernst equation. The principle of conductometric detection is that the conductivity of a zone is affected by the charged species in the zone. Different types of species would have their specific conductivity responses, which would also vary with different concentrations.

Electrochemical biosensors have suffered from a lack of surface architectures allowing high enough sensitivity and unique identification of the response with the desired biochemical event.

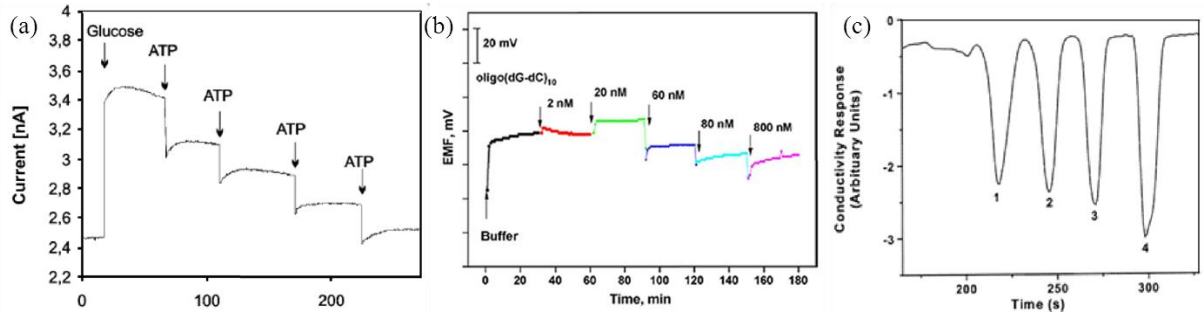

Figure 1.6 Three types of electrochemical detection methods for microfluidics:(a) amperometric[34], *(b) potentiometric*[35], *and (c) conductometric detection*[36].

1.2.3 Other Methods

High resolution NMR for microfluidic systems was realized in 2007 by Pine's group in UC Berkley on the study of multi-phase flows and catalyst deactivation[37]. Besides direct detection, the Pines' group also pioneered the remote monitor work of NMR-based microfluidic detections. In 2007, they reported the remote monitoring of spin coherence transfer in chemical transformations[38] and a double-phase encoded remote detector of the fluid diffusion through

membranes[39]. This technique is readily applicable mostly in hydrogenation reaction-related detection and imaging, and might be extended for more applications in microfluidics. However, the limited reaction time scale/polarization lifetimes remains a key technological bottle-neck for NMR-based microfluidic analytical detection.

In order to probably detect the stray field of the immobilized microbeads, a multilayered giant magnetoresistance (GMR) has been chosen as sensing element. The high sensitivity of GMRs at low magnetic fields makes them suitable for detection[40].

1.3 Acoustical method

The useful frequency range of scientifically based acoustics spans 15 orders of magnitude, as shown in Figure 1.7.

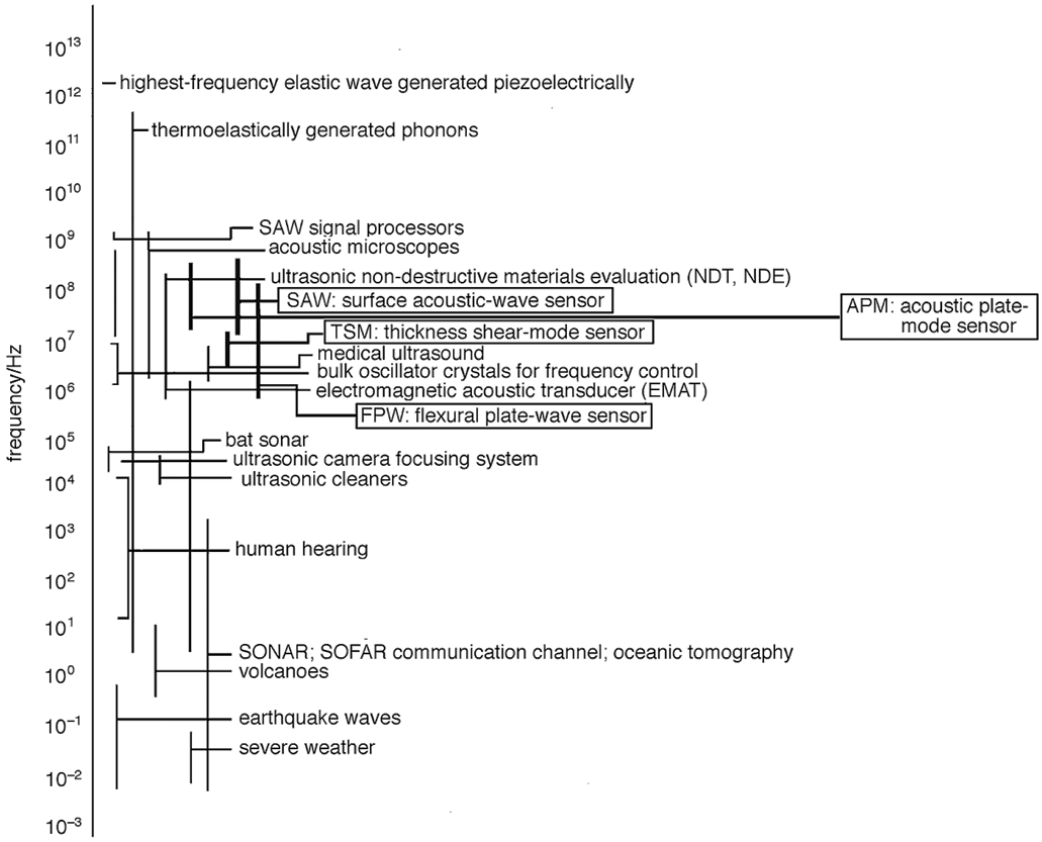

Figure 1.7 The range of acoustic wave excitation at the close of the 20th century[41].

Modern acoustics span a diverse range of disciplines, as illustrated from the following list[41]:

(1) underwater acoustics[42], oceanography[43], and sound navigation and ranging (SONAR);

(2) architectural[44] and musical acoustics;

(3) psychological and physiological acoustics and communication;

(4) noise and its control[45];

(5) medical ultrasonics[46] [47][48];

(6) physical acoustics[49]: phononics, actuation, levitation, and other physical phenomena;

(7) acoustic holography and imaging[50], and sensing[51].

1.3.1 Acoustic imaging

In the following part, we will pay more attention to high frequency and integrated acoustic techniques.

1.3.1.1 Acoustic microscopy

The acoustic microscope can be used to study the internal microstructure of nontransparent solids or biological materials which are imaged by ultrasound waves in acoustic microscopy. The reflection contrast provides a map of the spatial distribution of the mechanical properties. The first scanning acoustic microscope was created by Lemons and Quate [52]. It was mechanically driven and operated in the transmission mode. Katz develop a transmission SAM used the frequency (25MHz) pulse mode to study skeletal tissue [53]. In the pulse mode a single acoustic pulse is focused on the sample. It shows that the transmission SAM has some advantage at low resolution of the order of 100 μm, in that the attenuation and velocity can be measured simultaneously in samples up to several millimeter thicknesses.

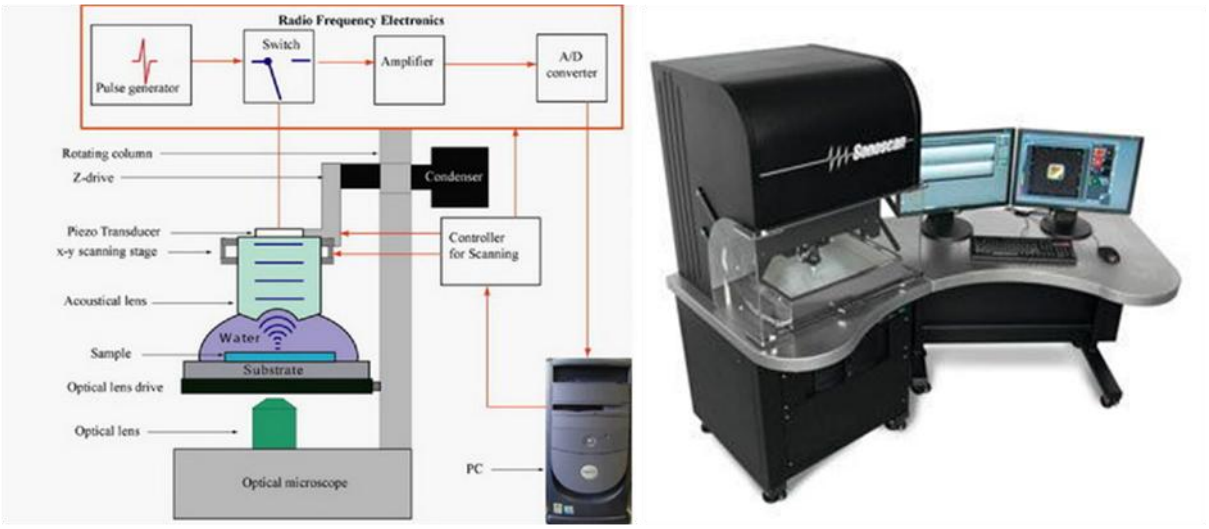

Figure 1.8 Left: The schematic diagram of the combined optical and acoustic microscope[54].*Right: A photograph of Socoscan Gen6 scanning acoustic microscope.*

Higher frequencies can obtain higher resolution of the order of several micrometers and lead to a greater attenuation. SAM in the reflection mode could work at higher frequencies. When the frequency is up to the order of GHz, this mode of SAM is known as the burst mode in which a wave of tens of sinusoids is used.

The scanning acoustic microscope (SAM) can be characterized in three domain- image generation by scanning, far-field wave imaging, and the use of acoustic waves[55]. The scanning acoustic microscope is a sequential imaging system in which a piezoelectric transducer emits a focused ultrasound beam that propagates through water, to the sample. The beam is scattered by the sample, and the scattered ultrasonic wave is detected. The output signal is just one single voltage. As the sample is scanned, the voltage is recorded in each scanning position of the focus and a grey-scale image is generated. The second principle use focused beam which is formed by converging propagating waves. The size of focal area is limited by diffraction. Imaging with ultrasound is the third principle. The operating frequencies of SAMs are between 100 MHz and 2 GHz; the high frequency provides the opportunity to obtain accurate measurement results for crack and void distributions with a resolution of up to 1 μm at a depth of 10 μm.

Table 1.1. Typical Design Parameters for Scanning Acoustic Microscopy[56]

	Property	30 MHz	1 GHz
Transducer	Material	Lithium niobate	ZnO (1.4 μm)
	Diameter	6 mm	200 μm
	Electrodes	Au-Cr	Au-Cr (0.2 μm)
Lens body	Material	Fused quartz	Sapphire
	orientation		C axis
	Diameter	10 mm	6 mm
	Length	10 mm	4 mm
Lens cavity	Diameter	5 mm	100 μm
	Opening	4 mm	
	Matching layer		Borosilicate glass

The SAM is mainly applied in two non-destructive evaluation and biomedical application. It provides a spatial resolution of image in the order of μm or sub-μm. The operating frequencies are restricted by the penetrating capacity of the acoustic wave in the medium. A specialized operating frequency can be chosen according to the application objective and the acoustic transducers.

For non-destructive evaluation, SAM is mainly used in three fields. The first is to measure and visualize the adhesion in layered structures. The second is the surface imaging. The most

common application is the detection of subsurface defects in coatings [57]. The third is the visualization of dynamic phenomenon caused by varying factors (stress, temperature, radiation) inside solid materials[58].

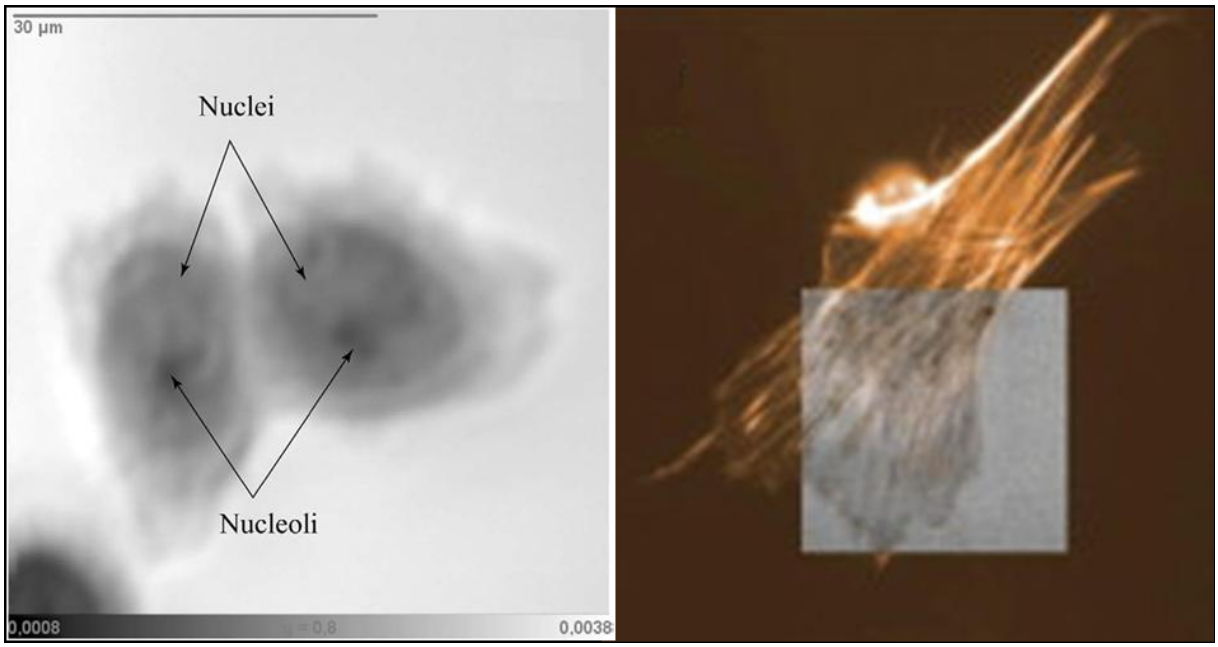

Figure 1.9 Left: acoustical image of a Hela cell (860 MHz)[54], right: acoustical image of embryonic chicken heart muscle cells (860 MHz)[59].

For the biomedical application, SAM is used not only for the investigation of cellular elastic properties, but also for the cell imaging and visualization. Ultrasonic data obtained with the high frequency SAM can be used for assessing echographic imaging. Acoustic impedance of the material could be deduced by the density and acoustic velocity. As a biological soft tissue may be considered as a liquid-like material, elastic bulk modulus is proportional to the square of the acoustic velocity and the density, which can be used to obtain its elastic properties. SAM is also used for pathological examination[60].

1.3.1.2 Ultrasound arrays

An ultrasound array sensor contains a number of individual sensor elements in the linear distribution or 2D horizontal distribution. It works as the same principal as the radar system. A typical ultrasound array transmits a sound pulse and receives the returning echoes. The transmitted signal and received signal can individually be delayed in time (phased array), which is done to electronically steer and focus each of a sequence of acoustic pulses through. The phased array can be used to obtain fast imaging frame rate and perform in-vivo real time imaging.

K.K. Shung et al.[61] develop a 64 element 35-MHz composite ultrasonic array using 2-5 composite elements. The pitch of the array elements is 50 μm which is interconnected with a custom flexible circuit in a ceramic frame. A scanning electron microscope (SEM) of the cross-section view of a composite is shown in Figure 1.10. An image acquired demonstrates resolution of this ultrasound array exceeding 50 μm axially and 100 μm laterally. It is indicate that with this array design, it is suitable for clinical application. K.K. Shung et al.[62] also develop and characterize a high frequency (65 MHz) ultrasound array. The linear array consists of 32 elements with an element width of 24 μm and a kerf width of 12 μm.which is made from bulk PZT and having the frequencies greater than 50MHz have developed using a DRIE dry etching technique.

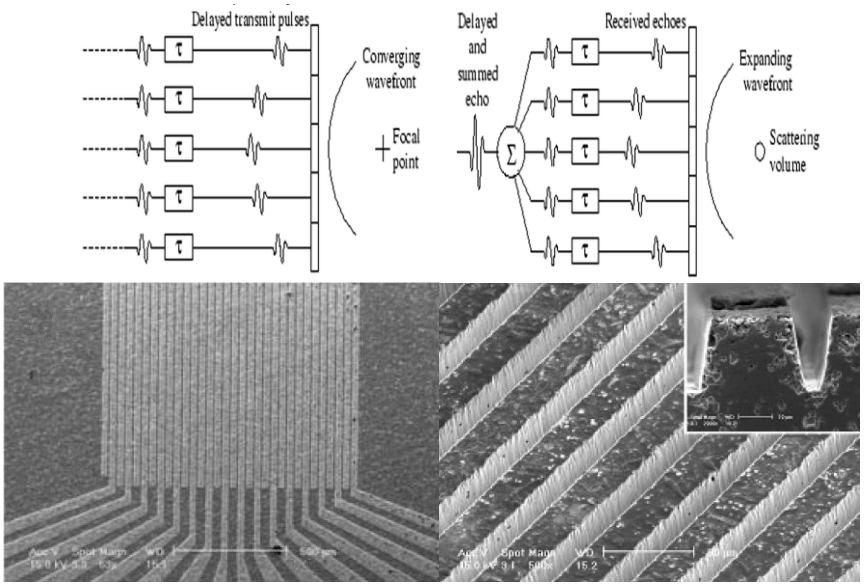

Figure 1.10 A conceptual diagram of phased array beamforming. (top-left)Appropriately delayed pulses are transmitted (top-right) The echoes returning are likewise delayed. SEM pictures of etched bulk PZT structures (bottom-left) top view, (bottom-right) 45 °cross-section view.

1.3.2 Acoustic wave sensors

Acoustic wave sensors are so named because their detection mechanism is based on the case of a mechanical or acoustic wave. The acoustic wave sensors are well-known to be high-resolution, low-cost, mass sensing devices[63][64]. The amplitude and the velocity of acoustic waves are affected by the interaction along their propagation path with the media under investigation. The frequency or phase changes can be monitored and analyzed for physical quantity evaluation. The acoustic wave can be generated by piezoelectric, eletrostrictive, magnetostrictive and other mechanisms. The well-known acoustic wave devices are the piezoelectric sensors, such as quartz crystal, lithium niobate and ZnO.

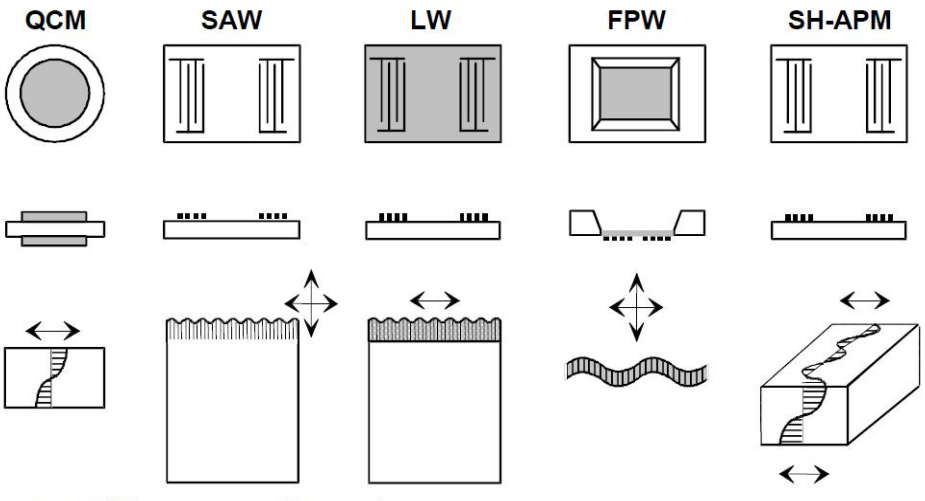

Figure 1.11 Different types of acoustic-wave sensors[65]

When an alternating electric field is applied on the piezoelectric sensors, it can generate a mechanical wave which propagates perpendicularly to the surface of the material (bulk acoustic wave BAW) or on the surface of the material (surface acoustic wave SAW).

- Bulk wave is the wave propagating through the substrate. The direction of the electrical field and the type of piezoelectric material allow choosing the type of the acoustic wave: compressional or shear wave for bulk acoustic wave. A lot of integrated acoustic sensors are based on resonators. The most commonly used bulk acoustic wave (BAW) devices are thickness shear mode (TSM) resonator and shear-horizontal acoustic plate mode (SH-APM).
- Surface wave is the wave propagating on the surface of the substrate. The most widely used surface wave devices are surface acoustic wave (SAW), shear-horizontal surface wave sensor (SH-SAW) sensor, Rayleigh wave sensor.

The different types of acoustic-wave sensors are shown in Figure 1.11. The polarization mode determines the sensors suitability in liquid phase applications.

For example, Rayleigh waves with the sagittal polarization has strong attenuation in liquid sensing due to compression wave has vertical component of particle motion while thickness shear mode (TSM) is widely used in liquid sensing application. The properties of acoustic wave sensors are summarized in Table 1.1. Recently, the biomedical application of acoustic wave based on MEMs techniques focus on the two types of devices: bulk acoustic wave sensors and surface acoustic wave sensors.

Table 1.1. Selected properties of acoustic wave sensor [66]

Property	Love	TSM	SAW	Lamb
Mode	Waveguide	Bulk	Reflected plate	plate
polarization	Shear-hor.	Shear-hor.	Shear-hor.	Sagittal
Frequency(MHz)	50-500	2-20	50-200	1-10
Sensitivity Determined by	Waveguide thickness frequency	Plate thickness	Plate thickness	Membrane thickness
Frequency Determined by	IDT period	Plate thickness	Plate thickness IDT period	Membrane thickness IDT period
Fabrication cost	Cheap	Medium	Expensive	expensive

1.3.2.1 Thickness shear mode

The quartz crystal microbalance (QCM) is a simple, cost effective, high-resolution mass sensing technique. The major advantage of the QCM is a sensitive detection capability for surface mass binging and surface viscoelastic characterization for the bound mass[67].The common frequency for the fundamental mode of quartz of the QCM devices is 5-20 MHz. Quartz crystal are cut in the AT form , at 35 °10' angle from Z-axis as shown in Figure 1.12. This design provides a stable oscillation without temperature fluctuation of frequency.

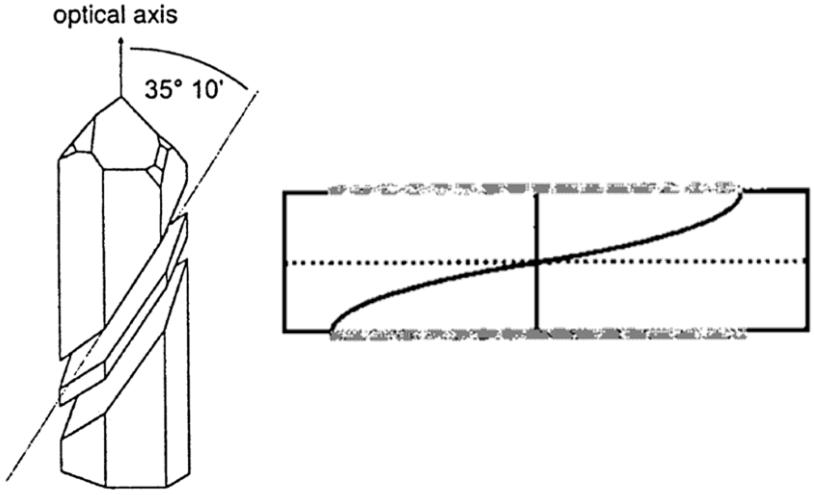

Figure 1.12 AT-cut a quartz crystal from which the metal coated QCM quartz crystals are produced and an on crystal view of the thickness shear mode TSM oscillation[68].

Yin et al. provided a new QCM configuration with ring-electrode piezoelectric sensor (REPs) [69].As shown in Figure 1.13, a ring electrode at the center of the resonant area was able to

monitor the Bovine serum albumin (BSA) absorption in real time. At the same time the design can avoid the direct contact with the liquid phase. The bare quartz surface of REPs can be used to study interface behavior of silicon dioxide face with adsorbate. The adsorption of BSA onto quartz surface is mainly due to the hydrogen bonding and Van Der Waals force. Edvadsson et al. extend the QCM –D technique in dual-frequency mode. They can not only conduct frequency and dissipation measurement, but also influence various surface binding reactions by oscillation amplitudes. The typical amplitude used in traditional decay-based measurements had no influence on any of the systems investigated. While adsorbed vesicles will increase in the shear stress and the kinetics of supported lipid bilayer formation on SiO_2 is influenced at oscillation amplitudes larger than ～11 and ～0.75 nm at 5 and 35MHz, respectively.

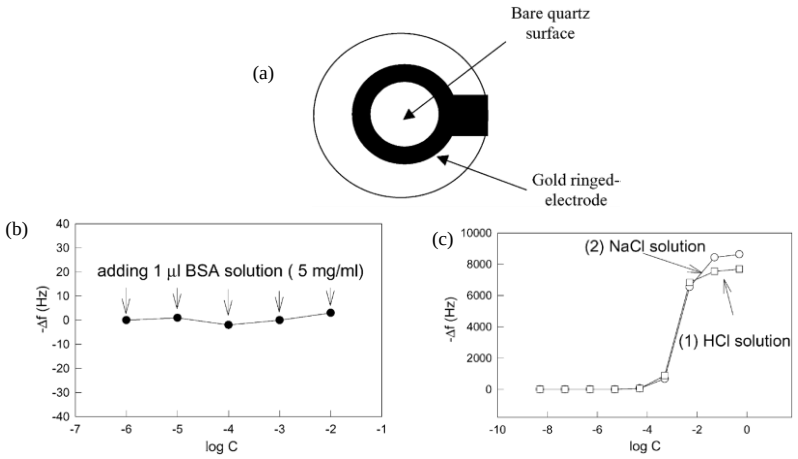

Figure 1.13 Yin. et al. (a) Structure of REPS. (b) The frequency shifts by adding 1 μl BSA to the different concentrqtion NaCl.(c) The frequency shift as a function of the common logarithm of the concentration of HCl or NaCl solution[69].

The thickness shear mode (TSM) resonator has been shown to be an effective functional biosensing device to monitor the process of cell adhesion to a surface in real time. A standing shear wave is generated with the maximum displacement which is sensitive to the surface perturbations [70]. The TSM resonator can be used for immunosensors, which is a very important application[71][72]. In the recent years, monitoring cell behaviors is another important application. TSM resonator can monitor the cell attachment and spreading on resonator surface. Wegener et al. demonstrated that the electrical signals of TSM acoustic wave sensors are affected by many factors, such as cell-substrate interactions, viscoelastic properties of cells, and the properties of the interfacial layer [73]. Li et al. [74] introduced a thickness shear mode (TSM) quartz crystal resonator attached with living cells, can be effectively used as a functional biosensor to determine viscoelastic properties of living cells.

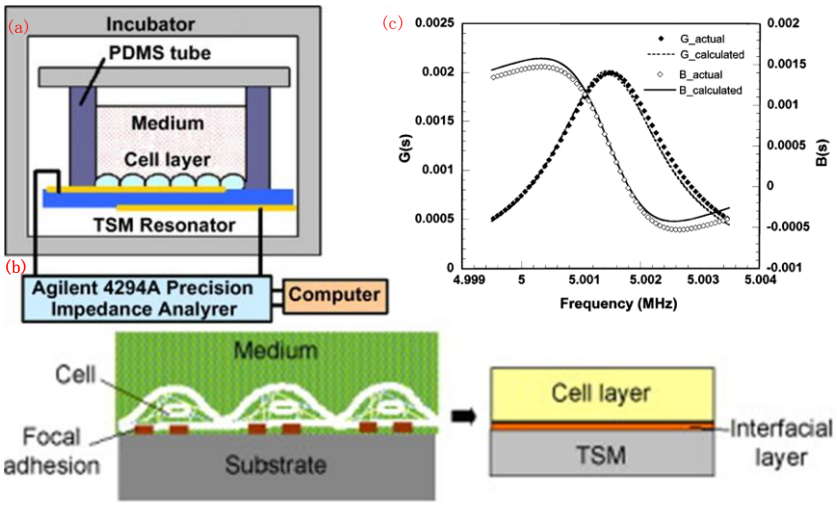

Figure 1.14 (a)steady state of cell adhesion on sensor surface (b) one-dimensional multilayer model of cell adhesion on sensor surface (c)experimental setup of thickness shear mode resonators for cell based functional biosensor [74].

The resonance frequencies of these devices are usually is from 10 to 50 MHz with higher frequencies the devices become too fragile for practical use. However, higher frequencies are most desirable, because the sensitivity increases with increasing frequency [75].

1.3.2.2 SAW based sensors

In general, SAW devices use interdigital transducers (IDT) to generate acoustic waves on the surface of a piezoelectric crystal [76]. The acoustic energy is strongly confined in the range of the acoustic wavelength at the surface[77], so SAW is very sensitive to any changes on the surface, such as mass loading, viscosity and conductivity changes. SAW sensor allow the use of high frequencies in the range of several hundred MHz to GHz, implying higher mass sensitivities

The SAW device is operated by the driving electronics and integrated in a sample flow carrying the analyte. SAW devices generate and detect the acoustic wave by means of IDTs on the surface of a piezoelectric substrate. Analyte-specific molecules (e.g., antibodies) are immobilized on the SAW device to catch analyte molecules (e.g., antigens) from the sample stream. Analytes binding to the immobilized capture molecules will influence the velocity of the SAW and hence the output signal generated by the driving electronics[78].

A ZnO/Si SAW device has been successfully used in the detection of Prostate-specific antigen (PSA) antibody-antigen immuno-reaction as a function of the PSA concentrations [79]. The portable device was integrated with functions of microfluidic transportation and bio-detection. Surface was modified with cystamine self-assembly monolayer and immobilized the anti-PSA antibody. The resonance frequency shifted to the lower range when Prostate-specific antigen-αl –Antichymotrypsin complex attached.

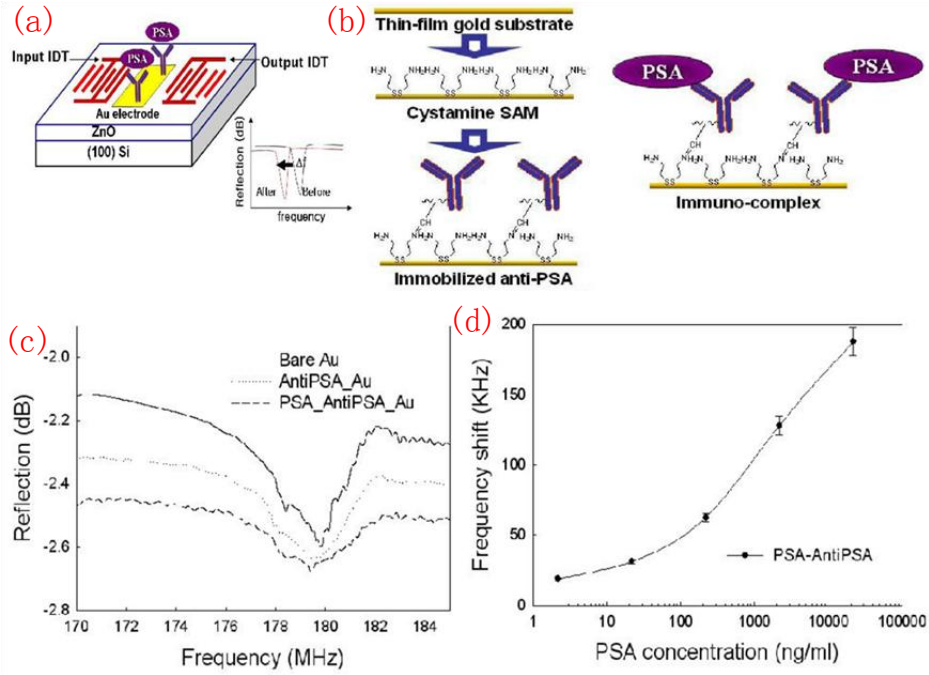

Figure 1.15 (a) working principle of the SAW devices (b) sequential diagram for PSA detection employing SAM layer, anti-PSA, anti-PSA antibody, and PSA antigen on gold electrodes.(c) frequency response curves in SAW biosensors when the anti-PSA antibody and PSA proteins are bounded sequentially on gold electrodes (d) frequency changes as a function of PSA concentration [79].

A big challenge for SAW biosensors is to realize the detection in a liquid environment. SH or Love mode SAW devices are promising technologies for biosensors used in liquid environments because of their high sensitivity and low energy dissipation. There are two optional methods to improve the SAW sensors applied in liquid environment:

1) a protection layer is used to isolate the liquid from the sensors, such as SiO_2[80].

2) High dielectric constant (ε) piezoelectric material is used, such as $LiTaO_3$ (ε= 47).

Chang and Shih [81]worked with SH SAW sensors based on LiTaO3. The device was coated with polyvinyl chloride to support the immobilization of an intermediate layer consisting of fullerene molecules. Hemoglobin was adsorbed on the fullerene surface, and the binding of the corresponding antibody could be detected。 The immobilized protein SAW immunosensors exhibited good sensitivity with low detection limits. Organic and inorganic bio-species in blood show nearly no interference to the sensitivity of the immunosensors. Rebière et al. [82]used a ST-cut quartz substrate with interdigital transducers to fabricate a love wave device for biosensing. Love-wave structure consists in a delay line on a quartz substrate covered by SiO_2 layer acting as a guiding layer on which there is a sensitive layer. Interdigital electrodes (IDTs) are placed parallel to the crystallographic axis (Euler's angle)[83]. When love wave device

and the biological system on SiO_2 layer worked separately, it allows detecting the AM13 sensitive coating as well as the immobilization of the M13 bacteriophages, which provides great potentialities for real time biodetecting.

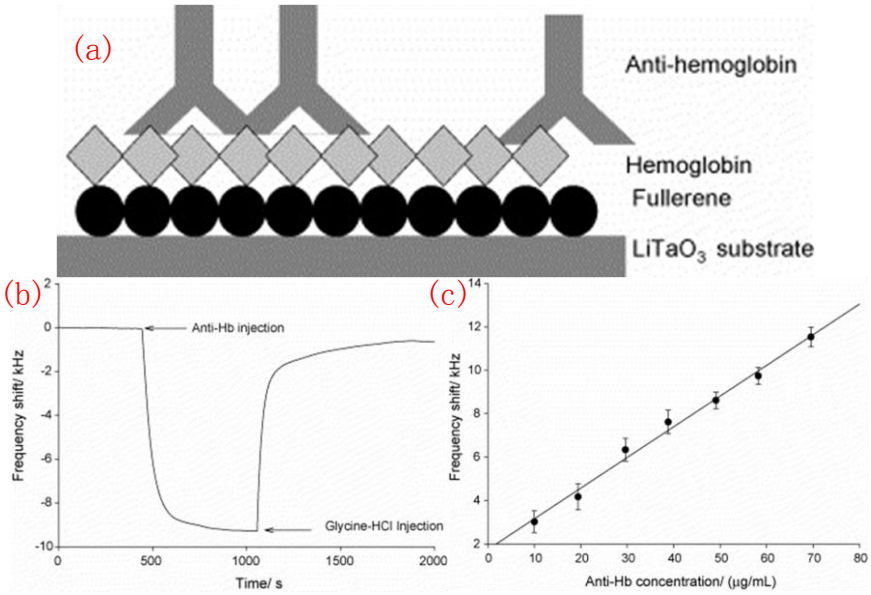

Figure 1.16 (a) Diagram of the C60-Hb-coated LiTaO3 SAW crystal for anti-Hb antibody. (b) Frequency response of a C60-Hb coated SAW immunosensor to anti-Hb antibody. (c) Effect of the concentration of anti-Hb antibody on the frequency response of a C60-Hb coated SAW immunosensor [81].

A microfluidic system integrated surface modified piezoelectric sensor is used for detection of target samples [84]. A nickel pillar array was patterned onto the surface of quartz crystal microbalance to introduce magnetic force control to the piezoelectric sensor. The suspended micro-beads were trapped in fluids onto the nickel pillar array with a controlled magnetic field. Simultaneously the accumulated mass is detected by the piezoelectric sensor. The smart microfluidic system also can be used to capture the cancer cells under magnetic field and obtain the accumulated mass b the piezoelectric sensor. The capturing process and accumulated mass detection are shown in Figure 1.17.

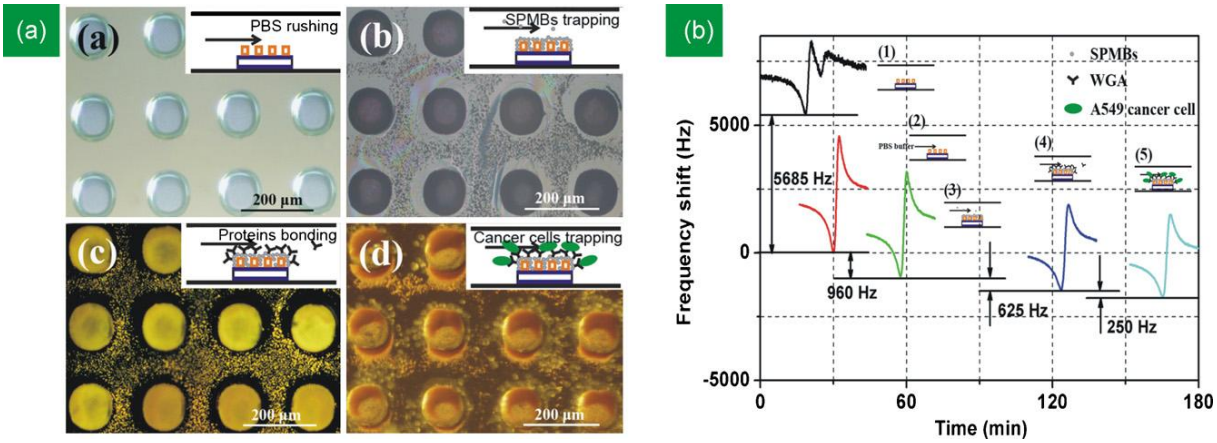

Figure 1.17 (a) Optical images of the capturing process , (b) Monitoring of the capturing process of A549 cancer cells by frequency shift in real time. Microfluidic system in air; (2), (3), (4), and (5) correspond to the processes in optical images (a), (b), (c) and (d) [84].

1.3.2.3 Film bulk acoustic resonator

The FBAR devices are composed of a thin piezoelectric film with two metal electrodes on the both side, which is a sensitive electromechanical devices. An alternative electric field applied on two electrodes generates a thickness longitudinal or shear mode bulk acoustic wave that travelling in the devices and loading material allow non-invasive measurements for the mechanical properties[85].

Firstly a FBAR device is illustrated in Figure 1.18 [86]， the piezoelectric thin film of zinc oxide based on the longitudinal mode can be used for thermal analysis and characterization. Because of good conductivity and affinity, Au is chosen as the electrode which is coated with bio-compatible material for biological application. The Q value of the devices is up to 120 for detection liquid medium improved by integrating the microfluidic channel whose height is comparable to the acoustic wavelength.

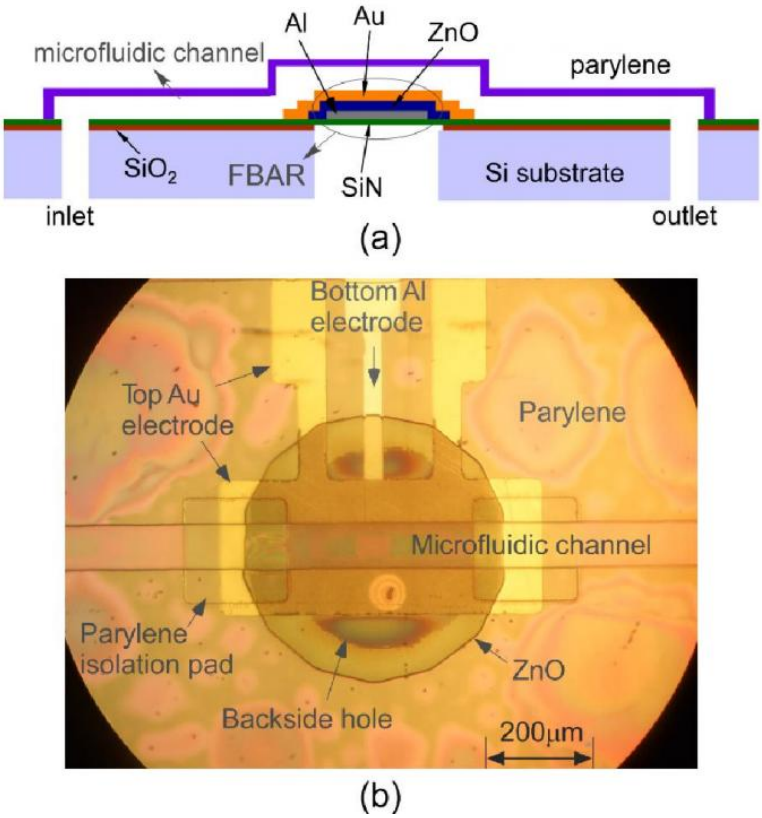

Figure 1.18 (a) Schematic of the FBAR sensor integrated with amicrofluidic channel, (b) Top view of fabricated FBAR sensor; a microchannel is across the FBAR sensor[73].

The second example is a shear mode FBAR devices[87] which is composed of the AlN thin film and microfluidic transport system as shown in Figure 1.19. The deposition of highly textured AlN thin film with uniform c-axis is developed. The backside etching for a cavity is made in the silicon substrate to reduce the liquid damping. The liquid in the microchannel is underneath the bottom electrode of the sensor. The resonator has a 1.2 GHz resonance frequency and a *Q* value in water is around 150.The detection limit of the devices is 0.3 ng/cm^2.

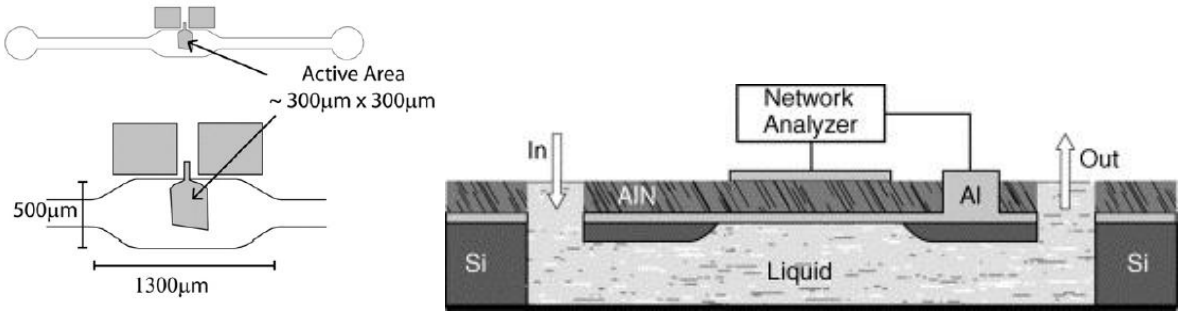

Figure 1.19 (a) Schematic top view of the shear mode FBAR biosensor with an integrated fluidic channel beneath the active area (b) schematic cross section view[74].

1.4 Conclusion and presentation of the concept of our lab on chip

Microfluidics-based analysis systems are powerful tools which facilitate novel experiments and have many applications in chemical and biological systems[88][89], cell analysis and high-throughput biological screening [90][91]. Following their development for genomics and DNA microarrays, microfluidics systems have been used for the integration of other biological analyses or biochemical reactions. The use of small volumes of reagents, the increase in the sensitivity of these microfluidic components and the ability to perform numerous analyses in parallel have widely contributed to the immense interest of lab-on–a-chip [92]. Various sensing technologies have been integrated in microfluidic systems (e.g. optics, RF, acoustics) making it possible to measure different physical properties. Over the last decades, these technologies have also been developed for the integration of actuators in microfluidic systems, including optical and magnetic tweezers [93][94], and electrical forces for manipulating small objects in aqueous solution [95]. The latter require high electrical power. However, the objective of this thesis is to present acoustic sensing applications only.

In recent years, many efforts have been devoted to integrating acoustic techniques in microfluidic systems, such as sensing [96], mixing [97], manipulating [98][99] and trapping [100]. These applications are based mainly on the use of low frequency waves and/or surface acoustic waves. The interest of using BAW for biological applications has been demonstrated with the development of high frequency acoustic microscopy in this domain. It is well known that some pathology modify the elastic properties of biological cells [101]. However, traditional acoustic microscopy is often a bulky, expensive or complex method of characterization, which is hard to integrate for on-line elastic evaluation. The use of some specific structures as reflectors for manipulation has been described before [102][103]. In comparison with the acoustic sensing systems above, high frequency bulk acoustic waves (BAW) have potential applications for the detection of biochemical micro-objects and characterization of the elastic properties of biological cells (e.g. blood cells).

High frequency ultrasonic transducers are now commonly used for high resolution ultrasonic imaging. High frequency transducers have found potential application in microfluidics for biological cell monitoring and in real time tissue differentiation. The combination of Radio-frequency magnetron reactive sputtering and lift-off lithography process can easily be used to realize 1GHz high frequency ZnO transducer for chemical and biological sample sensing. The wavelength of the acoustic beam is in the micro-scale, which can be integrated into microfluidic devices for detecting the mechanical and elasticity properties of single biological cell. Furthermore, the controlled microfluidic flow can be used in order to move the cell in front of the acoustic sensor for high resolution real time image and characterization.

In our case, the aim is to integrate bulk acoustic wave sensors to carry out measurements in a microfluidic channel in order to evaluate the elastic properties of fluids and single biological cells. In this work, we report a novel silicon-based high frequency (GHz range) bulk acoustic wave (BAW) sensing microsystem. BAWs are generated using miniature piezoelectric transducers (thin ZnO films can be easily used to integrate low power, high frequency transducers) and guided using acoustical mirrors parallel to the surface of the silicon wafer. The acoustic wave is then transmitted through the microfluidic channel manufactured using deep reactive-ion etching. Other easier methods exist for reflecting or scattering surface acoustic waves in microfluidic applications [104][105], but for the potential applications of our design, the components for acoustic wave guiding (such as cylindrical lenses or lenses with irregular curved surfaces which can control the phase of the acoustic beam) are easy to integrate using MEMs dry etching technology. Due to the non-contact nature and high resolution of acoustic waves in the field of non-integrated acoustic microscopy (a spatial resolution of one wavelength could be assumed, that is 1.5 μm at a frequency of 1GHz), such microfluidics-based high frequency BAW platforms are suitable for non-destructive characterization and detection in microfluidic channels.

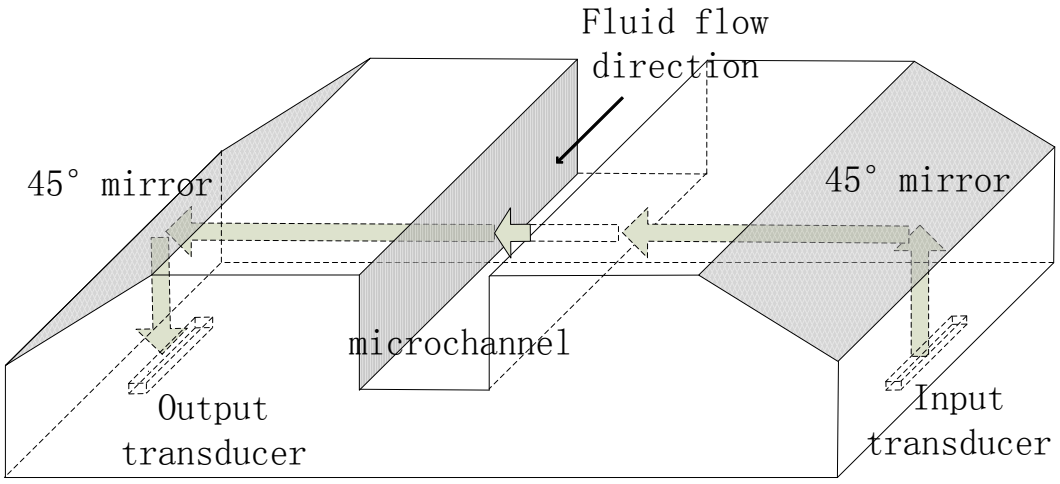

Figure 1.20 The scheme of our lab on chip (international patent; publication number WO2010/072944) [106]

As mentioned previously, the MEMs technologies provide the opportunities to achieve the devices miniaturization. In order to realize the micro devices with easy integration and multi-function, we design a microfluidic device for characterization and detection. This dissertation reports the microsystem fabrication and the optimization for the sake of increasing signal to noise ratio. Then the concentration characterization of chemical solution, particle detection, and blood cell characterization have been realized in our microsystem.

2 Acoustic waves propagation in our microsystem: theoretical aspects and modeling

2.1 Introduction

In our microsystem, acoustic transmission components and 1GHz thin film piezo-transducers are integrated on a silicon substrate. Firstly we present the back ground on acoustic waves and study the elastic wave propagation in three different media. Later we focus on the study of continuity conditions at the interface of two different materials (e.g. solid-air,) and we turn to study the elastic wave motion in piezoelectric solid. Finally we will evaluate the expected performance in different parts of microsystem in terms of mechanical and electrical impedance matching.

The rupture of acoustic impedances between two media has a great influence on acoustic characterization, so we need to realize the mechanical impedance matching. The material used for silicon-water interface matching is the anti-reflection layers of quarter wave length of silicon oxide which makes it possible to reduce the losses. At the same time, the silicon oxide coating layer between the solid media and gas media also plays an important role in the acoustic wave reflection.

2.1.1 Basic concept of acoustic waves

A solid is elastic if it returns to its initial state when the external forces responsible for deformations are removed. This return to the initial state is the work of internal stresses.

In a non-piezoelectric elastic solid, there is a relation between the stress and the strain. Experimental evidence shows that the elastic behavior of most substances is well described by the first-order term of Taylor expansion for the stress, with small deformations[107].

$$T_{ij}(\zeta_{kl}) = T_{ij}(0) + \left(\frac{\partial T_{ij}}{\partial \zeta_{kl}}\right)\Bigg|_{\zeta_{kl}=0} \cdot \zeta_{kl} + \frac{1}{2}\left(\frac{\partial^2 T_{ij}}{\partial \zeta_{kl}\partial \zeta_{mn}}\right)_{\substack{\zeta_{kl}=0 \\ \zeta_{mn}=0}} \zeta_{kl}\zeta_{mn} + ... \; i,j,k,l,m,n = 1,2,3 \quad (2.1)$$

Since $T_{ij}(0)=0$, it obtains

$$T_{ij} = c_{ijkl} \cdot \zeta_{kl} \quad (2.2)$$

Where we define $c_{ijkl} = \left(\frac{\partial \mathrm{T}_{ij}}{\partial \zeta_{kl}} \right)\Big|_{\zeta_{kl}=0}$, the coefficients c_{ijkl} are components of the rank four stiffness tensor which expresses the most general possible linear relation between the second rank tensors T_{ij} (the mechanical internal stress) and ζ_{kl} (mechanical strain). It was first stated by Hooke.

A four rank tensor has 81 components. Because the tensors of T_{ij} and ζ_{kl} are symmetric, Hooke's law becomes

$$\mathrm{T}_{ij} = \frac{1}{2} c_{ijkl} \cdot \frac{\partial u_k}{\partial x_l} + \frac{1}{2} c_{ijkl} \cdot \frac{\partial u_l}{\partial x_k}$$

Since $c_{ijkl} = c_{ijlk}$,

$$\mathrm{T}_{ij} = c_{ijkl} \cdot \frac{\partial u_l}{\partial x_k} \tag{2.3}$$

The above symmetry relations reduce the number of independent elastic constants to 36. A pair of indices (i, j) can give only six independent values as follow:

Table 2.1 Index and notation of the matrix

Tensor Index	11	22	33	23,32	13,31	12,21
Contracted index	1	2	3	4	5	6

The independent elastic moduli can thus be represented in terms of only two indices α and β , thus Hooke's law can be written

$$\mathrm{T}_{\alpha} = c_{\alpha\beta} \cdot \zeta_{\beta} \tag{2.4}$$

It is usual to adopt the convention $\mathrm{T}_{\alpha} = \mathrm{T}_{ij}$

However, it must be noted that this requires ζ_{β} defined as

$$\zeta_1 = \zeta_{11},\ \zeta_2 = \zeta_{22},\ \zeta_3 = \zeta_{33},\ \zeta_4 = 2\zeta_{23},\ \zeta_5 = \zeta_{13},\ \zeta_6 = \zeta_{12} \tag{2.5}$$

The mechanical strain ζ_{ij} of equation 2.1is defined as Cauchy's infinitesimal strain tensor:

$$\zeta_{ij} = \frac{1}{2}\cdot\left(\frac{\partial u_i}{\partial x_j} + \frac{\partial u_j}{\partial x_i}\right)(i, j = 1,2,3) \tag{2.6}$$

According to the Maxwell's relation which is valid for all solids $c_{\alpha\beta} = c_{\beta\alpha}$,

The 6×6 matrix of the coefficients $c_{\alpha\beta}$ is therefore symmetric, so that

$$c_{\alpha\beta} = \begin{pmatrix} c_{11} & c_{12} & c_{13} & c_{14} & c_{15} & c_{16} \\ c_{12} & c_{22} & c_{23} & c_{24} & c_{25} & c_{26} \\ c_{13} & c_{23} & c_{33} & c_{34} & c_{35} & c_{36} \\ c_{14} & c_{24} & c_{34} & c_{44} & c_{45} & c_{46} \\ c_{15} & c_{25} & c_{35} & c_{45} & c_{55} & c_{56} \\ c_{16} & c_{26} & c_{36} & c_{46} & c_{56} & c_{66} \end{pmatrix} \tag{2.7}$$

This property reduces the number of independent components to 21.

To the isotropic solid, the elastic tensor c_{ijkl} must be invariant for any change of axes-rotation. The only quantities unaffected by these orthogonal transformations are a scalar tensor δ_{ij}. Because of the symmetry $\delta_{ij} = \delta_{ji}$ the tensor takes the form[108]

$$c_{ijkl} = \lambda\delta_{ij}\delta_{kl} + \mu(\delta_{ik}\delta_{jl} + \delta_{il}\delta_{jk}) \tag{2.8}$$

Thus, the properties of an isotropic solid are specified by two independent constants, the tensor gives the form

$$\mathrm{T}_{ij} = \lambda\zeta\delta_{ij} + 2\mu\zeta_{ij} \tag{2.9}$$

Where $\zeta = \zeta_{11} + \zeta_{22} + \zeta_{33}$

Assigning values of $c_{\alpha\beta}$ [109]

$$c_{11} = c_{22} = c_{33} = \lambda + 2\mu$$
$$c_{12} = c_{23} = c_{13} = \lambda \qquad (2.10)$$
$$c_{44} = c_{55} = c_{66} = \mu$$

Where λ and μ are the Lam éparameters.

The other twelve moduli c_{ijkl} are zero since they have an odd number of distinct indices. The matrix $c_{\alpha\beta}$ takes the following form

$$c_{\alpha\beta} = \begin{pmatrix} c_{11} & c_{12} & c_{12} & 0 & 0 & 0 \\ c_{12} & c_{11} & c_{12} & 0 & 0 & 0 \\ c_{12} & c_{12} & c_{11} & 0 & 0 & 0 \\ 0 & 0 & 0 & c_{44} & 0 & 0 \\ 0 & 0 & 0 & 0 & c_{44} & 0 \\ 0 & 0 & 0 & 0 & 0 & c_{44} \end{pmatrix} \quad isotropic \qquad (2.11)$$

2.2 Waves propagation theory

2.2.1 Acoustic wave equation in the solid media

We consider a disturbance which propagates through the solid which is locally in motion. The displacement u_i with coordinates x_k varies with time, so that $u_i = u_i(x_k, t)$. The equation of motion follows the Newton's law:

$$\frac{\partial}{\partial x_j} \mathrm{T}_{ij} = \rho \frac{\partial^2 u_i}{\partial t^2} \qquad (2.12)$$

The Hooke's law is written as:

$$\mathrm{T}_{ij} = c_{ijkl} \cdot \frac{\partial u_l}{\partial x_k}$$

and combining this with Eq. (2.12) :

$$\frac{\partial}{\partial x_j}\left(c_{ijkl} \cdot \frac{\partial u_l}{\partial x_k} \right) = \rho \frac{\partial^2 u_i}{\partial t^2} \qquad (2.13)$$

For homogeneous materials in which elastic constants and density are constant, the equation

can be represented as:

$$c_{ijkl} \cdot \frac{\partial^2 u_l}{\partial x_j \partial x_k} = \rho \frac{\partial^2 u_i}{\partial t^2} \tag{2.14}$$

Considering harmonic plane waves moving through a homogeneous or anisotropic medium,

$$u_i = U_i e^{j(k_j \cdot x_j - \omega t)} = U_i e^{j(k \cdot n_j x_j - \omega t)} \tag{2.15}$$

Where U_i is the displacement amplitude vector component, k_j is the wave number vector component and k is the modulus and n_j is the unit vector of the direction.

Replacing the (2.15) into (2.14), we can obtain:

$$c_{ijkl} \cdot n_j n_k U_l = \rho v_p^2 U_i \tag{2.16}$$

This is known as Christoffel's equation. $v_p = \frac{\omega}{k}$ corresponds to the phase velocity of the plane wave. U_i is the polarization

And the Eq. 2.13 can be written in the Christoffel matrix.

$$[\Gamma_{il} - \delta_{il} \rho v_p^2] U_k = 0 \tag{2.17}$$

Where $\Gamma_{il} = c_{ijkl} \cdot n_j n_k$ known as the Christoffel tensor. The eigenvalues and associated eigenvectors of the Christoffel matrix Γ_{il} are ρv_p^2 and U_k, which correspond to respectively the solutions for the phase velocity v_p and the polarization of plane wave.

For a given direction, there are in general three phase velocities which are the solutions of the secular equation

$$\left| \Gamma_{il} - \delta_{il} \rho v_p^2 \right| = 0 \tag{2.18}$$

expressing the compatibility condition for the three homogeneous equations. For each velocity there is a corresponding eigenvector giving the direction of the displacement of the material.

Expanding the sum over the indices j and k gives

$$\Gamma_{il} = c_{i11l}n_1^2 + c_{i22l}n_2^2 + c_{i33l}n_3^2 + (c_{i12l} + c_{i21l})n_1 n_2 + (c_{i13l} + c_{i31l})n_1 n_3 + (c_{i23l} + c_{i32l})n_2 n_3 \quad (2.19)$$

So the Christoffel matrix components Γ_{il} can be represented as:

$$\begin{aligned}
\Gamma_{11} &= c_{11}n_1^2 + c_{66}n_2^2 + c_{55}n_3^2 + 2c_{56}n_2n_3 + 2c_{15}n_3n_1 + 2c_{16}n_1n_2 \\
\Gamma_{22} &= c_{66}n_1^2 + c_{22}n_2^2 + c_{44}n_3^2 + 2c_{24}n_2n_3 + 2c_{46}n_3n_1 + 2c_{26}n_1n_2 \\
\Gamma_{33} &= c_{55}n_1^2 + c_{44}n_2^2 + c_{33}n_3^2 + 2c_{34}n_2n_3 + 2c_{35}n_3n_1 + 2c_{45}n_1n_2 \\
\Gamma_{23} = \Gamma_{21} &= c_{56}n_1^2 + c_{24}n_2^2 + c_{34}n_3^2 + (c_{23} + c_{44})n_2n_3 + (c_{36} + c_{45})n_3n_1 + (c_{25} + c_{46})n_1n_2 \\
\Gamma_{13} = \Gamma_{31} &= c_{15}n_1^2 + c_{46}n_2^2 + c_{35}n_3^2 + (c_{36} + c_{45})n_2n_3 + (c_{13} + c_{55})n_3n_1 + (c_{14} + c_{56})n_1n_2 \\
\Gamma_{12} = \Gamma_{32} &= c_{16}n_1^2 + c_{26}n_2^2 + c_{45}n_3^2 + (c_{25} + c_{46})n_2n_3 + (c_{14} + c_{56})n_3n_1 + (c_{12} + c_{66})n_1n_2
\end{aligned} \quad (2.20)$$

The polarization vectors are orthogonal. If propagation direction of waves is parallel to polarization direction, such waves are longitudinal waves (compression waves); if propagation direction of waves is perpendicular to polarization direction, such waves is shear waves (transversal waves). In a general anisotropic solid (for example, microsystem fabricated with Si wafer) usually has one quasi-longitudinal wave and two quasi-shear waves.

Figure 2.1 illustrates an example of the velocity surfaces for a non piezoelectric material as silicon single crystal has a cubic (m3m) symmetry that has the same velocity sections in the planes {001}, {010} and {100}

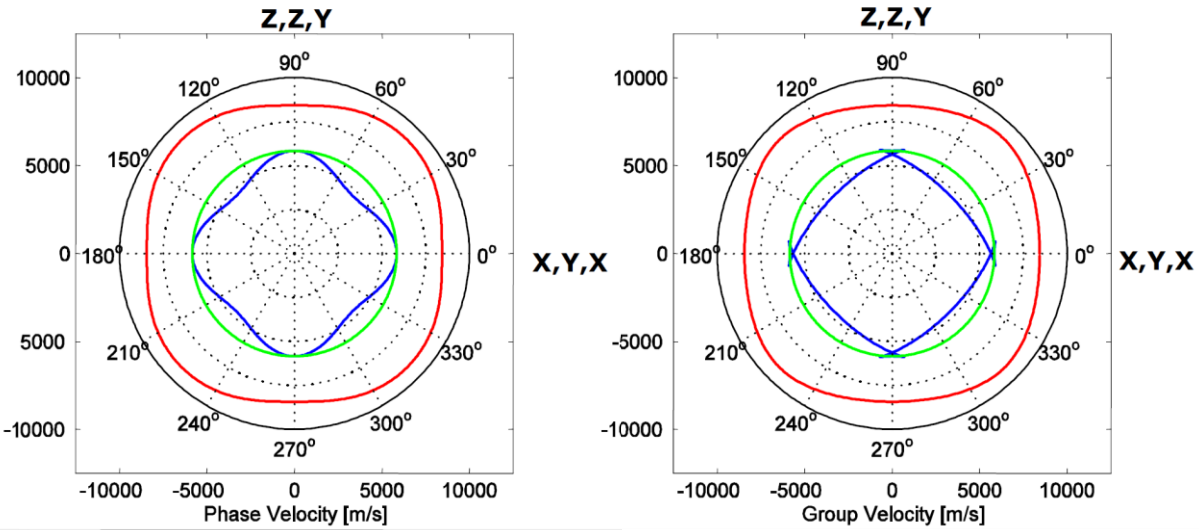

Figure 2.1 Sections of the phase velocity and the group velocity surfaces for silicon in {001}, {010}] and {100} planes (red line for quasi-longitudinal wave, blue and green lines for two quasi-shear waves) [110].

For an isotropic solid, the tensor Γ is independent of the propagation direction, being the same as that for propagation along an axis. For propagation along z axis ($n_1 = n_2 = 0, n_3 = 1$), the tensor Γ_{il} becomes

$$\Gamma_{ij} = c_{i33l} = \begin{bmatrix} c_{55} & c_{45} & c_{35} \\ c_{45} & c_{44} & c_{34} \\ c_{35} & c_{34} & c_{33} \end{bmatrix} \tag{2.21}$$

and combining Eq.(2.21) with Eq. (2.11) for the stiffness constants

$$\Gamma = \begin{bmatrix} c_{44} & 0 & 0 \\ 0 & c_{44} & 0 \\ 0 & 0 & c_{11} \end{bmatrix} \quad isotropic$$

2.2.2 Acoustic wave equation in the piezoelectric media

This Hooke's law relation does not fully describe the response of a solid to acoustic strain. Piezoelectric materials will be electrically polarized when they are strained. This direct piezoelectric effect experimentally manifests itself by the appearance of bound electrical charges at the surfaces of a strained medium. It is a linear phenomenon, and polarization changes sign when the sign of the strain is reversed. The direct piezoelectric effect is always accompanied by the converse piezoelectric effect, whereby a solid becomes strained when placed in an electric field.

In the case of piezoelectric solid, the Hooke's Law for non-piezoelectric solid Eq. (2.2) should be induced by electric field

$$\mathrm{T}_{ij} = c^{E}_{ijkl} \cdot \zeta_{kl} - e_{kij} E_k \tag{2.22}$$

c^{E}_{ijkl} means these constants describe elastic properties measured under constant electric field.

E_k is the electric field and e_{kij} is the proportionality piezoelectric constant tensor.

The constitutive relation of the electric displacement is $D_j = \varepsilon_{jk} E_k$ is induced

$$D_j = \varepsilon^{\zeta}_{jk} E_k + e_{jkl} \zeta_{kl} \tag{2.23}$$

Piezoelectric constants e_{jkl} relate changes of displacement D_j to strain ζ_{kl} in the solid, with the electric field held constant, so that

$$e_{jkl} = \left(\frac{\partial D_j}{\partial \zeta_{kl}} \right)_E \tag{2.24}$$

Since $\zeta_{kl} = \zeta_{lk}$, the tensor e_{jkl} is symmetric with respect to the last two indices, so that $e_{jkl} = e_{jlk}$. Thus the number of independent constants is reduced from 27 to 18

Derived the wave propagation in piezoelectric solid, consider Eqs. (2.14)and(2.22)

$$c_{ijkl}^E \frac{\partial^2 u_l}{\partial x_j \partial x_k} - e_{kij} \frac{\partial E_k}{\partial x_j} = \rho \frac{\partial^2 u_i}{\partial t^2} \tag{2.25}$$

If coupling Eq.(2.25) with the Maxwell's electromagnetic wave equation and assumed in an unbounded solid material, by comparison with the influence of the quasi-static electric field, the associated electromagnetic wave can be negligible [127]. The quasi-electric field E_k is related to the scalar electric potential ϕ

$$E_k = -\frac{\partial \phi}{\partial x_k} \tag{2.26}$$

The electric displacement satisfy the Poisson equation in a free charged isolate medium

$$\frac{\partial D_j}{\partial x_j} = 0 \tag{2.27}$$

Substituting respectively Eq.(2.26) and (2.27) into Eq. (2.25)and (2.23), we can obtain:

$$\begin{cases} c_{ijkl}^E \dfrac{\partial^2 u_l}{\partial x_j \partial x_k} + e_{kij} \dfrac{\partial^2 \phi}{\partial x_j \partial x_k} = \rho \dfrac{\partial^2 u_i}{\partial t^2} \\ e_{jkl} \dfrac{\partial^2 u_l}{\partial x_j \partial x_k} + \varepsilon_{jk}^{\zeta} \dfrac{\partial^2 \phi}{\partial x_j \partial x_k} = 0 \end{cases} \tag{2.28}$$

Supporting the plane waves propagate in a given direction:

$$u_i = U_i e^{j(k \cdot n_j x_j - \omega t)}, \phi = \Phi e^{j(k \cdot n_j x_j - \omega t)} \tag{2.29}$$

Eq. (2.28) is replaced by Eq.(2.29):

$$\begin{cases} c_{ijkl}^{E} k^2 n_j n_k U_l + e_{kij} k^2 n_j n_k \Phi = \rho\omega^2 U_i \\ e_{jkl} k^2 n_j n_k U_l + \varepsilon_{jk}^{\zeta} k^2 n_j n_k \Phi = 0 \end{cases} \tag{2.30}$$

As $v_p = \dfrac{\omega}{k}$, Eqs. (2.30) can be written as:

$$\left(c_{ijkl}^{E} n_j n_{kl} + \frac{\left(e_{kij} n_j n_k\right)\left(e_{jkl} n_j n_k\right)}{\varepsilon_{jk}^{\zeta} n_j n_k} \Phi \right) U_l = \rho v_p^2 U_i \tag{2.31}$$

As $\gamma_l = e_{jkl} n_j n_k$ and $\varepsilon^{\zeta} = \varepsilon_{jk}^{\zeta} n_j n_k$,

$$\left[\left(\Gamma_{il} + \frac{\gamma_i \gamma_l}{\varepsilon^{\zeta}} \right) - \partial_{ij} \rho v_p^2 \right] U_k = 0 \tag{2.32}$$

It has nearly the same form as the Christoffel equation (2.17) for non-piezoelectric materials. $\Gamma_{il} + \dfrac{\gamma_i \gamma_l}{\varepsilon^{\zeta}}$ is called piezoeletrically stiffened elastic constant. In the matrix coefficient subscripts, the equivalent Christoffel matrix components Γ_{il} and $\dfrac{\gamma_i \gamma_l}{\varepsilon^{\zeta}}$ can be calculated by Eqs. (2.15) and Eqs (2.26)

$$\begin{gathered} \gamma_1 = e_{11} n_1^2 + e_{26} n_2^2 + e_{35} n_1^2 + (e_{25} + e_{36}) n_2 n_3 + (e_{15} + e_{31}) n_3 n_1 + (e_{16} + e_{21}) n_1 n_2 \\ \gamma_2 = e_{16} n_1^2 + e_{22} n_2^2 + e_{34} n_1^2 + (e_{24} + e_{32}) n_2 n_3 + (e_{14} + e_{36}) n_3 n_1 + (e_{12} + e_{26}) n_1 n_2 \\ \gamma_3 = e_{15} n_1^2 + e_{24} n_2^2 + e_{33} n_1^2 + (e_{23} + e_{24}) n_2 n_3 + (e_{13} + e_{35}) n_3 n_1 + (e_{14} + e_{25}) n_1 n_2 \\ \varepsilon^{\zeta} = \varepsilon_{11}^{\zeta} n_1^2 + \varepsilon_{22}^{\zeta} n_2^2 + \varepsilon_{33}^{\zeta} n_1^2 + 2\varepsilon_{23}^{\zeta} n_2 n_3 + 2\varepsilon_{13}^{\zeta} n_3 n_1 + 2\varepsilon_{12}^{\zeta} n_1 n_2 \end{gathered} \tag{2.33}$$

As $c_{ijkl}^{D} = c_{ijkl}^{E} + \dfrac{\left(e_{kij} n_k\right)\left(e_{jkl} n_j\right)}{\varepsilon_{jk}^{\zeta} n_j n_k}$ and $\overline{\Gamma_{il}} = c_{ijkl}^{D} n_j n_k$,, Eq. (2.32) can be deduced as:

$$\left[\overline{\Gamma_{il}} - \partial_{ij} \rho v_p^2 \right] U_k = 0 \tag{2.34}$$

Due to the piezoelectric effect, the stiffness changes can be expressed by

$$c_{ijkl}^{D} = c_{ijkl}^{E} \left(1 + \frac{\Delta c_{ijkl}^{E}}{c_{ijkl}^{E}} \right) = c_{ijkl}^{E} \left(1 + \mathrm{K}^2 \right) \tag{2.35}$$

$\mathrm{K} = \left(\frac{\Delta c_{ijkl}^{E}}{c_{ijkl}^{E}} \right)^{1/2}$ is a parameter describing piezoelectricity effect which depends on the propagation direction. Thus, the phase velocity of a piezoelectric material can be solved by Christoffel equation (2.34)

$$v_p = \sqrt{\frac{c^D}{\rho}} = \sqrt{\frac{c^E + e^2/\varepsilon^\zeta}{\rho}} = \sqrt{\frac{c^E}{\rho}\left(1+\mathrm{K}^2\right)} \tag{2.36}$$

Without considering the piezoelectricity effect, a virtual phase velocity $\overline{v_p}$:

$$\overline{v_p} = \sqrt{\frac{c^E}{\rho}} \tag{2.37}$$

So

$$\mathrm{K}^2 = \left(v_p / \overline{v_p}\right)^2 - 1 \tag{2.38}$$

The electromechanical coupling constant k_t is defined:

$$k_t^2 = \frac{\mathrm{K}^2}{1+\mathrm{K}^2} \tag{2.39}$$

Δv is the difference between v_p and $\overline{v_p}$ which is much smaller, so k_t is estimated approximately by

$$\begin{aligned} k_t^2 &= 1 - \frac{\overline{v_p}^2}{{v_p}^2} = \frac{(2v_p - \Delta v)\Delta v}{{v_p}^2} \cong \frac{2\Delta v}{v_p} \\ \mathrm{K}^2 &= \left(v_p / \overline{v_p}\right)^2 - 1 = \frac{(2v_p - \Delta v)\Delta v}{\overline{v_p}^2} \cong \frac{2\Delta v}{\overline{v_p}} \end{aligned} \tag{2.40}$$

Eq. (2.40) shows there is no obvious difference between K and k_t, which means the piezoelectric effect of materials is small.

Zinc oxide is a popular piezoelectric material for high frequency ultrasonic transducer, which has been widely used. As shown in Figure 2.2, the maximum k_t value of longitudinal mode is 0.27 in the direction of z axis.

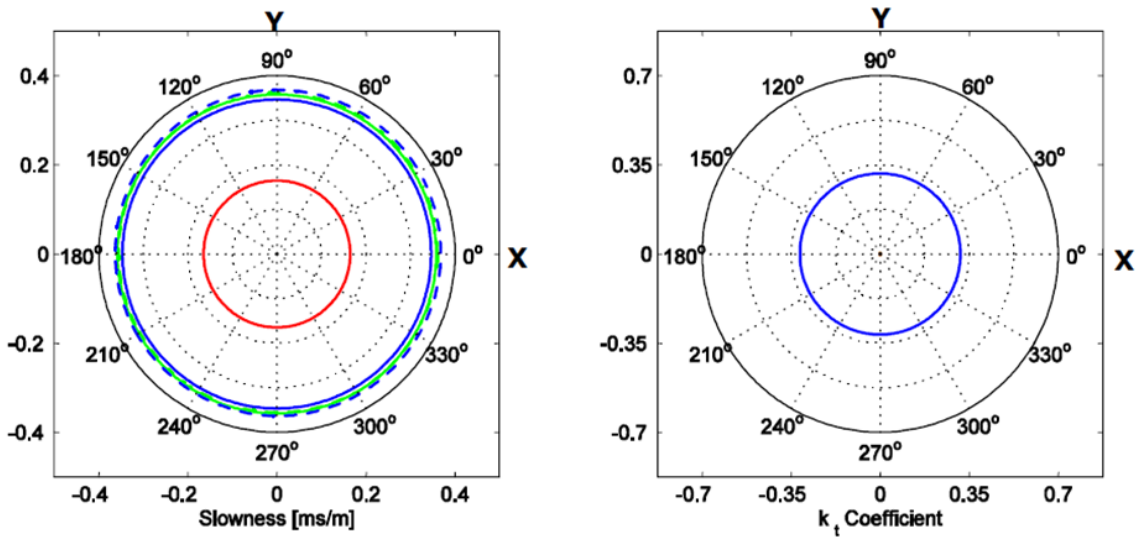

Figure 2.2 Sections of the slowness and the electromechanical coupling coefficient surfaces k_t *for ZnO (class: hexagonal 6mm) (dashed lines correspond to the inactive piezoelectric-effect slowness curves; line in red for quasi-longitudinal wave; lines in blue and green for two fast and slow quasi-transversal waves)* [110].

2.3 Acoustic Waves reflection and transmission

2.3.1 Acoustic wave reflection on solid-air interface (Normal incidence)

A plane wave encountering an interface between two materials is divided into two components: some energy at the interface is transmitted and the other is reflected. Consider an incident harmonic plane wave σ_I traveling in x direction to an interface for normal incidence, as shown in Figure 2.3. A part of the wave is reflected σ_R and the other part is transmitted σ_I

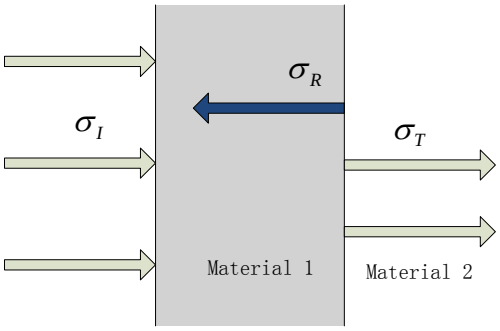

Figure 2.3 Normal incidence

Since the elastic field is independent of the y direction, all derivatives with respect to y will vanish from the equations of motion. In this simple case, the governing equation is applicable for either longitudinal or shear waves

$$\frac{\partial^2 u_x}{\partial x^2} = \frac{1}{v_p^2}\frac{\partial^2 u_x}{\partial t^2} \tag{2.41}$$

Consider the incident waveform as

$$u_x^I = A_I e^{i(k_1 x - \omega t)}, \quad k_1 = \frac{\omega}{v_p^{(1)}}. \tag{2.42}$$

In this case the reflected field can be written as

$$u_x^R = A_R e^{-i(k_1 x - \omega t)} \tag{2.43}$$

The transmitted field in the second medium is

$$u_x^T = A_T e^{i(k_2 x - \omega t)}, k_2 = \frac{\omega}{v_p^{(2)}}$$

A_I is the displacement amplitude of incident waves, A_R and A_T are the displacement amplitude of reflected and transmitted waves.

Boundary conditions are as follow:

$$\begin{aligned} u^{(1)}\Big|_{x=0} &= u^{(2)}\Big|_{x=0} \\ \mathrm{T}_x^{(1)}\Big|_{x=0} &= \mathrm{T}_x^{(2)}\Big|_{x=0} \\ \mathrm{T}_{xy}^{(1)}\Big|_{x=0} &= \mathrm{T}_{xy}^{(2)}\Big|_{x=0} \end{aligned} \tag{2.44}$$

According the boundary condition， we obtain

$$A_I + A_R = A_T \tag{2.45}$$

For one-dimensional case, the generalized Hooke's Law is

$$\begin{aligned} \mathrm{T}_x &= (\lambda + 2\mu) \cdot \frac{\partial u_x}{\partial x} \\ \mathrm{T}_{xy} &= 0 \end{aligned} \tag{2.46}$$

According the boundary condition， we obtain

$$\rho_1 v_p^{(1)} (A_I - A_R) = \rho_2 v_p^{(2)} \cdot A_R \tag{2.47}$$

Solution of Eq. (2.45) and Eq. (2.47) gives

$$\begin{aligned} A_R &= \frac{\rho_1 v_p^{(1)} - \rho_2 v_p^{(2)}}{\rho_1 v_p^{(1)} + \rho_2 v_p^{(2)}} \cdot A_I \\ A_R &= \frac{2\rho_1 v_p^{(1)}}{\rho_1 v_p^{(1)} + \rho_2 v_p^{(2)}} \cdot A_I \end{aligned} \tag{2.48}$$

Defining acoustic impedance as $Z = \rho v_p$, the reflection coefficient can be written as

$$R = \left. \frac{\mathrm{T}_x^{(R)}}{\mathrm{T}_x^{(I)}} \right|_{x=0} = -\frac{A_R}{A_I} = \frac{Z_2 - Z_1}{Z_1 + Z_2};$$

The transmission coefficient is

$$T = \left. \frac{\mathrm{T}_x^{(T)}}{\mathrm{T}_x^{(I)}} \right|_{x=0} = \frac{(\lambda_2 + 2\mu_2) k_2}{(\lambda_1 + 2\mu_1) k_1} \cdot \frac{A_T}{A_I} = \frac{2Z_2}{Z_1 + Z_2}$$

The formula for energy partition at the interface into transmission and reflection modes can be derived by considering energy as proportional to the square of the pressure magnitude. The energy flow per unit area normal to the direction of propagation is defined as the intensity of the wave (I_I , I_R or I_T).The intensity is evaluated over on cycle and depends on the amplitude as follows [111]:

$$\mathrm{I}_R = \frac{A_R^2}{2\rho_1 v_p^{(1)}}, \mathrm{I}_T = \frac{A_T^2}{2\rho_2 v_p^{(2)}}$$

2.3.2 Oblique incidence at a solid-air interface

In the case of a free boundary surface, well approximated by a solid in contact with air, there is no transmitted wave. The only boundary condition to be satisfied is that the mechanical traction must be zero at all point on the surface

Continuity of the displacements u_i and mechanical tractions T_i are expressed by

$$\begin{cases} u_i^I + \sum_R u_i^R = \sum_T u_i^T \\ T_i^I + \sum_R T_i^R = \sum_T T_i^T \end{cases} \tag{2.49}$$

For mechanical tractions $T_i = T_{ij} l_j$, we use Hooke's law to obtain

$$T_{ij} = c_{ijkl} \frac{\partial u_k}{\partial x_l} = -ic_{ijkl} k_l U_k e^{i(\omega t - \mathbf{k}\cdot\mathbf{x})} \tag{2.50}$$

And this gives

$$c_{ijkl} l_j (k_l^I U_k^I + \sum_R k_l^R U_k^R) = c'_{ijkl} l_j \sum_T k_l^T U_k^T \tag{2.51}$$

Where c'_{ijkl} denotes the stiffness constants of the adjacent media.

Thus $T_{ij} l_j = 0$, giving

$$c_{ijkl} l_j (k_l^I U_k^I + \sum_R k_l^R U_k^R) = 0 \tag{2.52}$$

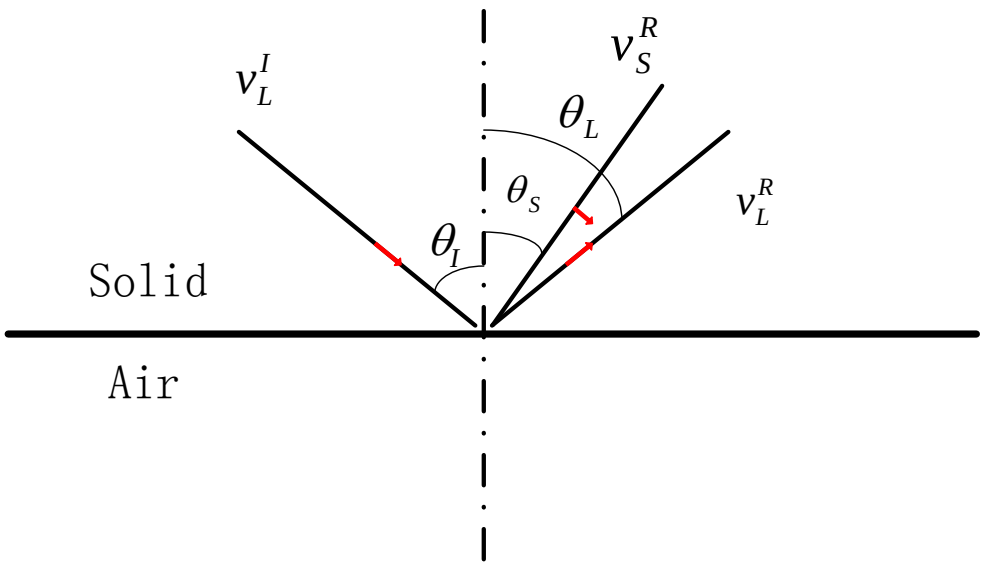

Figure 2.4 Reflection of a plane longitudinal wave at the free surface of isotropic solid.

At a free surface of an isotropic solid, a longitudinal wave is reflected in both a longitudinal wave and a shear wave, as shown in Figure 2.4. We have

$$k_L = k_I = \frac{\omega}{v_L} \text{ and } \frac{k_S}{k_I} = \frac{v_L}{v_S}$$

These waves are denoted by indices L and S which means longitudinal wave and shear wave. v is the velocity and k is the wave number.

And the Snell-Descartes law gives

$$\theta_L = \theta_I \quad \text{and} \quad v_S \sin\theta_I = v_L \sin\theta_S \tag{2.53}$$

Expanding Eq. (2.50), the mechanical stresses in the xz plane are

$$\begin{cases} T_{22} = -i\omega[(U_I + U_L)Z_L \cos 2\theta_S - U_S Z_S \sin 2\theta_S] \\ T_{12} = -i\omega \dfrac{v_S}{v_L}[(U_I - U_L)Z_S \sin 2\theta_I - U_S Z_L \cos 2\theta_S] \end{cases}$$

Where $Z_L = \rho v_L$ and $Z_S = \rho v_S$

The reflection coefficient for the longitudinal wave is

$$R_{LL} = \frac{U_L}{U_I} = \frac{\sigma^2 \sin 2\theta_I \sin 2\theta_S - \cos^2 2\theta_S}{\sigma^2 \sin 2\theta_I \sin 2\theta_S + \cos^2 2\theta_S} \quad \text{with} \quad \sigma = \frac{v_S}{v_L} \tag{2.54}$$

And the coefficient for conversion into the shear wave is

$$R_{LS} = \frac{U_S}{U_I} = \frac{2\sigma \sin 2\theta_I \cos 2\theta_S}{\sigma^2 \sin 2\theta_I \sin 2\theta_S + \cos^2 2\theta_S} \tag{2.55}$$

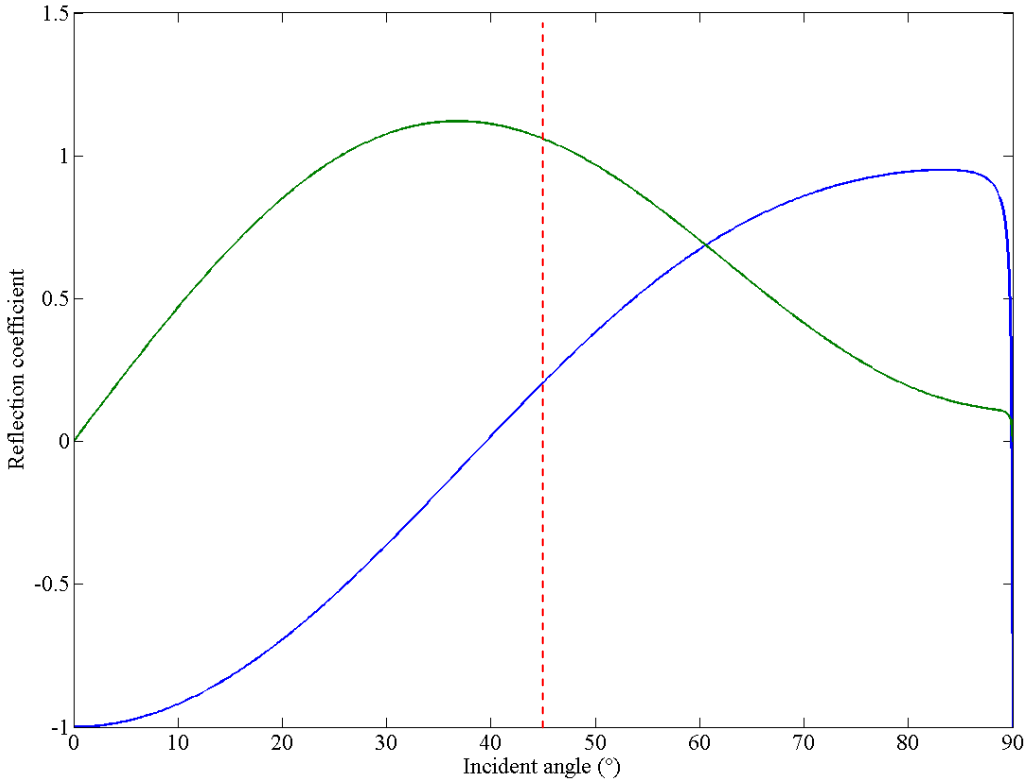

Figure 2.5 Reflection coefficient of a longitudinal wave at the free surface of an isotropic solid, as a function of the angle of incidence. For silicon.

Figure 2.5 shows that with an incidence angle of 45 °, almost all the incidence of longitudinal wave is converted into shear wave after the reflection. For unit amplitude of incidence longitudinal wave, the reflection amplitude of the longitudinal wave is equal to 0.21 while that of the shear wave is 1.05. The amplitude of the longitudinal reflection wave is significantly lower than that of the shear reflection wave. We can quantify the attenuation of 13.5dB for the longitudinal wave.

We will improve the amplitude of the reflected longitudinal wave by the method of depositing a coating layer of SiO_2 at the free surface. In an anisotropic material, such as silicon, there can be two quasi-shear reflection waves which do not lie in the plane of the incident wave. In that case, there are three equations for stress balance which generally require numerical solution.

Because of the mode conversion and using the Snell law, the velocity can be computed in any direction by solving the Christoffel eigenvalues problem. The velocity of the incident longitudinal acoustic wave v_i in the {001} direction is the same as the velocity of the

reflected longitudinal acoustic wave v_r in the {010} direction (v_L = 8432 m/s). The angle between the incident longitudinal wave and the reflected longitudinal wave is 90 ° when the wave incident at the 45 ° direction. In these directions, the Poynting vector is collinear with the wave vector. It is not the same for the longitudinal to shear polarization, neither for the shear to longitudinal polarization deflection.

2.3.3 Acoustic impedance and mechanical matching

We use impedance Z and wave number k to characterize the wave propagation in the homogeneous medium.

$$\begin{pmatrix} \mathrm{T} \\ v \end{pmatrix} = \begin{pmatrix} \cos(kd) & -j \cdot Z \cdot \sin(kd) \\ -\frac{j}{Z}\sin(kd) & \cos(kd) \end{pmatrix} \begin{pmatrix} \mathrm{T} \\ v \end{pmatrix}$$

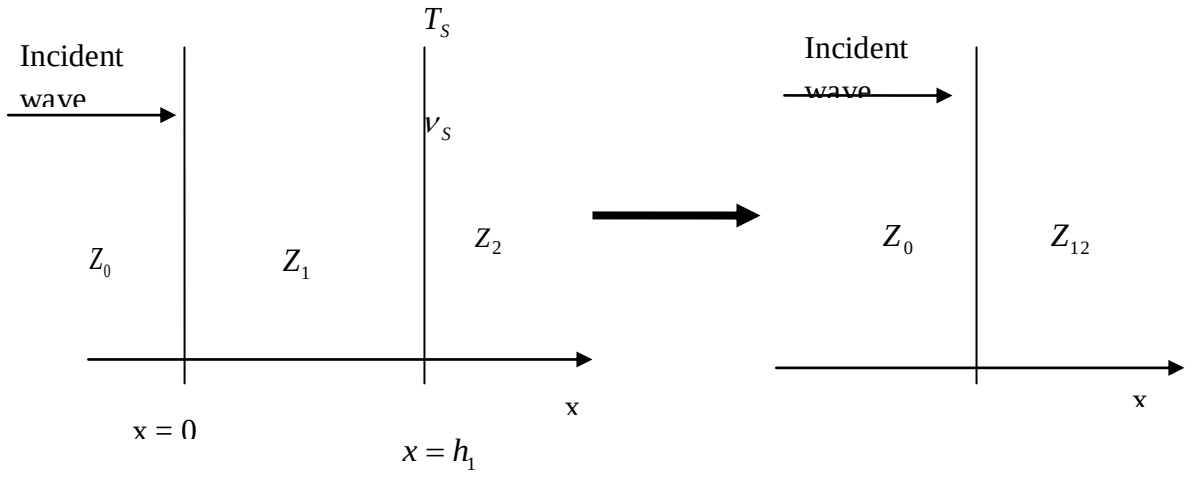

Figure 2.6 Equivalent impedance of medium 1 and medium 2.

Consider a layer of impedance Z_1 and thickness d, inserted between two media having different acoustic impedance: Z_0 for the incident medium and Z_2 for the transmission medium. From KLM model, the acoustic impedance as seen by the incident medium and inserted layer is

$$Z_{12} = Z_1\left(\frac{Z_2 \cdot \cos((k_1 h_1)) + j \cdot Z_1 \cdot \sin((k_1 h_1))}{Z_1 \cdot \cos((k_1 h_1)) + j \cdot Z_2 \cdot \sin(k_1 h_1)}\right) \tag{2.56}$$

The pressure reflection and transmission coefficients by and through the layer can be calculated from

$$R\ (f) = \left(\frac{Z_{12} - Z_0}{Z_{12} + Z_0}\right) \text{ and } T(f) = \left(\frac{2 \cdot Z_{12}}{Z_{12} + Z_0}\right)$$

and the transmission coefficient in power density

$$T^e = 1 - R\ (f) R^*(f) = T\ (f) T^*(f) Z_0 / Z_2$$

where $R(f) = \dfrac{(Z_2 / Z_0 - 1) + j(Z_1 / Z_0 - Z_2 / Z_1)\tan(2\pi f d / v_1)}{(Z_2 / Z_0 + 1) + j(Z_1 / Z_0 - Z_2 / Z_1)\tan(2\pi f d / v_1)}$

It is possible to achieve an anti-reflection layer

when $d = (2n+1)\dfrac{\lambda_1}{4}$, there is $Z_{12} = Z_1^2 / Z_2$ .So

$$Z_0 = Z_1^2 / Z_2 \text{ or } Z_1 = \sqrt{Z_2 \cdot Z_0}$$

We consider the two medium of impedance Z_1 and Z_2 with the relation of reflection coefficient R_{12} :

$$R_{12} = \left(\frac{Z_2 - Z_1}{Z_2 + Z_1}\right)$$

The reflected energy at the surface of two medium is proportional to $|R_{12}|^2$, and the insertion loss IL is defined as

$$IL = -10 \cdot \log_{10}[1 - |r_{12}|^2] \tag{2.57}$$

2.3.4 Modeling of piezoelectric ZnO transducer

In our work, we will use piezoelectric transducers based on zinc oxide to generate longitudinal waves. To determine the electrical impedance of the transducer, we must take

into account all the layers that constitute the acoustic load. Thus by calculating the impedances of all layers, we can achieve the modeling of the transducer.

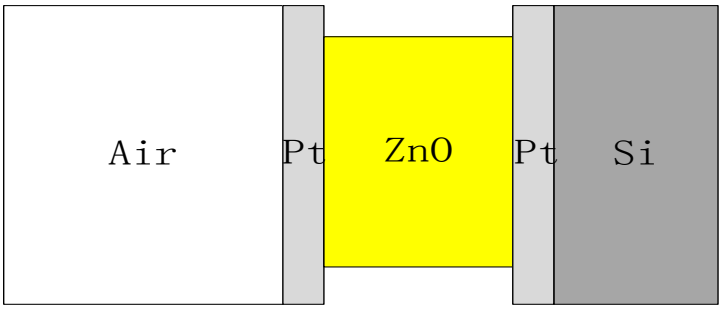

Figure 2.7 ZnO structure in the microsystem

According to Eq. (2.56),

$$Z_{Air/Pt} = Z_{Air} \cdot \frac{Z_{Pt} \cdot \cos(\theta_{Pt}) + j \cdot Z_{Air} \cdot \sin(\theta_{Pt})}{Z_{Air} \cdot \cos(\theta_{Pt}) + j \cdot Z_{Pt} \cdot \sin(\theta_{Pt})} \tag{2.58}$$

Z_{Air} is the impedance of air, Z_{Pt} is the impedance of platinum, $\theta_{Pt} = 2\pi f \frac{d_{Pt}}{v_{Pt}}$, d_{Pt} is the thickness of platinum layer and v_{Pt} is the velocity of longitudinal wave in the platinum layer and f is the frequency of longitudinal wave.

Similarly,

$$Z_{Si/Pt} = Z_{Air} \cdot \frac{Z_{Pt} \cdot \cos(\theta_{Pt}) + j \cdot Z_{Si} \cdot \sin(\theta_{Pt})}{Z_{Si} \cdot \cos(\theta_{Pt}) + j \cdot Z_{Pt} \cdot \sin(\theta_{Pt})}$$

The electrical impedance of the transducer can be obtained from

$$Z_{elZnO} = \frac{1}{jC_{0ZnO}2\pi f} + \frac{K_{ZnO}^2}{C_{0ZnO}2\pi f} \frac{Z_{ZnO}}{\theta_{ZnO}} \frac{2Z_{ZnO}(\cos(\theta_{ZnO}) - 1) + j(Z_{Air/Pt} + Z_{Si/Pt})\sin(\theta_{ZnO})}{Z_{Zno}(Z_{Air/Pt} + Z_{Si/Pt})\cos(\theta_{ZnO}) + j(Z_p^2 + Z_{Air/Pt}Z_{Si/Pt})\sin(\theta_{ZnO})}$$

K_{ZnO} is the electromechanical coupling coefficient of ZnO, $C_{0ZnO} = \frac{\varepsilon_{ZnO} \cdot d_{ZnO}}{S_{ZnO}}$ is the static capacitance of ZnO, d_{Zno} is the thickness of the ZnO transducer, ε_{Zno} is the dielectric permittivity, Z_{ZnO} is the characteristic impedance of ZnO, S_{ZnO} is the active surface of ZnO,

$$\theta_{ZnO} = k_{ZnO} \cdot d_{ZnO} = 2\pi f \cdot \frac{d_{ZnO}}{V_{ZnO}}.$$

For the single crystal of ZnO oriented along the direction<100> and the velocity of longitudinal wave is 6330 m/s. With unloaded mode, the resonance frequency of 3.12μm thickness of ZnO is 1GHz. While with loaded mode, the resonance frequency of 2.4μm thickness of ZnO is 1GHz, shown as in Figure 2.8. The simulation value of ZnO transducer is as follows:

$v_{Pt} = 2680$ m/s, $\varepsilon_{ZnO} = 7{,}4 \times 10^{-11} F/m$, $S_{Zno} = \pi \cdot a^2$ with $a = 75$ μm, $Z_{Si} = 20$ MRayls,

$Z_{Pt} = 41$ MRayls, $d_{Pt} = 100$ nm, $v_{ZnO} = 6330$ m/s, $Z_{ZnO} = 36$ MRayls, $k_{ZnO} = 0{,}27$.

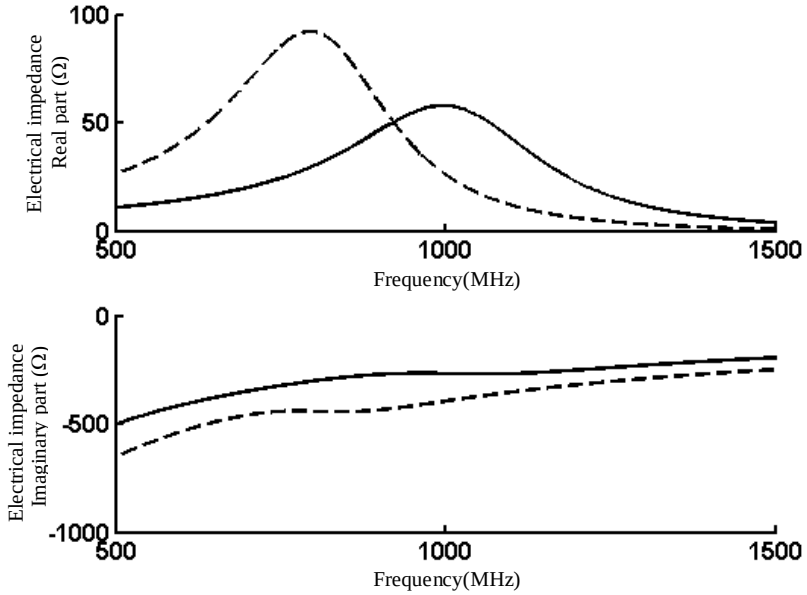

Figure 2.8 Electrical impedance simulation of ZnO transducer (solid line: 2.4μm ZnO, dashed line: 3.12μm ZnO)

2.3.5 Modeling of wave guiding using two 45 °mirrors

In our designed microsystem (Figure 1.20) including two 45 °mirrors; it is observed that the shear wave never reconverts into longitudinal wave as it reaches the mirror above the critical angle $\sin\theta_i \geq \frac{v_i}{v_r}$.

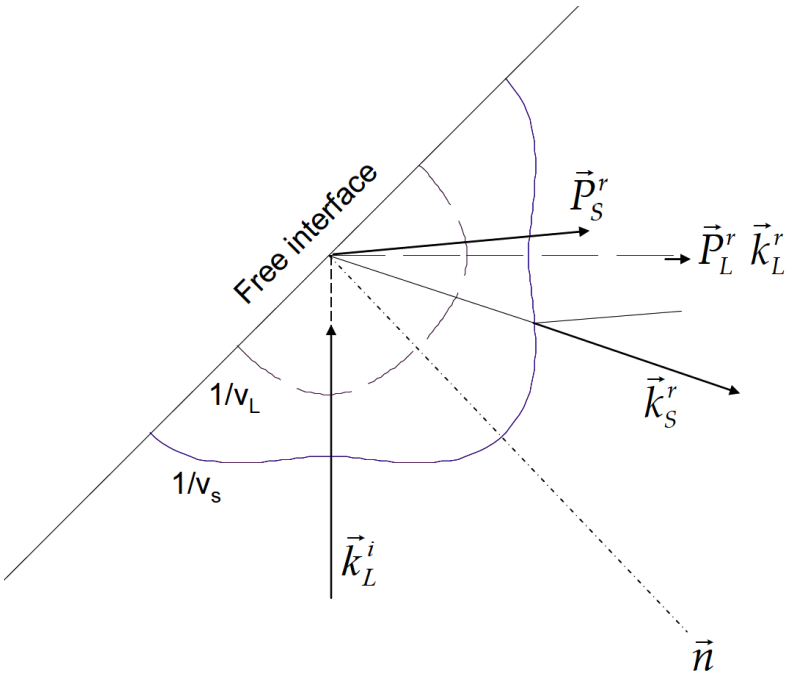

Figure 2.9 Longitudinal wave reflection at 45 °acoustic mirror in silicon.

v_L and v_S velocity of longitudinal and shear wave. $\vec{k}_L^i$ and $\vec{k}_L^r$ incident and reflected longitudinal wave vectors. $\vec{k}_S^r$ reflected shear wave vectors. $\vec{P}_L^r$ and $\vec{P}_S^r$ reflected longitudinal and shear Poyning vectors.

In this case, only the conversion of longitudinal wave into shear wave will be solved hereafter. On the second mirror, from which the Snell's law is solved in terms of reflection angle (θ_{rs} = 27) and velocity (v_s = 5398 m/s). The direction of the shear energy propagation is given by the Poynting vector which is normal to the slowness curve $\left(\frac{1}{v}(\theta)\right)$ as shown in Figure 2.9. One can deduce that the energy of the shear wave propagates nearly vertically with an included angle of about 95 ° between the incident longitudinal wave and the reflected shear wave. So a quasi-shear wave can reach the receiver. To reach the receiver, the incident wave must be launched from the emitter with an angle of 2 °which is allowed by the aperture of the transducers (about 5 °). On the first mirror, this longitudinal wave is converted into shear wave of which the wave vector and the Poynting vector are about 19 ° below and 4 ° above the horizontal direction, respectively. Then this shear wave is symmetrically deflected on the second mirror.

To estimate the wave reflection of different modes at the surface of the silicon mirror, we take a simplified isotropic model for silicon material and calculated the wave reflection coefficient in amplitude and in energy as a function of the incident angle for a longitudinal incident wave. A simplified model has been considered here because the use of the longitudinal acoustic

wave is mainly interesting. Moreover, after reflected on a 45° mirror, the direction of propagation of such wave is equivalent to its propagation before the mirror due to the cubic crystalline structure of silicon. It is shown in Figure 2.10 that at 45° incidence, only less than 10% of energy is converted into the longitudinal wave. However, the simulations have shown that the deposition of a thin film on the mirror can improve the reflection of the longitudinal wave on the mirror instead of converting it in a shear wave. It can be observed in Figure 2.10 that with this layer 90% of the longitudinal wave is reflected. Previous experimental results has shown that 4 µm-thickness SiO_2 thin film was deposited on the mirrors could improve the efficiency of the propagation of the longitudinal wave and limit the conversion of longitudinal wave to shear wave[112].

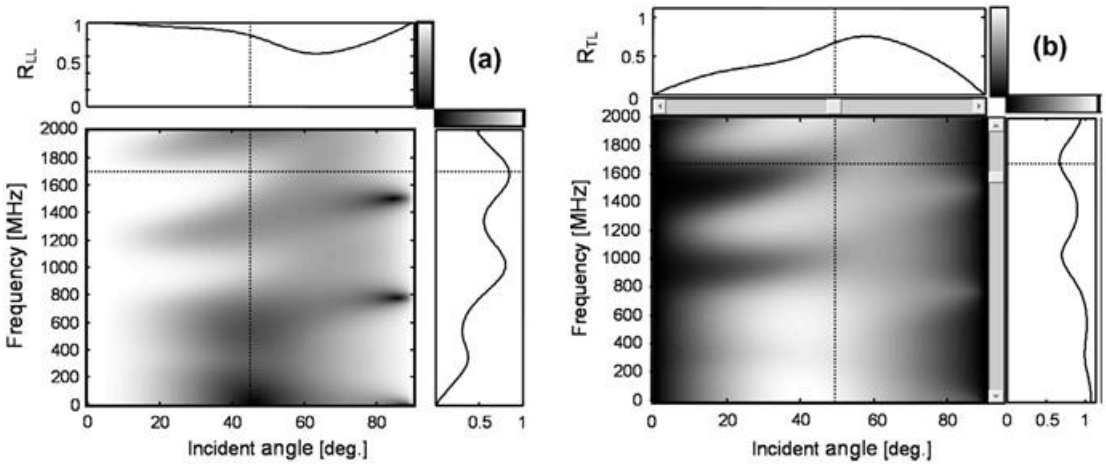

Figure 2.10 Reflection coefficient in amplitude of (a) longitudinal mode RLL and (b) transverse mode RTL, for a longitudinal wave incidence at silicon–SiO_2 layer (4 µm thickness) -vacuum system (ultrasonic characteristics of SiO_2: v_L = 6050 m/s; v_s = 4100 m/s; ρ = 2200 kg/m^3) [113].

Commercial COMSOL software was also used to study the propagation of the acoustic wave in the system. Figure 2.11 shows the simulations of the propagations of 1 GHz longitudinal and shear acoustic wave in the silicon wafer. The contrast presents the amplitude of the displacement of elements of the silicon wafer when the acoustic waves were propagating in the wafer. Partial Derivate Equation (PDE) model in COMSOL was also used to estimate the propagation of the acoustic beam in the microsystem. The mesh was defined as 1 µm for each unit cell and it is smaller than $\lambda_L/9$ and $\lambda_S/4$, in which λ_L and λ_S are the wavelength of the longitudinal acoustic wave and shear wave in the silicon at 1 GHz, respectively. As presented by the following experimental process, piezoelectric zinc oxide (ZnO) thin films will be used as the transducers. The simulations were simplified with a 2D model to avoid the tremendous meshes of the 3D model. The 2D model which presents the cross-section of the system reserves the same convergence of the propagation of the acoustic wave compared to the 3D model. Perfectly matching layer (PML) [114] was used as absorbers to limit the reflection on

the side walls under the mirror and on the topside of the wafer and the area of the backside of the wafer where the transducer as receiver will be placed.

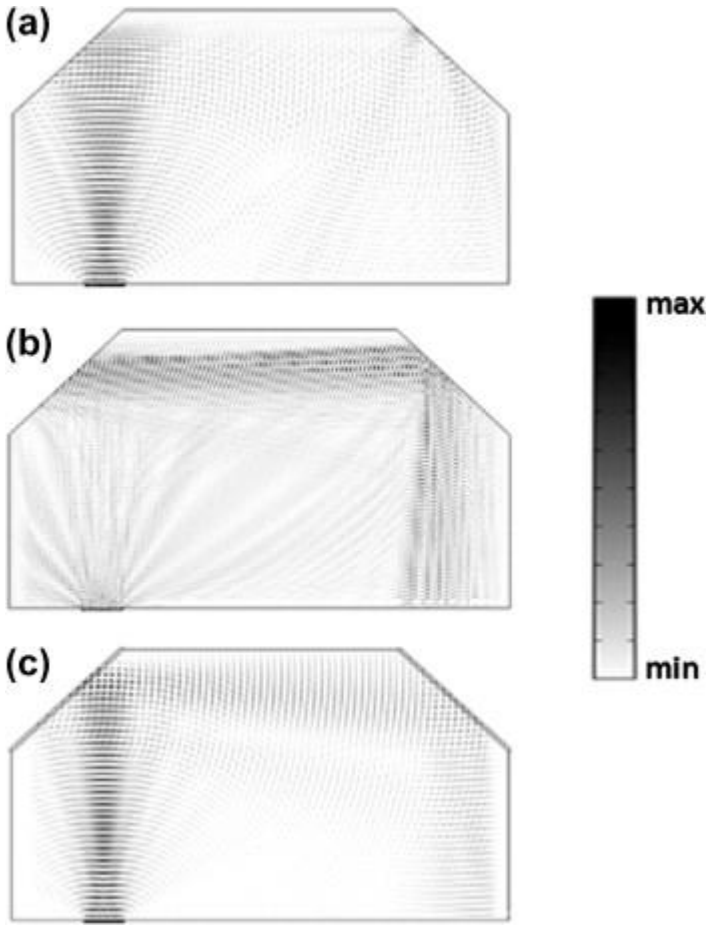

Figure 2.11 Simulation of the propagation of 1 GHz (a) longitudinal, (b) shear acoustical waves in the silicon wafer without silicon oxide layer on the mirror, (c) simulation of the propagation of 1 GHz longitudinal acoustical wave in the silicon wafer with silicon oxide layer on the mirror [113].

Considering the experimental process, water was put on the top side of the wafer to attenuate the surface acoustic wave. The surface acoustic wave which may occur in the same plane of the two transducers will have largely different echo times compared to the acoustic waves which were generated by the emitter and finally detected by the receiver after twice reflected by the mirrors. The side walls were continuous with other silicon elements. So, PML conditions were used reasonably here.

In that way, it is possible to observe the beam going from the emitter, reflected on the first mirror, going through the media to be characterized and reflected on the second mirror in the direction of the receiver. The amplitude of the displacement of the elements of the silicon wafer when 1 GHz longitudinal and shear acoustic wave propagate in the silicon without a

SiO_2 layer (thickness about 4 μm) on the 45° mirrors are shown in Figure 2.10 a and b, respectively.

It was found that the amplitude of the displacement of the silicon elements was higher when the shear acoustic waves propagated in the silicon than when the longitudinal acoustic waves did. This was proved by the experimental results shown in chapter 4. A forehand studies showed that deposition of a thin film on the mirror could improve the reflection of the longitudinal wave on the mirror instead of converting it into a shear wave. It has been achieved that 90% of the longitudinal wave was reflected at the frequency of 1.7 GHz with a thin SiO_2 thin film (4 μm) deposited on the mirror [88]. The propagation of 1 GHz longitudinal acoustic wave in the silicon wafer with a SiO_2 layer on the mirror is also shown in Figure 2.11c. It can be seen that after being reflected twice the longitudinal and shear wave generated by the transducer propagated in the silicon wafer as expected. The contrast presents the displacement of elements of the silicon wafer at 1 GHz. The mesh was set up as 1 μm (~λ_L/9) during the simulation. The right side bar represents the amplitude of the displacement of elements of the silicon when the acoustical waves propagate. The width of the transducer on the bottom side of the silicon wafer is 50 μm.

2.3.6 Modeling of the acoustic wave transmission at the silicon-water interface of our system

In our design, the longitudinal wave emitted by ZnO transducer propagates inside silicon substrate and transmits through the microchannel filled with water, the insertion loss at silicon/air interface are defined by Eq. (2.57)

$$IL_{Si/H_2O} = 10 \cdot \log_{10}\left[1 - \left|r_{Si/H_2O}\right|^2\right] \quad \text{with} \quad R_{Si/H_2O} = \left(\frac{Z_{Si} - Z_{H_2O}}{Z_{Si} + Z_{H_2O}}\right)$$

The acoustic impedance of water and silicon are respectively 1.5MRayls and 20MRayls. The insertion loss between silicon and water is equal to 6 dB. The mechanical impedance matching should be achieved in order to detect the bio-objects mixed with water in the microchannel. The matching layer of impedance is $Z_m = \sqrt{Z_{Si} \cdot Z_{H_2O}}$ =5.5MRayls and the thickness of the layer is $d_m = \frac{v_m}{4 \cdot f_0}$

The velocity of longitudinal acoustic wave in silicon oxide is 5968m/s and the impedance is 13.3 MRayls. The velocity of longitudinal acoustic wave in photoresist SU-8 is 2886m/s and the impedance is 3.5Mrayls. The two materials are inserted between silicon and water to estimate the insertion loss of the interface. The calculation of insertion loss for SU-8 is as

follow

$$Z_{SU-8/H_2O} = Z_{SU-8} \cdot \left(\frac{Z_{H_2O} \cdot \cos(k_{SU-8} \cdot d_{SU-8}) + j \cdot Z_{SU-8} \cdot \sin(k_{SU-8} \cdot d_{SU-8})}{Z_{SU-8} \cdot \cos(k_{SU-8} \cdot d_{SU-8}) + j \cdot Z_{H_2O} \cdot \sin(k_{SU-8} \cdot d_{SU-8})} \right)$$

$$Z_{SiO_2/H_2O} = Z_{SiO_2} \cdot \left(\frac{Z_{H_2O} \cdot \cos(k_{SiO_2} \cdot d_{SU-8}) + j \cdot Z_{SiO_2} \cdot \sin(k_{SiO_2} \cdot d_{SiO_2})}{Z_{SiO2} \cdot \cos(k_{SiO_2} \cdot d_{SU-8}) + j \cdot Z_{H_2O} \cdot \sin(k_{SiO_2} \cdot d_{SiO_2})} \right)$$

where $k_{SU-8} = \frac{w}{v_{SU-8}}$, $k_{SiO_2} = \frac{w}{v_{SiO_2}}$ and d_{SU-8} is the thickness of SU-8, d_{SiO_2} is the thickness of the SiO_2.

Then we calculate the reflection coefficient $R_{Si/(SU-8/H_2O)}$ and $R_{Si/(SiO_2/H_2O)}$ by

$$R_{Si/(SU-8/H_2O)} = \frac{Z_{SU-8/H_2O} - Z_{Si}}{Z_{SU-8/H_2O} + Z_{Si}}$$

$$R_{Si/(SiO_2/H_2O)} = \frac{Z_{SiO_2/H_2O} - Z_{Si}}{Z_{SiO_2/H_2O} + Z_{Si}}$$

The insertion loss of the SU-8 and SiO_2 are

$$IL_{Si/SU-8/H_2O} = -10 \cdot \log_{10}\left[1 - \left|R_{Si/(SU-8/H_2O)}\right|^2\right]$$

$$IL_{Si/SiO_2/H_2O} = -10 \cdot \log_{10}\left[1 - \left|R_{Si/(SiO_2/H_2O)}\right|^2\right]$$

We will do the same calculation of the bilayer SU-8/SiO_2

$$Z_{SiO_2/SU-8/H_2O} = Z_{SiO_2} \cdot \left(\frac{Z_{SU-8/H_2O} \cdot \cos(k_{SiO_2} \cdot e_{SiO_2}) + j \cdot Z_{SiO_2} \cdot \sin(k_{SiO_2} \cdot e_{SiO_2})}{Z_{SiO_2} \cdot \cos(k_{SiO_2} \cdot e_{SiO_2}) + j \cdot Z_{SU-8/H_2O} \cdot \sin(k_{SiO_2} \cdot e_{SiO_2})} \right)$$

$$R_{Si/(SiO_2/SU-8/H_2O)} = \frac{Z_{SiO_2/SU-8/H_2O} - Z_{Si}}{Z_{SiO_2/SU-8/H_2O} + Z_{Si}}$$

$$IL_{Si/(SiO_2/SU-8/H_2O)} = -10 \cdot \log_{10}\left[1 - \left|R_{Si/(SiO_2/SU-8/H_2O)}\right|^2\right]$$

The simulation of insertion losses between silicon and water with different matching layer is shown in Figure 2.12. At the center frequency of 1GHz, the insertion loss can be reduced to 3 dB using a SU-8 layer while it can be reduced to 1dB using a SiO_2 layer for the layer

thickness of quarter wave length. For the bilayer of SU-8/SiO_2, there is no insertion loss at the central frequency of 1GHz and it can provide matching with a large banwidth.

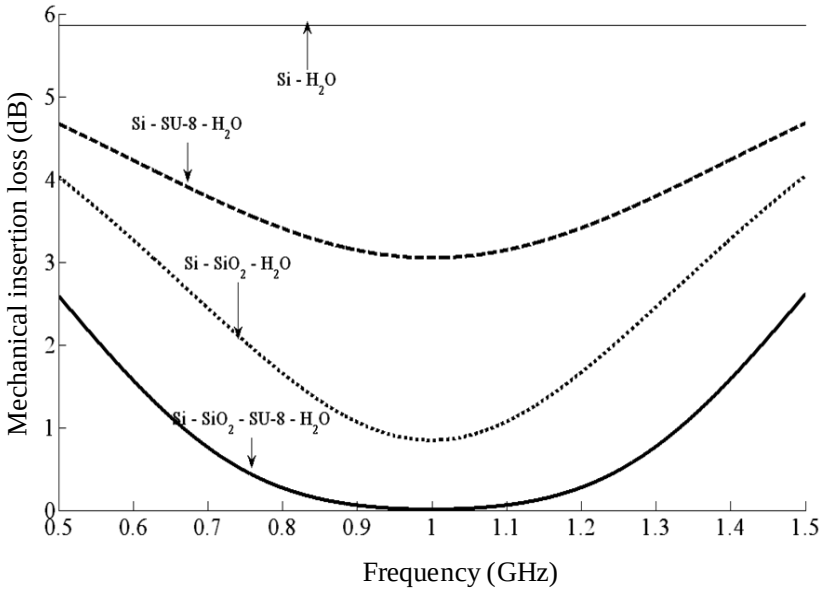

Figure 2.12 Mechanical insertion loss between silicon and microchannel a) without matching layer, b) SU-8, c)SiO_2, d) the bilayer of SiO_2/SU-8

2.3.7 Modeling of the electrical matching

After theoretical research of the mechanical impedance matching, we will turn to study the electrical impedance matching of transducer. We can choose the active surface of transducer so that the real part of its electrical impedance is 50Ω and the imaginary part can be offset by self-inductance. The insertion loss of the transducer S_{11}^{elZnO}

$$S_{11}^{elZnO} = \frac{Z_{elZnO} - Z_{el0}}{Z_{elZnO} + Z_{el0}} \quad \text{with} \quad Z_{el0} = 50\Omega$$

And

$$S_{11dB}^{elZnO} = -10 \cdot \log_{10}\left(1 - \left|\left(S_{11}^{elZnO}\right)\right|^2\right)$$

The electrical insertion loss is 7dB at the resonant frequency, shown in Figure 2.13

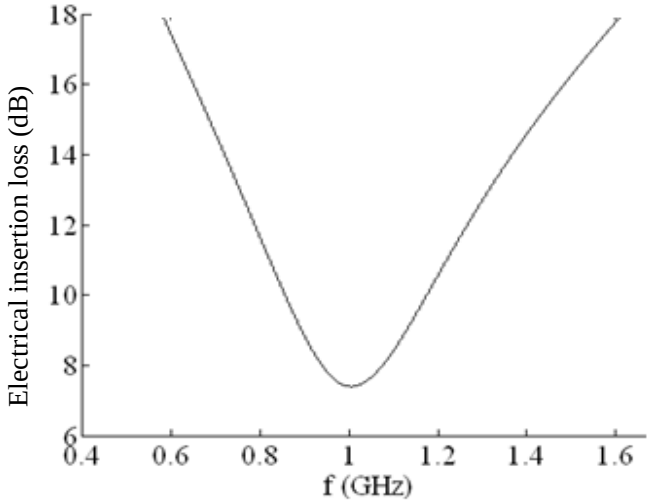

Figure 2.13 Electrical insertion loss of transducers

In order to eliminate the imaginary part, one approach is to neutralize the capacitance $\frac{1}{j\omega c_0}$

by adjusting in series an inductance $L_o C_0 \omega^2 = 1$

where C_0 =0.73pF, $\omega = 2\pi f_0$ and f_0 =1GHz. So the L_o =34nH

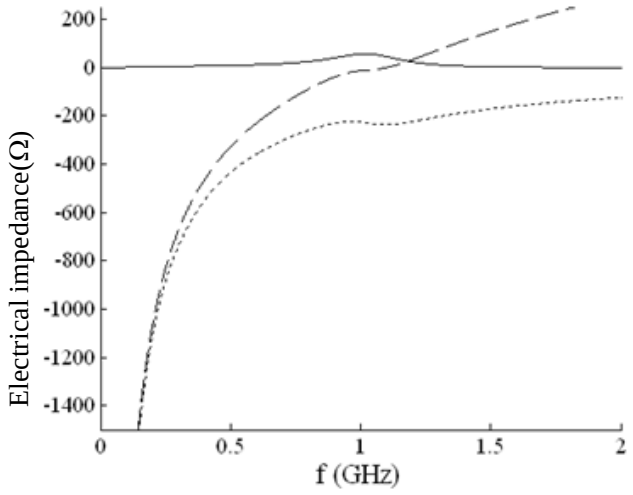

Figure 2.14 The imaginary part of the transducer

We compare the two situations of electrical insertion losses of transducer with and without inductance, as shown in Figure 2.15. We observe that at the resonance frequency the losses are 7 dB when the imaginary part is not balanced with the self component compensation.

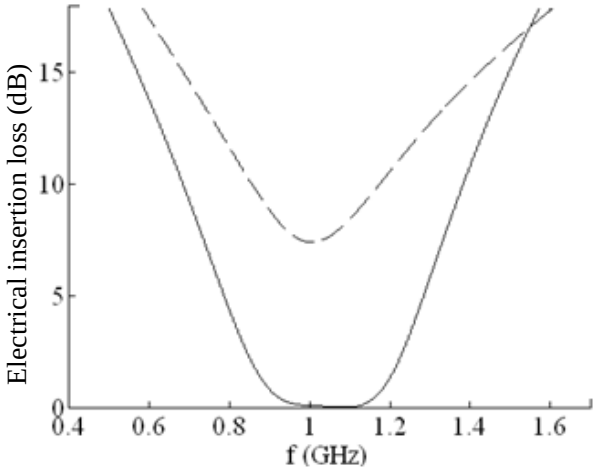

Figure 2.15 Comparison of insertion loss with and without inductance

2.3.8 Modeling of the insertion losses of our microsystem

We calculate the absorption losses of our microsystem. These are losses during propagation in silicon substrate and in the microchannel. The attenuation in silicon is equal to $1\,\mathrm{dB/mm/}GHz^2$ [115]. The propagation distance inside the silicon substrate is equal to 1070 microns, so the absorption losses equal to 1.1 dB in the substrate. The attenuation in water is about $220\,\mathrm{dB/mm/}GHz^2$ [91]. The absorption loss equals to 11 dB when the width of microchannel is 50μm. So absorption losses in the microsystem are equal to 12.1 dB. We will make an assessment on the loss estimation and the expected performance in our microsystem, as shown in Figure 2.16

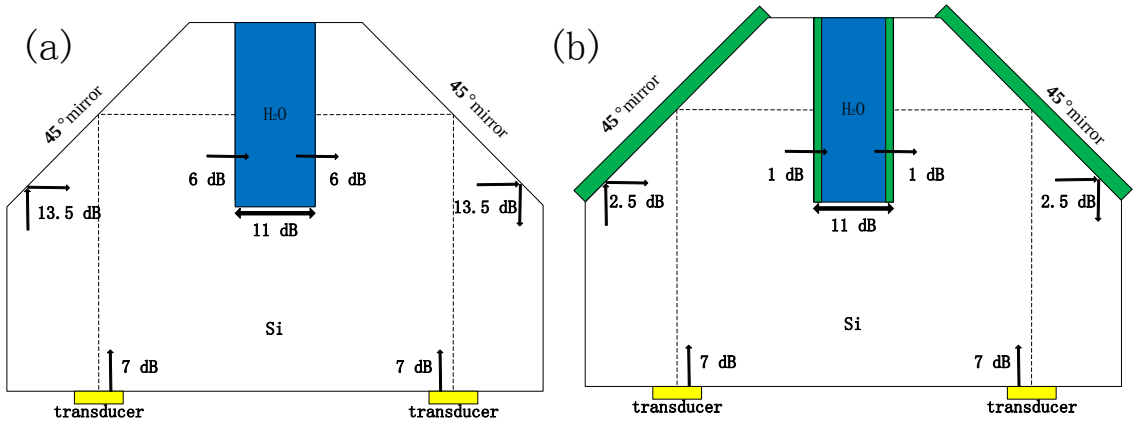

Figure 2.16 Expected losses at the interface of different components of microsystem. a) Without coating and matching layer, b), with coating and matching layer.

If we take the microsystem without the different types of layers to improve losses in different propagation components of the microsystem, we have in total 66.1 dB of losses (Figure 2.16a).

The loss decreases to 32.1 dB with the introduction of the matching layers and the layers for conversion mode reduction in the microsystem (Figure 2.16b). The theoretical calculation of absorption losses is seen that we have the opportunity to reduce losses in the propagation components.

For the transducer, we expect to improve the electrical impedance mismatch with 7dB losses. We can eliminate the loss around the center frequency by keeping in series with an inductance of 34 nH. The loss of longitudinal waves at the interface of the mirrors with a layer of 4 µm silicon oxide is equal to 2.5 dB while the losses are equal to 13.5 dB without the layer of silicon oxide. The contribution of 4 microns of silicon oxide allows us to reduce the mode conversion that occurs at the mirrors interface. Between the interface of silicon substrate and the microfluidic channel, the losses are 6 dB. The addition of a layer of SiO_2 or a bilayer SiO_2/SU-8 can improve the transmission by increasing the amplitude of the transmitted acoustic wave. It is to be noted that losses are 1dB around the center frequency 1 GHz for a single SiO_2 layer.

2.3 Summary

This chapter presents the theoretical fundamentals of acoustic wave propagation. Wave equation in fluids, isotropic and anisotropic solid and piezoelectric materials are given, electromechanical coupling coefficient are presented by numerical solution of Christoffel equation.

Acoustic wave reflection and transmission in anisotropic solid (silicon) have been studied. Normal incidence and the oblique incidence at the solid-air interface have been discussed, especially the incidence angle of 45 °. The mode conversion happens when the acoustic wave is reflected by the oblique interface. The coating layer of SiO_2 was studied to improve the efficiency of the propagation of the longitudinal wave and limit the conversion of longitudinal wave to shear wave. The anti-reflection layers of quarter wave length which is used for solid-liquid interface matching also have been studied. The mechanical impedance matching with the layer SiO_2 at the silicon-water interface can give the opportunity to increase 5dB for each transmission.

Finally, we calculate the absorption losses of the microsystem with and without the different types of layers. The losses decrease from 66.1dB to 32.1dB when the microsystem is achieved with good electrical and mechanical impedance matching.

3 Technological development for microsystem fabrication

3.1 Introduction

We design a novel silicon based microsystem using high frequency (GHz range) bulk acoustic wave (BAW) for sensing. Sputtering or sol-gel technologies are often chosen when ZnO / PZT are the piezo-active materials in the development of high frequency ultrasonic transducer. In our experiments, the BAWs are generated by miniature piezoelectric transducers (ZnO thin film can be used easily to achieve the integration of low power and high frequency transducers) and guided thanks to acoustical mirrors in the direction parallel to the surface of silicon wafer. Then BAWs are transmitted through the microfluidic channel which is fabricated with deep reactive-ion etching.

In this chapter, we will introduce the fabrication details to fabricate the microsystem, such as lithography, deposition process, anisotropic wet etching, plasma etching and so on. In order to investigate the microsystem properties and to obtain the desired characterization results, some important parameters of the micro-structures fabrication have been discussed. The surface roughness of the micro-structures is a key point for BAWs transmission, as well as the perpendicularity of the microchannel. The illustration of our micro-device is shown in Fig 3.1.

The fabrication flow of the micro-device is shown in Figure 3.2. The first step is to fabricate the 45 °mirrors which are used as one of the transmission components. It can guide acoustic waves from the thickness direction to a direction parallel to the surface of the wafer. The second step is to fabricate a microchannel between a pairs of 45 °mirrors. It is used to transport the measured sample. The third step is zinc oxide fabrication and annealing. Finally polydimethylsiloxane (PDMS) as the package material is used to assemble the microdevice. Next we will briefly introduce the MEMs technology and give the details of our fabrication process.

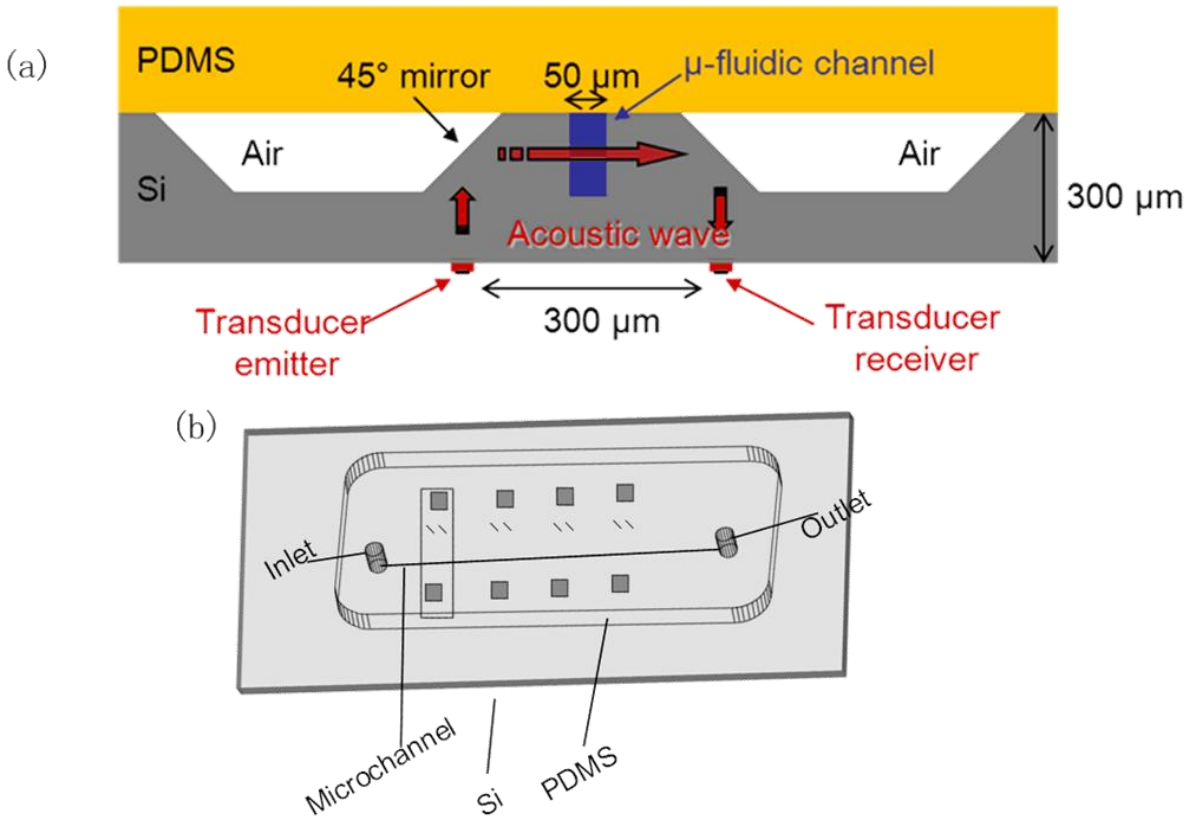

Figure 3.1 The schematic view of the micro-device (a) cross-section view, (b) schematic illustration of the microsystem.

3.2 Microsystem fabrication

Our micro-devices fabrication is based on the silicon microtechnology, so we will firstly introduce the MEMs technology.

Microtechnology is technology with features near one micrometer. In the 1960s large numbers of microscopic transistors are arranged on a single chip and microelectronics circuits could be built and dramatically improved performance. Besides with the functionality and reliability, microtechnology can reduce the cost and increase volume [116].

In the recent decades, the term MEMs, for Micro Electro Mechanical Systems, was coined to describe new, sophisticated mechanical systems on a chip, such as micro electric motors, resonators, and so on. Recently, the MEMs fabricated in a batch process is used to any microdevice with a mechanical function. The MEMs processes are mainly classified into a number of categories, such as surface machining, bulk machining, lithography (LIGA), and electrochemical fabrication (EFAB). Some has fairly simple geometries, while others offer more complex 3-D geometries and more versatility [117].

In an age where everything must be smaller, faster, and cheaper, MEMs offers a compelling solution and a tremendous amount of excitement. Due to the vast range of important applications MEMs can provide previously attainable performance and reliability standards. MEMs have a profound influence on certain applications such as automotive sensors and inkjet printers.

Microfabrication is the term that describes processes to fabricate the miniature structures in micrometresizes and even smaller. The early microfabrication processes were used for integrated circuit fabrication, also known as "semiconductor manufacturing". In the last two decades microelectromechanical systems (MEMs) and their subfields, microfludics/lab-on-a-chip, optical MEMs (also called MOEMs), RF MEMS, PowerMEMs, BioMEMs and their extension into nanoscale have been re-used, adapted or extended microfabrication methods. Flat-panel displays and solar cells are also using similar techniques.

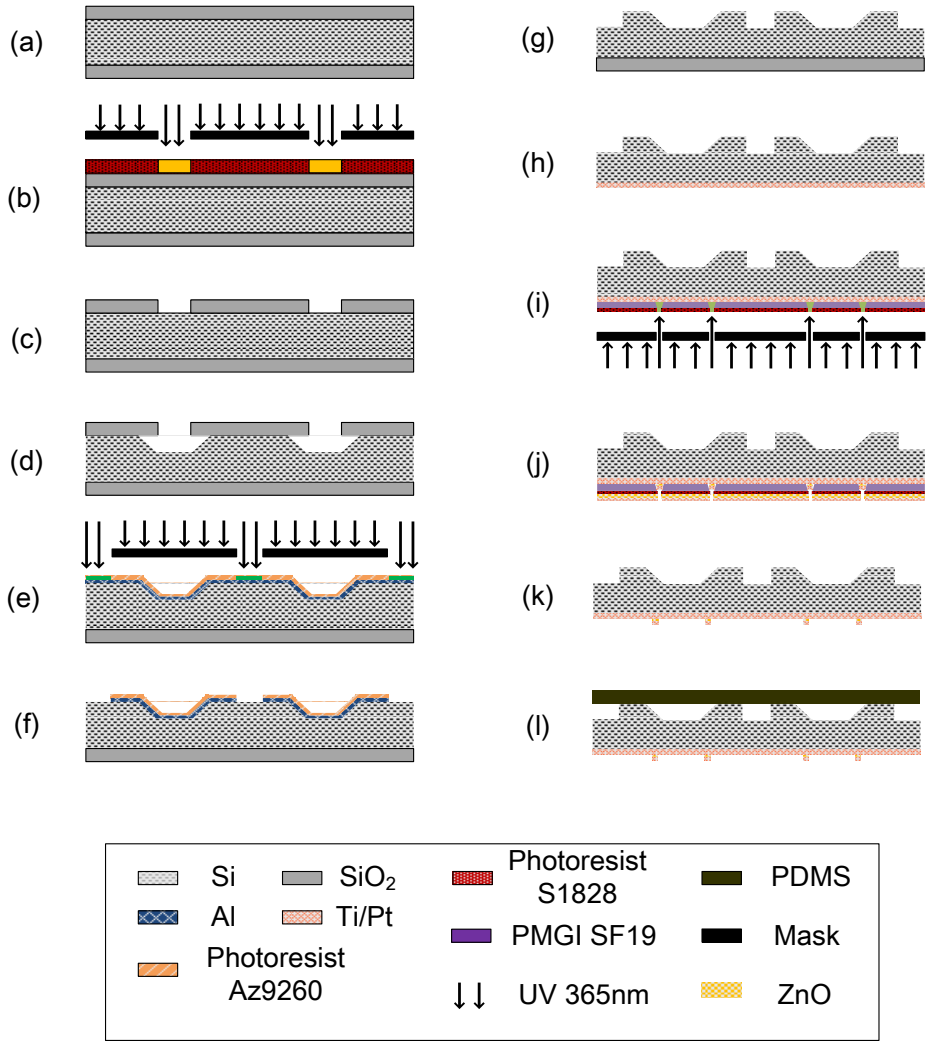

Figure 3.2 Flow chart of the fabrication.

Miniaturization of various devices presents challenges in many areas of science and engineering: physics,chemistry, material science, computer science, ultra-precision engineering, fabrication processes, and equipment design. It is also giving rise to various kinds of interdisciplinary research [118]. The major concepts and principles of microfabrication are microlithography, doping, thin films deposition, etching, bonding and polishing.

To fabricate a microdevice, there are many processes that must be performed, classifying the top-down process and bottom-up process. These processes typically include depositing a film, patterning the film with the desired micro features, and removing (or etching) portions of the film. Microfabrication resembles multiple UV exposure, with many patterns aligned to each other to create the final structure.

In the fabrication process of our microsystem, three major micro-components (45 ° mirror, microfluidic channel and piezoelectric transducer) will be made. Passive 45 ° mirror obtained by wet chemical etching is employed to reflect the bulk acoustic wave (Figure 3.2b-c). A microfluidic channel used for real time biosensing applications is fabricated using ICP technology (Figure 3.2e-g). Zinc oxide (ZnO) thin film transducers were deposited by radio frequency sputtering on the other side of the wafer (Figure 3.2h-k). The flow chart of the fabrication is shown in Figure 3.2.

3.2.1 45 °mirror fabrication

3.2.1.1 Silicon wet etching

Etching is to physicochemically remove the layers from the wafer surface during manufacturing. Etching is a critically important process in microfabrication. For many etch steps, there will protect parts of the wafer by mask material, which resists etching. In some cases, the mask material is a photoresist which has been patterned using photolithography. Other situations require a much more durable mask, such as silicon oxide.

In the case of liquid-phase ("wet") etchants: the wafer can be immersed in a bath of etchant, where the agitation can be controlled. Different etchants can be used to pattern the surface. Normally the wet etching is isotropic. A wet etching process involves multiple chemical reactions that consume the original reactants and produce new reactants, which can be described by three steps: 1) Diffusion of the liquid etchant to the structure 2) The reaction between the liquid etchant and the material being etched away. 3) Diffusion of the byproducts away from the reacted surface.

Nevertheless some wet etchants are used to etch crystalline materials at the different rates depending on which crystal face is exposed. In single-crystal materials (e.g. silicon wafers), this effect can allow very high anisotropy, as shown in the Figure 3.3.

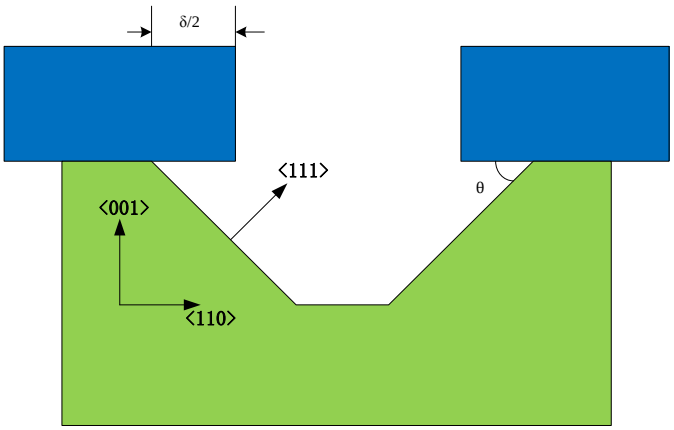

Figure 3.3 An anisotropic wet etch on a silicon wafer creates a cavity with a trapezoidal cross-section

Several anisotropic wet etchants are available for silicon, as shown in Table 3.1. For instance, potassium hydroxide (KOH) displays an etch rate selectivity of 400 comparing <100> crystal directions to the <111> directions. The <111>-oriented sidewalls have an angle to the surface of the wafer is θ. If the original rectangle is perfect, the wafer is etched as a pyramidal shape. The undercut δ is under an edge of the masking material.

Table 3.1 Common anisotropic etchants for silicon[119]

Etchant	Operating temp (℃)	R_{100} (μm/min)	S= R_{100}/R_{111}	Mask materials
Ethylenediamine pyrocatechol	115	0.47	20	Si_3N_4, SiO_2,Au Cr, Ag, Cu
Potassium hydroxide/Isopropyl alcohol	85	1.0	300	Si_3N_4, SiO_2
Tetramethylammonium hydroxide (TMAH)	80	0.6	37	Si_3N_4, SiO_2

3.2.1.2 Experiment- Anisotropic Silicon Etching

Optical communications require various types of acoustic wave manipulations that can be realized monolithically on a single silicon bench. This approach enables integration of mechanical, electrical and optical components and functions in a single complex microstructure resulting in improved performance and reduced cost. Monolithic optical silicon benches with micromachined mirrors that will meet demands for desired reflected angle and low beam scattering in conjunction have been published [120][121][122]. Our acoustic mirror can be developed from this optical mirror and can be used as a reflector for acoustic waves. One segment of acoustic links where the losses can be optimized is reflection mirrors, reflecting the

in-plane to the out-of-plane acoustic signal or vice versa.

Strong alkaline substances (pH > 12) such as aqueous KOH- or TMAH-solutions etch Si via

$$\mathrm{Si} + 4\mathrm{OH}^- \rightarrow \mathrm{Si(OH)}_4 + 4e^-$$

Since the bonding energy of Si atoms is different for each crystal plane, and KOH/TMAH Si etching is not diffusion- but etch rate limited, Si etching is highly anisotropic: while the {100}- and {110}-crystal planes are being etched, the stable {111} planes act as an etch stop:

(100)-orientated wafers form square-based pyramids with {111} surfaces. These pyramids are realized on c-Si solar cells for the purpose of reflection minimization [123].

The degree of anisotropy (etch rate selectivity between different crystal planes), the etch rates, and the etching homogeneity depend on the etching temperature, atomic defects in the silicon crystal, intrinsic impurities of the Si crystal, impurities (metal ions) by the etchant, and the concentration of Si atoms already etched[124].

Ultrasound mirror planes are characterized by several factors. The most important factors are the degree of reflectance and the dispersion angle of reflected acoustic wave. Dispersion of reflected acoustic wave is a function of mirror surface roughness which causes scattering. When the mask is aligned in the <1 1 0> direction and etched with KOH or TMAH, standard V grooves with {1 1 1} side planes are obtained ending with a {1 1 1} mirror under 54.74 °with respect to the {1 0 0} surface as shown in Figure 3.3. These are the most common planes of interest and offer an atomically smooth mirror surface [125].

Compared to {1 1 1} mirror planes, {1 1 0} mirror planes with an angle of 45 ° is more controllable for acoustic wave reflection. To obtain such mirrors on {1 0 0} silicon, two conditions have to be fulfilled simultaneously: the etch mask must be aligned in the <1 0 0> direction and IPA additive or some surfactants must be mixed with the alkaline solutions. It is known from previous work [126] that by adding IPA to KOH or TMAH, the etching anisotropy ratio between {1 0 0}, {1 1 0} and {1 1 1} is changed significantly and different crystal planes emerge, such as {1 1 0} under 45 °toward the {1 0 0} surface. The V groove is limited by {1 1 0} side planes. The degree of anisotropy is strongly dependent on etching chemical solution that further determines the dominant planes potentially used as reflected mirrors.

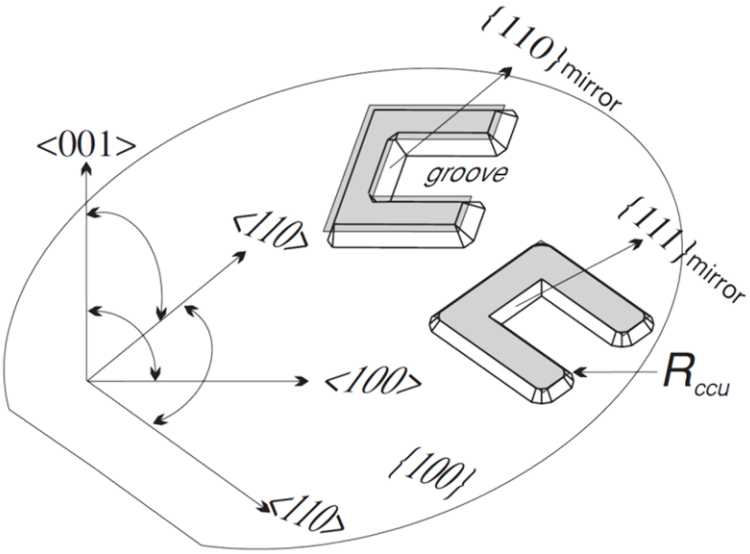

Figure 3.4 Orientation of mask and resulting microstructure appearance on (1 0 0) silicon wafer [127].

In our study, besides isopropyl alcohol (IPA) additive, ammonium persulfate (AP) is investigated as an additive to TMAH etching solution. IPA is commonly used in the microelectronics processing as a surfactant due to the surface tension decline on low-dimensional features during the etching process. Another advantage of IPA is that the etching temperature of the mixture solution can be increased. We focus on the influence of additions in TMAH etchant to provide an appropriate etching parameters for obtaining {1 1 0} mirrors with low loss of reflected acoustic beams.

The experimental work was performed on double sided polished silicon wafer with 〈1 0 0〉 crystal orientation (Siltronix, France). 500nm thick SiO_2 mask were deposited on both sides of the wafer by PECVD (Plasma Enhanced Chemical Vapor Deposition) at 300 ℃. To achieve photolithography steps, a chromium mask was designed with the mirror microstructure (0.5×1.3 mm^2). Wet micromachining of silicon wafer was performed and it is used in this study with solutions of KOH and TMAH. The solution of 35% KOH–water was prepared as well as 25% commercially available TMAH solution. Samples were etched in a closed thermo-stated (±1◦C) glass vessel with the total content of 2L of etching solution which connected with a condenser. All experiments were performed with agitation by a magnetic stirrer at 250 rpm.

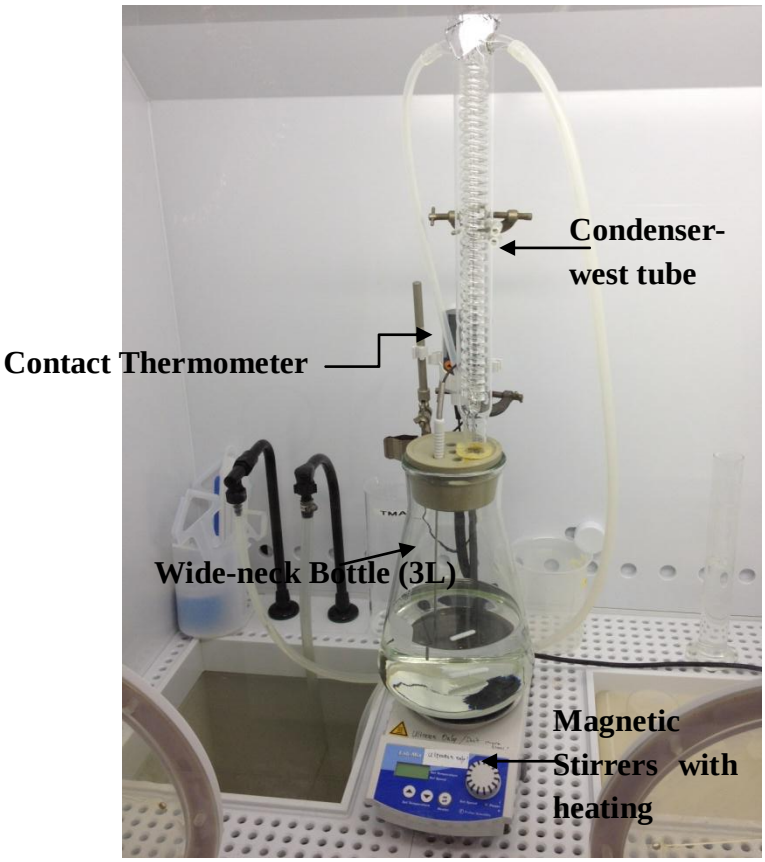

Figure 3.5 The schematic of the wet etching equipment.

The depth of the mirror and the lateral etching distance are measured by Tencor alpha step profiler. The scanning electron microscope (SEM, Zeiss ultra 55) is used to investigate the quality of the mirror surface. The optical microscopy is performed to investigate the roughness of the side planes and bottom of the mirrors, as well as to characterize mask under etching. The angle of mirror can be obtained by the cross section view of the SEM image.

Zubel et al. introduce the KOH or TMAH etching system with IPA additive[128], there have been studied the mechanism and role of IPA how to affect the etch rate ratio between different silicon crystal planes. IPA can slight affect the {1 0 0} etch rate than other crystal plane; however, it does decrease {1 1 1} and {1 1 0} etch rates significantly. Meanwhile, IPA adsorbs on the etched surfaces to hinder the access of the reactive OH^- ions, which can reduce the etching rates of particular crystallographic. But IPA itself can not involve in the reaction. Merlos et al. [129] also found a very similar behavior using the TMAH–IPA–water etching system.

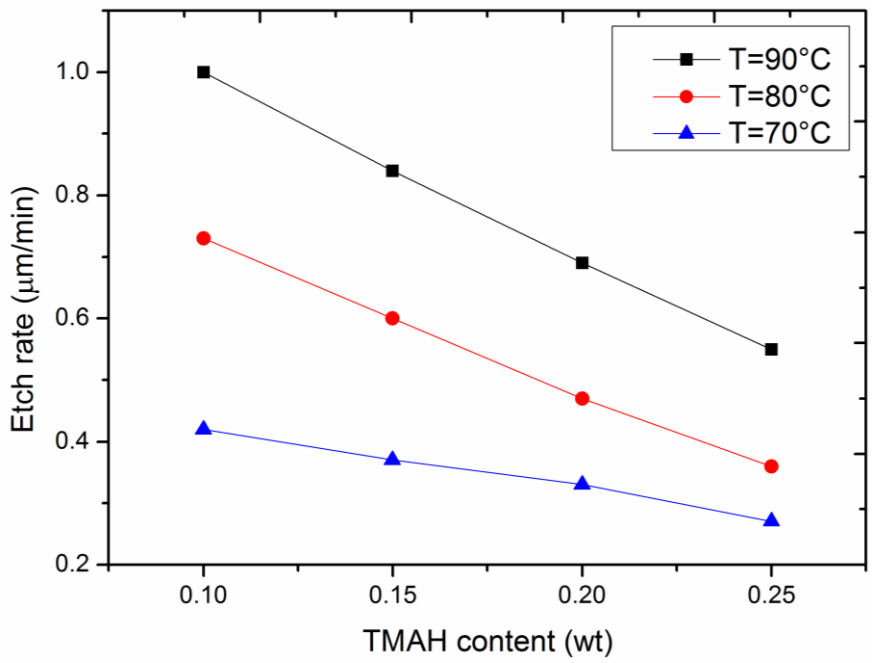

Figure 3.6 {1 0 0} etch rate of silicon versus different concentration of TMAH at three etching temperatures

Figure 3.6 shows the etch rate based on the different concentration of TMAH solutions at three different temperatures. The concentration of TMAH and the operating temperature both affect {1 0 0} surface roughness. The surface roughness is given by alpha step profiler and optical microscope investigation. Comparing the surface roughness of three different temperatures, the surface is smoothest when the mirror is etched at 80 ℃. When the TMAH concentration increases from 10% to 25%, the average roughness of the mirror surface at 80 ℃ is from 1 μm to 500nm, but the etching rate decreases from 0.73 μm/min to 0.39 μm/min. In order to obtain deep etched 45 ° mirror (>120 μm) and the comparative smooth mirror surface, we use 10% TMAH for the next experiments.

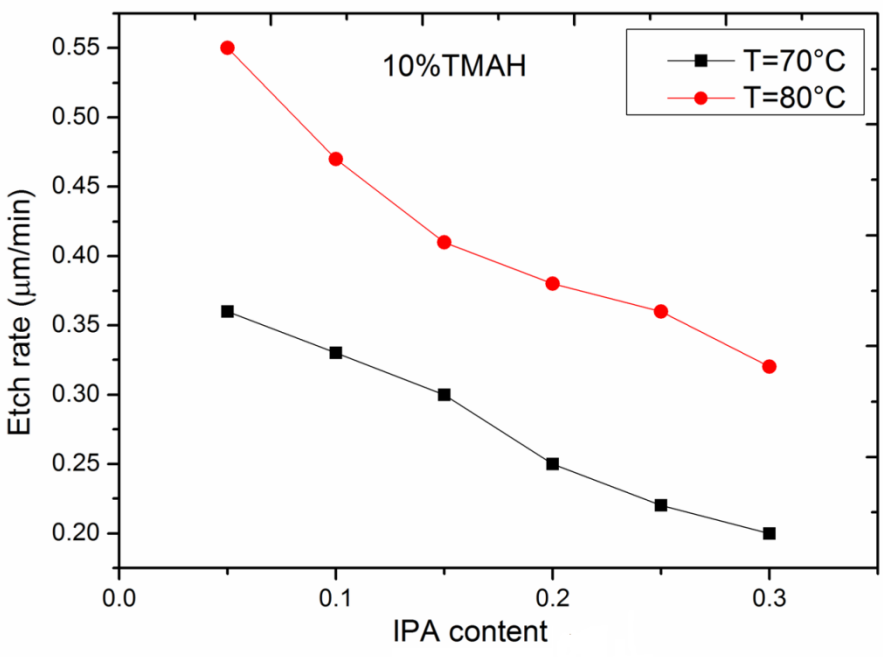

Figure 3.7 {1 0 0} etch rate of silicon versus content of added IPA to 10% TMAH at 70 ° C and 80 ° C

Using optical microscopy, we can observe that the mirror surface etched at 90 ℃ is much rougher than the mirror surface etched at 70 ℃ and 80 ℃. So we only consider these two temperatures when we use IPA as an additive to modify the surface roughness. It is possible to characterize the effect of IPA concentration on the smoothness of resulted surface. It has been shown that the mixture of IPA and 10% TMAH results in better improvement of mirror morphology.

Figure 3.7 shows that the six different concentrations of IPA addition (5-30%) were prepared and started for each temperature. At least three measurements on each sample were performed and etch experiments were repeated twice with fresh solutions. {1 0 0} surface roughness was affected obviously by IPA concentration. When the concentration reaches 20%, there are no pyramids at the bottom of mirrors. Comparing the six concentration of IPA addition, 45 ° acoustic mirror is much smoother when the concentration of IPA is 15% and 20%. For 10%TMAH solution, the amount of IPA is necessary to improve the etched surface quality since it will solve the worsening situation with the increase in hydroxide. In very lower concentration of IPA (<10%), IPA addition can be inadequately adsorbed onto the etching surface. The etching rate of the planes is changed with the different crystallographic orientation. The higher concentration IPA is necessary to improve its quality.

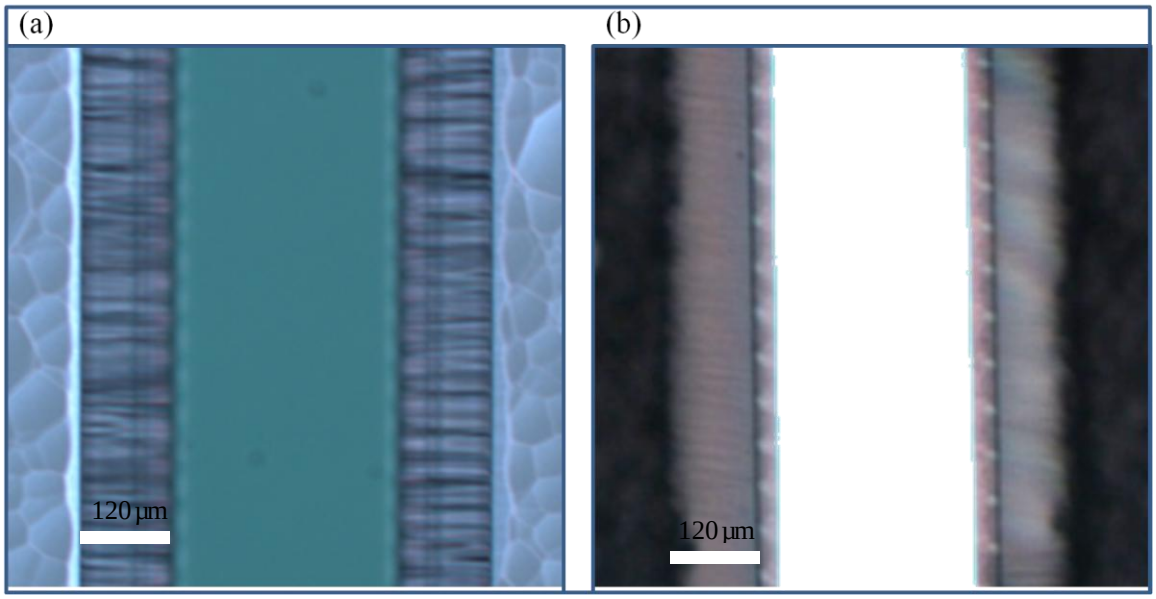

Figure 3.8 Top view optical micrograph of mirrors: (a) 10%TMAH+30%IPA at 80 ℃, (b) 10%TMAH+15%IPA at 80 ℃.

Figure 3.8(a) shows a 45 °mirror obtained by the TMAH-IPA etching system and {100} mirror planes are visually rough. Figure 3.8(b) presents the much smoother {100} mirrors, however, in this case the bottom surface had lots of pyramids which extended to the {100} mirror surface and partially broke the mirror surface. These pyramids have different dimensions, from several micrometers to tens of micrometers. The phenomenon of different dimension pyramids in these experiments indicate that IPA is absorbed on the etched surfaces and hinder the access of reactive OH^- ions, which results in the reduction of etching rates in the crystallographic planes. In the adsorption effect of IPA on {100} silicon surface the access of OH^- ions would be disturbed. Then the equilibrium between the oxidation and diffusion of reaction products have been established what is necessary to obtain the surfaces with satisfactory smoothness. The reduction of the reaction rate caused by IPA adsorption leads to uniform etching of silicon surface [128].

A lot of pyramids appear at the bottom surface of mirror because the etching rate of {111} surface is lower than the etching rate of {100} silicon by TMAH solution. In the continuous etching process, the small pyramids become larger and the amount of pyramids increases. In the end the bottom surface obtained is much rougher. The growth of the pyramids affects not only the lithography process in the later experiments, but also the roughness of the mirror surface. In order to solve this problem, we use Ammonium Persulfate (AP) as another additive to improve the surface roughness of 45 °mirror.

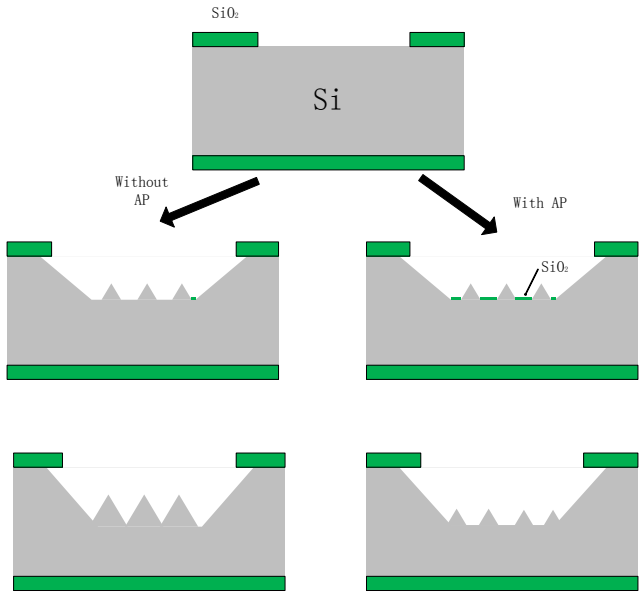

Figure 3.9 The role of AP in TMAH-IPA solutions.

AP has the strong oxidation[130], which can form the very thin silicon dioxide film in reaction activity. The etching rate of SiO_2 is several orders of magnitude smaller than the etching rate of silicon. The SiO_2 attached to the bottom of pyramids forms a pseudo-mask so as to protect this region. Due to continuous etch with the top of pyramids, the roughness of the bottom surface decreased. As the reaction is proceeding, the pyramids are etched to a concave shape. The region covered by pseudo-mask can form a new pyramid. On the other hand, in the high temperature AP can release oxygen which combined with hydrogen on the silicon surface. As a result, the etching solution easily reaches the silicon surface and makes the mirror etched smooth and continuous[131].

In order to obtain smoother 45 °surface and to prevent the pyramids generation, AP is added to improve the profile of mirror surfaces in the following experiments. Figure 3.10 presents optical micrographs of mirrors fabricated by different concentration of AP. With the AP content increases from 0.2% to 1%, pyramids in the bottom become less and smaller. When the AP concentration reaches 1%, it minimizes the dimension and quantity of the pyramids. There is no more remarkable improvement for surface roughness when the AP content increases to more than 1%. Meanwhile, the addition of AP will slightly affect etching rate of the {100} surface. During the same etching time (6h) and all other conditions being equal, the depth of the mirror in the solution containing 1% AP is 125 μm, while the depth of the mirror in the solution containing 0.1% AP is 133 μm. In a conclusion, we can obtain a smooth bottom of mirror with 1% AP and also maintain the etching rate.

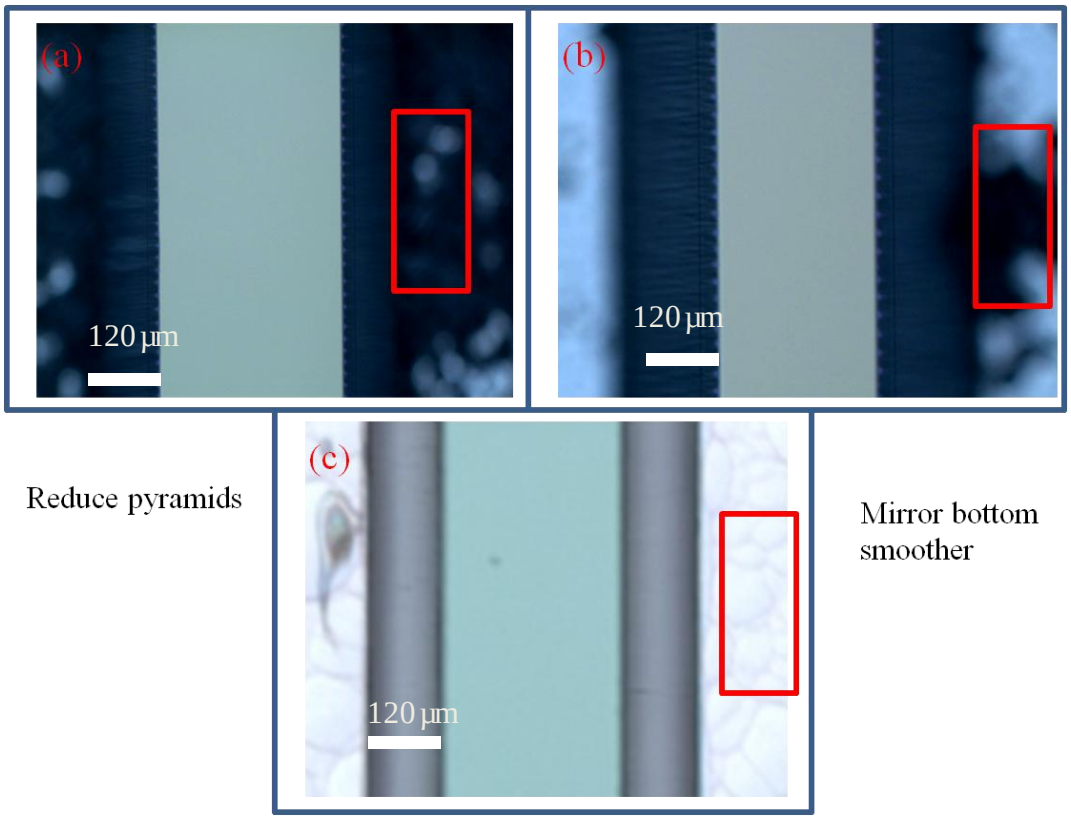

Figure 3.10 Top view optical micrography of mirrors etched by different concentration of ammonium persulfate: (a) 0.2% AP (b) 0.5% AP, (c) 1% AP.

3.2.1.3 Mirror fabrication process

As shown in Figure 3.2a, a SiO_2 layer with thickness of 500 nm was deposited on both sides of a silicon wafer (n-type <100>, 360 µm thick, Double-side polished and 3 inch diameter) by Plasma Enhanced Chemical Vapor Deposition (PECVD) at 300 ℃. Then it was spin-coated with photoresist (Shipley Miroposit S 1828) at 3000rpm for 12 second and baked at 110 ℃ for 1min. The lithography process was performed with SUSS MicroTec MA/BA6 system and a mask aligner (Figure 3.2b). The rectangular grooves were aligned parallel to the <100> direction. The wafer was then developed in MF 319(shipley) for 50s. The opened SiO_2 was etched by CF_4 and O_2 (CF_4:O_2=1:1) as illustrated in Figure 3.2c. Anisotropic aqueous TMAH and IPA mixed etchant with AP was performed to obtain smooth {110} plane as 45 °mirrors.

Table 3.2 The wet etching parameter of 45 °mirror

Temperature (℃)	Rotation speed (RPM)	TMAH (wt%)	IPA (wt%)	AP(g)	Solution weight(g)	Time	Etch rate (µm/min)
80	250	10	20	15	1815	6h	0.35

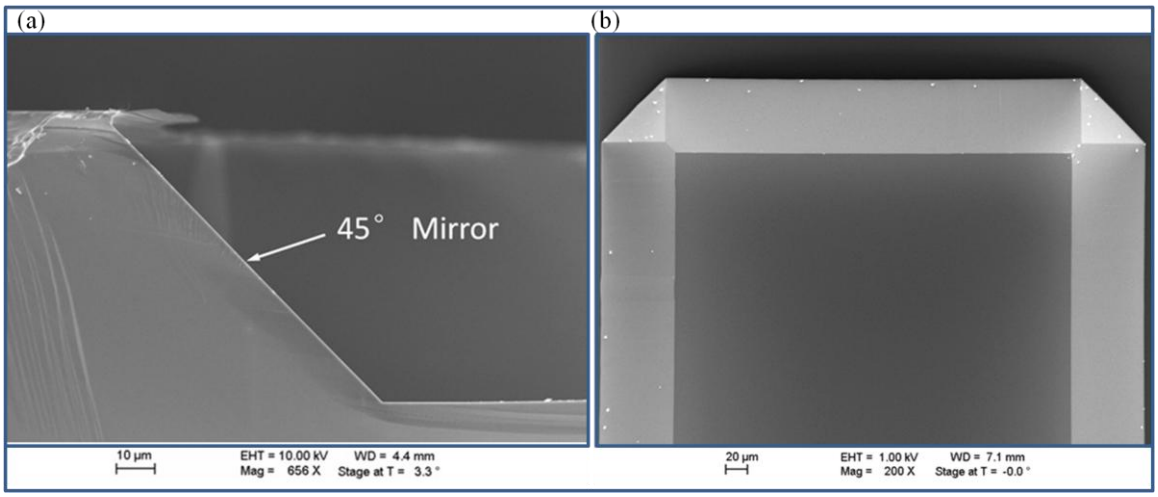

Figure 3.11 SEM images of the 45 °mirrors: (a) cross-section view and (b) top view.

Figure 3.11 illustrated that the surface of 45 °mirrors etched by TMAH-IPA-AP. The parameter of the mixed solution is shown in Table 3.2. The 45 °mirror was fabricated with smooth mirror surface and without any pyramids at the bottom.

3.2.1.4 Conclusion for 45° mirror

In the above studies, {1 1 0} silicon crystal planes that can be used as 45 °acoustic mirrors for reflecting acoustic beams inside the Si wafer were investigated. Besides the well-known etchants KOH and TMAH, the implementation of different concentration of IPA and the ammonium persulfate as an additive in anisotropic etching of {100} silicon was analyzed.

When the 20% wt. IPA is added into the 10% wt. TMAH etchant, it increases the anisotropic ratio (R_{100}/R_{110}) by decreasing the {110} etch rate and keeping the {100} etch rate. {110} surface roughness is greatly improved. There are still some small pyramids at the bottom surface, which will affect the following fabrication process. Addition of ammonium persulfate as the other additive can remarkably eliminate the pyramid and obtain much smoother bottom surface. So 45 °mirror etched by the TMAH–IPA-AP system well satisfies requirements for acoustic wave (GHz) reflection

3.2.2 Microchannel fabrication

3.2.2.1 Deep reactive-ion etching (DRIE)

Deep reactive-ion etching (DRIE) is an anisotropic plasma etch process, which is used to achieve deep penetration, steep-sided holes and trenches in wafers with high aspect ratios . Cryogenic and Bosch are two main technologies of high-rate DRIE. Bosch processes can

fabricate the walls which are slightly tapered, e.g. 88 ° or 92 ° ("retrograde"). Another mechanism is sidewall passivation. SiO_xF_y functional groups are used to condensate on the sidewalls and to protect them from lateral etching. As a combination of these processes deep vertical structures can be achieved[132].

3.2.2.2 Bosch physical etching process presentation

The Bosch process, named after the German company Robert Bosch GmbH which patented the process[133], also known as pulsed or time-multiplexed etching, alternates repeatedly between two modes to achieve nearly vertical structures.

1. A standard, nearly isotropic plasma etch. The plasma contains some ions, which attack the wafer from a nearly vertical direction. Sulfur hexafluoride (SF_6) is often used for silicon.
2. Deposition of a chemically inert passivation layer. (For instance, C_4F_8 source gas yields a substance.)[134]

The requirement of our microdevice is to fabricate deep vertical microchannel between the pair of 45 °mirrors

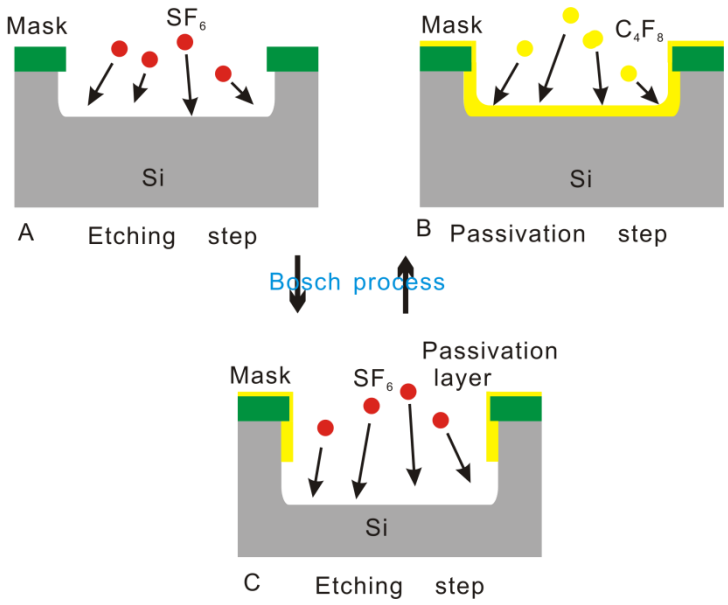

Figure 3.12 Bosch process.

In the Bosch process, each phase lasts for several seconds. The passivation layer protects the entire substrate from further chemical attack and prevents further etching. However, during the etching phase, the directional ions that bombard the substrate attack the passivation layer at the bottom of the trench (but not along the sides). They collide with it and sputter it off, exposing the substrate to the chemical etchant, which was shown as in Figure 3.12[133].

There are four major issues in the microchannel fabrication process: etching rate, silicon profile control, sidewall roughness and silicon grass. In addition to fabricate deep perpendicular microchannels between the pairs of 45 °mirrors in our experiments, it decrease the undulation of the sidewall[135]. Simultaneously it should avoid by-products generation at the bottom of the microchannel which is formed due to the residual passivation layer[136].

3.2.2.3 Etching parameters optimization for the fabrication of the microchannel

This study investigates factors in such a way to obtain perpendicular microchannel and slight sidewall undulation without any silicon grass generation at the same time. Trench profile and sidewall roughness are critical issues for acoustic characterization. Etching rate affect the thickness of the photoresist mask. The realization of biological characterization relies heavily on the smooth bottom of microfluidic channel, so the silicon grass should be avoided.

The fabrication process here is carried out in a Surface Technology System (STS) Multiplex inductively coupled plasma system[137]. In the STS Multiplex inductively coupled plasma system, the source plasma is generated by an inductively coupled coil generator (1 kW, 13.56 MHz). The platen electrode is powered by a 13.56 MHz generator, which allows independent control of the bias potential of the wafer relative to the source plasma. The wafer temperature can be cooled by pressuring helium to the back of platen. The system is equipped with an automatic pressure control valve. The valve is automatically adjusted to maintain the chamber pressure. After performing the dry silicon etching, the etch profile of the trench and sidewall roughness are evaluated thanks to a Scanning Electron Microscope (SEM).

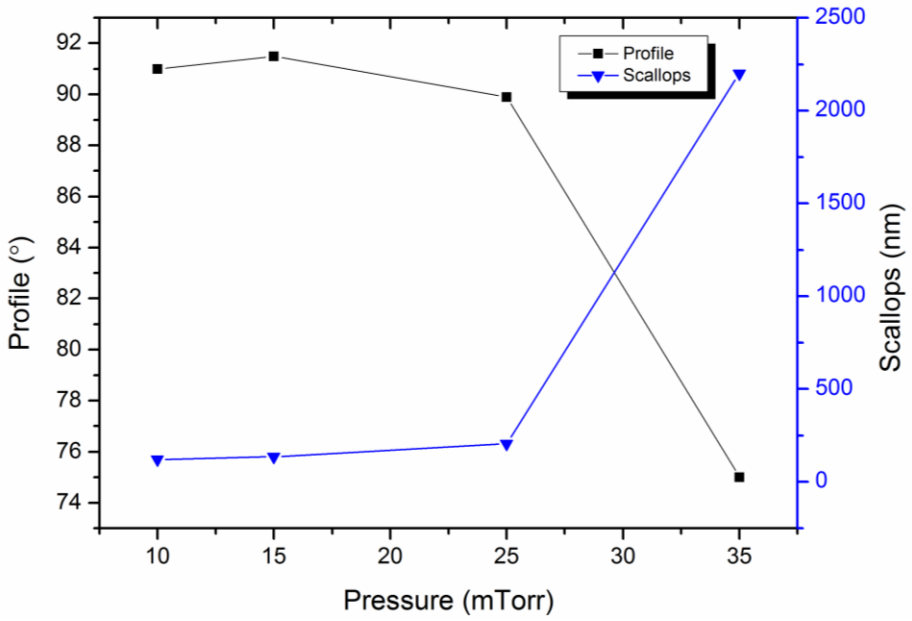

Figure 3.13 Effect on the etching profile and scallops of pressure parameters

SF_6 is used as isotropic etchant due to low toxicity compared to F_2. O_2 typically used with SF_6 to combine with SF_x so that F ion does not combine with them which can keep F ion concentration higher. O_2 can passivate the surface where mask has eroded and reacts with polymer film to keep it from getting too thick.

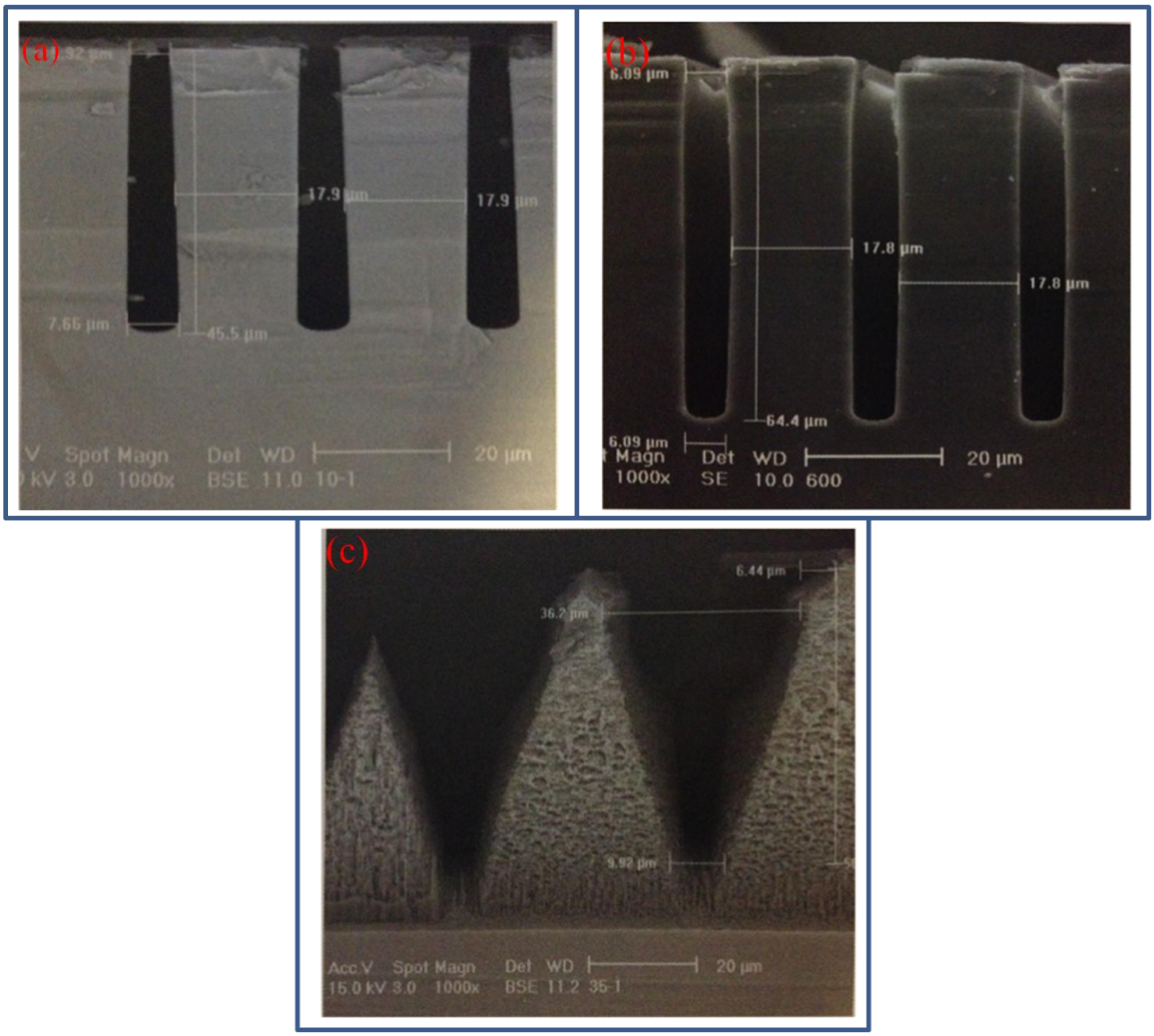

Figure 3.14 SEM micrographs of deep trenches of pressure parameter. (a) pressure 10 mTorr; (b) pressure 25 mTorr;(c) pressure 35 mTorr[138].

Figure 3.13 shows that the etching profile and scallops change along with the pressure increasing. When the pressure is around 25mTorr, the etching profile is near 90 °(Figure 3.14b). When the pressure is lower than 20 mTorr, the profile values have a small fluctuation around 91 ° (Figure 3.14 a). However, the etching structure will be damaged with the pressure more than 30 mTorr (Figure 3.14 c). The scallop sizes slowly grow with the increase of the pressure when the pressure is lower than 25 mTorr, while the scallop sizes sharply increase as the pressure is higher than 30mTorr.

The STS machine works with high plasma density at low pressure, there are several advantages: 1) low pressure reduces the ion scattering and maintains ion trajectory as mostly vertical, 2) it will better control the etch profiles; 3) it improves transport of species into deep trenches. But low pressure will lead to fast pumping and reduce the etch rate. So the pressure chosen is around 25mTorr to make the good profile but the scallops is a little rough, which should be improved in the later experiments.

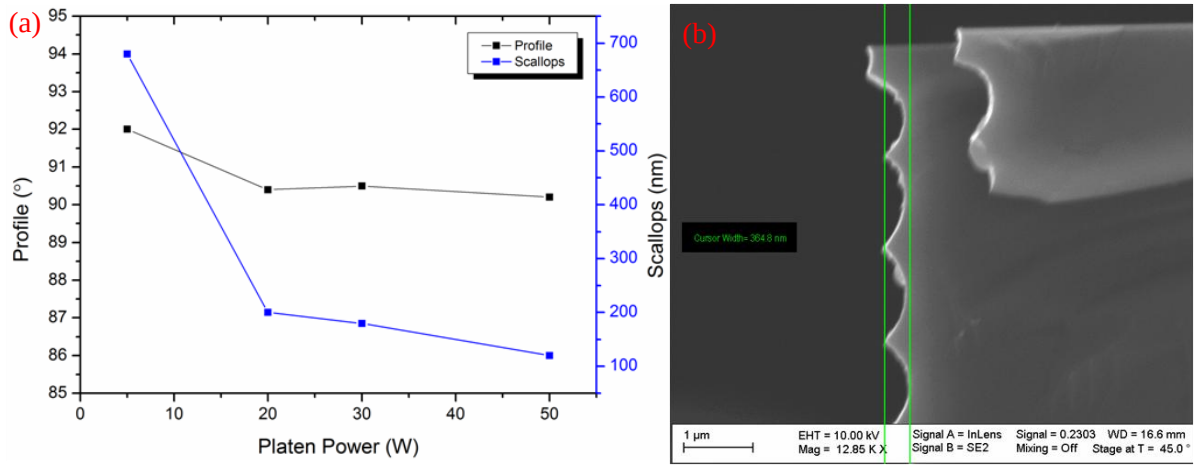

Figure 3.15 (a)Effect on etch profile and scallops of the platen power, (b)The scallop etched at 30W of the platen power.

Platen power, which can accelerate ions through a sufficiently high potential, plays a very important role in deep silicon etching[139]. The high speed ions can remove the passivation from the base of the feature whilst leaving the side wall passivation intact, thereby promoting an anisotropic etching. The influence of platen power on profile and scallops of trench is shown in Figure 3.16. It is found that increasing platen power decreases the profile of silicon trench, as well as decreases the scallops of silicon. When platen power is less than 30 watt, the silicon grass appear at the bottom of etching region (Figure 3.16 a). The increase of platen power will eliminate the generation of silicon grass. However, platen power should be lower than 60 watt, as shown in Figure 3.16c

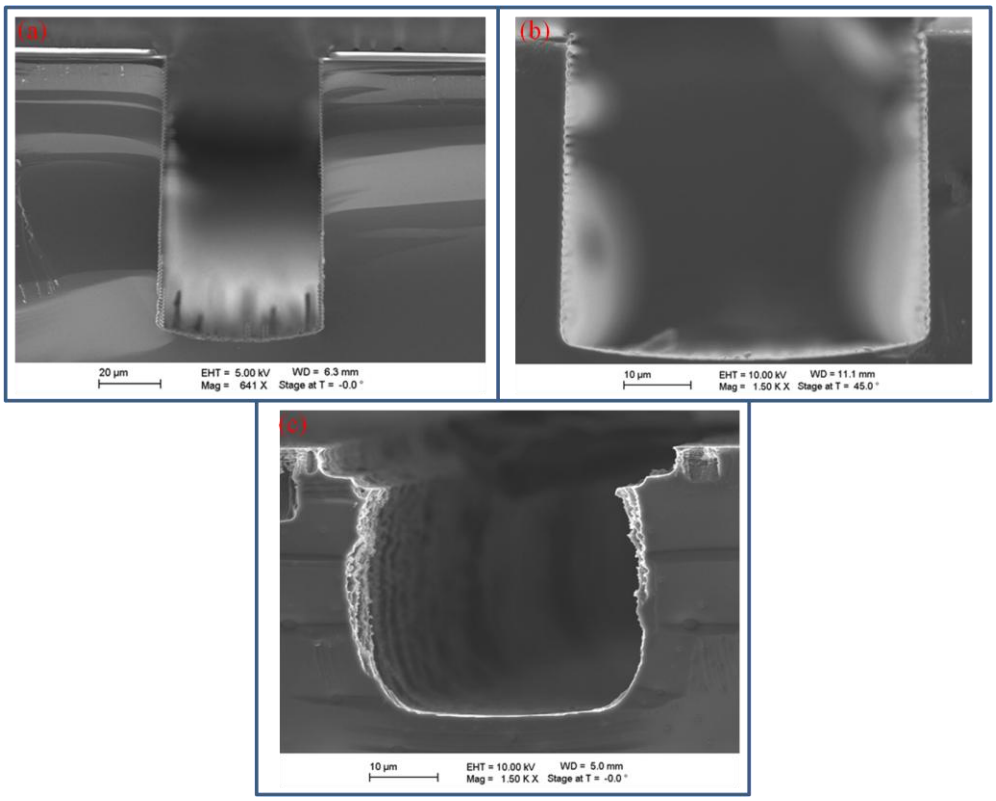

Figure 3.16 SEM micrographs of deep trenches of platen power. (a) platen power 20W, (b) platen power 50W, (c) platen power 60W

Coil power mainly generates the high plasma density in low pressure. The silicon etching rate increases with coil power increase and vice versa. When coil power is higher than 2500W, silicon grass will be generated at the bottom of the trench, the side wall of the trench will be also damaged by sputtering. So the coil power of 2000W will reduce the grass and maintain the high etching rate as much as possible.

Table 3.3 Details of ICP-RIE process parameters used in the experiments.

No.1	SF_6/O_2 Flow rate(sccm)	C_4F_8 flow rate (sccm)	etch/pass time (s)	coil/platen power(W)	Temp (° C)	Etch time (min)
1	350/35	300	3.5/2	2000/50	0	20
2	400/40	300	3.5/2	2000/50	0	20
3	45045	300	3.5/2	2000/50	0	20
4	500/50	300	3.5/2	2000/50	0	20
5	350/35	300	8.5/3.5	2000/50	0	10
6	400/40	300	8.5/3.5	2000/50	0	20
7	450/45	300	8.5/3.5	2000/50	0	20
8	550/50	300	8.5/3.5	2000/50	0	20

Through the effect of three critical parameters on silicon deep etching, experimental results indicate that low pressure and suitable platen power will obtain the perpendicular deep trench and smooth scallops. We choose 25mTorr (pressure), 50W (platen power) and 2000W (coil power) as the references to investigate other parameters.

Table 3.4 Geometrical dimensions and profile angle of trenches etched at different SF6 flow rate

No.	SF_6/O_2 flow rate (sccm)	Designed width (μm)	Top width (μm)	Bottom width (μm)	Etching depth (μm)	Profile angle (°)	Etching rate (μm/min)
1	350/35	50	47	50.1	123.8	90.7	6.2
2	450/45	50	52.1	52.4	90	90.1	4.5
3	550/55	75	94.9	92	23	86.3	2.3

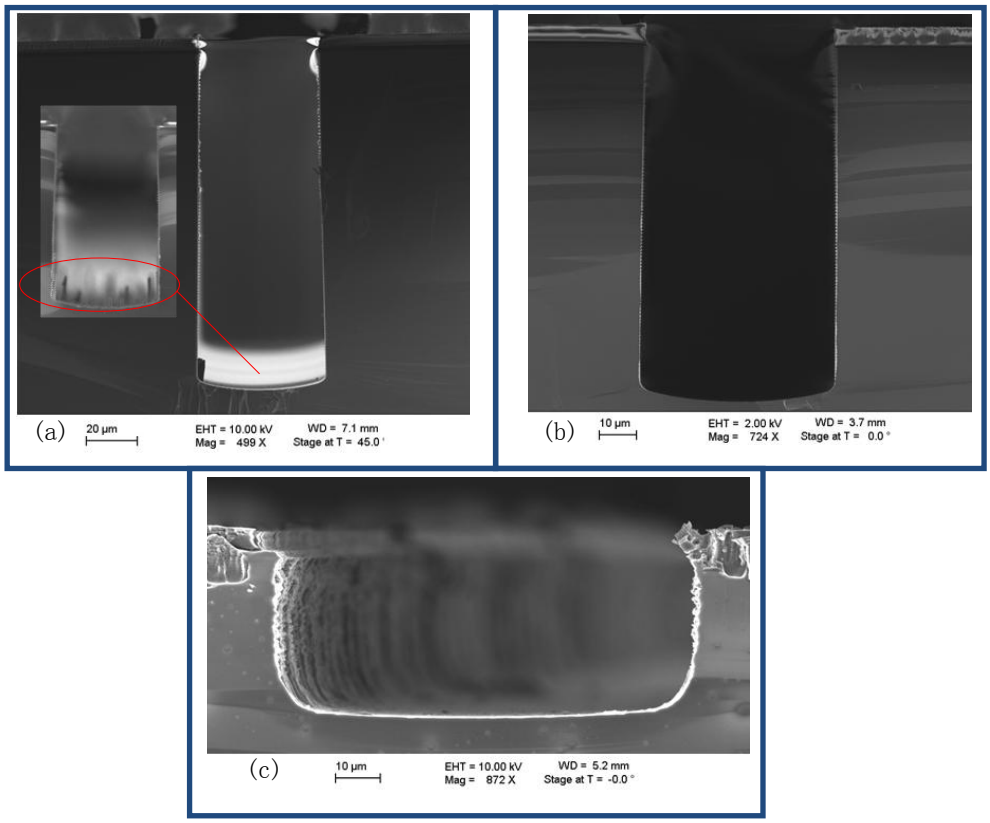

Figure 3.17 The profile of trenches etched with variable SF_6 flow rate (a). Negative (opening) profile at 550 sccm (profile angle ~91) (b). Straight profile at 450 sccm (c). Positive (closing) profile at 350 sccm (profile angle ~86)

Effect of SF_6 flow rate on the etched shape profile of the trenches is clearly shown in Figure

3.17. Figure 3.17a shows negative profile (profile angle ~91 ٩) of a trench when it is etched at SF_6 flow rate of 500 sccm. With a flow rate of 450 sccm, almost vertical profile is obtained. Shape profile is changed from positive to negative, when the flow rate is reduced to 350 sccm.

Since an increased sidewall impact by fluoride ions, the negative slope of the side wall is caused by a lateral etching rate, which increases with the depth of the trench. This impact can either be the result of ion deflection due to mirror charges on the sidewall or ion back-sputtering from the trench bottom. When the SF_6 flow increases (~450 sccm) with all the other parameters kept constant, the passivation quality of the layer diminishes. Fluoride ions have isotropic nature of etching, i.e. etching rate remains the same in all directions. A number of fluoride ions start etching the side walls and thus lateral etching start. Due to sidewall etching, bottom diameter of trench increases and negative profile is formed.

The etching of the trench bottom depends on the density of ions and electrons, as well as the removal of the reaction products. In normal case, there is equilibrium between the transport of etchant to the surface and the products transport away from surface; however at large depth, this equilibrium does not remain balanced and transport mechanism of reactants and waste products become complicated. Fluoride ions try to descend down to etch the bottom surface, while the gaseous products (SiF_xO_y) try to come out of the trench. In this transport process, some of the fluoride ions lose their etching capability[140].

When the SF_6 flow rate increases gradually, etching rate reduces thus results in positive profile. An optimum SF_6 flow rate is needed to get perfectly perpendicular profile. In this case, we have found that the profile of vertical etched shape is achieved at a flow rate of about 450 sccm.

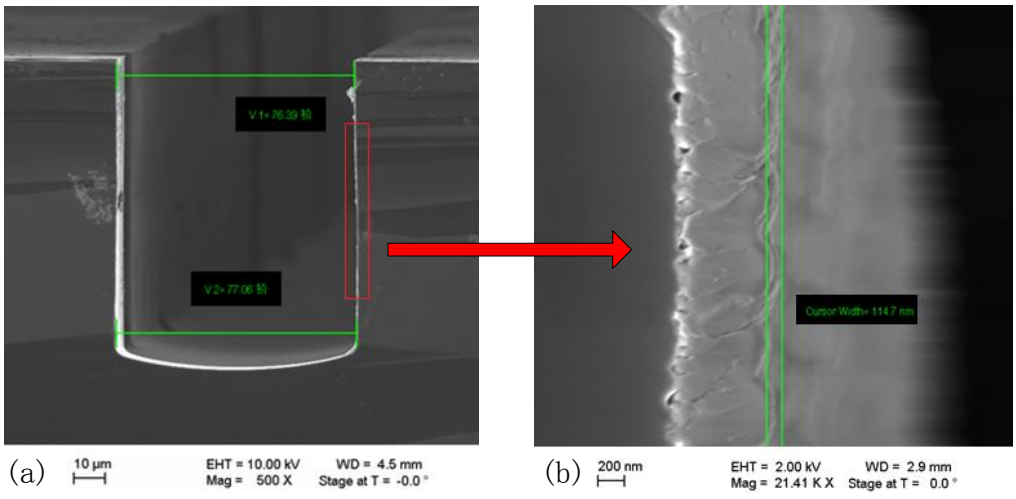

Figure 3.18 SEM micrograph of trenches (a)the profile, (b)the scallops.

The reason of grass formation is not clear yet. At first when the etching depth is low, the silicon

grass will be prevented by the high dispersion of fluoride ions. But with the etching process continuing, the concentration of incoming fluoride ions is not enough to reach the bottom of etching part so that the silicon grass generates. Thus with the incoming fluoride ions is highly collimated, grass is formed at the bottom. In order to prevent the silicon grass formation, SF_6 flow rate and the time ratio of etch and passivation should be precisely controlled [141].

In this part, it shows the effect of three critical DRIE parameters, such as platen power, coil power, pressure, SF_6/O_2 gas flow rate and ratio of etching to passivation cycle time. The profile of trenches is changed from negative to positive profile with the changes of five critical DRIE parameters. Effect of several parameters on bottom grass formation is also shown here. In terms of 50 μm wide trench, thanks to optimization of these five DRIE parameters, we finally obtain perpendicular trenches (~90 °) whose scallops are around 110nm, without grass generation at the bottom (Figure 3.18).

3.2.2.4 Microchannel fabrication process

As shown in Figure 3.2f, RIE technology enabled (O2 and CF4) to etch the rest of SiO_2 and evaporation process is used to deposit Al (500nm) on the silicon surface. Then it was spin-coated with photoresist (Shipley Miroposit AZ 9260) at 2500rpm for 60 second and baked at 110 ℃ for 1min. After the lithography, microchannels were fabricated by deep reactive ion etching (Surface Technology System Company).

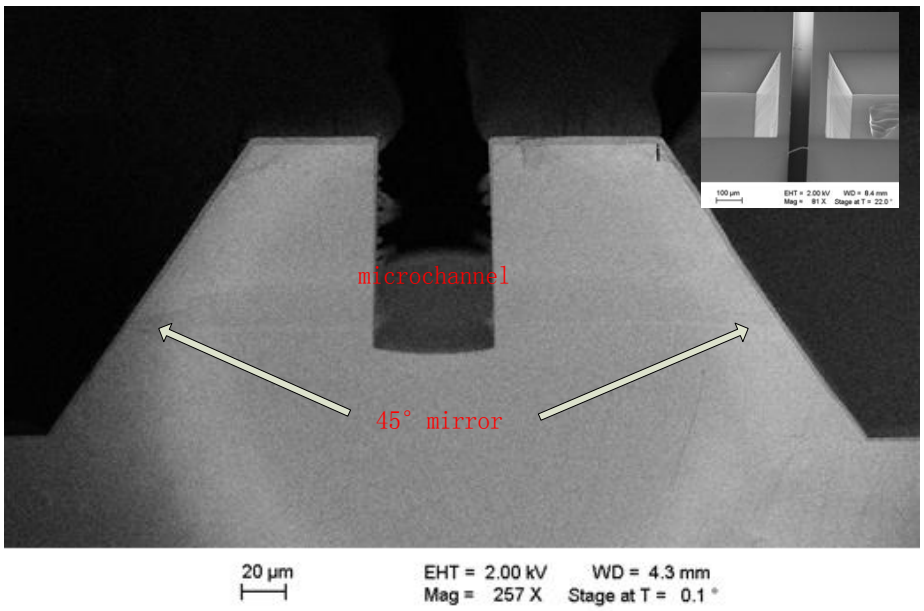

Figure 3.19 SEM micrograph of mirror and channel.

Figure 3.18a shows the cross section images of the microsystem obtained by scanning electron

microscopy (SEM). The width difference between the top and the bottom of the microchannel is less than 1%. Most part of acoustic waves will transmit through nearly 90 °channel wall of the microchannel. Because of high frequency acoustic wave (at the frequency of 1GHz, the wavelength of the longitudinal wave in silicon is 8.4 μm), it is necessary to downsize the scallops of channel walls to make sure the roughness is much smaller than the acoustic wavelength so as to limit the diffraction of the acoustic wave (Figure 3.18b). The micro-device fabricated in the front side of Silicon wafer is shown in Figure 3.19.

3.2.3 Piezoelectric transducer fabrication

3.2.3.1 Introduction

Most of the acoustic devices have been made from bulk piezoelectric materials, such as lithium tantalate ($LiTaO_3$), lithium niobate ($LiNbO_3$) and also use of sapphire (Al_2O_3). These bulk materials are expensive, and are less easily integrated with electronics for control and signal processing. Piezoelectric thin films such as ZnO have good piezoelectric properties, good electro-mechanical coupling coefficient, high sensitivity and reliability [142]. They can be grown in thin film form on a variety of substrates, including silicon, making them perhaps the most promising material for integration with electronic, aiming for disposal, low-price and mass production[143].

Table 3.5 A comparison of different types of deposition methods.

	Sol-gel	CVD	Sputtering	MEB	Laser ablation
Deposition rate	High	low	medium	Very low	Low
Compatibility with MEMs Processing	Good	ok	Good	poor	Poor
Quality	Poor	Good	Good	excellent	Good
Temperature	R.T.	300-900 ℃	25-400 ℃	300-800 ℃	200-600 ℃
cost	cheap	medium	cheap	High	medium
Deposition size	large	large	large	medium	small
Epitaxial growth	difficult	ok	possible	Highly	Ok

ZnO, AlN and PZT are the three dominant piezoelectric thin film materials which can be integrated into MEMS and microelectronics processes. Gallium arsenide (GaAs), silicon carbide (SiC), polyvinylidene fluoride (PVDF) and its copolymers are less common. Thin film piezoelectric (PE) materials. Among these, PZT has the highest piezoelectric constant and electro-mechanical coupling coefficient. However, for biosensor applications, PZT films have

disadvantages such as higher acoustic wave attenuation, lower sound wave velocities, and poor biocompatibility[148]. Piezoelectric AlN thin films have a much higher phase velocity, and are hard and chemically stable. However, the deposition of AlN films and texture control are more difficult compared with that for ZnO. Compared with AlN, ZnO shows a higher piezoelectric coupling, and it is much easier to control the film stoichiometry, texture and other properties[149].

There are many different methods reported for the deposition of ZnO films, including sol–gel processes, chemical vapor deposition, sputtering, molecular beam epitaxial, filtered vacuum arc deposition and atomic layer deposition[144][145][146][147]. Table 3.5 compares different deposition methods for the ZnO films. From a MEMS fabrication point of view, radio-frequency (RF) magnetron reactive sputtering is one of the best methods, with good reproducibility and compatibility with planar device fabrication technology[150].

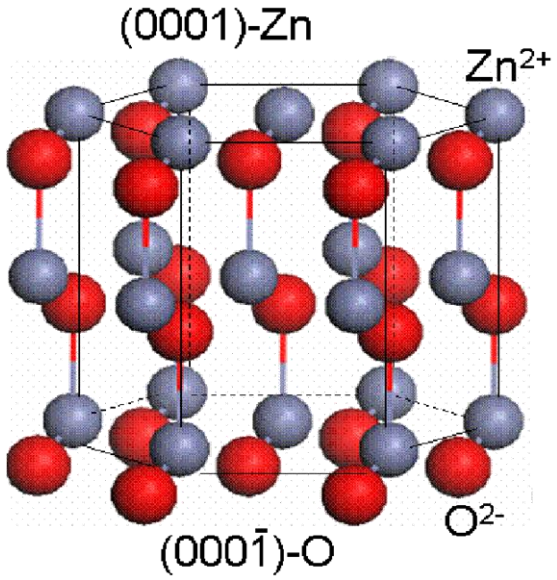

Figure 3.20 ZnO Wurtzite crystalline structure[151]

The microstructure, texture and piezoelectric properties of the ZnO films are normally affected by sputtering conditions such as plasma power, gas pressure, and substrate material and temperature as well as film thickness. During sputtering, the energetic ion bombardment has significant effects on the stoichiometry, size, shape and orientation of ZnO crystals, intrinsic stress, defects, electrical and optical properties, as well as surface and cross-section morphologies. The effects of the processing parameters, such as sputtering gas pressure, RF power, total flux density, bias voltage and substrate temperature, have been successfully described using modified Thornton models[152].

ZnO normally crystallizes in a hexagonal, quartzite type crystalline structure [151](see Figure 3.20), The O_2/Ar gas ratio and gas pressure have frequently been reported to have significant effects on the film stress and texture[153][154]. ZnO acoustic wave devices with a (0001) film texture can be used for sensing in air or gaseous environments also for bio-sensing in liquids.

For ZnO acoustic wave devices, the most frequently used electrode material is aluminum. However, aluminum electrode is limited due to the lifetime of the aluminum electrode in aqueous media. The other common electrode materials include Au, Ni, Pt. The electro-mechanical coupling coefficient (k^2) of the ZnO/Si acoustic wave devices depends on[155]: (1) normalized thickness of ZnO film; (2) acoustic wave mode; (3) film texture; (4) substrate materials; (5) electrode materials.

3.2.3.2 ZnO transducer fabrication process

In this work, we present the fabrication of high frequency thin film transducer of ZnO(~ 1GHz). For piezoelectric applications, the crystallite orientation of ZnO thin film should have the c-axis perpendicular to the substrate. The flow chart is illustrated in Fig. 3.3. As shown in Fig.3.3a, after SiO_2 deposition at the backside is etched by CF_4 and O_2 (CF_4:O_2=1:1), evaporation process is used to deposit ground layer of Ti/Pt (100 Å/1000 Å) on the backside of the silicon wafer. Then a double layer of PMGI SF19 (MicroChem Corp. , Newton, MA ; 7.2μm) and S1828 (Shipley Corporation, 2μm) are patterned by Cr/quartz mask, Double-sided alignment lithography was performed to pattern ZnO transducers under the mirror {110} planes on a SUSS MicroTec MA/BA6 system (see Fig. 3.3i). In the Fig. 3.3j, thick layer was locally etched using a commercial MF 319 developer(Microposit, Shipley Corporation , Malborough, MA) through a mask made of S1828 Photoresist(Shipley Corporation) to obtain the piezoelectric rectangle area (200 m × 100 m) , which ensure a good electrical matching of the transducer(a real part of the impedance of 50Ω at the resonance frequency).

ZnO film and Pt are deposited on silicon substrate by radio frequency magnetron sputtering (The detail parameters of ZnO were shown in table 3.5). Finally piezoelectric transducers (Pt (100nm)/ZnO(2.4μm)/Pt(100nm)/Ti(10nm)) is fabricated by lift-off process in the Remover PG solution(MicroChem Corp. US.).

Table 3.6 The sputtering parameter of ZnO

Power	Pressure	Gas ratio (Ar/O_2)	Time	Sputtering rate
120W	15mT	8	3H	13nm/min

For deposition of high crystal quality ZnO films, the large lattice mismatch and the thermal expansion coefficients between ZnO films and substrate unavoidably cause residual stress[156]. The thermal annealing treatment is used to improve the crystalline quality of ZnO film.

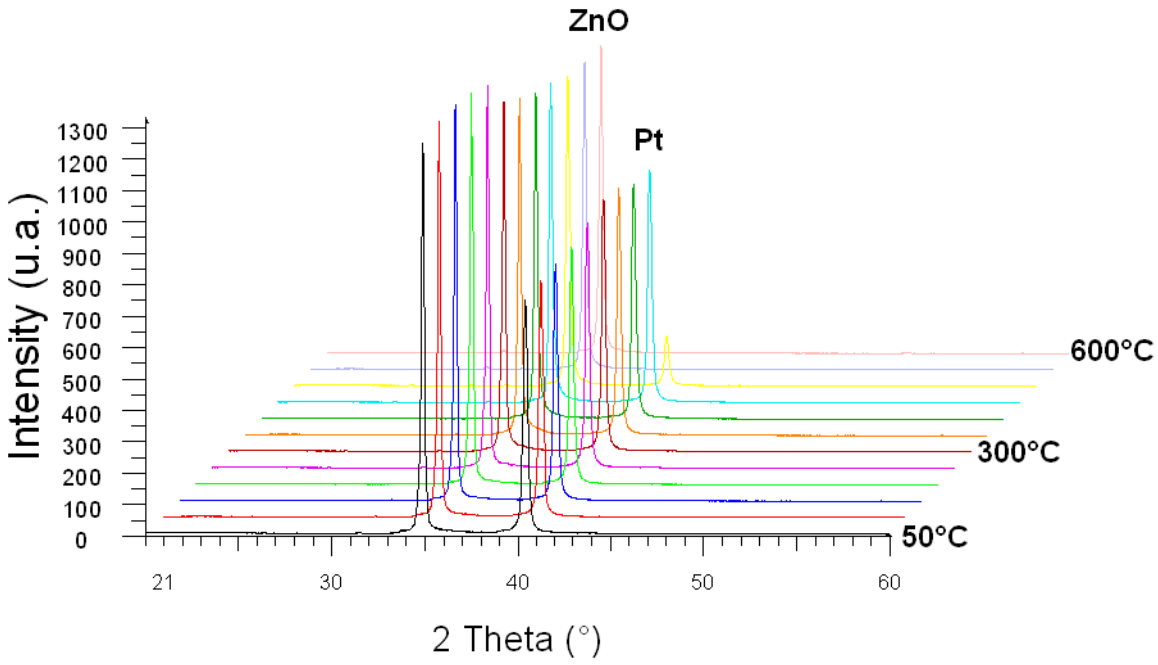

Figure 3.21 XRD pattern of ZnO thin film with different annealing temperature.

Figure 3.21 displays the XRD patterns of the annealed ZnO films with different annealing temperature. Figure 3.21 shows the XRD pattern for samples annealing at several temperature (ranging from 50 to 600 ℃). The peak at about 34 °corresponds to the diffraction from the {002} plane of the ZnO which exhibit a preferred c-axis orientation. The intensity of the peak at first increased when it reaches a maximum at 300 ℃, and then intensity of the peak drops down. So 300 ℃ is chosen as the annealing temperature for half an hour and the heating ratio is 2 ℃/min. The annealed ZnO film is shown in Figure 3.22.

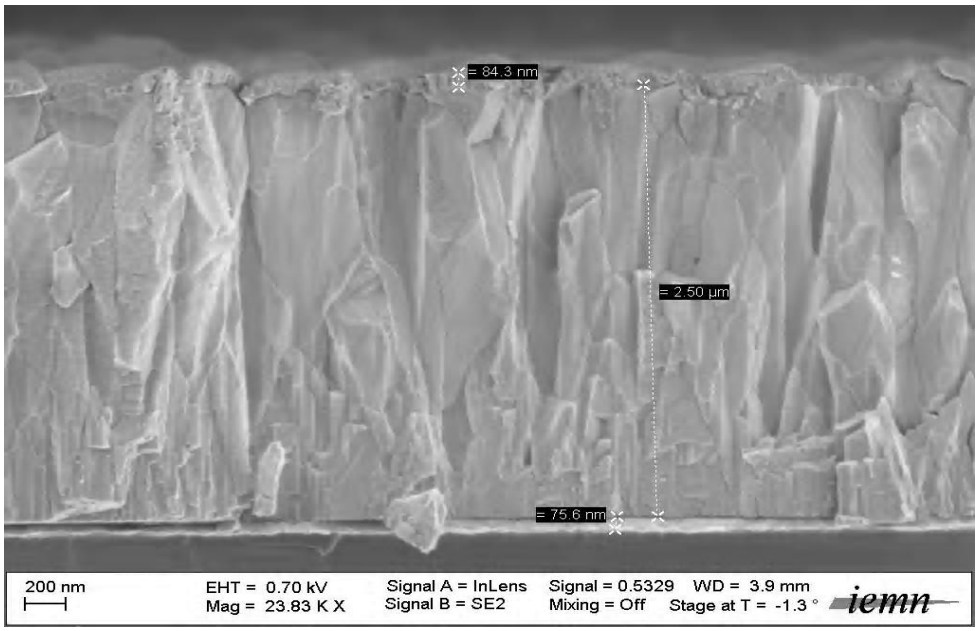

Figure 3.22 The cross-sectional view of ZnO film

The bulk capacitance is given by $C = \varepsilon_0 \varepsilon_r \frac{S}{l}$, ε_0 is the permittivity of ZnO in vacuum ($8.9 \times 10^{-12} F/m$), l is the thickness of the transducer, ε_r is the dielectric constant of ZnO, S is the surface area of ZnO. So we can obtain the $\varepsilon_r = 9.7$ for the ZnO transducer. The dissipation factor $\tan\delta = \frac{\varepsilon_i}{\varepsilon_r} = 0.04$. The theory and experiment data are shown in Figure 3.23.

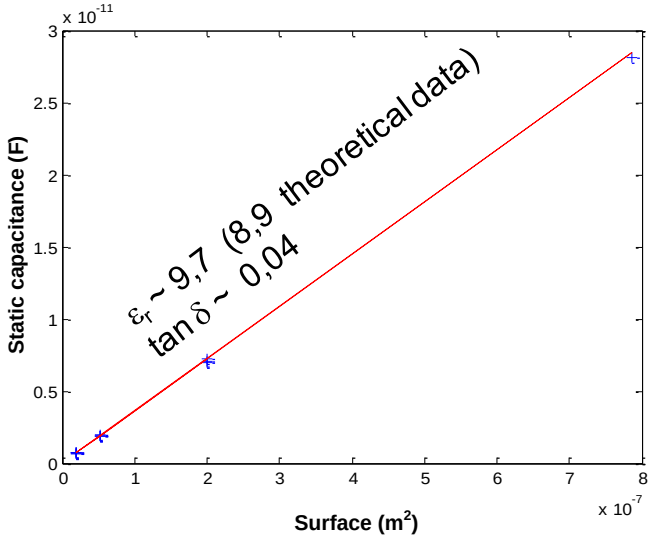

Figure 3.23 Evaluation of the permittivity from transducers of different sizes

3.2.4 PDMS assembly

The use of polydimethylsiloxane (PDMS)[157] elastomer for miniaturized bioassays has numerous advantages over silicon and glass. PDMS as a material is inexpensive, flexible, and optically transparent down to 230 nm (and therefore compatible with many optical methods for detection). It is compatible with biological studies because it is impermeable to water, nontoxic to cells, and permeable to gases. A final, major advantage of PDMS over glass and silicon is the ease with which it can be fabricated and bonded to other surfaces. For the development of bioassays, where many designs may need to be tested, the ease of rapid prototyping in PDMS is a critical advantage.

It is difficult to perform metal deposition and dielectric deposition on PDMS. This severely limits the integration of electrodes and resistors. Nevertheless, this problem is minimized by the fact that PDMS easily attaches to a glass slide using a plasma treatment. Thus, the various thin layer metal or dielectric depositions can be performed on the glass slide. PDMS is a material that ages, therefore after a few years the mechanical properties of this material can be changed. PDMS adsorbs hydrophobic molecules and can release some molecules from a bad cross-linking into the liquid. This can be awkward for some biological study in PDMS microfluidic devices. PDMS is permeable to water vapor which makes evaporation in PDMS device difficult to control. PDMS is sensitive to exposure to some chemicals

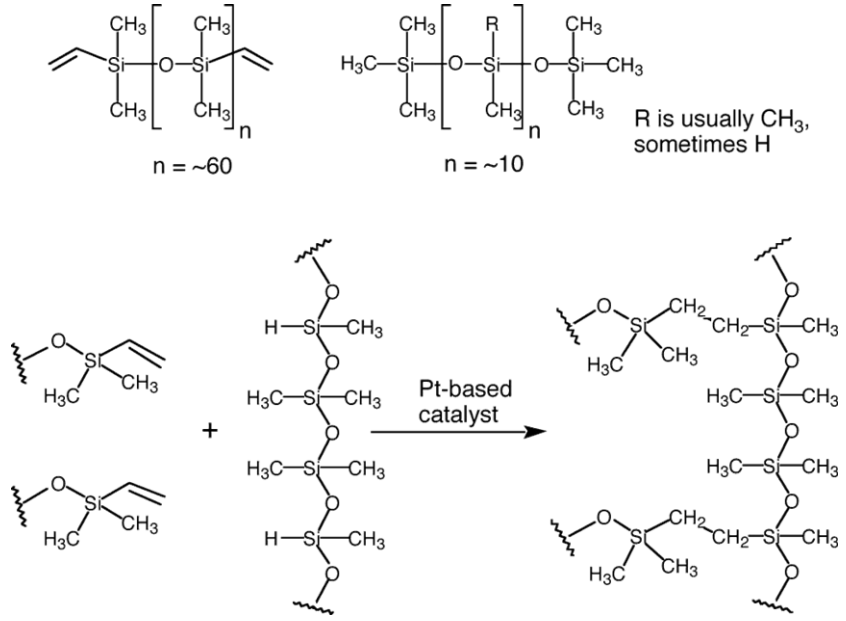

Figure 3.24 Cross-linking of Polydimethylsiloxane

One of the most common used PDMS elastomers is Sylgard 184 (Dow Corning). Sylgard 184 is a two part resin system containing vinyl groups base polymer and hydrosiloxane groups (curing agent) shown in Figure 3.24 below. Mixing the two resin components together leads to a cross-linked network of dimethyl siloxane groups.

The recipe is as follow: firstly add 25 g of Sylgard polymer base to a large glass beaker using a disposable plastic spoon. Add 2.5 g of curing agent using a disposable dropper. Secondly thorough mixing of the PDMS components is essential for good curing. Proper stir is needed to mix the polymer components so that they will yield an adequately cured sample. Bubbles degrade the optical qualities of cured PDMS so bubbles should be removed before curing. Most bubbles trapped during mixing of the components will eventually rise to the top of the liquid where they may be broken by blowing across the surface. Glass beaker containing the mixed PDMS components on the water in sonicated bath might help remove the bubbles. Then the mixture is deposited on a new silicon wafer deposited with octafluorocyclobutane and placed it into the oven at 70 ℃ for 12 hours.

Table 3.7 Parameter of oxygen plasma for PDMS silanization

O2 pressure	power	Time
100mT	20W	30s

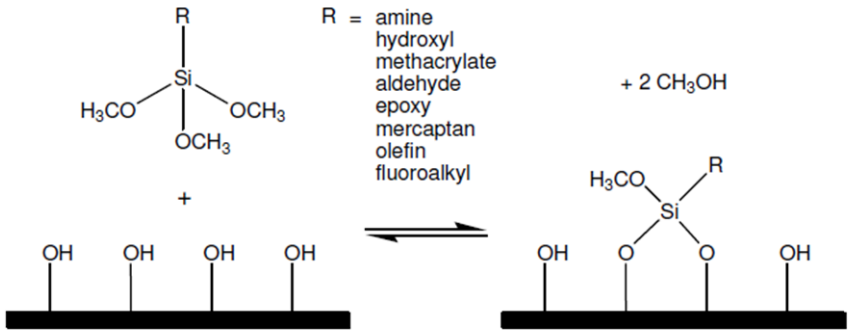

Figure 3.25 Silanization of plasma-exposed PDMS.

Once PDMS is peeled from the silicon wafer, it is prepared for assembly to a final microdevice fabricated. PDMS surface can be chemically modified in order to obtain the interfacial properties of interest. The most reliable method to covalently functionalize PDMS is to expose it to oxygen plasma, whereby surface Si-CH3 groups along the PDMS backbone are transformed into Si-OH groups by the reactive oxygen species in the plasma as shown below in Figure 3.25. The silanization process of PDMS was done by PICO standard plasma system (electronic diener comp.) The detailed parameters of oxygen plasma for PDMS silanization are

shown in Table 3.7. The Si-OH groups in the surface of PDMS easily link with the Si-OH groups in the surface of the SiO_2 thin film deposited on the silicon wafer. Finally the silanization PDMS cover is bonded with the silicon wafer fabricated with 45 ° mirrors and microchannel (Figure 3.26).

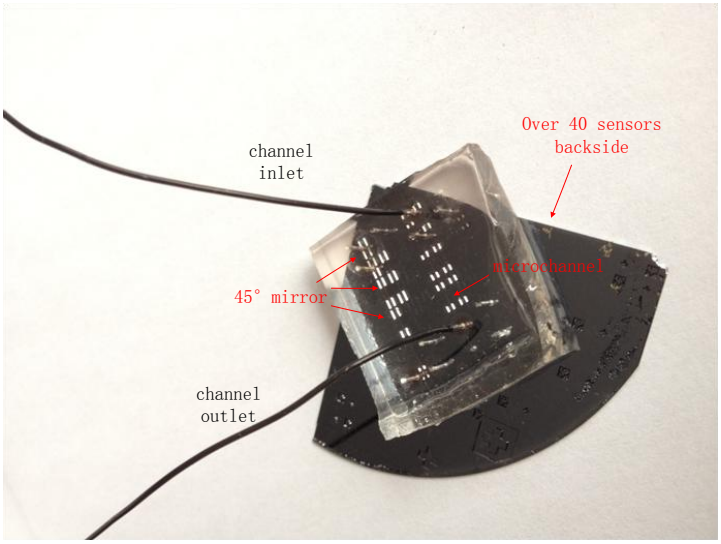

Figure 3.26 Photograph of microsystem

3.3 Discussion and summary

This chapter focuses on the microfabrication especially on the three major micro-components: 45 ° mirror, microchannel and piezoelectric transducer. In order to guide the high frequency (～1GHz) acoustic wave inside the silicon wafer and to achieve characterization in the micro-channel, ZnO thin film (2.4μm) will be fabricated.

Due to acoustic wave reflection, the surface roughness and the profile of the micro-components have a great influence on wave transmission. Only 45 °mirror can guide the acoustic wave from thickness direction to the direction parallel to the surface. The roughness of mirror surface will cause the acoustic wave scattering and attenuation, so reduction the mirror surface roughness is necessary. The bottom pyramids will break the edge of the 45 °mirror and affect the acoustic wave transmission to a certain extent. In the experiments, the average of the mirror roughness is lower than 200nm which is much smaller than the acoustic wavelength at 1GHz. The pyramids were decreased which is not only useful for the acoustic wave transmission but also not convenient for the following micro-fabrication.

As far as the microchannel is concerned, the perpendicular trench, the scallops and the bottom grass have a great influence on wave transmission. In order to avoid the oblique incidence of

acoustic wave, the perpendicular trench is necessary. The scallops will cause the acoustic wave scattering and attenuation as the mirror roughness. Silicon grass will make micro size objects move irregularly, which will impact the sensing accuracy and generate some acoustic noise. By the above experiments, the perpendicular trench fabricated is around 89.7 °-90.3 °. The scallop of the microchannel is less than 150nm and the silicon grass is eliminated.

By means of the microfabrication and improvement, we fabricate a sensing microdevice meeting with the requirement of acoustic transmission inside silicon wafer.

4 Microsystem improvement and application to viscoelastic properties characterization

4.1 Acoustic wave characterization

4.1.1 Scattering parameter

In the S-parameter approach, an electrical network is regarded as a 'black box' containing various interconnected basic electrical circuit components or lumped elements such as resistors, capacitors and inductors, which interacts with other circuits through ports. The network is characterized by a square matrix of complex numbers called its S-parameter matrix, which can be used to calculate its transfer function. For the S-parameter definition, it is understood that a network may contain any components so that the entire network behaves linearly with incident small signals. It may also include many typical communication system components or 'blocks' such as amplifiers, attenuators, filters, couplers and equalizers assuming that they are also operating under linear and defined conditions[157].

An electrical network to be described by S-parameters may have any number of ports. Ports are the points at which electrical signals either enter or exit the network. Ports are usually pairs of terminals [158]. S-parameters are used at frequencies where the ports are often coaxial or waveguide connections.

The following information must be defined when specifying a set of S-parameters: 1) the frequency, 2) the characteristic impedance (often 50Ω), 3) the allocation of port numbers.

Figure 4.1 The scheme of 2-ports network

The S-parameters matrix for the 2-ports network is the most commonly used and serves as the basic building block for generating the higher order matrices for larger networks[159]. In this case the relationship between the reflected, incident amplitude waves and the S-parameter matrix is given by:

$$\begin{pmatrix} b_1 \\ b_2 \end{pmatrix} = \begin{pmatrix} S_{11} & S_{12} \\ S_{21} & S_{22} \end{pmatrix} \begin{pmatrix} a_1 \\ a_2 \end{pmatrix}$$

Expanding the matrices into equation gives:

$$b_1 = S_{11}a_1 + S_{12}a_2$$

and

$$b_2 = S_{21}a_1 + S_{22}a_2$$

Each equation gives the relationship between the reflected and incident amplitude waves at each of the network ports, 1 and 2, in terms of the network's individual S-parameters, $S_{11}, S_{12}, S_{21}, S_{11}$. If one considers an incident amplitude wave at port 1(a_1) it may result from the mismatching of system impedance (Z_0)[160].

$$\mathrm{S}_{11} = \frac{b_1}{a_1} = \frac{V_1^-}{V_1^+} \text{ and } \mathrm{S}_{21} = \frac{b_2}{a_1} = \frac{V_2^-}{V_1^+}$$

Where V_1^+ and V_1^- is the voltages across port 1 and V_2^+ and V_2^- is the voltage across port 2.

Similarly, if port 1 is matched to the impedance then a_1 becomes zero, giving

$$\mathrm{S}_{12} = \frac{b_1}{a_2} = \frac{V_1^-}{V_2^+} \text{ and } \mathrm{S}_{22} = \frac{b_2}{a_2} = \frac{V_2^-}{V_2^+}$$

Each 2-ports S-parameter has the following generic descriptions: S_{11} is the input port voltage reflection coefficient. S_{12} is the reverse voltage gain. S_{21} is the forward voltage gain. S_{22} is the output port voltage reflection coefficient.

4.1.2 Signal processing and method used for acoustic measurement

Electrical measurements using network analyzers are of common use in electronics characterizations. Their major interest is the high sensitivity (-110dBm). We measure the S_{11} and S_{21} scattering parameters defined respectively as the ratio of the complex amplitudes of the reflected and transmitted voltage thanks to a Suss Microtech prober coupled with a ROHDE&SCHWARZ ZVA8 Vector Network Analyzer (VNA). It has been shown that this parameter is composed by two terms, a purely electrical one, and an acoustical one[161]:

$$\mathrm{S}_{ij}(f) = \mathrm{S}_{ij}^{elect} + K\mathrm{S}_{ij}^{acoust}$$

Where K is the electromechanical coupling constant for the piezoelectric material

The origin of the electrical term is due to the reflection of the electrical wave on the transducer.

This term vanishes if the transducer is perfectly electrically matched to the impedance of the line. The second term represents the acoustic wave propagating in the silicon wafer, and so on, reconverted by the transducer into an electrical signal. The network analyzer is calibrated in the plane of the transducer which provides us a phase or time origin. The inverse Fourier transform of the S_{11} parameter can be interpreted as the impulse response of the system.

In the time domain, the two terms of S_{11} are separated. The electrical term occurs just after the origin of time and the acoustical one is delayed by the acoustic propagation time. Figure 4.2a presents the real and imaginary parts of the S_{11} parameter in the frequency domain given by the network analyzer and Figure 4.2b presents the modulus (dB scaled) of S_{11} in the time domain for which the previous explanation can be easily observed. For these measurements, since the opposite face of the wafer in respect to the transducer is free of material, we can get out the acousto- electric parameter K which is simply the amplitude of the first acoustical echo, commonly named the first arrival.

These measurements on the transducer are done through the material to characterize the interface at the opposite face of the silicon wafer from the transducer. We achieve the characterization by comparing the measured signals with and without the sample. We have encountered two kinds of situations-the absorption of the acoustic wave in the material is:

- weak enough to observe an acoustic reflection on the free surface of the layer (method 1);
- too large to detect the reflection on the free surface. In such a case it is difficult to evaluate speed of sound in the material.

We will show a method to overcome this difficulty.

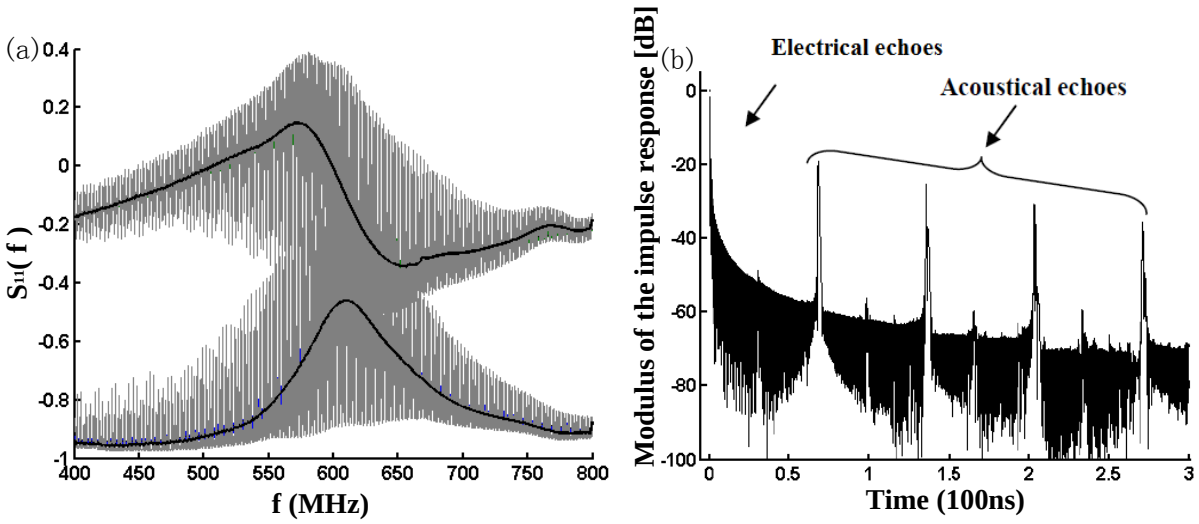

Figure 4.2 Real and imaginary parts of S_{11} parameter function of frequency (MHz) (Thick curves represent the electrical term) (b) Modulus of the impulse response, inverse Fourier transform of the S_{11} parameter function of time.

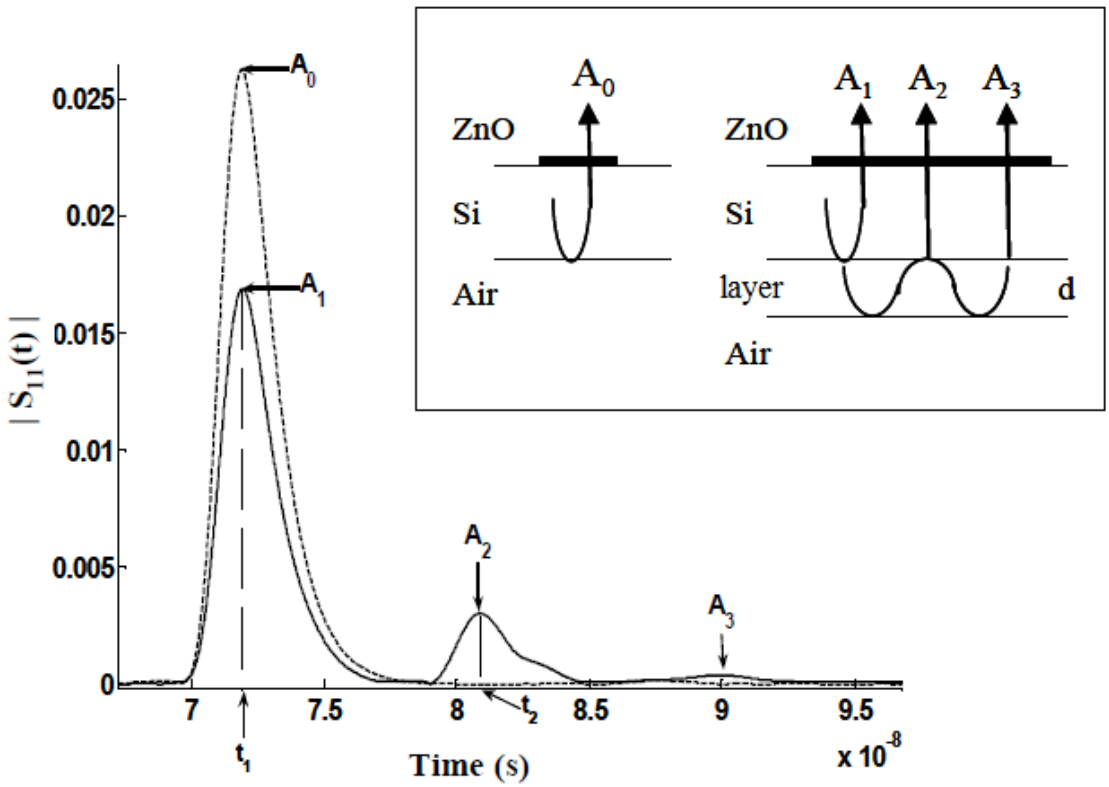

Figure 4.3 Modulus of the impulse response (dB), inverse Fourier, Transform of the S_{11} parameter function of time (s), dot line: without sample, solid line: with a specific layer

In the first method, we use measurement on the layer of a material to be characterized by the mean of a 1GHz longitudinal ZnO transducer. We have superimposed on the modulus of the inverse Fourier transform of the S_{11} parameter in dB scale.

Time delay between echoes labeled 'i' or 'j' enabled the phase velocity to be evaluated:

$$\nu = \frac{2(j-i)e}{t_j - t_i},$$

where e is the thickness of the material.

We compute the absorption coefficient α using the amplitude of impulses:

$$\alpha = \frac{\log_{10}\left(\frac{1}{r^{j-i}} \cdot \frac{A_j}{A_i}\right)}{2(j-i)e}, \; i \neq 0,$$

with $r = \frac{A_0}{K}$, and A_j the amplitude of echo number j.

We first isolate electrical term from the acoustical term. Therefore, we apply an erasing window $W_e(t)$ that set the acoustical term to zero and take the Fourier transform of the product.

$$S_{11}^{elec}(f) = \mathfrak{F}\{\mathfrak{F}^{-1}[S_{11}(f)] \cdot W_e(t)\} = S_{11}(f) \otimes \mathfrak{F}[W_e(t)]$$

We can get the acoustical term by subtracting the electrical term from the measure:

$$S_{11}^{acoust}(f) = S_{11}(f) - S_{11}^{elec}(f)$$

The first acoustic echo can be obtained by using the same method. An erasing window $W_a(t)$ sets to zero the whole signal except for the first arrival:

$$S_{11}^{acoust\ -1}(f) = \mathfrak{F}\{\mathfrak{F}^{-1}[S_{11}^{acoust}(f)] \cdot W_a(t)\} = S_{11}^{acoust}(f) \otimes \mathfrak{F}[W_a(t)]$$

The effect on the signal is shown on the Figure 4.4 which can be compared to the Figure 4.2a. A zoom of this image shows clearly that the first acoustic arrival term is only composed by a complex exponential of a single time of flight. The same signal processing is applied to the reference signal. Then we get out the reflection coefficient of the acoustic wave at the interface between silicon wafer and the sample by computing the ratio of these two filtered signals.

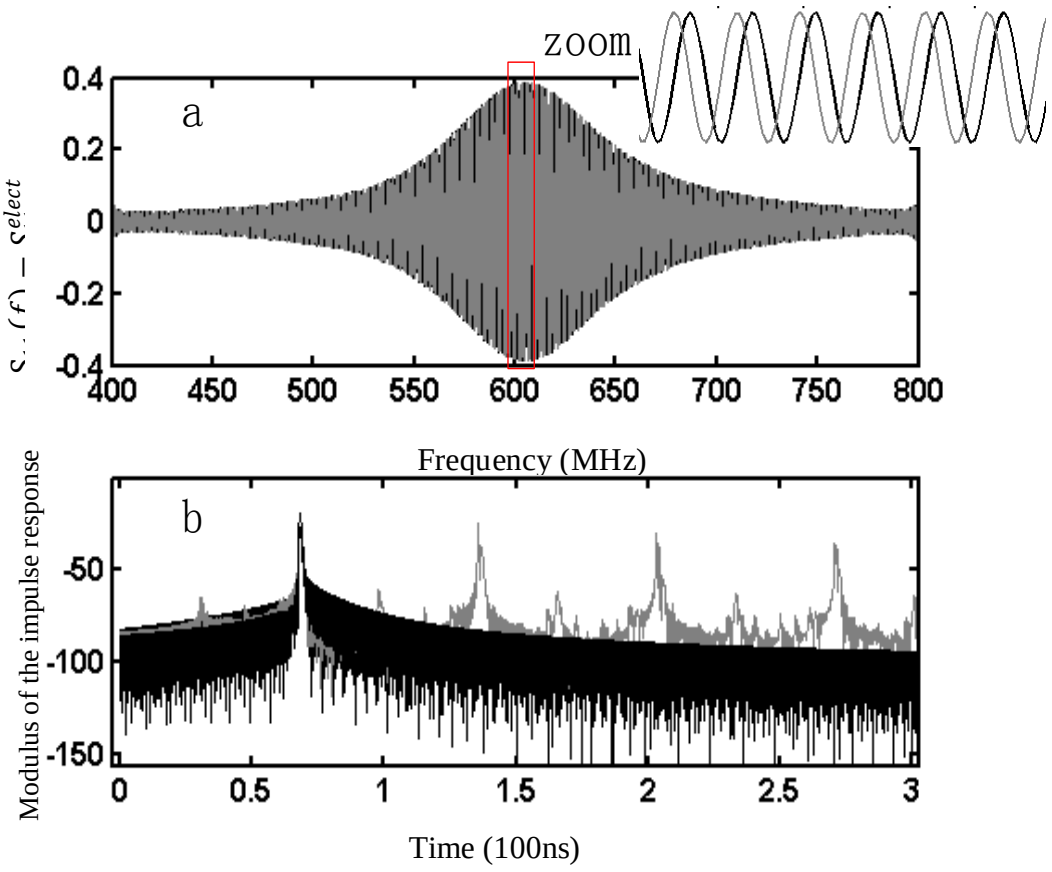

Figure 4.4 Real and imaginary part of the filtered signal function of frequency (MHz), gray: imaginary part, black: real part b) Modulus of the impulse response (dB), inverse Fourier Transform of the S_{11} parameter function of time (100ns), gray: before filtering, black: after filtering

This reflection coefficient can be modeled by:

$$R = \frac{Z_M - Z_{Si}}{Z_M + Z_{Si}}$$

where Z_M is the characterized material mechanical impedance and Z_{Si} is the mechanical impedance of the silicon wafer

From this reflection coefficient we can get out the acoustic impedance of this material

$$Z_M = \rho_M V_M$$

The phase velocity V and the absorption coefficient β are linked to complex velocity V_M

by $k_M = \frac{\omega}{V_M} = \frac{\omega}{V} - i\beta f^2$

So, we carry out the sound velocity and the absorption coefficient in the layer by minimizing distance from the measured reflection coefficient and the result of simulation, assuming that the density of the material is known. The method can expand to the transmission echoes and the analysis of the impulse response of S_{21} parameter.

4.1.3 Experimental set up for acoustic wave characterization

The acoustic test system consists of manual probe system (Cascade Microtech), multi-channel signal generator, Rhode&Scharwtz vector network analyzer and microfluidic controlling system (MFCS pressure-driven flow controller) as shown in Figure 4.5.

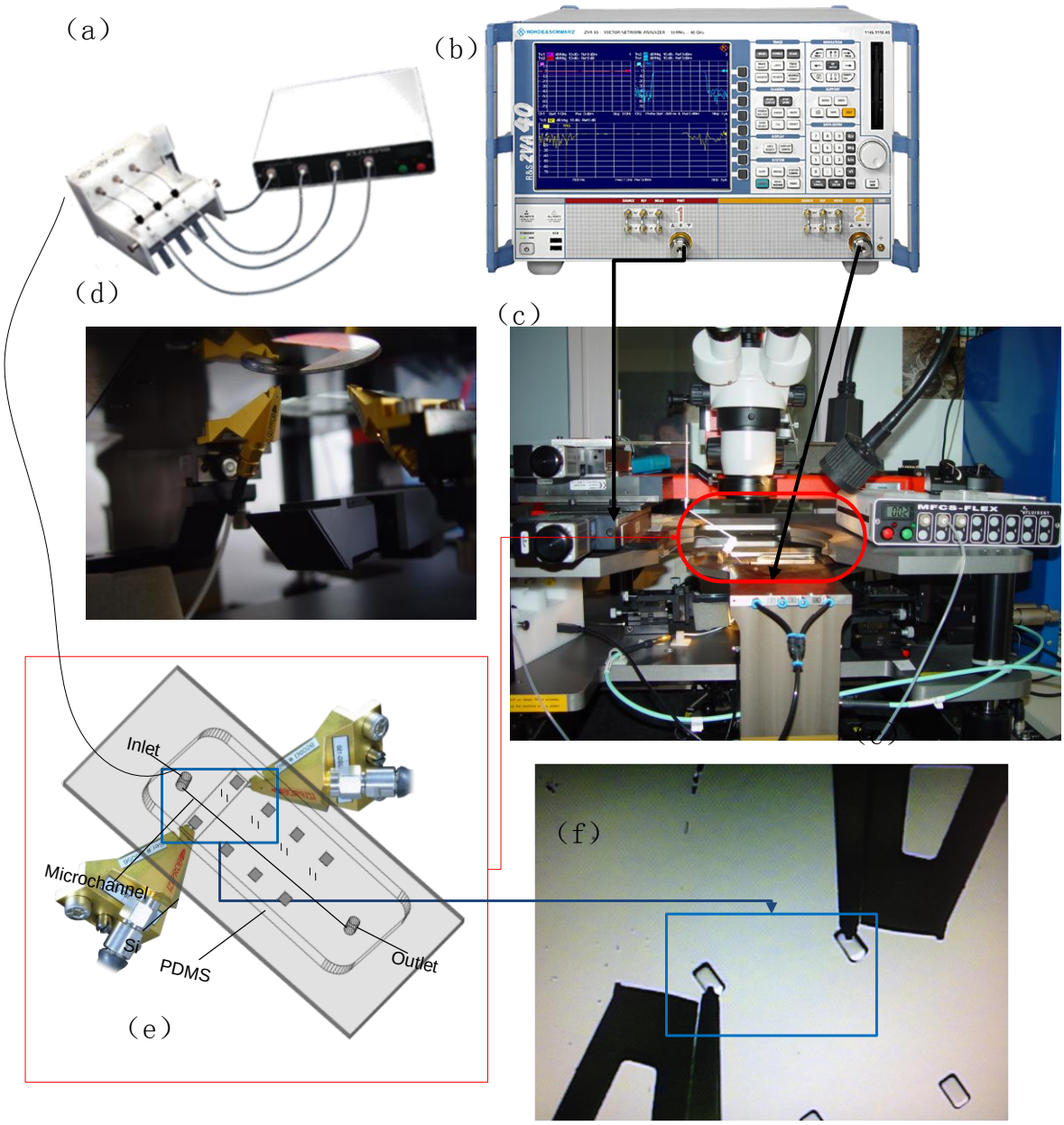

Figure 4.5 Acoustic characterization system: (a) multi-channel signal generator (b) rhode&Scharwtz vector network (c) PM8 system (d) scheme of backside probe contact (e) picture of probe and ZnO transducers (contact mode).(f)MFCS(microfluidic Flow Control Systems) are pressure-driven flow controlller

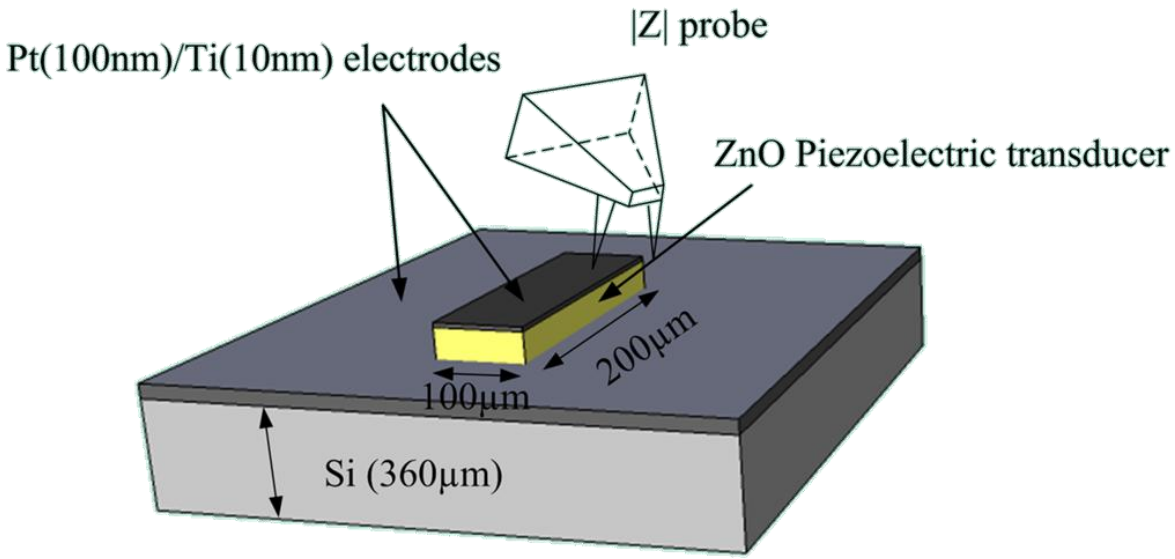

Figure 4.6 Scheme of the probe excitation of the ZnO transducer.

The rectangular piezoelectric area of ZnO transducer is 200 µm×100 µm(Figure 4.6), which ensures the real part of the impedance of 50Ω at the resonance frequency[162]. The electrical impedance of a transducer is defined at the resonance frequency by $Z(f_r) = \frac{A}{Sf_r^{\,2}} - j\frac{1}{c_0}\frac{1}{2\pi f_r}$.

In the case of ZnO:

- A is a constant characterizing the piezoelectric material ($A = 1.0458\times10^{12}\,\Omega\cdot m^2 Hz^2$),
- S is the area of the piezoelectric transducer
- and c_0 is the static capacitance.

First, measurements were carried out on reference devices: ZnO/Si/air (1GHz transducer). In this case, as the reflection coefficient at the Si/air interface is −1, S_{11} can be written as:

$$S_{11} = S_{11}^{elec} - Ke^{-2i\theta_0} + ...$$

Isolating the first echo allows us to obtain the acousto-electric parameter *K*.

Figure 4.7 shows the impedance of the transducer deduced from the measurement of S_{11}. The continuous line represents the numerical simulation derived from the KLM model [16] and the dashed line results from experimental measurements.

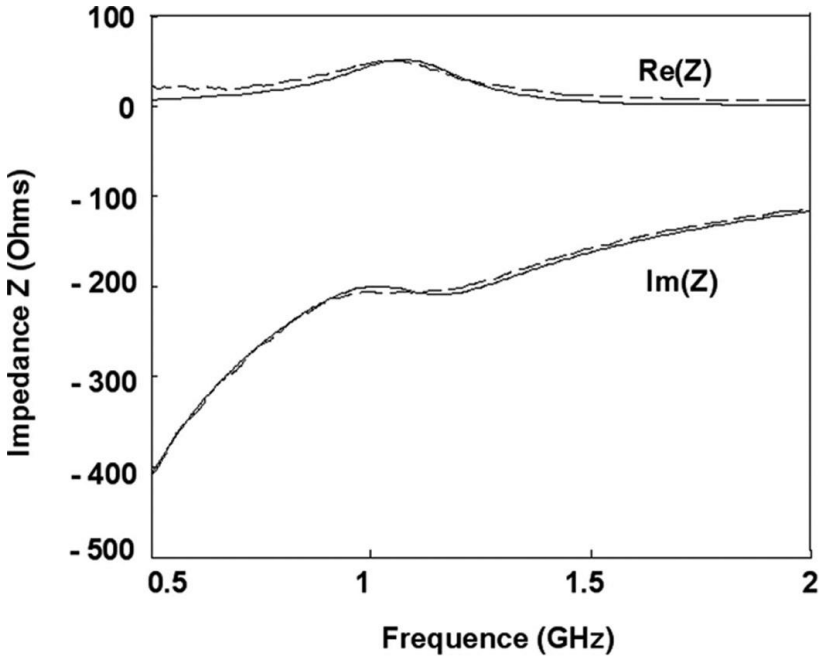

Figure 4.7 Electrical impedance of the ZnO 1-GHz transducer [Pt (100 nm)/ZnO (2.4 μ m)/Pt (100 nm)/Ti (10 nm)/Si] obtained by measurement of S11. The continuous line represents the numerical simulation and the dashed line results from experimental measurements.

The manual probe system is composed of PM8 system and Karl Suss |z| probe. The PM8 system is the simple and highly precise to the probing solution. The MFCS provides pulseless and highly stable (-0.1%) flows as well as great responsiveness and ensure the full integrity of your samples for all your microfluidic applications.

We acquire the information by measuring the S_{ij} scattering parameters of acoustic test system. The calibration of test system should be finished before measurement. With the calibration kit, the compensation of cables and probes impedances is achieved using a TOSM (Through-Open-Short-Match) calibration technique. As illustrated in Figure 4.5e, there are two tips in the Karl Suss |z| probe, one tip contacts with the top electrode over the ZnO thin film, the other tip contact with the bottom electrode over the Silicon substrate.

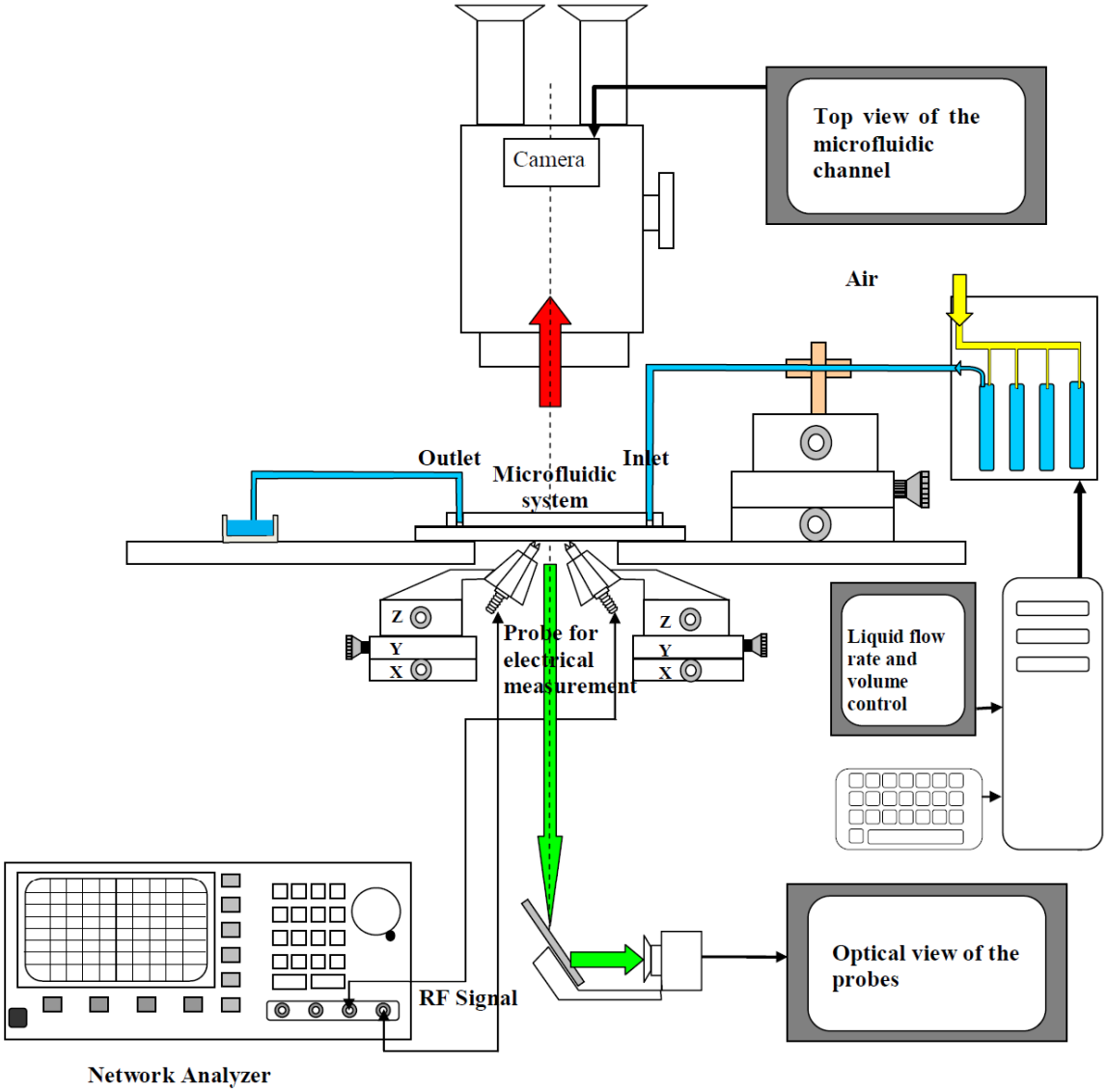

Figure 4.8 The schematic of the workbench for characterization

4.2 Acoustic wave guiding characterization

4.2.1 Wave guiding inside silicon wafer using two 45°mirrors

A schematic view of the system is presented in Figure 4.9d. After the 45° mirrors were achieved on one side of the silicon wafer, piezoelectric transducers were deposited on the other side of the wafer. As shown in Figure 4.9d, a pair of transducers was aligned to be under the mirrors and the other pair of transducers was aligned under the bottom of mirror. Moreover, shifting the position of the transducer under this kind of 45°mirror makes it

possible to choose the depth of the acoustic beam from the surface of the wafer. The transducers can be achieved by bonding single crystals or depositing thin films on a host wafer. We present ZnO thin films as transducers. The frequency of the transducer was proposed to be around 1 GHz. An embedded acoustic wave propagating parallel to the surface of the silicon wafer is then generated by using the mirrors mentioned above.

Here we measure the S_{11} and S_{21} scattering parameters defined as the ratio of the complex amplitudes of the reflected and transmitted to the incident voltage thanks to a Suss Microtech prober on PM8 manual probe system(CASCADE MICROTECH) coupled with a ROHDE&SCHWARZ ZVA8 Vector Network Analyzer (VNA). The impulse response of the system $S_{ij}(t)(i, j = 1 \text{ or } 2)$ was obtained by computing the inverse Fourier transform of the complex data collected by the VNA. We observed the transmitted and reflected echogram and used the physical analysis to validate their propagation delay using the wave velocity.

The thickness of the silicon wafer is about 370μm. The distance between the top of the mirrors and the distance between the transducers are about 370μm and 390μm, respectively. Short edges of the transducers are a little bigger than the designed size due to the lithography process during the fabrication, so a little part of the transducers is aligned below the horizontal surface plane. This allows us to measure a little signal which propagates vertically and returns to the emitter by the S11 parameter characterization. The energy of this signal is weak enough to detect the shear wave which is also emitted at very low level. Because of the fabrication limitation by RF sputtering technology, the ZnO thin film is not able to exhibit a perfect c-axis orientation perpendicular to the substrate surface. The polycrystalline ZnO still exit in the thin film, so when the ZnO thin film is exited, not only longitudinal wave but also shear wave will be generated. It is observed that there are longitudinal and shear waves propagating on this vertical path, see Figure 4.9a.

The predicted time of flight is about 87.6 ns for the longitudinal wave (LL, means the longitudinal acoustic wave emitted by the transducer and reflected as longitudinal one by the top surface of the silicon wafer) and 125.7 ns for the shear wave (SS, means the shear acoustic wave emitted by the transducer and reflected as shear one by the top surface of the silicon wafer) which are close to the measured values with only about 0.4% of error. One can also observe that a part of longitudinal wave emitted obliquely was converted into a shear wave (named as LS) which returned to the emitter thanks to the curvature of the slowness curve in silicon for this orientation. A predicted time of flight of 107.2 ns is also close to the measured value with some 0.4% of difference. This first analysis validates the data used in the simulation (stiffness tensor, density and size of the system).

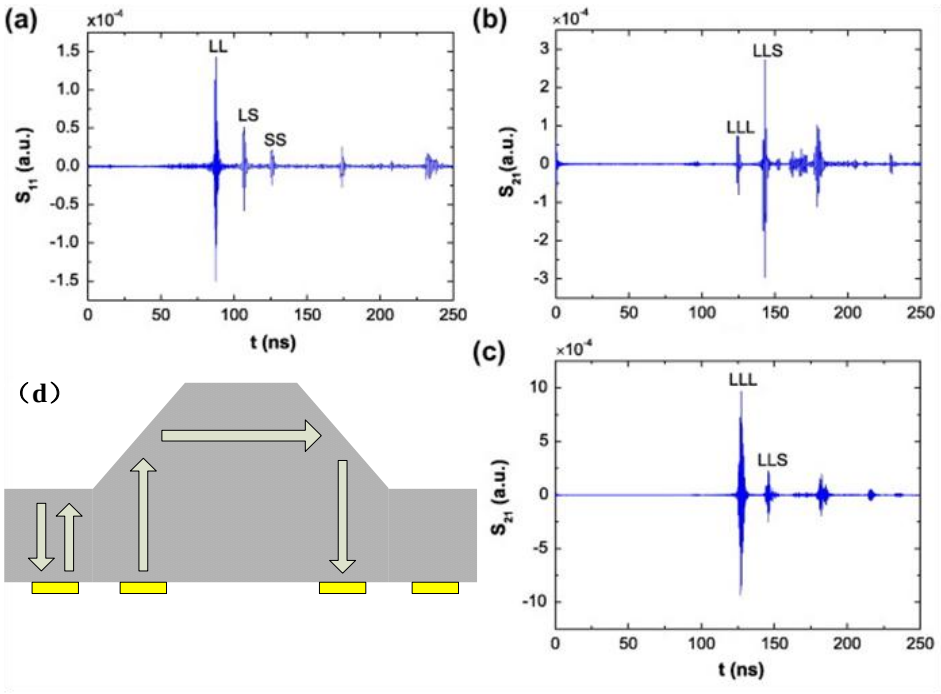

Figure 4.9 Real part of the impulse response of the system vs. time (ns): (a) S_{11}, (b) S_{21} without silicon oxide on the mirror and (c) S_{21} with a 4μm silicon oxide layer on the mirrors (d) Propagation paths inside microsystem.

The impulse response S_{21} shows several pulses which can be explained analyzing the time of flight in the system, as shown in Figure 4.9 b. LLL represents the longitudinal acoustic wave emitted by the transducer has been reflected twice on the 45 ° mirrors before reaching the receiver. LLS represents that the longitudinal acoustic wave converted into shear acoustic wave after being reflected on the second mirror during the propagation. LSS represents the longitudinal acoustic wave converted into shear acoustic wave when reflected on the first mirror and remaining as shear acoustic wave after reflected on the second mirror during the propagation. SSS represents the shear acoustic wave propagated from the emitter and being reflected twice on the 45 ° mirrors before reaching the receiver. The results of the predicted and measured time of flight of the waves are summarized in Table 4.1. The differences are less than 3% for LLL and SSS and 6% for LLS. The LSS signal seems to be composed of a lot of waves overlaps in time domain and we cannot measure it precisely.

Considering the amplitude of the longitudinal wave and shear wave converted from longitudinal wave, we can deduce that the silicon mirrors are efficient to guide the longitudinal acoustic waves. Figure 4.9c shows the S_{21} impulse response with a silicon dioxide layer on the mirror. Without the silicon dioxide layer the amplitude of the peaks for the S_{21} transmission is evaluated at 0.8×10^{-4} for LLL while with the silicon oxide layer The transmission peak is 9.5×10^{-4} for LLL. It implies that the efficiency of the reflection of the longitudinal wave on the mirror can be improved by means of the deposition of a SiO_2 layer

on the two mirrors. The increase of amplitude of the LLL signal is more than 20 dB.

Table 4.1 The predicted time of flight and deduced from S_{21} impulse response with the two 45 °mirrors

	Predicted(ns)	Measured(ns)	Difference (%)
LLL	128.1	124.7	2.7
LLS	150.3	142.9	5.2
LSS	180.4	160.7-172.0	
SSS	184.8	180.0	2.7

4.2.2 Study of the microsystem including the microchannel

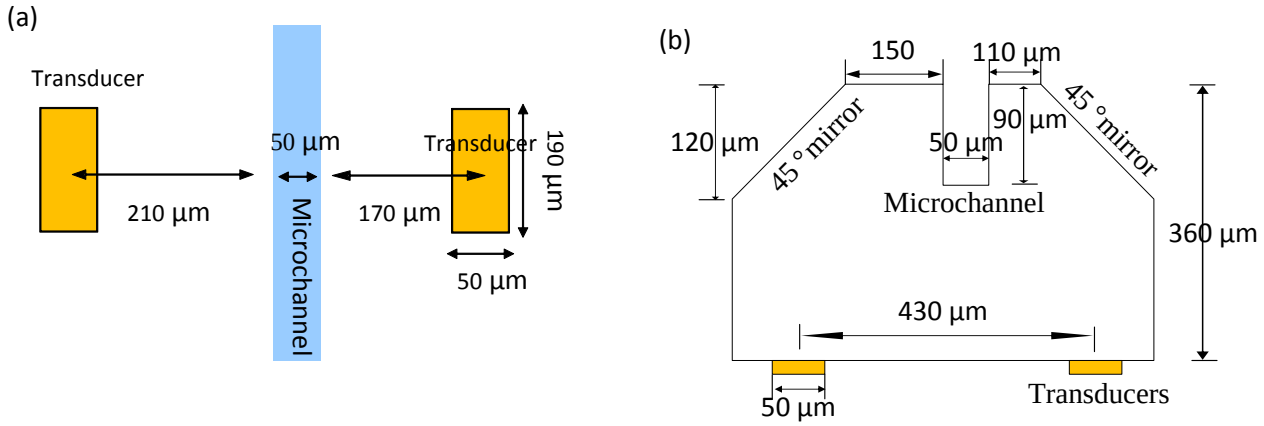

The reflected impulse response $S_{11}(t)$ shows three reflected signals due to the time of flight shown in Figure 4.11.

LL-LL represents the longitudinal wave propagates through path I and path II, then which is reflected by the first sidewall of the microchannel and returned back to same transducer.

LS-SL represents the longitudinal wave which is converted into shear wave at the interface of 45 °mirror (path II).

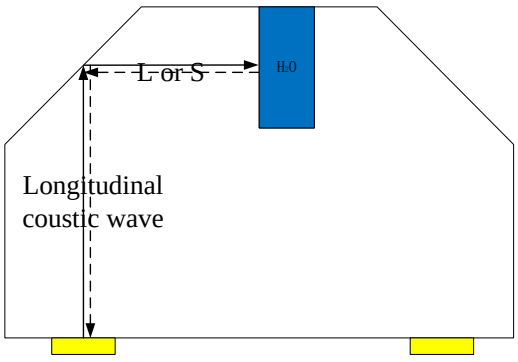

Figure 4.10 LL-LL and LS-SL: the refection interface is the first sidewall of the microchannel

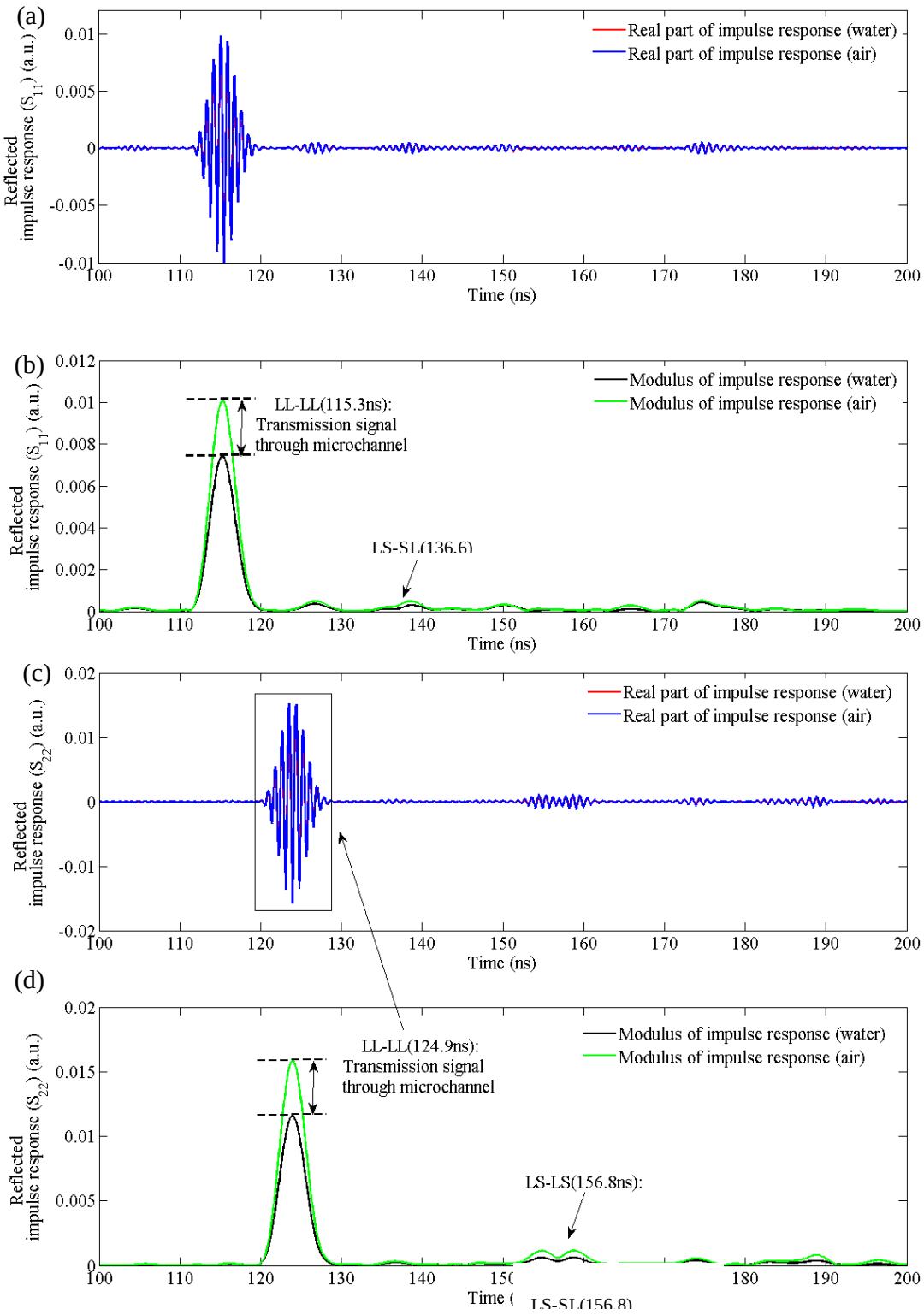

Figure 4.11 The reflected pulse echogram (the microsystem with the microchannel and 45 °mirrors) (a) The real part of the transmitted impulse response (blue curve: the microchannel without water, red curve: the microchannel filled with water), (b) The modulus of the transmitted impulse response (green curve: the microchannel without water, black curve: the microchannel filled with water)

The total thickness of the silicon wafer is about 360 μm. The distances between upper limit of the mirrors and between the backside transducers are about 270 μm and 430 μm respectively. The width of the microchannel is about 50 μm. It is observed that longitudinal and shear waves propagate on this vertical path, see also Figure 4.12. A continuously sinusoidal wave was used as excitation. The central resonance frequency of the ZnO transducers was characterized at about 1.3 GHz.

We can see the reflected impulse responses $S_{11}(t)$ shown in Figure 4.11. Through the basic calculation of time of flight, we can observe three amplitude peaks which are identified as LL-LL and LS-SL reflected paths. The differences between theoretical and experimental values are less than 5% for the paths LL-LL, LS-SL, which are shown in Table 4.2. When the channel is filled with the deionized water, the amplitude of LL-LL peak is lower than when channel is empty. The same situation happens in the peaks of LS-SL. We can conclude that a part of acoustic wave is transmitted through the microchannel. The other phenomenon observed is that the double peaks appear when the longitudinal wave is converted into the shear wave by 45° mirror.

Table 4.2 The predicted and measured reflected impulse response (Inverse Fourier transform of S_{11} and S_{22})with 45° mirror and microchannel

	S_{11}		S_{22}		Relative
	Predicted(ns)	Measured(ns)	Predicted(ns)	Measured(ns)	Differencce(%)
LL-LL	111.5	115.3	121.0	124.9	3.2
LS-SL	133.0	136.6	149.0	156.8	4.8

The relative difference of the time of flight between expected value and measurement is calculated as follow (Figure 4.10):

$$D = \left| \frac{S_{11M} + S_{22M} - (S_{11Exp} + S_{22Exp})}{S_{11M} + S_{22M}} \right|$$

where S_{11Exp} and S_{22Exp} are the predicted time of flight, S_{11M} and S_{22M} are the measured time of flight. D is the relative difference.

Figure 4.12 shows a microsystem used to compare the transmitted impulse response $S_{21}(t)$ in two cases: microfluidic channel filled with deionized water and microfluidic empty channel. There are five paths of the acoustic beam in the microsystem, which are labeled in Figure 4.12 (path Ⅰ-path Ⅴ). L and S mean respectively longitudinal acoustic wave and shear wave.

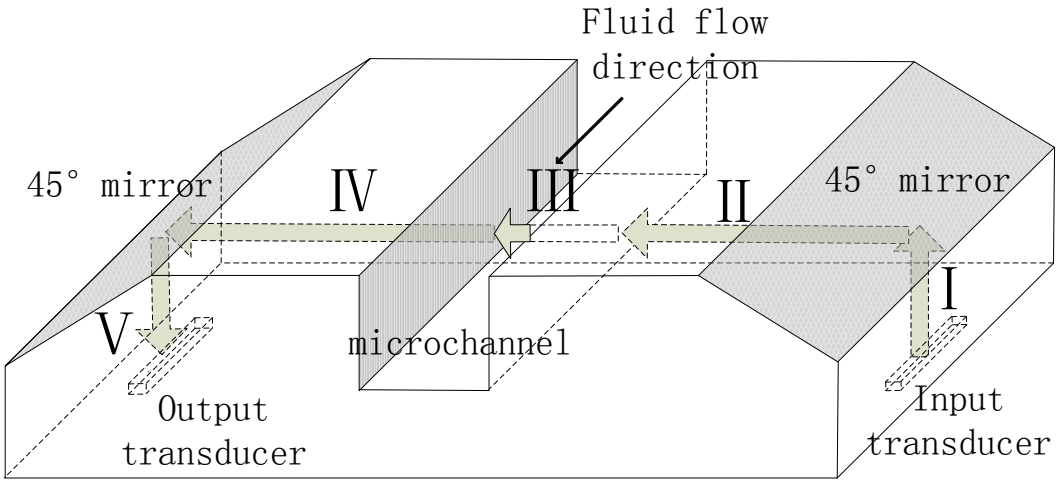

Figure 4.12 The scheme of the microsystem including two 45° mirror and a microchannel (illustration the transmission paths of acoustic wave: path Ⅰ-path Ⅴ)

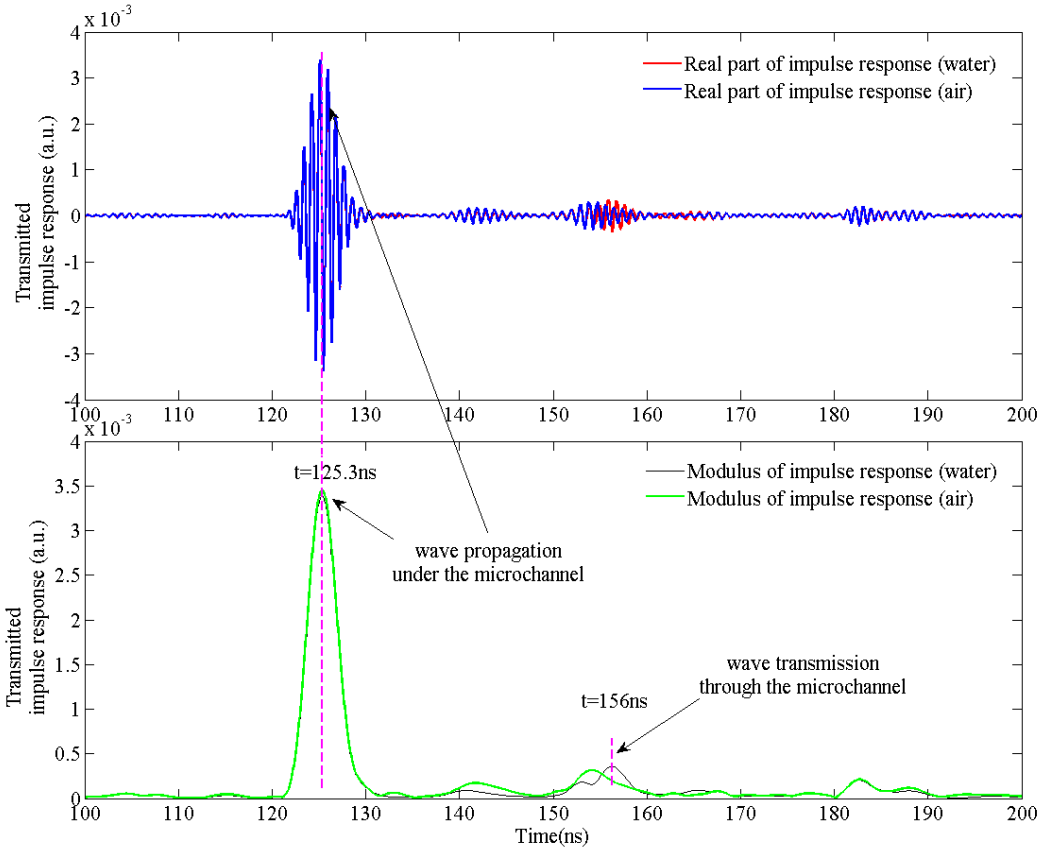

Figure 4.13 The transmitted impulse response echogram vs. time (ns) through the microsystem including a microchannel and two 45 ºmirrors (a) The real part of transmitted impulse response (blue curve: the microchannel without water, red curve: the microchannel filled with water),

(b) The modulus of transmitted impulse response (green curve: the microchannel without water, black curve: the microchannel filled with water)

Using the Snell law $\frac{\sin\theta_i}{v_i} = \frac{\sin\theta_r}{v_r}$ we can obtain the directions of the wave vectors of acoustic waves. (v_i is the velocity of the incident wave and θ_i is the incident angle, v_r is the velocity of the reflected wave, which can support longitudinal or shear polarization, and θ_r is the reflected angle). The longitudinal wave is deflected by 90 ° on the 45 ° mirror (i = 45 °) and the shear wave cannot be converted on the second 45 ° mirror depending on the Snell law. Only the pulse corresponding to LLLLS and LLLLL signals can be observed.

The impulse response $S_{21}(t)$ presents several pulses which can be classified versus the time of flight in the system as shown in Figure 4.13. We have demonstrated that mode conversion happened in the oblique surface of 45 °mirror and we also know that the shear wave could not propagate through the microchannel filled with deionized water. So only two main transmitted peaks can be observed. LLLLL represents the longitudinal acoustic wave emitted by the transducer and reflected on the two 45 ° mirrors before reaching the receiver. After the first reflection and being reflected toward the receiver by the second mirror, the longitudinal wave went through the microchannel when it is filled with water. The results of the predicted and measured time of flight of the waves are summarized in Table 4.3. The differences are less than 2% for LLLLS. In Figure 4.13, we hardly distinguish the transmission signal comparing two situations in the microchannel. With empty channel the theoretical amplitude of this transmitted peak for S_{21} transmission should be zero, because of the acoustic parasitic noise, the amplitude of S_{21} transmission signal is evaluated at time of 156.3ns and the amplitude is 1.93×10^{-4} for LLLLL while for the channel full with deionized water the amplitude of the peak is 3.6×10^{-4}. The signal to noise ratio is approximately equal to 1.87, which is a very low value for the targeted application. In parallel the amplitude of the parasitic signal transmitted under the microchannel is 3.5×10^{-3}, which is ten times bigger than the useful acoustic signal, leading to many identification troubles.

Table 4.3 The predicted and measured transmitted impulse response with 45 °mirror and microchannel

	Predicted(ns)	Measured(ns)	Difference (%)
LLLLL	159.3	156.3	1.8
LLLLS	177.9	173.9	2.2

4.3 Transmission microsystem improvement and characterization

4.3.1 Acoustic parasitic signals and improvements

In the previous discussion, we mentioned the various acoustic signals in our microsystem. Now, we will discuss the generation mechanism of these signals through the analysis of time of flight in the transmission echogram. We will then propose a way to eliminate the noise so as to increase the signal to noise ratio of our microsystem.

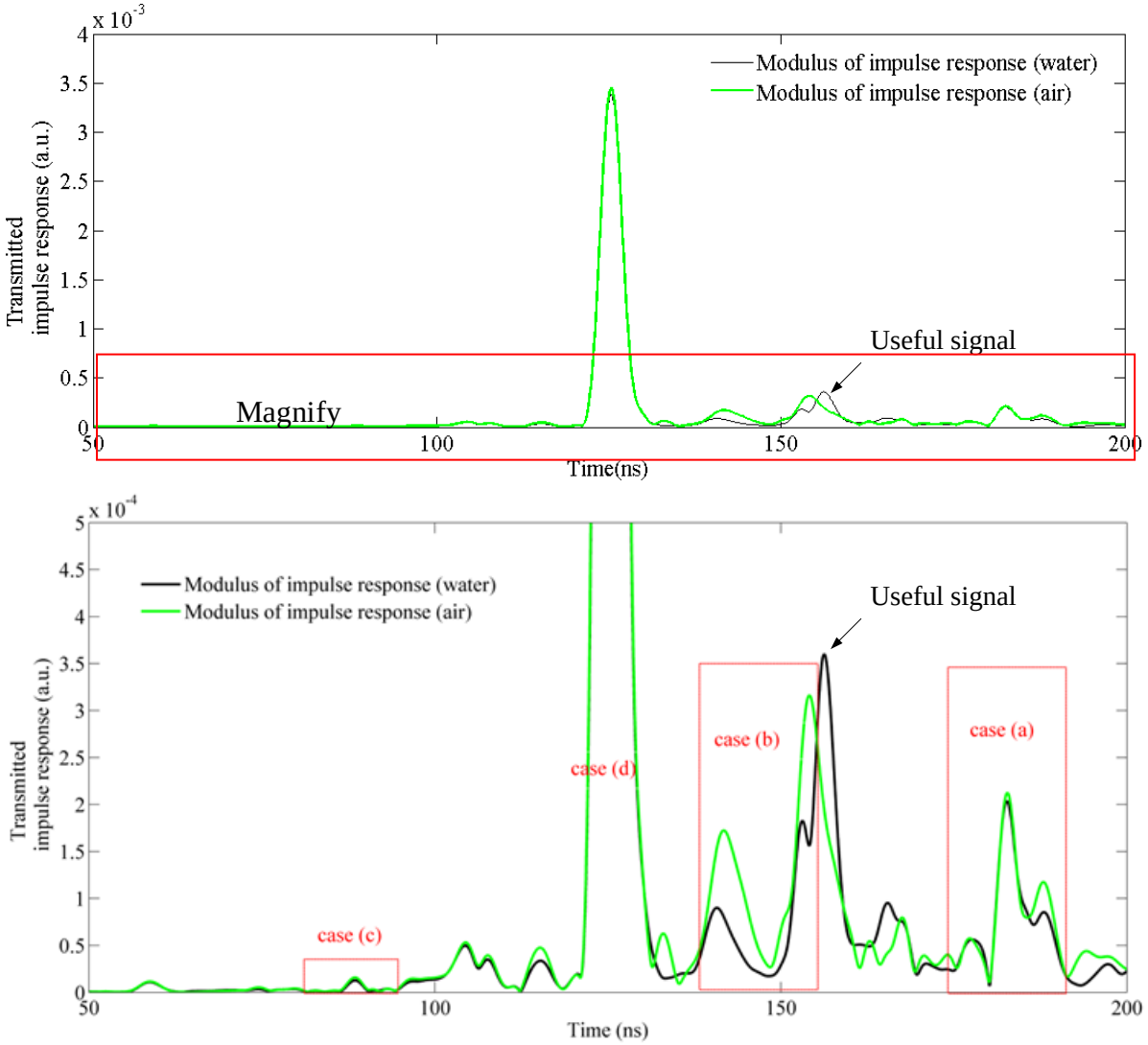

Figure 4.14 The parasitic signals labeled with different contributions in the transmission echogram.

The parasitic signals have been labeled in the transmission impulse response, which is shown in Figure 4.14. In order to explain the different sources of the parasitic echoes, we calculated the different times of flight in the echogram in the case of four assumptions of acoustic wave transmission paths which are shown in Figure 4.15

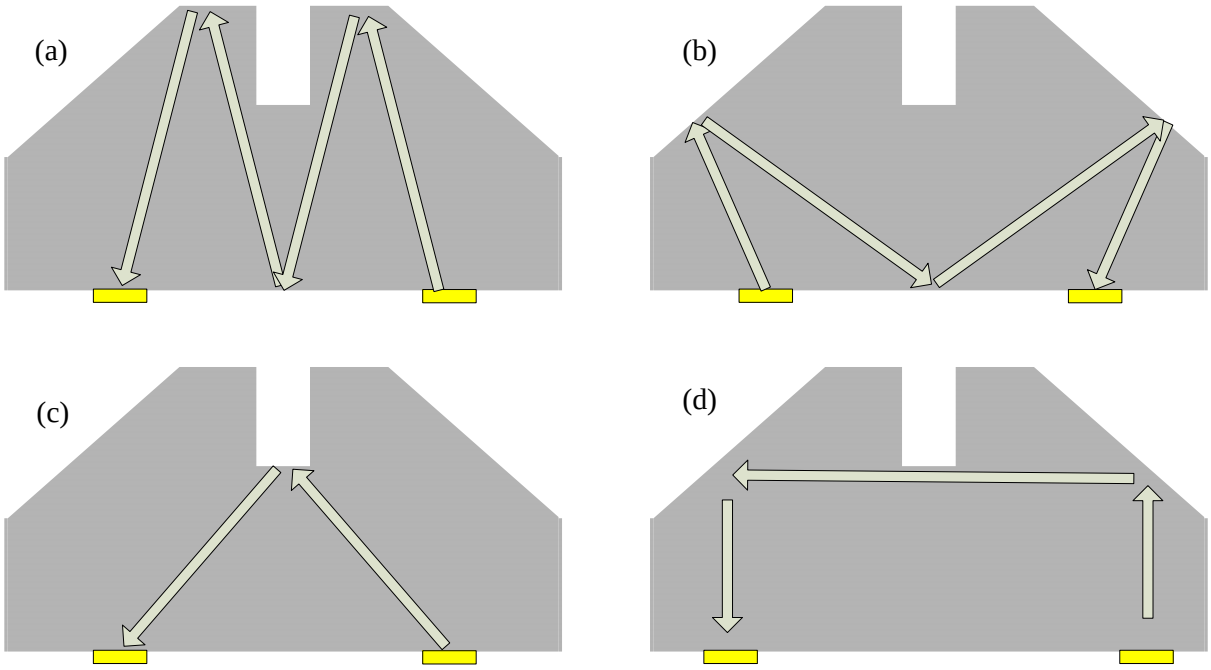

Figure 4.15 The different parasitic acoustic wave paths

As shown in Figure 4.15, the pair of transducers arranged on the same axis is the key factor which explains the generation of the parasitic echoes. The acoustic waves can be reflected by the 45 °mirrors, the surface of silicon wafer and the bottom of the microchannel. We can deduce the propagation distance of the parasitic acoustic wave and calculate the time of flight in the case of the four assumption paths (Table 4.4)

Table 4.4 The predicted and measured time of flight of the parasitic acoustic wave

	Predicted(ns)	Measured(ns)	Differencce(%)
Case A	181.8	182.8	0.5
Case B	147-158	141 or 154	
Case C	85.5	88.5	3.4
Case D	128.1	125.3	2.2

In case A the acoustic wave reflected third times by the surface of silicon substrate is not transmitted through the microchannel. The time of flight difference between the expected and measured values is less than 1%. The time of flight is around 180ns, which doesn't affect the transmitted acoustic wave through microchannel. Similarly, the delay of the parasitic acoustic wave in case C is around 88ns, which cannot interfere with the useful signals.

In case D a part of acoustic wave is transmitted under the microchannel. The amplitude of this echo is 3.5×10^{3}, which is about 10 times bigger than the amplitude of the acoustic wave transmitted through the microchannel. There is no doubt that this parasitic echo in case D has a great influence on the observation of the useful transmitted signal.

In case B a part of the acoustic wave is reflected twice by the 45 °mirror and once by the bottom surface of silicon wafer. The reflection path depends on the reflected angle at the interface of the 45 °mirror. The reflected paths of two peaks (141ns and 154ns) can be explained through this hypothesis. The time of flight in this case is very close to the transmission signal delay which can contribute to decrease the SNR. This leads to some difficulties in the characterization of biological samples in the application of our microsystem.

According to the parasitic signal discussion above, no matter whether the microchannel is filled with deionized water or not, we measured nearly the same echo amplitude around a time of flight of 125ns. Based on previous analysis, we are convinced that the biggest amplitude of the peak is a part of parasitic acoustic signal transmitted under the microchannel. An easy way to solve this problem is to maintain the microchannel with the same depth as the 45 ° mirror. However, to increase the channel as same depth as mirror leads to the detection problem in the later experiment. The main reason for this is that the objects in the fluid will fall down to the bottom of microchannel while acoustic wave will transmit upon the objects. In order to solve the cases B and D at the same time, the acoustic wave filter should be applied and the transducers should be removed at different axis.

4.3.2 Wave guiding using 45° mirrors and vertical mirrors

A pair of vertical mirrors was fabricated between the two 45 ° mirrors, as shown in Figure 4.16a. Using this configuration, the propagating direction of the acoustic waves can be modulated much more conveniently.

The two vertical mirrors could be obtained by inductively coupled plasma (ICP) etching (Figure 4.16b). The acoustic wave generated by the emitting transducer will be reflected four times before it reaches the receiving transducer. Based on this design, the acoustic wave could be well controlled in the plane parallel to the wafer surface.

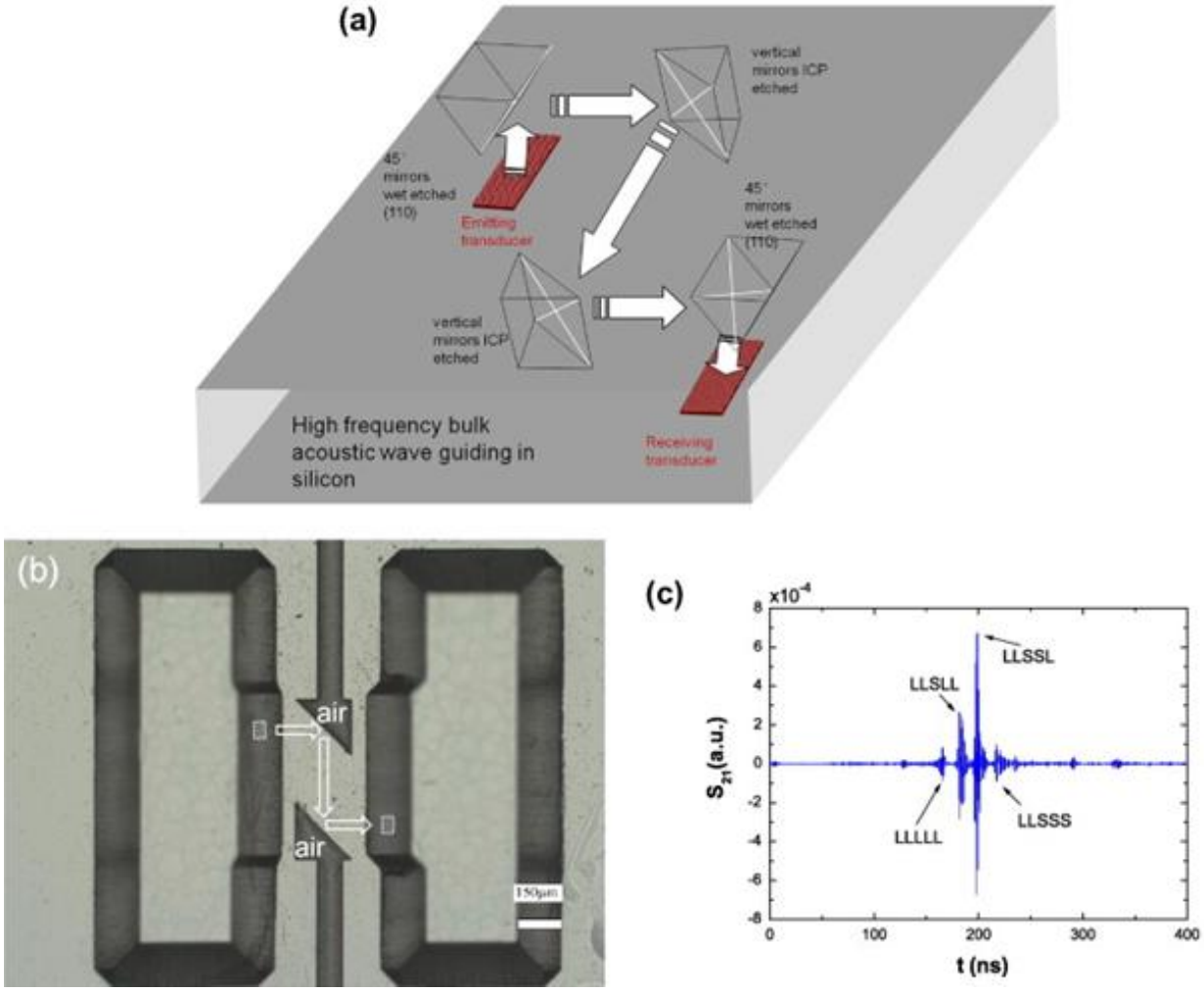

Figure 4.16 Guiding high frequency bulk acoustic wave transmission in 3D directions in silicon: (a) a scheme of the design with four mirrors; (b) an optical microscopy image of the mirrors, the dashed zones present the transducers on the backside of the silicon wafer and the arrows show the propagation of the acoustic wave; (c) the impulse response of the system.

Figure 4.16c shows the measured transmitted pulse response as a function of time. As explained before, water was deposited on the top surface to attenuate the propagation of the surface acoustic wave if it would appear. However, no difference was found with or without water during the measurements. It implies that the main peaks are not due to a surface acoustic wave.

In Figure 4.16a, the distance between the transducer and the 45 ° mirror is 290 µm. The distance between the incident point of the acoustic wave on the mirror and the vertical mirror is 220 µm. The distance between the two vertical mirrors is 320 µm. The speed of longitudinal acoustic wave is 8432 m/s and the speed of shear wave is 5398 m/s. After considering the possibilities of acoustic wave modes conversion after being reflected by the vertical and 45 ° mirrors and calculating the time of flight of the acoustic waves from the emitter to the

receiver, the peaks in Figure 4.16c can be determined. The 159 ns peak presents the longitudinal wave LLLLL (the sequence represents the propagation steps of the acoustic wave emitted by the first transducer and which finally reaches the other transducer) which reaches the receiving transducer and is reflected four times by the 45 °mirrors and vertical mirrors as shown in Figure 1.16c without conversion into shear wave. The strongest peak (195 ns) can be related to the longitudinal wave LLSSL received by the transducer. This echo implied that some part of longitudinal wave is converted into shear wave when it reaches the first vertical mirror and is finally again converted into longitudinal wave after being reflected by the second 45 °mirror.

The peak around 180 ns is related to the LLSLL wave received by the receiving transducer. The peak around 214 ns is related to the LLSSS wave received by the receiving transducer. In this section, we show the possibility to control the direction of propagation and the polarization of the acoustic waves in the silicon wafer.

In the Figure 4.16, it is observed that the longitudinal wave has been converted into shear wave at the interface of vertical mirror. We can observe the same result mentioned previously, if the thickness of SiO_2 coating layer is not 4 µm on the vertical mirrors. In the following section, we will discuss it in detail.

4.3.3 Fabrication of an improved microsystem

As mentioned previously, the new design of the microsystem contains two improvements:

1) two transducers not at the same axis,

2) two vertical mirrors added as an acoustic filter.

The new microsystem is illustrated in Figure 4.17.

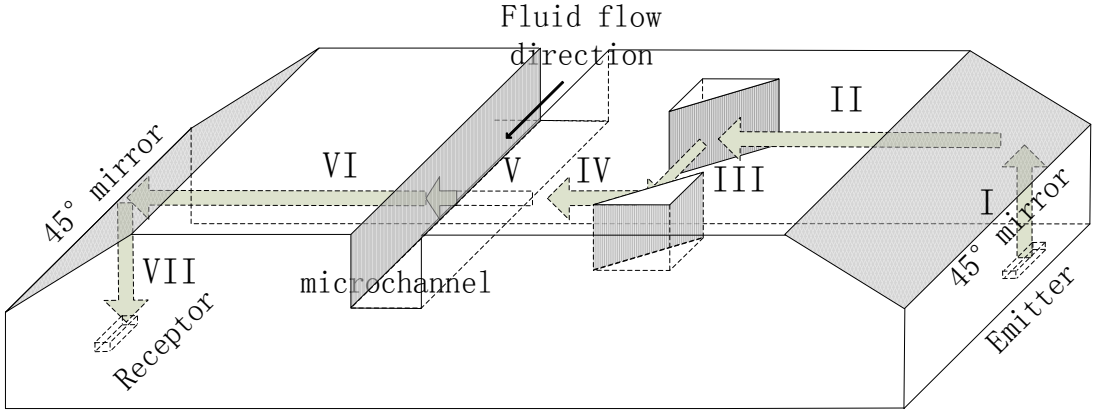

Figure 4.17 The scheme of the microsystem including vertical mirrors and the propagation

paths of acoustic wave.

In the microfabrication process, the microchannel and the vertical mirrors should be etched at the same time by the ICP process to make sure that the two structures have the same depth. It will reduce the parasitic waves propagating under the microchannel as much as possible. The fabrication flow of the new microsystem is basically the same as the process illustrated in chapter 3.The thickness of SiO_2 layer deposited by the PECVD depends on the angel of source with respect to the surface. In our microsystem, three different structure surfaces (45 °mirror, vertical mirror and microchannel) should be deposited with SiO_2.

The deposition process of the SiO_2 layer is shown in Figure 4.18.

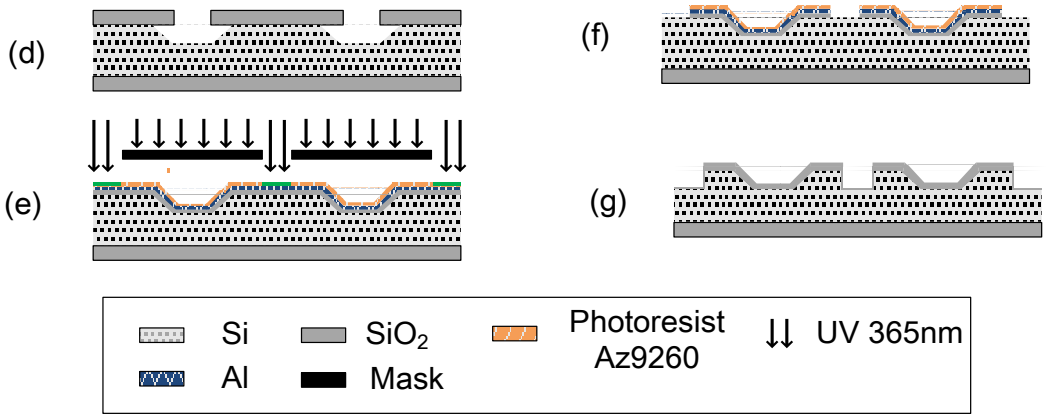

Figure 4.18 Flow chart of vertical mirror fabrication and SiO_2 deposition

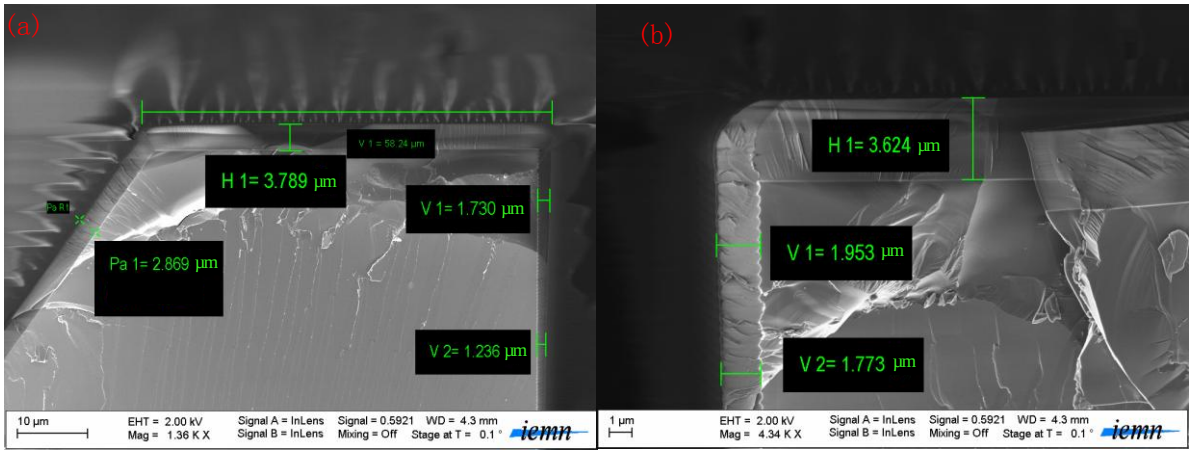

Figure 4.19 The thickness of deposition SiO_2 film in different inclination surfaces.

Due to the fabrication process designed, the thickness of SiO_2 layer on 45 °mirror is 4µm and the thickness of SiO_2 layer on the vertical mirror and microchannel wall is 1.5µm. The different thicknesses of SiO_2 layers are shown in Figure 4.19. On the top surface of silicon substrate, the thickness of SiO_2 layer is 3.6µm. The thickness of SiO_2 layer on the mirror surface is around 3µm. On the top of microchannel wall, the thickness of SiO_2 is about 1.8µm and from the top to the bottom the thickness of SiO_2 layer deposited on the channel wall decreases gradually as well as for the vertical mirror wall.

As we added the vertical mirror, the thickness of SiO_2 coating layer at the surface of 45 °mirrors can't be as the same as on the surface of vertical mirrors. Because the average thickness of SiO_2 layer is around 1µm on the trench wall of vertical mirrors, mode conversion happened at the interface of vertical mirrors when the longitudinal acoustic wave is reflected by the vertical mirror wall.

It is verified and is shown in Figure 4.16. The LLSLL peak is bigger than the LLLLL peak, which demonstrates that most part of the longitudinal acoustic wave has been converted into shear wave at the interface of the first vertical mirror. In an anisotropic solid (e.g. silicon), there are two quasi-shear waves after being reflected by the first vertical mirror. A small part of shear wave has been converted into the longitudinal wave at the interface of the second vertical mirror. It explains that the LLSLL peak is smaller than the LLSSL peak.

Between 45 °mirror and microchannel, a pair of vertical mirrors has been added. The depth of the vertical mirror is the same as the depth of the microchannel, which eliminate the parasitic acoustic wave transmitted under the microchannel. The top view and the cross-section view of new structure are shown in Figure 4.20.

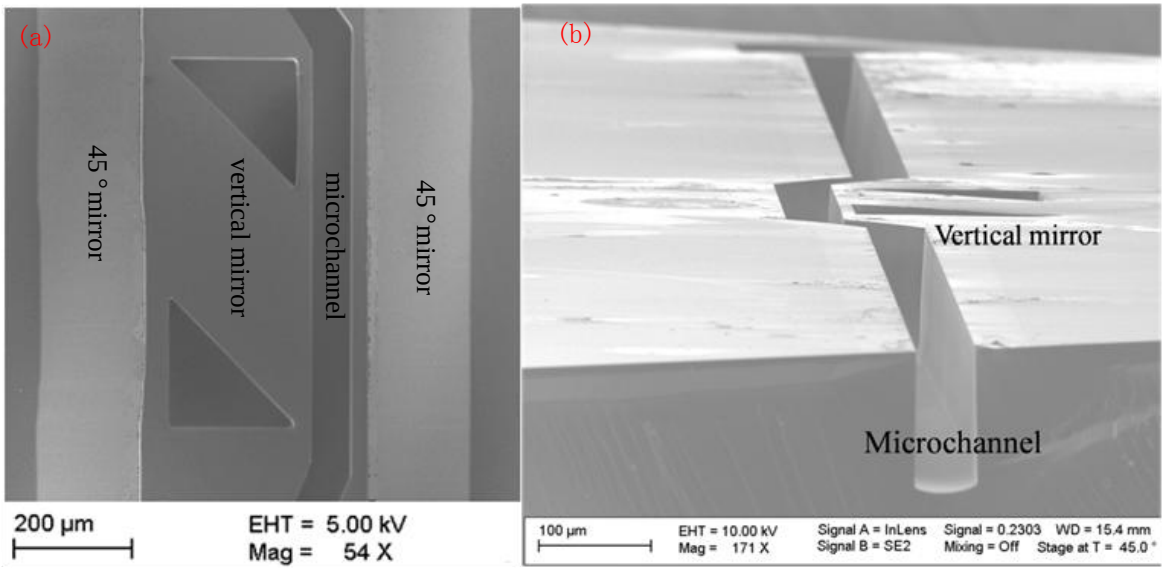

Figure 4.20 The scheme of the microsystem: a. SEM image of top view of the Si micro-structure, b. SEM image of the vertical mirror and the microchannel.

However, for the limitation of the MEMs technology, it is not possible to deposit the same thickness of SiO_2 layer on the trench. For the coating layer of the vertical mirror, at the top part of the vertical mirror, the thickness of SiO_2 is about 2μm and at the bottom part of the vertical mirror the thickness is less than 1μm and different thicknesses of coating layer will generate much more complex situations in mode conversion.

The wave guiding microsystem has been integrated along the wall of microchannel which is shown in Figure 4.20. As the high attenuation, the acoustic wave (longitudinal wave and shear wave) cannot be transmitted through the empty channel and the shear wave also cannot be transmitted through the microchannel filled with deionized water.

The biggest peak of LLSSL in Figure 4.16c cannot be used for chemical solution and biological cell characterization because shear wave cannot cross the fluid inside the channel. So the LLSLL peak will be used for the following applications.

4.4 Measurements in microfluidic channel

The proposed improvements contain the SiO_2 coating layer, integration with the vertical mirrors and the piezoelectric transducers translated into the different axes. The acoustic wave reflected by the 45° mirrors and vertical mirrors have been validated to be used for measurements in the microfluidic channel. Two improved micro-devices with different dimensions have been used for further experiments which are named Model i and Model ii in this chapter.

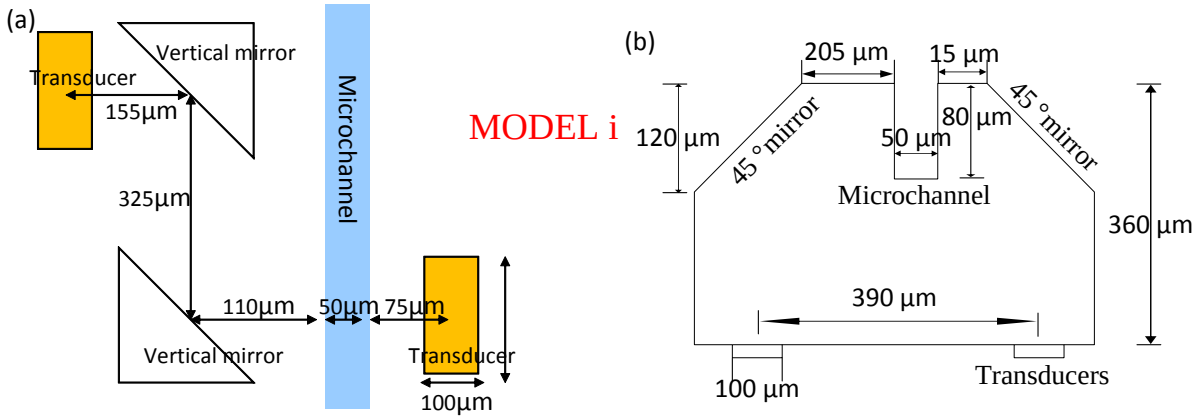

Figure 4.21 Geometry of the device model i (a) The dimensions on the top view of the microdevice, (b) The dimension of cross-section view of the microdevice.

As shown in Figure 4.21, the thickness of the silicon wafer is about 360μm. The distances between the top edge of the mirrors and between the backside transducers are respectively about 270μm and 390μm. The horizontal distance between the edge of a 45° mirror and the

vertical mirror is about 95 μm. The distance of two vertical mirrors is 325 μm. The channel width is 50 μm. The distance between channel and vertical mirror is 110 μm while the distance between channel and the edge of the other 45 ° mirror is 15 μm. The depths of 45 ° mirror and microchannel are respectively about 120 μm and 80 μm. The speed of longitudinal acoustic wave is 8432m/s and the speed of shear wave is 5398m/s. we can deduce the time of flight of an acoustic wave shown in Figure 4.17.

Because of the fabrication process, the coating layer of the vertical mirror is designed to 2 μm thickness. As we discussed before, without the suitable thickness of SiO_2 coating layer (4 μm thickness of SiO_2 for 1GHz acoustic wave is suitable mentioned in chapter 2), most part of the longitudinal acoustic wave will be converted into shear wave between these two vertical mirrors.

We assume that all the pathways of the acoustic wave are the longitudinal wave except the pathway between the vertical mirrors. The propagation pathway can be represented as LLSLLLL. The flying time of LLSLLLL in the microdevice is about 204.2ns. The model i of our microdevice is used in order to characterize liquid media.

4.4.1 Measurement through the microfluidic channel filled with deionized water

Firstly we used deionized water (DIW) to characterize the model i microsystem. Figure 4.22 shows the S_{ij} modulus versus time and a comparison between the empty microchannel and microchannel filled with deionized water. We can consider seven section of the acoustic wave transmission path in the microsystem (path Ⅰ-Ⅶ), as shown in Figure 4.17. A continuously sinusoidal wave is used as the excitation provided by the network analyzer. The central frequency of the ZnO transducers was characterized at about 1.3 GHz. The acoustic wave mode can be converted by the 45 ° mirrors and by the vertical mirrors and the letter L and S indicate longitudinal acoustic wave and shear wave, respectively for each path section. Longitudinal waves and shear waves were observed inside the silicon substrate.

The different echograms contain several peaks which can be classified due to the time of flight as shown in Figure 4.22a. LLSLLLL indicates that the longitudinal acoustic wave was emitted by ZnO piezoelectric transducer and reflected still as a longitudinal wave by the first 45 ° mirror. Then the longitudinal wave was converted into shear wave by first vertical mirror and the shear wave was then converted back into longitudinal wave by the second vertical mirror. Afterwards the longitudinal wave went through the microchannel filled with deionized water. Finally the transmitted acoustic wave remained as the longitudinal wave reflected by the second 45 ° mirror. The differences in the time of flight are less than 5% for LLSLLLL, LLSLLLS and LSSLLLS, which are shown in Table 4.5.

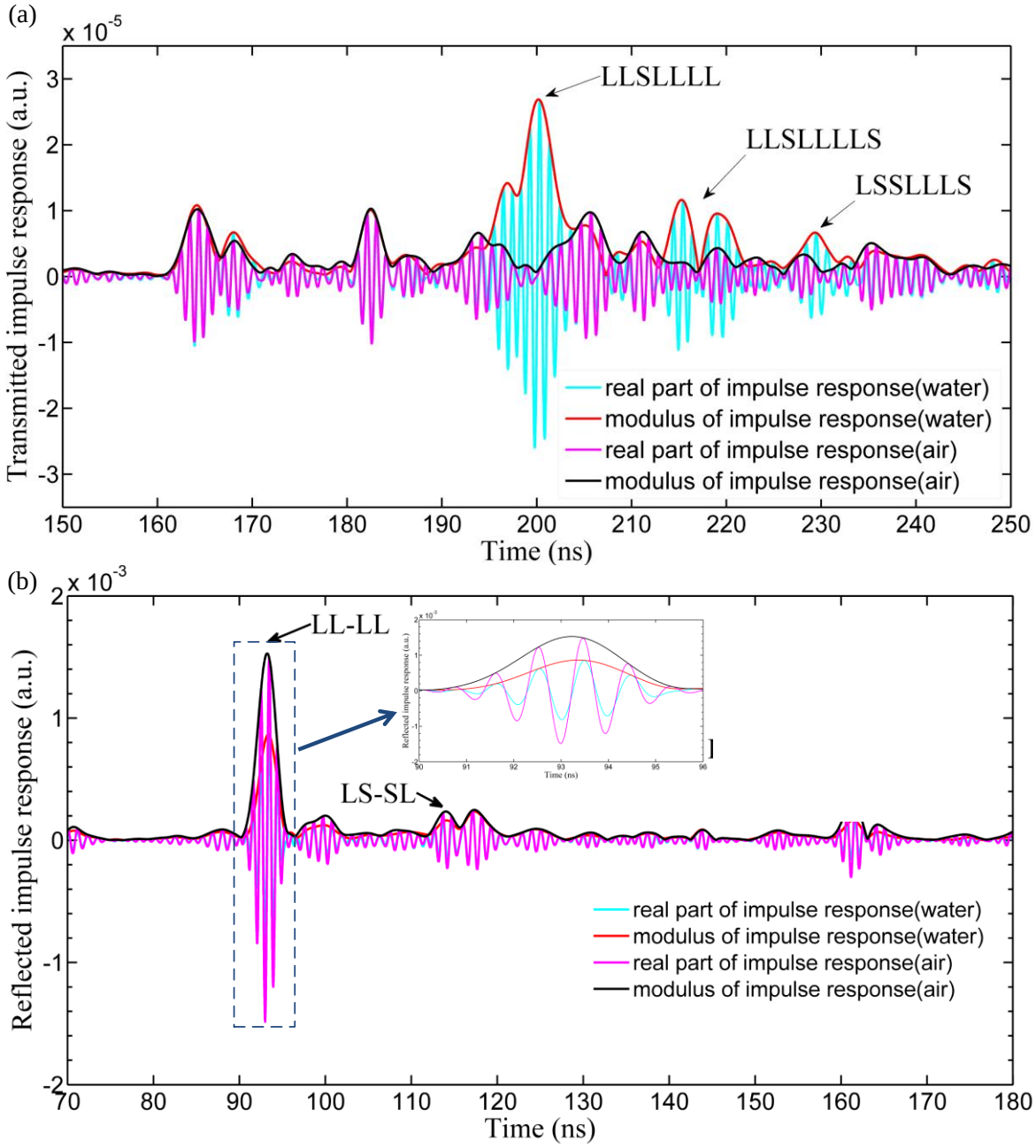

Figure 4.22 The impulse response of the system vs. time (ns): (a)S_{21}, (b) S_{22} (blue curve: real part of the impulse response without deionized water; green curve: modulus of the impulse response without deionized water, red curve: real part of the impulse response with deionized water, black curve: modulus of the impulse response with deionized water)

Because of the mode conversion happened at the interface of vertical mirrors, the most part of the longitudinal acoustic wave converted into shear wave. As shown in Figure 4.22, there is no LLLLLLL amplitude peak observed.

Table 4.5 The predicted and measured delay of transmitted acoustic waves

	Predicted(ns)	Measured(ns)	Difference (%)
LLSLLLL	206.2	200.2	2.9
LLSLLLS	225.8	215.3	4.7
LSSLLLS	234.2	229.6	2.0

On the other side, acoustic wave should propagate through the microchannel filled with fluid, so only longitudinal acoustic wave can be observed in the path Ⅳ-Ⅵ.

In the Figure 4.22a, the useful acoustic signal is increased with the introduction of deionized water into the microchannel in comparison with the empty channel. The amplitude of S_{21} transmission signal due to the parasitic acoustic signals is evaluated at 9.3×10^{-7} with empty channel for the LLSLLLL wave propagation time while with channel filled with deionized water the amplitude of the peak is 2.7×10^{-5}. The signal to noise ratio is 29dB. This value allows us to use this acoustic wave to characterize liquid properties or achieve particles detection.

The reflected impulse response includes reflected signals due to the different time of flight shown in Figure 4.22b. LL-LL is the longitudinal wave which propagates through path Ⅶ and path Ⅵ, then reflected by the microchannel and returned back to the same transducer. The differences between theoretical and experimental values are less than 7% for the paths LL-LL and LS-SL, which are shown in Table 4.6. Because of the mismatching between the mechanical impedance of the silicon and that of water, the amplitude of the transmitted signal is only 10^{-5}.

Table 4.6 The predicted and measured time of flight of the reflected acoustic waves

	Predicted(ns)	Measured(ns)	Difference (%)
LL-LL	99.6	93.3	6.6
LS-SL	116.3	114	2.0

4.4.2 Different concentration of KI solution characterization

Due to the low amplitude of useful testing signal (10^{-5}), we use potassium iodide (KI) solution to evaluate our microsystem because the velocity variation and attenuation in this solution as a function of the concentration at a frequency of 1 GHz, which have been already published in 1976.

It is well known that this chemical solution keep the same acoustic wave velocity as a function of the KI concentration whereas the propagation attenuation decreases with this parameter unlike a lot of other chemical solutions. In order to use the ultrasound for chemical

or biological sensing, the measurements have always to be performed in liquids solutions or suspensions. The absorption of ultrasound in chemical solutions limits the accuracy and the sensitivity of the characterization method. The attenuation of ultrasound in water is about 220dB/mm at 1GHz for a 24 ℃ temperature.

For many liquids, α is a function of the frequency and for water $\frac{\alpha}{f^2}$ is a constant over a wide range of the frequency. It is known that when an electrolyte such as sodium chloride is added to water the absorption coefficient $\frac{\alpha}{f^2}$ decreases. Potassium iodide is well-known solution for ultrasound absorption research. The attenuation decreases when the concentration of KI solution is increased.

Different concentrations of Potassium iodide (KI) solutions have been used to evaluate our microsystem which also use the model i microdevice. Figure 4.23 illustrates different magnitude spectra that can be observed around the delay of 200ns versus different concentrations of KI solution in the microchannel. The concentration of KI solution varies from 1M/L to 8M/L and the magnitudes of the spectra are compared with that of the empty channel and the channel filled with deionized water. In Figure 4.23a, the amplitude of $S_{21}(t)$ transmission peaks for LLSLLLL are measured from 2.7×10^{-5} to 5.7×10^{-5} for the different concentrations of KI solution while for the microchannel with deionized water the amplitude reaches 2.2×10^{-5}. All the curves of KI concentrations show the same trend.

We can deduce from $S_{21}(t)$ amplitude the attenuation $\frac{\alpha}{f^2}$ as a function of the concentration of KI solutions as shown in Figure 4.23b. Through the experiments, it is proved that the attenuation decreases when the concentration of KI solution increases.

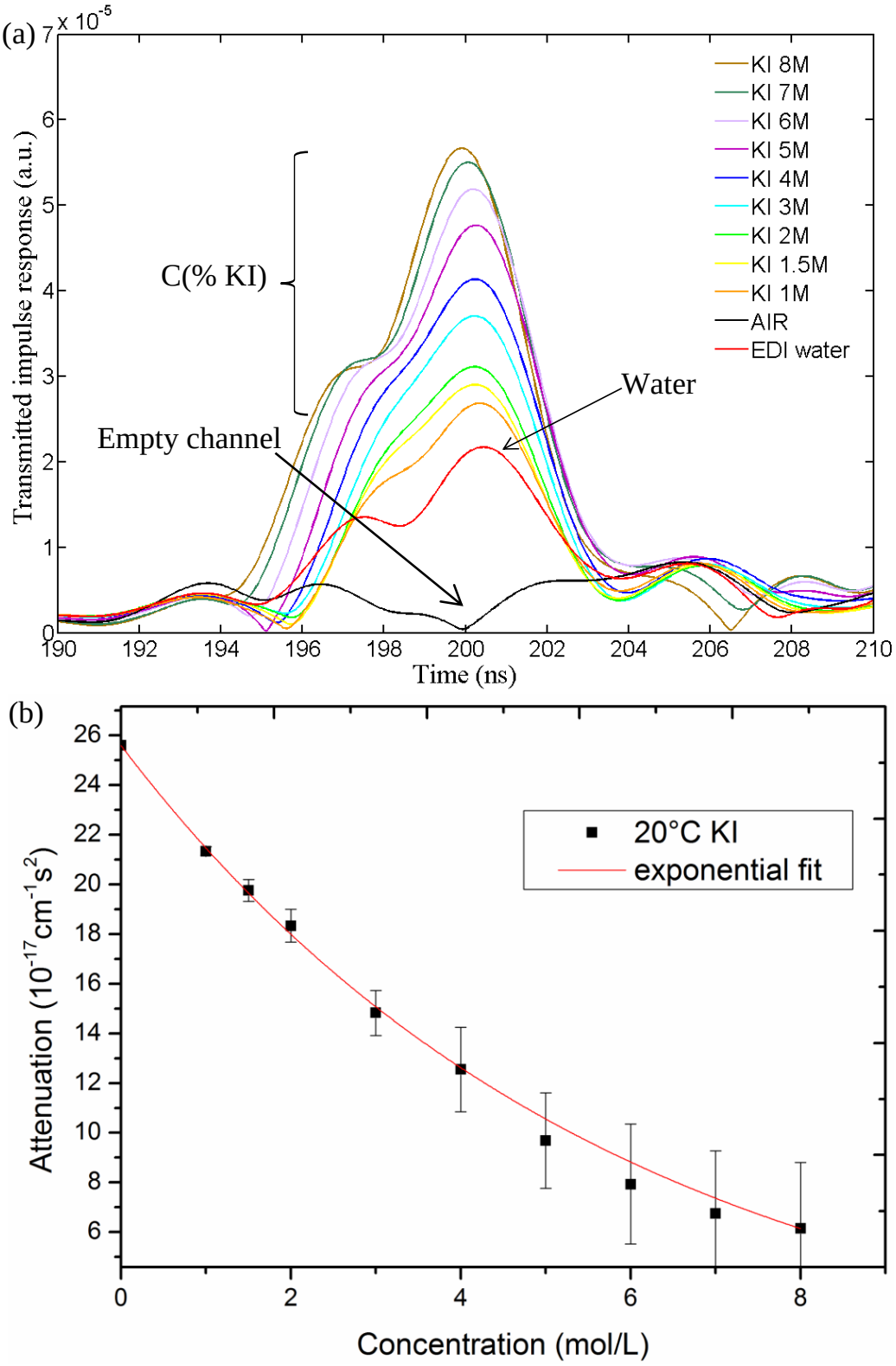

Figure 4.23 The impulse response of the system vs. time (ns): (a) S_{21} (different concentrations of KI solution(C=1,1.5,2,3,4,5,6,7,8 mol/L)), deionized water(c=0 mol/L) and empty water shown by different color curves), (b) Ultrasonic absorption in KI solutions as a function of the molar concentration.

Typically, at 20 ℃ $\frac{\alpha}{f^2}$ is $2.56 \times 10^{-16} cm^{-1} sec^2$ [163].

The attenuation coefficients in $dB \cdot cm^{-1} \cdot s^2$ units were deduced using:

$$\alpha(f)_{KI} = \alpha(f)_w - \frac{1}{d}\log_{10}[A_{KI}(f)/A_w(f)]$$

Where $A_{KI}(f)$ and $A_w(f)$ are the amplitude of the useful echoes, d is the width of the microchannel.

Each amplitude, for different concentration of KI solution, has been measured five times, as shown in Figure 4.23b. for the lower concentration of KI solution, the measurement are reproducible, but for higher concentration, the amplitude changes a lot.

The reasons are that: 1) the larger surface area to volume ratio of the microchannel will lead to the faster evaporation rate and the air permeability of the PDMS makes t surface molecules in the liquids are able to escape 2) for high concentration, precipitation of KI crystals and recrystallization procedure happened, more and more KI crystals are generated and lead to block the channel. This explains that the transmitted amplitude shows such variations.

4.4.3 Variation of the microchannel width

In the microdevice model i, we found that the space between microchannel and one side of 45 ° mirror is small, resulting in liquid leakage by PDMS bonding. In order to characterize new material, we designed and named the model ii microdevice which enlarges the space between different components of the microdevice as well as to introduce a variation of the channel width from 35 µm to 75 µm. The dimension of the model ii is illustrated in Figure 4.24

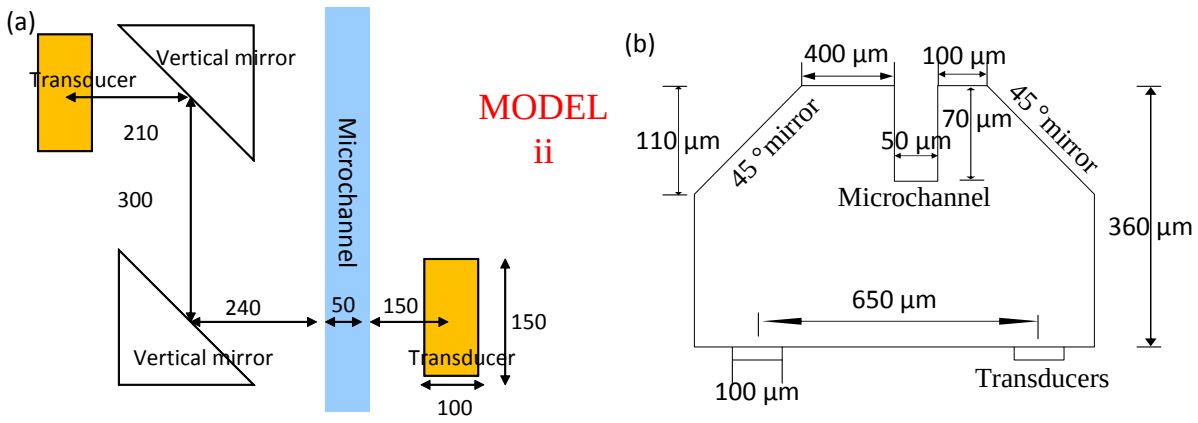

Figure 4.24 The geometry of the device of model ii (a) top view of the microdevice, (b) cross-section view of the microdevice.

As shown in Figure 4.24, the thickness of the Silicon wafer is about 360 µm. The horizontal distance between two transducers is about 650 µm.The distance between the incidence point of the acoustic wave on the mirror and the vertical mirror is 210 µm. The designed width of the microchannel is altered from 35 µm to 80 µm, as shown in 0. The distance between the two vertical mirrors is 300 µm. The time of flight of the LLSLLLL wave has been chosen to identify the different transmitted signals versus the width of the microchannel. Two micro-devices with different channel widths have been fabricated in order to measure the relationship between the time of flight of the LLSLLL echo and the microchannel width. This study will led to estimate the ability of our microsystem to perform absolute measurements of the attenuation and acoustic wave velocity in liquids.

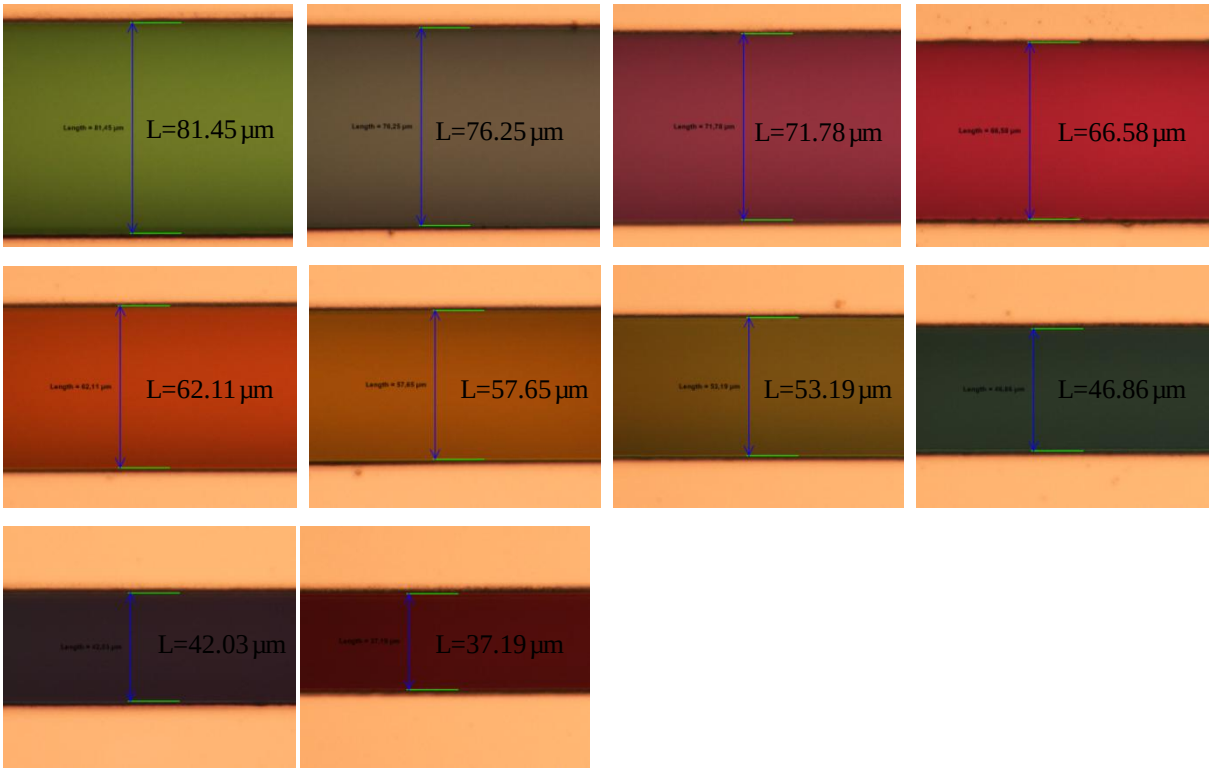

Figure 4.25 Optical images of the microchannel for different width (around 2 µm difference with the designed channel width).

Table 4.7 presents the predicted and measured time of flight of the transmitted peak (LLSLLLL) as a function of the channel width.

As shown in Table 4.7, the propagation distance of acoustic wave in our microsystem, which we used for the calculation of expected time is the distance designed in the mask. The expected times are calculated depend on a simple model of the ideal condition (supposed that the acoustic wave propagates in the isotropic solid and the velocities of longitudinal and shear

acoustic wave are respectively 8432 m/s (v_L) and 5498 m/s (v_s), as well as the velocity of longitudinal wave in water is 1493 m/s (v_w)).

In Figure 4.26, the slope of the line fitting theory is respectively 0.551 ns/μm, which are calculate by

$$\text{Slope} = 1000(\frac{1}{v_w} - \frac{1}{v_L})$$

So we can obtain the experimental acoustic velocity in water ($\overline{v_w}$) by the slope of the line fitting experiment. $\overline{v_w} = 1475$ m/s. The difference between expected time of flight and measured time of flight is about 5ns, because we use the simple model of the ideal condition and also the dimension of each micro-components fabricated is not the same as the designed dimension. For example, the between designed and measured width is about 2 μm, which will bring about 1.3ns difference.

For the same width of the microchannel, the difference between the measured time of flight and the predicted one is less than 3%. The black square points measured in the sample distribute on both sides of the black line which is calculated with a linear fit, and the theoretical values of the transmission time of the microsystem are shown in Figure 4.26. The line fitting the experimental values is nearly parallel to the theoretical line. It is further convinced that the LLSLLLL of acoustic wave can be used to detect the micro-objects.

Table 4.7 The predicted and measured transmitted impulse response (N indicate the bad experiment result)

Designed channel width (μm)	80	75	70	65	60	55	50	45	40	35
Predicted time(ns)	259.9	257.1	254.3	251.5	248.8	246	243.2	240.5	237.7	235
Measured channel width (μm)	81.5	76.3	71.8	66.6	62.1	57.7	53.2	46.9	42	37.2
Measured time(ns)	267.1	N	260	257.6	256	252.6	N	246.6	N	242
Difference(%)	2.7	N	2.2	2.5	2.9	2.7	N	2.5	N	2.5

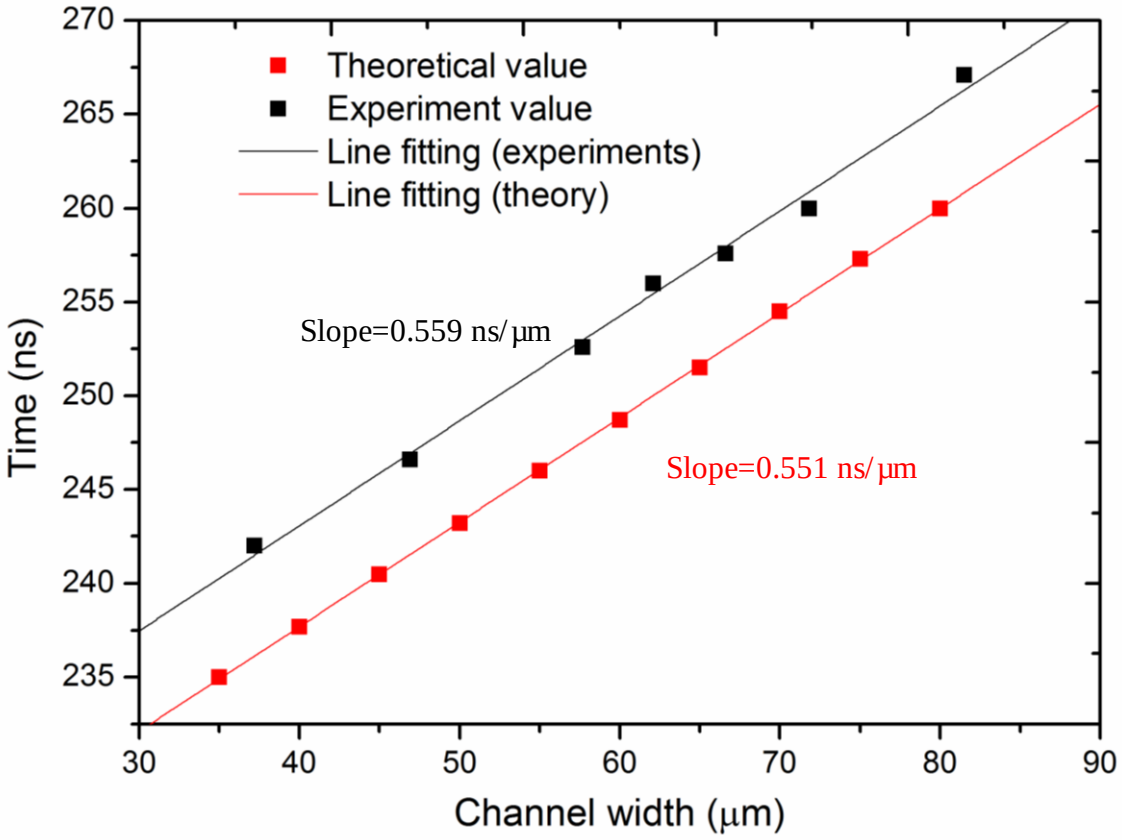

Figure 4.26 Time of flight of the system vs. width of the microchannel

4.4.4 Detection in microfluidic channel

We used a microdevice model i to characterize the deionized water and KI solution through the analysis of the transmitted echogram. The LLSLLLL peak not only provides a good signal to noise ratio, but also shows its ability to measure different concentrations of KI solution. Then we used a microdevice of model ii with different channel width to repeat the experiment mentioned above. The predicted and measured values are in good agreement. We target now to validate that LLSLLLL peak can indubitably be used for detection of micro particles and for characterization of biological samples.

4.4.4.1 Latex particles detection

We chose two methods to inject of the polystyrene (PS) latex particles (granuloshop, 10% monodisperse suspension, 30 μm). On one hand, the monodisperse suspension of PS latex particles has been diluted to 0.1% concentration and injected into the microchannel with the quasi-static method. The MFCS controller can accurately control the driven pressure without time delay. Due to the performance of MFCS controller, we can detect the latex particle with 30 μm in diameter in a quasi-static fluid. As illustrated in Figure 4.27, 0.1% concentration of

30 µm PS latex particles is driven into the microchannel. Through the microscope integrated in the PM8 probe system, we could observe the particle moving into the microchannel. The pressure is decreased slowly when the particle is driven near the detection region to limit the particle velocity. Finally the particle can be settled in front of acoustic wave transmission path with the fine control.

We use the model i microdevice to realize this experiment. The transmitted echograms are shown in Figure 4.27. The depth of the microchannel is about 80 µm and the width of the channel is about 50 µm as well as the diameter of the latex particle is 30 µm. It means that latex particles cannot totally block the acoustic wave transmitted through the channel. Figure 4.27 shows transmitted impulse response as the function of the time of flight. As explained previously, there are also seven sections in the transmission path of the acoustic wave. Thanks to the 0.1% latex particles concentration in the microchannel, the amplitude of transmitted impulse response is evaluated at 8.8×10^{-6} for LLSLLLL peak. Compared to the same channel filled with deionized water, the amplitude is 2.6×10^{-5}. It shows that the sensitivity of our microsystem allows detecting a latex particle.

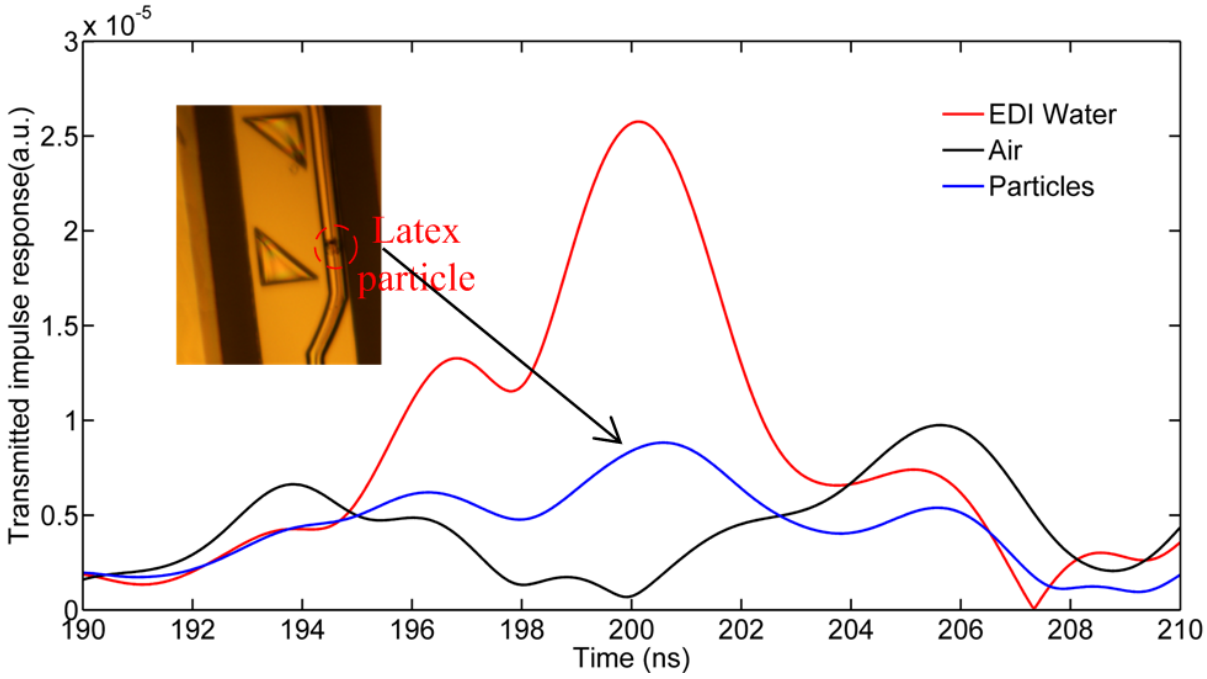

Figure 4.27 The impulse response of the system vs. time (ns) of S_{21} (black: empty channel, blue: latex particle in deionized water, red: only deionized water), an optical image of 30 µm latex particles in deionized water stopped in front of the transducers.

On the other hand, latex particles injection by a continuous flow has been used and we realize the experiments using the model ii. Three different concentrations of PS latex particles have been prepared and injected into the microchannel. As shown in Figure 4.28, it illustrates the

variation of the amplitude of the LLSLLLL peak that can be observed at the delay of around 200ns. The concentrations of latex particles vary from 1%, 2% and 5%. The amplitude of the LLSLLLL peak evaluated are 2.17×10^{-5} to 1.99×10^{-5} as a function of the concentrations of PS latex particles (1% and 2%), and compared to the microchannel filled with deionized water 2.51×10^{-5}. The amplitude decreases to 1.23×10^{-6} when the concentration of PS latex particles is 5%, comparing to the amplitude of 3.97×10^{-7} when the channel is empty. The microchannel is filled with the particles and is nearly blocked, so the acoustic waves transmitted through the channel and strongly attenuated. All the curves for different concentrations of PS latex particles show the same tendency. Comparing the amplitude of LLSLLLL peak, we are able to characterize latex particles solutions in this microfluidics based platform.

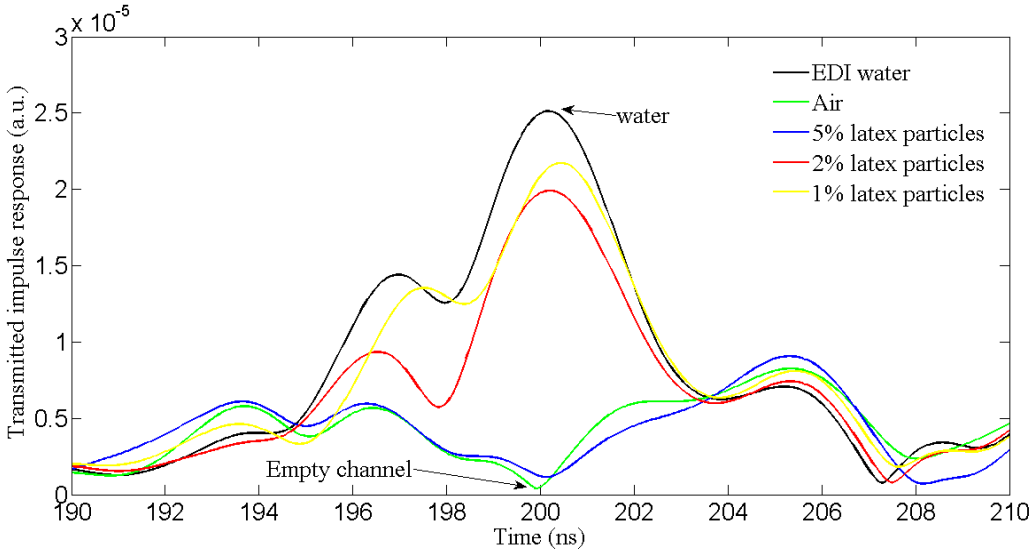

Figure 4.28 The impulse response of the system vs. time (ns): S_{21} (green: empty channel, black: deionized water, blue: 5% latex particles in deionized water, red: 2% latex particle in deionized water, yellow: 1% latex particle in deionized water).

4.4.4.2 Biological cells measurements

The model ii microdevice has been used to characterize biological samples. The measurement with three concentration of hemolyzed blood has been achieved through a continuous flow. The experimental results are shown in Figure 4.29. The time of flight of the transmitted impulse response of LLSLLLL peak is around 255ns, three different amplitudes can be observed by the introduction of three different concentrations of hemolyzed blood into the microchannel. The concentrations of hemolyzed blood sample are 0.1%, 0.5% and 1%. These amplitudes of LLSLLLL peak in the case of hemolyzed blood samples are compared to the amplitude when channel is empty and the channel is filled with deionized water. In Figure 4.29 the amplitude of

the transmitted impulse response for LLSLLLL peak are evaluated to 4.74×10^{-6}, 4.52×10^{-6} and 3.95×10^{-6} for respectively 0.1%, 0.5% and 1% concentration of hemolyzed blood. When the microchannel is filled with deionized water it is 1.49×10^{-5}. All the curves of hemolyzed blood concentrations show the same trend.

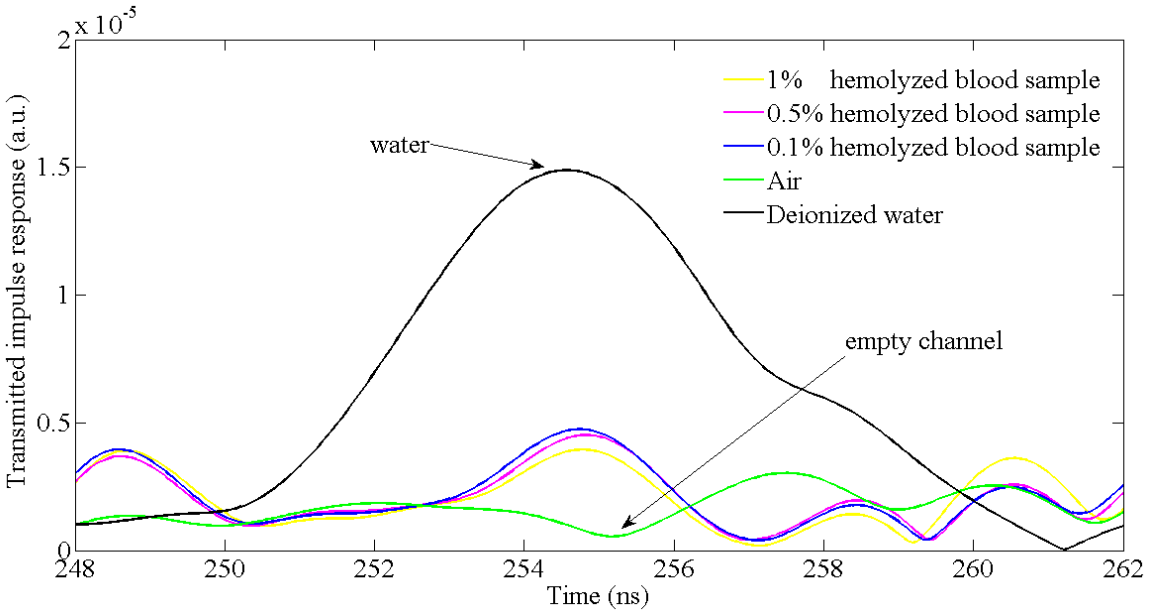

Figure 4.29 The impulse response of the system vs. time (ns): S_{21} (green: empty channel, black: deionized water, blue: 10% hemolysed blood in 0.9% NaCl solution, magenta: 5% hemolysed blood in 0.9% NaCl solution, yellow: 1% hemolysed blood in 0.9% NaCl solution,).

4.4.5 Cylindrical lenses integration and validation of focalization through the microfluidic channel

Due to acoustic wave propagation parallel to the sample surface, it is easy to integrate acoustic components along the microchannel. We integrated a pair of acoustic confocal lenses in our microsystem which focus the parallel acoustic incident wave by the first lens and convert the divergent transmitted acoustic wave into parallel beam. The integrated microsystem using acoustic lenses is shown in Figure 4.30.

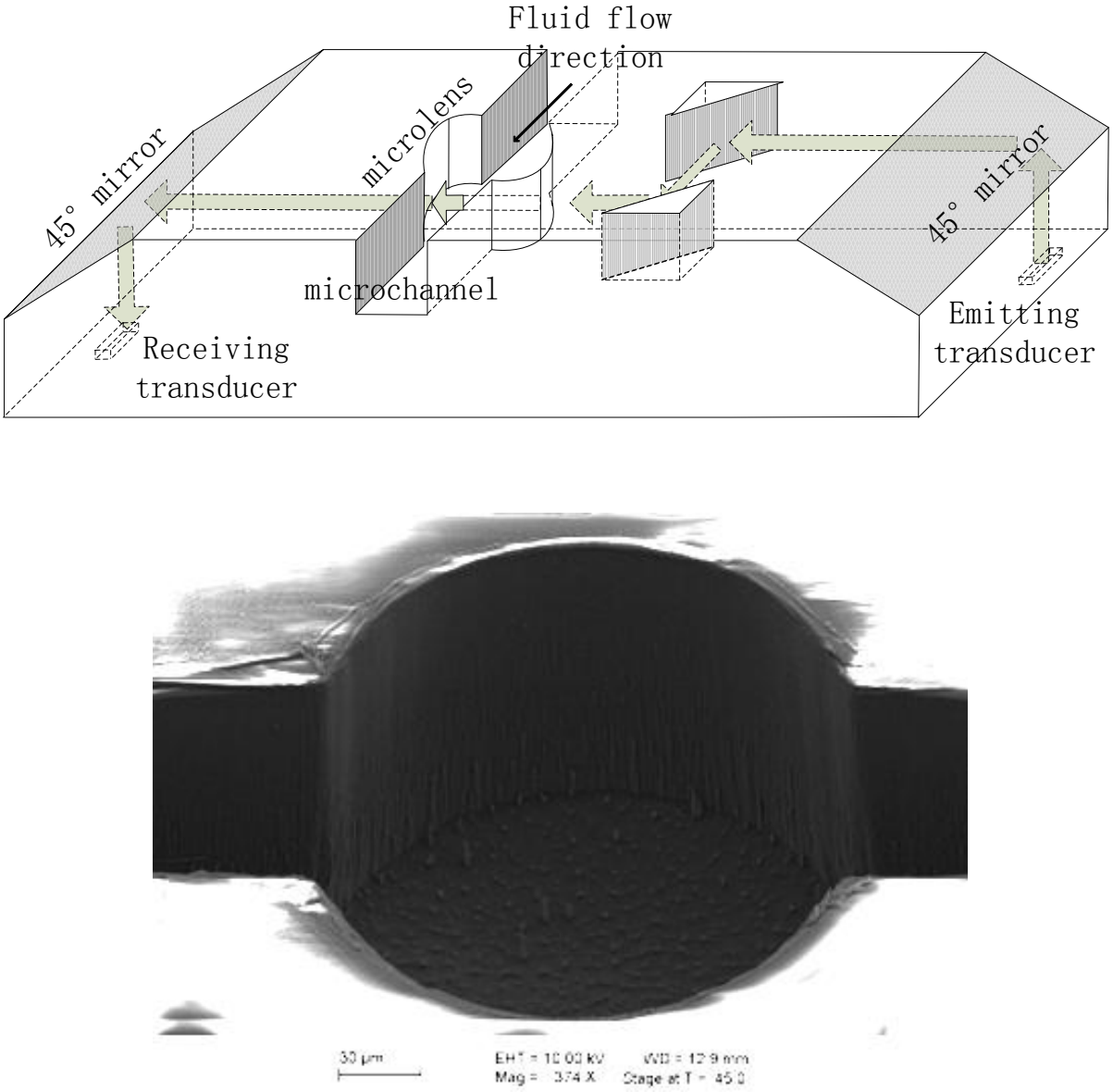

Figure 4.30 Scheme of the microsystem: (a) 45 ºmirrors, microchannel, vertical mirrors, lenses and transducers.(b) The SEM image of the microlens (top view).

4.4.5.1 Microfluidic measurements through the integrated lenses

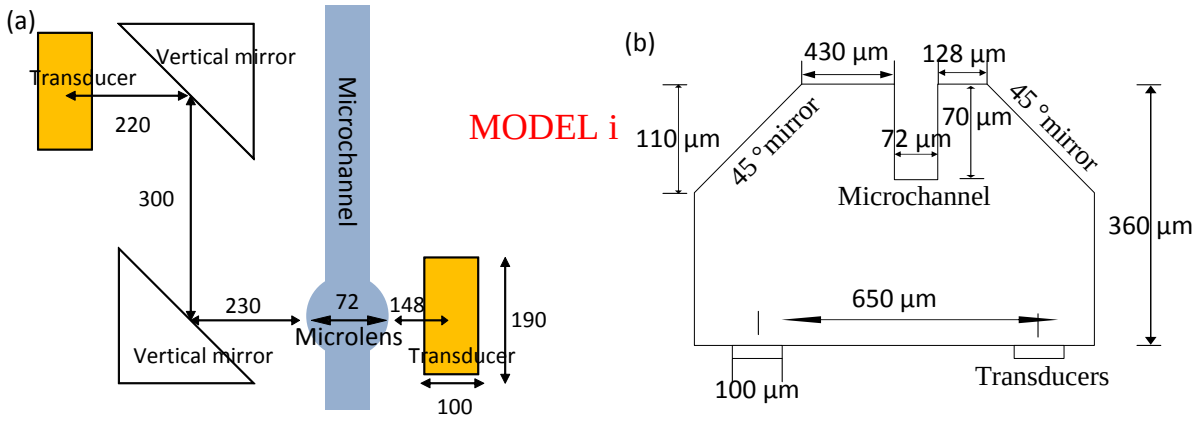

Figure 4.31 Geometry of the microdevice integrated with cylindrical lenses (a)The dimension of top view of the microdevice, (b) the dimension of cross-section view of the microdevice

The cylindrical lenses have been integrated into the microchannel. Two cylindrical lenses can constitute a confocal lens system. The advantages of a confocal lens system are:

1) Compared to the parallel channel wall, the cylindrical lens confocal system can gather much more acoustic energy diffracted by the encountered obstacles, such as blood cell.

2) The confocal lenses can concentrate the acoustic beam into a small area so as to improve the spatial resolution and the sensitivity of the microsystem. Due to the confocal lenses, we expect to detect small variation of biological cells elastic properties, even for a single cell.

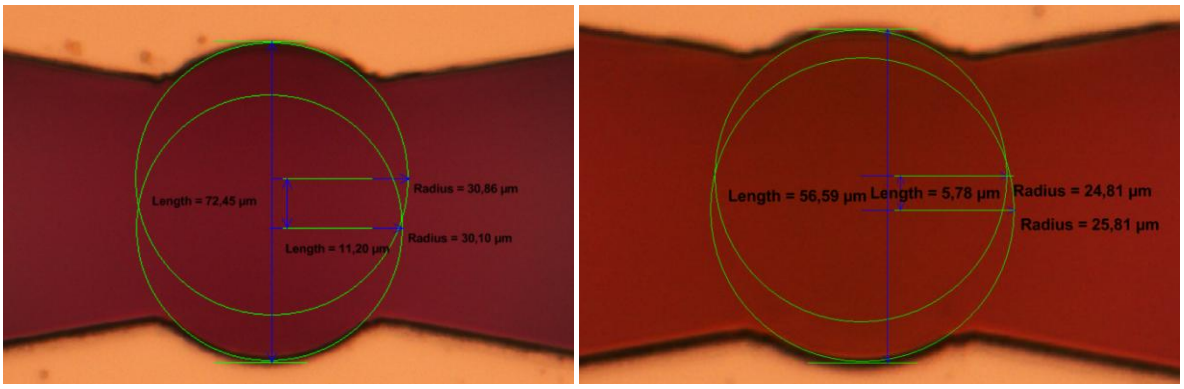

Figure 4.32 Optical microscopy image of confocal lenses: (left) focal length 36 µm, (right) focal length 30 µm.

Using a sample geometrical model we can demonstrate, due to the high refraction index of the lenses, which limits the geometrical aberrations, that the focal distance can be approximated by $F = \frac{nR}{n-1}$ (focal length measured from the top of the lens).

where $n = \frac{v_{si}}{v_w} \approx 5.7$ if v_{si} is the velocity of the acoustic wave in silicon and v_w is the velocity of the acoustic wave in liquid and R is the radius of curvature of the lens.

We design two groups of pair of cylindrical lenses which are integrated into the microchannel in order to characterize the focalization response and to measure the amplitude response versus the distance between the two lenses.

In one group, the radius and focal length of the cylindrical lens are respectively 30 µm and 36 µm. In the other group the radius and focal length of the cylindrical lens are respectively 25 µm and 30 µm. The detail parameters of cylindrical lenses are shown in Figure 4.33 in Table 4.8.

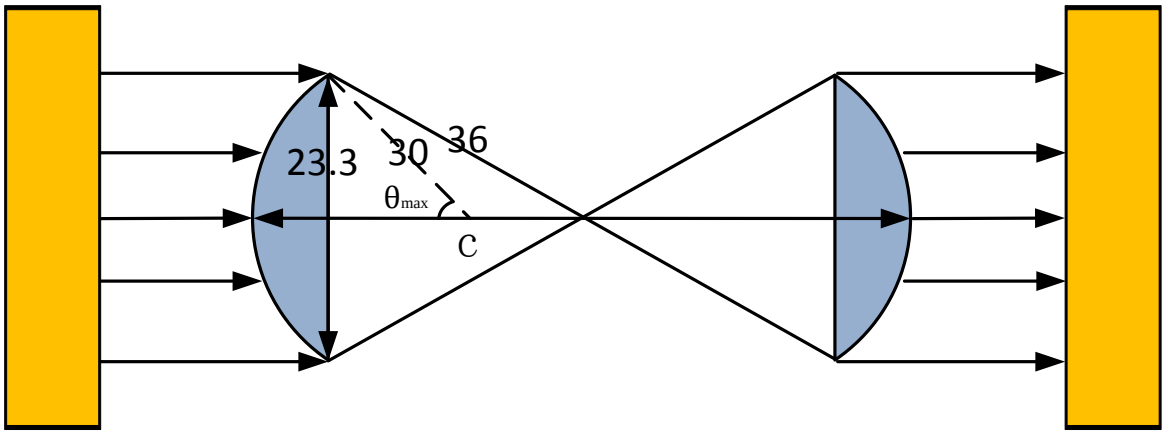

Figure 4.33 The scheme of the acoustic wave transmission through a confocal lens in the case of 30 µm lens radius. C is the center of curvature of the lens.

Table 4.8 Geometrical parameters of the cylindrical lenses

	Lens radius(R) 30 µm				Lens radius (R) 25 µm		
Lens distance(D)	66	68	70	72	56	58	60
Aperture (µm)	41.8	43.2	45.2	46.6	34	35.4	36.8
θ_{max}	44.2 °	46.1 °	48.9 °	51.0 °	42.8 °	45.1 °	47.4 °

Above all, deionized water is used to calibrate the microsystem with a confocal lens system (R=30 µm).

In the Figure 4.34a, the time of flight of the LLSLLLL peak is around 260ns. In this delayed window, the amplitude of the transmitted signal due to the parasitic acoustic signals is

evaluated at 1.2×10^{-6} with an empty channel, while the channel filled with deionized water the amplitude of the peak is 9.4×10^{-6}. We can use this peak to characterize liquid properties or to achieve biological sample detection.

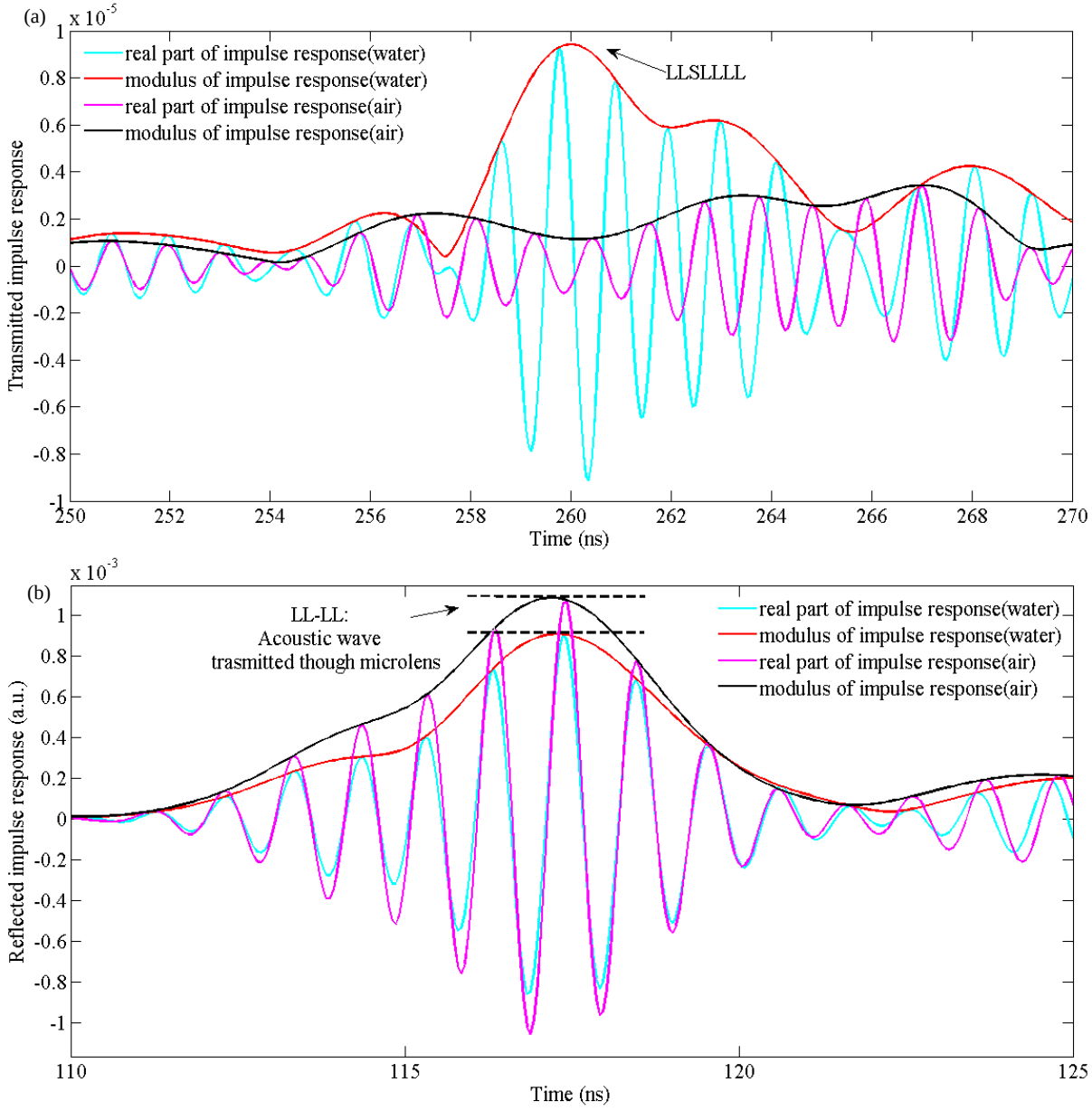

Figure 4.34 The impulse response of the system vs. time (ns): (a)transmitted response $S_{21}(t)$, (b)reflected signal $S_{22}(t)$ (blue curve: real part of impulse response without deionized water; green curve: modulus of impulse response without deionized water, red curve: real part of impulse response with deionized water, black curve: modulus of impulse response with deionized water)

The reflected impulse response is shown in Figure 4.34b. LL-LL is the longitudinal wave

propagated through path Ⅶ and path Ⅵ, then reflected by the microlens and returned back to the same transducer.

The time of flight of the reflected peak (LL-LL) is around 115ns. For this delay the amplitude of the LL-LL peak is 1.1×10^{-3} when channel is empty, as well as the amplitude of LL-LL peak is 9.1×10^{-4} when the channel is filled with deionized water. The difference amplitude between these two peaks represents a part of the acoustic waves transmitted through the cylindrical lens. The differences between theoretical and experimental values are less than 2% for the paths LL-LL, LLSLLLL, as shown in Table 4.9.

Table 4.9 The predicted and measured impulse response of the transmitted and reflected a acoustic waves

	Predicted(ns)	Measured(ns)	Difference (%)
LLSLLLL	255.5	260	1.8
LL-LL	115.7	117.2	1.3

And then all the different dimensions of cylindrical lenses have been calibrated by deionized water.

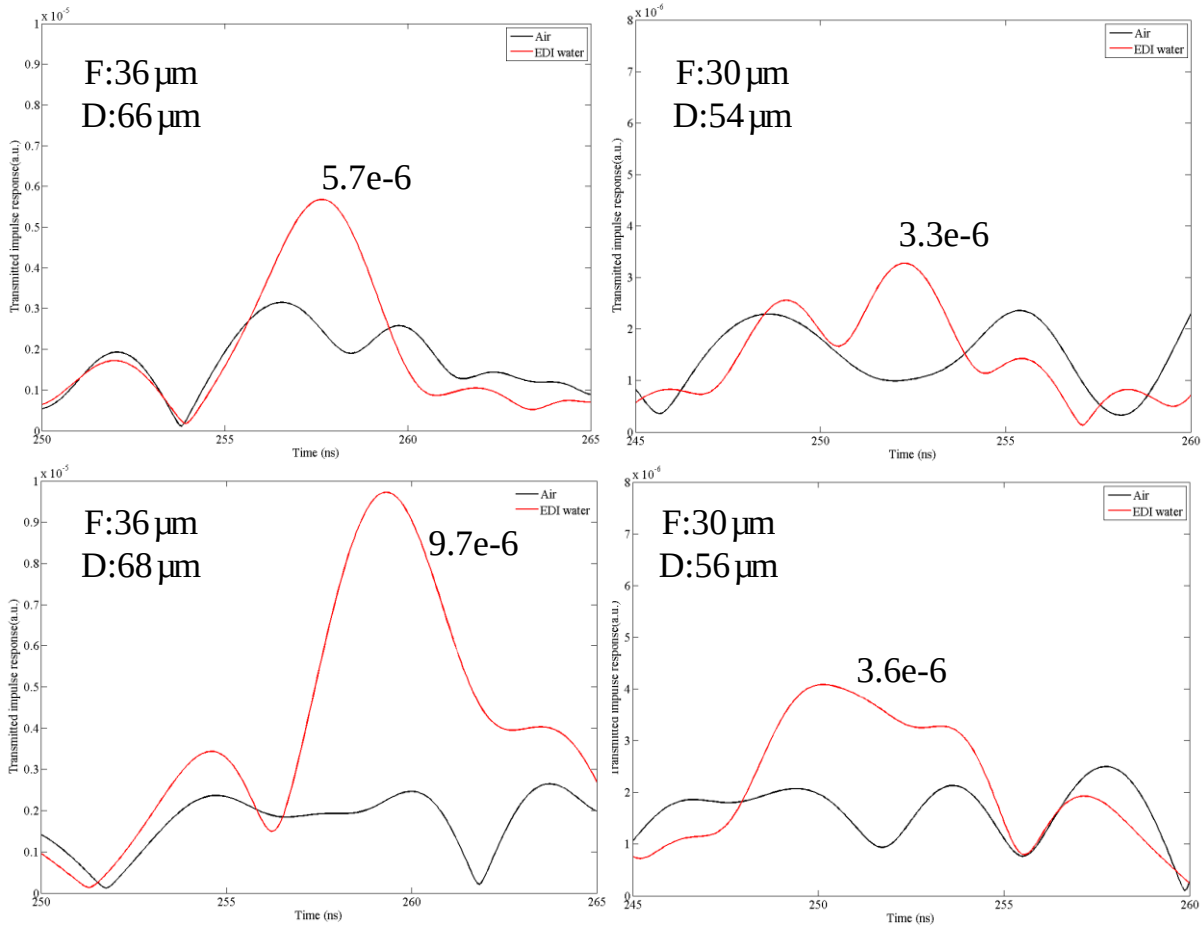

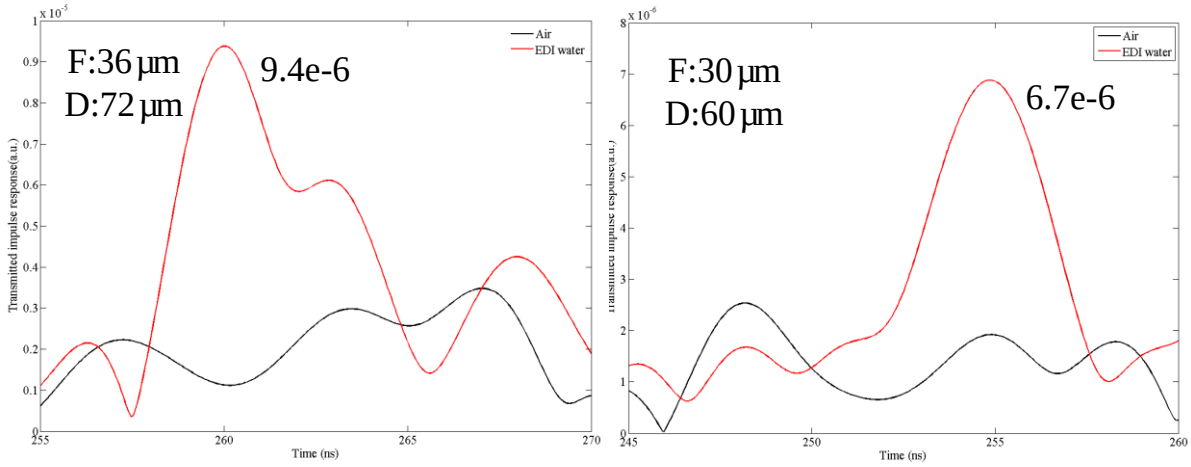

Figure 4.35 The impulse response of the system vs. time (ns). Left: focal length is 36 µm, right: focal length is 30 µm

We can see that in the case of the 30 µm radius of the lens (F=36 µm) it is difficult to determine the confocal position. A delayed secondary maximum appears in the fall time of the main echo which confirm that it is not the confocal position.. This can be a consequence of some technological problems.

In the case of the 25 µm radius (F=30 µm) the measured confocal position seems to support the theoretical model.

Then KI solution has been used to evaluate the new microsystem integrated with confocal microlenses. The measured results are shown in Figure 4.36. For the microlenses with a 36 µm focal length, the time of flight of the LLSLLLL peak is around 260ns. The delay and the amplitude of the maximum of the impulse response are shifted when the lenses distance is modified. The same situation appeared for the microlenses with 30 µm in focal length. For all the dimension of the lenses, the amplitude of the LLSLLLL peak increases with the concentration of KI solution increase.

Comparing the two confocal lenses, the amplitude of the LLSLLLL peaks shows the same trend for all the concentration of KI solution in Figure 4.37.

Traditionally acoustic wave transmitted through 30 µm confocal lens has the lower attenuation than the acoustic wave transmitted though 36 µm confocal lens.

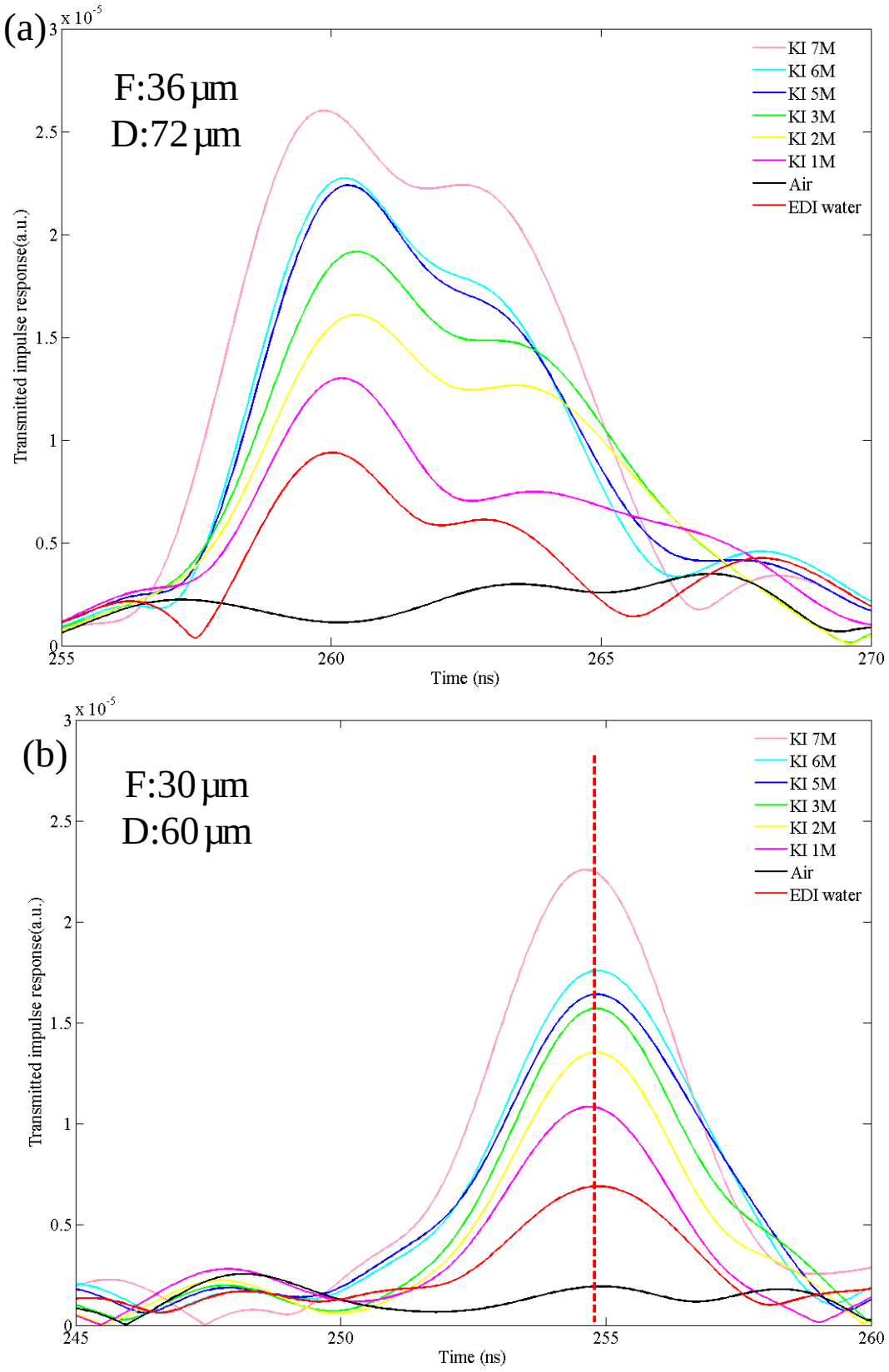

Figure 4.36 The transmitted impulse response of the system vs. time (ns) for different KI concentration (a) focal length 36 µm,(b) focal length 30 µm

But in our microsystem, the length of transducer is 200 µm which is much longer than the aperture of both confocal lenses. The wall profile between the lens edge and the main microchannel, has a 10 ° incline angle with the channel direction. The acoustic wave transmitted through this structure will be totally reflected by the wall. It explains when the focal length of lens is 36 µm, the amplitude is stronger than that when the focal length of lens is 30 µm

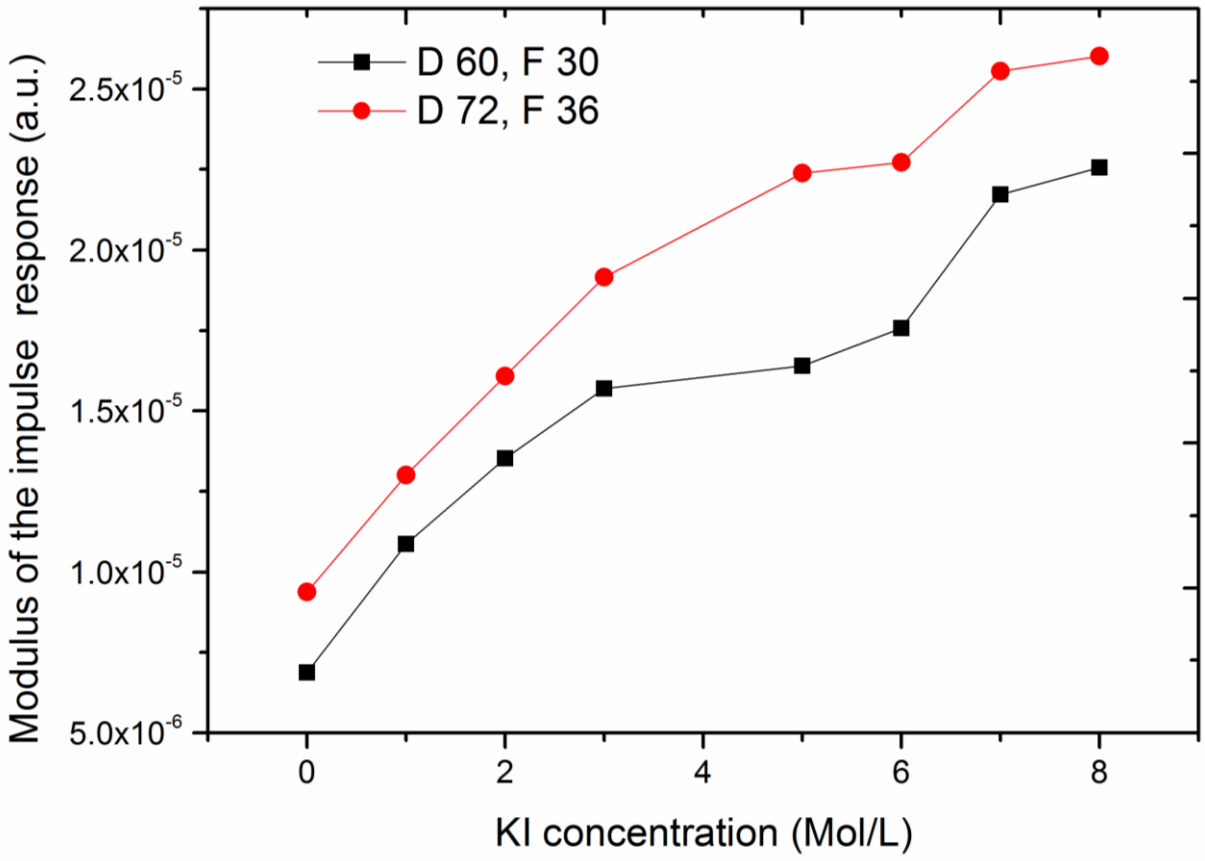

Figure 4.37 The impulse response of the system vs.KI concentration

4.4.5.2 Biological cells measurements through the confocal lenses

The microsystem evaluated with KI solution has a good S/N ratio. For the different concentration of KI solution the microsystem using lenses demonstrated a good sensitivity. We use the same micro-device to measure the transmitted acoustic signal for different concentration of blood. The results are shown in Figure 4.38.

The focal length is 36 µm. The impulse response through blood samples shows a time shift

comparing to the impulse response through sodium chloride solution. Where lens distance is 72 µm, the time shift is around 0.8ns and where lens distance is 60 µm, the time shift is about 0.6ns. The accuracy of our measurements which need to be validated again doesn't allow giving a strong scientific interpretation of this result. Nevertheless the relative variation of the mean amplitude of the transmitted wave with respect to the red blood cell concentration in the fluid seems to be in good agreement with the physics.

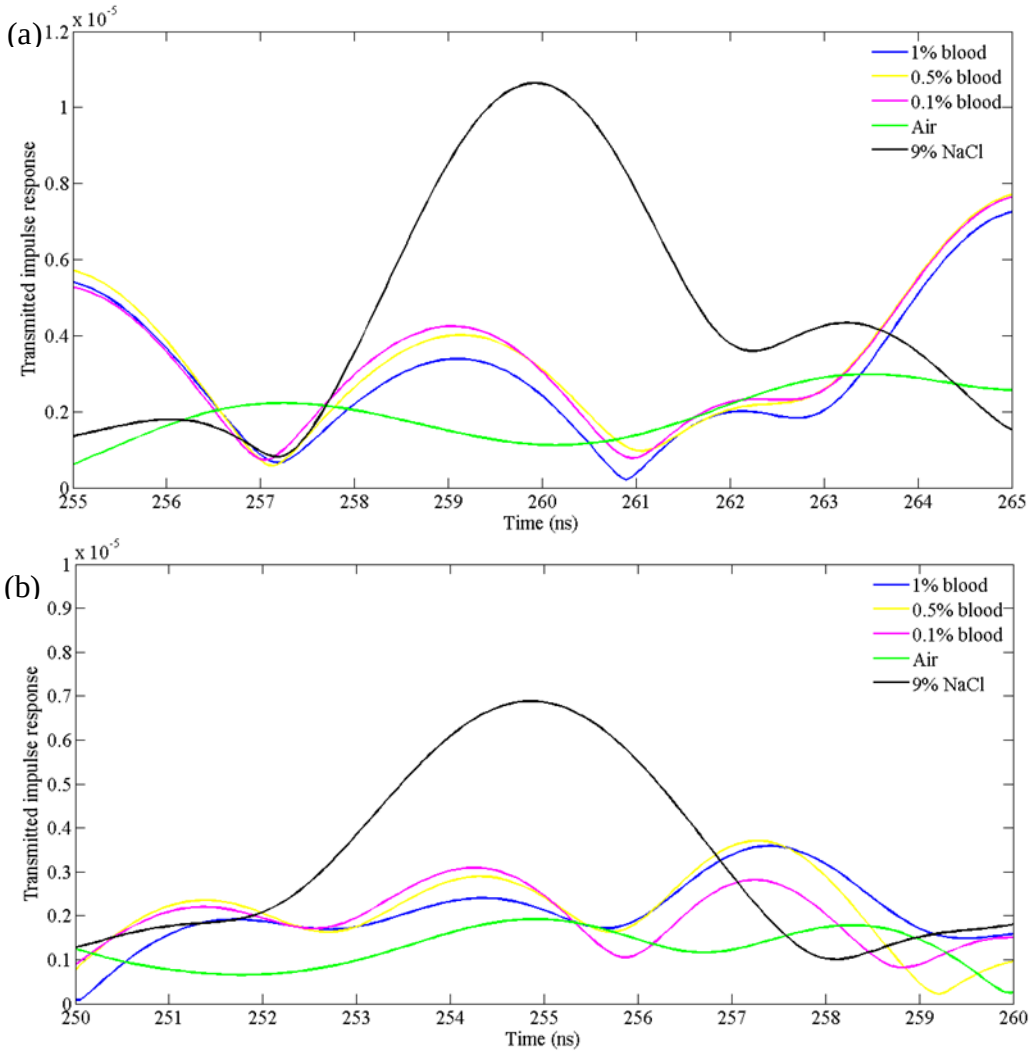

Figure 4.38 The impulse response of the system vs. time (ns) with S_{21}: (a) the focus length of lens 36 µm, the distance between two lenses 72 µm (b) the focus length of lens 30 µm, the distance between two lenses 60 µm

Figure 4.39 represents the real part of impulse response versus the different blood concentration.

The data of red circle are obtained from lens with a 36 µm focal length and 72 µm between lenses distance. The data of black squares has been obtained from the lens with focal length of 30 µm and between lenses distance of 60 µm. The tendency of the two symbol lines is nearly

the same.

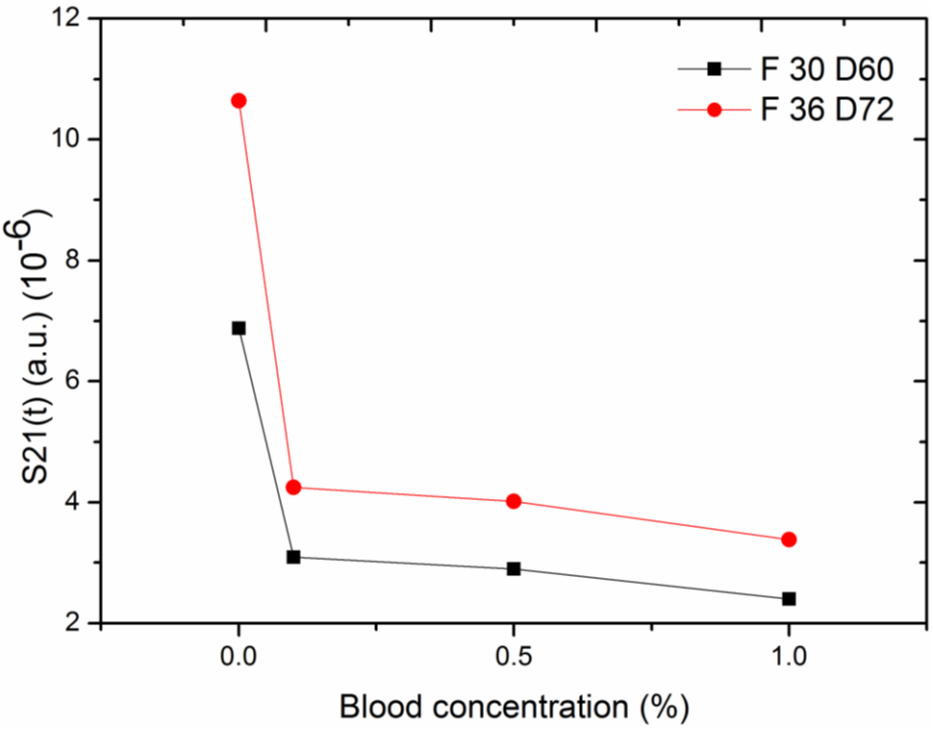

Figure 4.39 The impulse response of the system vs. blood concentration

4.5 Summary

We presented in this chapter the performances of a new microfluidic device which can widen the applicability of BAW for the elastic characterization of biological samples and also provide a micro-platform which is versatile and easy to be integrated.

The basic components of our microsystem are microchannel, ZnO transducers and 45 °mirrors. Inside silicon wafer the research of acoustic wave guiding has been studied. Using a 4 µm SiO_2 layer, we can increase the amplitude impulse response of transmitted acoustic wave. The efficiency of this oxide layer can be estimated through the amplitude variation of the acoustic wave starting from 0.8×10^{-4} for LLL without the layer and reaching a value of 9.5×10^{-4} with the oxide layer. It implies that the efficiency of the reflection of the longitudinal wave on the mirror can be improved by means of the deposition of a SiO_2 layer on the mirrors. The increase of amplitude of the LLL signal is more than 20 dB.

Due to the low signal to noise ratio in a first achievement, the pair of vertical mirrors, acting as a spatial filter, has been integrated into the microsystem.. The depths of vertical mirrors and of the microchannel are the same. This led to separate the two ZnO transducers axis, which

remove a part of spurious acoustic signals. Based on the improvement, the S/N ratio has been increased up to 29.

The integrated microdevice with vertical mirrors has been used in order to characterize the different concentrations of KI solutions and to detect 30 μmin diameter latex particles. The experimental results show a good sensitivity and are in good agreement with the theory.

In order to further improve the sensing accuracy and sensitivity, microlenses have been integrated into microsystem. Different results for a set of concentrations of KI solution and blood suspensions have been presented. The results show that with microlens integration the amplitude of impulse response has been enhanced, especially for blood measurements.

Based on the sensing microsystem, ultrahigh frequency acoustic waves can be used to characterize and detect a lot of chemical and biological samples.

Conclusion

In this thesis, an integrated system for characterization in transmission mode through a microfluidic channel using wave guiding micro-components has been developed on a silicon wafer. It was experimentally calibrated using deionized water and KI solution, in order to detect the latex particles and measure the concentration of blood cells.

In order to profoundly understand the bulk acoustic wave transmission in the silicon substrate, the theoretical fundamentals of acoustic wave have been presented, especially acoustic wave reflection and transmission in anisotropic solid (silicon) have been studied. Normal incidence and the oblique incidence at the solid-air interface have been discussed, especially the incidence angle is 45 °. The mode conversion happens when the acoustic wave is reflected by the oblique interface. The coating layer of SiO_2 was studied to improve the efficiency of the propagation of the longitudinal wave and limit the conversion of longitudinal wave to shear wave. The anti-reflection layers of quarter wave length which are used for solid-liquid (silicon-water) interface matching also have been studied. The mechanical impedance matching with the bilayer of SiO_2 and SU-8 was observed better than that of only SiO_2 at the silicon-water interface. Eventually, we calculate the absorption losses of the microsystem with and without the different types of layers. The absorption losses can be decreased of about 40dB when the microsystem is optimized with good electrical and mechanical impedance matching.

Due to acoustic wave reflection, the surface roughness and the profile of the micro-components have a great influence on wave transmission. Only 45 °mirror can guide the acoustic wave to the direction parallel to the surface so as to propagate through the microchannel. The roughness of mirror surface will cause the acoustic wave scattering and attenuation, so the reduction of the mirror surface roughness was necessary. The bottom pyramids would break the edge of the 45 °mirror and affect the acoustic wave transmission to some extent. In the experiments, the average of the mirror roughness was lower than 200nm which is much smaller than the acoustic wavelength at 1GHz. The pyramids were eliminated totally which is not only useful for the acoustic wave transmission but also convenient for the following micro-fabrication. As far as the microchannel is concerned, the perpendicular trench, the scallops and the bottom grass have a great influence on wave transmission. In order to avoid the oblique incidence of acoustic wave, the perpendicular trench is necessary. The scallops will cause the acoustic wave scattering and attenuation for the mirror roughness. Silicon grass will make micro size objects move irregularly, which will impact the sensing accuracy and generate some acoustic noise. By the above experiments, the perpendicular trench fabricated is around 89.7 °-90.3 °. The scallops of the microchannel is less than 150nm and the silicon grass was eliminated.

The basic components of microsystem are microchannel, ZnO transducers and 45 °mirrors. Inside silicon wafer the research of acoustic wave guiding had been studied. By deposited with 4 µm SiO_2, we could increase the impulse response of transmission acoustic wave. Without the silicon oxide layer the amplitude of the peaks for the transmitted acoustic wave was evaluated

at $0.8 \times 10{-}4$ for longitudinal wave transmission while with the silicon oxide layer it is $9.5 \times 10{-}4$. It implies that the efficiency of the reflection of the longitudinal wave on the $45°$ mirror can be improved by means of the deposition of a SiO_2 layer on the mirrors. The increase of amplitude of the LLL signal was more than 20 dB.

We also compared two situation of the microchannel with or without deionized water by echoes of acoustic transmitted wave. Due to the low signal to noise ratio, the pair of vertical mirrors, as a filter, had been integrated into the microsystem. The depth of vertical mirror and microchannel is the same. At the same time, the two ZnO transducers (as emitter /acceptor) have been horizontally separated. Based on this improvement, the S/N ratio has been increased up to 29dB. It was possible to measure the velocity of longitudinal acoustic wave in water with a deviation less than 2% in comparison with the literature references. As far as attenuation is concerned, we used different width of the channel, so the couple of transducers were different. These changes would have to be taken into account to achieve an absolute measurement of attenuation of water. Nevertheless, the microdevice integrated with vertical mirrors was used to characterize the different concentration of KI solution and to detect the 30μm latex particles. The result shows good sensitivity and agreement between the experimental results and theoretical results.

In order to further improve the sensing accuracy and sensitivity, the cylindrical microlenses(radius curve of 30μm or 25μm) have been integrated into microsystem. The microlenses can converge the acoustic waves to increase the S/N ratio. Different concentration of KI solution and blood were presented. The result shows that with microlens integration the amplitude of impulse response has been enhanced, especially to the blood detection. Based on the sensing microsystem, ultrahigh frequency acoustic waves could be used to characterize on line and detect a variety of chemical and biological samples.

References

[1] S. C. Terry, J. H. Jerman, and J. B. Angell, “A gas chromatographic air analyzer fabricated on a silicon wafer,” *Electron Devices, IEEE Transactions on*, vol. 26, no. 12, pp. 1880 – 1886, Dec. 1979.

[2] A. Manz, N. Graber, and H. M. Widmer, “Miniaturized total chemical analysis systems: A novel concept for chemical sensing,” *Sensors and Actuators B: Chemical*, vol. 1, no. 1–6, pp. 244–248, Jan. 1990.

[3] D. R. Reyes, D. Iossifidis, P.-A. Auroux, and A. Manz, “Micro total analysis systems. 1. Introduction, theory, and technology,” *Anal. Chem.*, vol. 74, no. 12, pp. 2623–2636, Jun. 2002.

[4] T. Vilkner, D. Janasek, and A. Manz, “Micro Total Analysis Systems. Recent Developments,” *Anal. Chem.*, vol. 76, no. 12, pp. 3373–3386, Jun. 2004.

[5] K. E. Herold and K. E. H. and A. Rasooly, *Lab on a Chip Technology, Volume 1: Fabrication and Microfluidics*. Horizon Scientific Press, 2009.

[6] G. M. Whitesides, “The origins and the future of microfluidics,” *Nature*, vol. 442, no. 7101, pp. 368–373, Jul. 2006.

[7] H. A. Stone, A. D. Stroock, and A. Ajdari, “ENGINEERING FLOWS IN SMALL DEVICES,” *Annual Review of Fluid Mechanics*, vol. 36, no. 1, pp. 381–411, 2004.

[8] T. M. Squires and S. R. Quake, “Microfluidics: Fluid physics at the nanoliter scale,” *Rev. Mod. Phys.*, vol. 77, no. 3, pp. 977–1026, Oct. 2005.

[9] S. Park, “Electrokinetic and acoustic manipulations of colloidal and biological particles,” TEXAS A&M UNIVERSITY, 2009.

[10] J. El-Ali, P. K. Sorger, and K. F. Jensen, “Cells on chips,” *Nature*, vol. 442, no. 7101, pp. 403–411, Jul. 2006.

[11] H. A. Stone and S. Kim, “Microfluidics: Basic issues, applications, and challenges,” *AIChE Journal*, vol. 47, no. 6, pp. 1250–1254, Jun. 2001.

[12] S. Haeberle and R. Zengerle, “Microfluidic platforms for lab-on-a-chip applications,” *Lab Chip*, vol. 7, no. 9, pp. 1094–1110, Aug. 2007.

[13] D. J. Beebe, G. A. Mensing, and G. M. Walker, “Physics and Applications of Microfluidics in Biology,” *Annual Review of Biomedical Engineering*, vol. 4, no. 1, pp. 261–286, 2002.

[14] J. Wang, “From DNA biosensors to gene chips,” *Nucleic Acids Res*, vol. 28, no. 16, pp. 3011–3016, Aug. 2000.

[15] Y. H. Ghallab and W. Badawy, *Lab-On-A-Chip: Techniques, Circuits, and Biomedical*

Applications. Artech House, 2010.

[16] Y. H. Ghallab and W. Badawy, *Lab-On-A-Chip: Techniques, Circuits, and Biomedical Applications*. Artech House, 2010.

[17] J. Logan, K. Edwards, and N. A. Saunders, *Real-Time PCR: Current Technology and Applications*. Horizon Scientific Press, 2009.

[18] B. Regenberg, U. Krühne, M. Beyer, L. H. Pedersen, M. Simón, O. R. T. Thomas, J. Nielsen, and T. Ahl, "Use of laminar flow patterning for miniaturised biochemical assays," *Lab Chip*, vol. 4, no. 6, pp. 654–657, Nov. 2004.

[19] P. P. Banada and A. K. Bhunia, "Antibodies and Immunoassays for Detection of Bacterial Pathogens," in *Principles of Bacterial Detection: Biosensors, Recognition Receptors and Microsystems*, M. Zourob, S. Elwary, and A. Turner, Eds. Springer New York, 2008, pp. 567–602.

[20] A. P. Lee, "Microfluidic cellular and molecular detection for lab-on-a-chip applications," in *Annual International Conference of the IEEE Engineering in Medicine and Biology Society, 2009. EMBC 2009*, 2009, pp. 4147 –4149.

[21] R. N. Zare and S. Kim, "Microfluidic Platforms for Single-Cell Analysis," *Annual Review of Biomedical Engineering*, vol. 12, no. 1, pp. 187–201, 2010.

[22] E. Brouzes, M. Medkova, N. Savenelli, D. Marran, M. Twardowski, J. B. Hutchison, J. M. Rothberg, D. R. Link, N. Perrimon, and M. L. Samuels, "Droplet microfluidic technology for single-cell high-throughput screening," *PNAS*, vol. 106, no. 34, pp. 14195–14200, Aug. 2009.

[23] R. Bogue, "MEMS sensors: past, present and future," *Sensor Review*, vol. 27, no. 1, pp. 7–13, 2007.

[24] B. Kuswandi, Nuriman, J. Huskens, and W. Verboom, "Optical sensing systems for microfluidic devices: A review," *Analytica Chimica Acta*, vol. 601, no. 2, pp. 141–155, Oct. 2007.

[25] J. Wu and M. Gu, "Microfluidic sensing: state of the art fabrication and detection techniques," *J. Biomed. Opt*, vol. 16, no. 8, pp. 080901–080901, Aug. 2011.

[26] N. J. Petersen, K. B. Mogensen, and J. P. Kutter, "Performance of an in-plane detection cell with integrated waveguides for UV/Vis absorbance measurements on microfluidic separation devices," *ELECTROPHORESIS*, vol. 23, no. 20, pp. 3528–3536, 2002.

[27] S. Balslev, A. M. Jorgensen, B. Bilenberg, K. B. Mogensen, D. Snakenborg, O. Geschke, J. P. Kutter, and A. Kristensen, "Lab-on-a-chip with integrated optical transducers," *Lab Chip*, vol. 6, no. 2, pp. 213–217, Jan. 2006.

[28] O. Hofmann, G. Voirin, P. Niedermann, and A. Manz, "Three-Dimensional Microfluidic Confinement for Efficient Sample Delivery to Biosensor Surfaces.

Application to Immunoassays on Planar Optical Waveguides," *Anal. Chem.*, vol. 74, no. 20, pp. 5243–5250, Oct. 2002.

[29] O. Hofmann, X. Wang, A. Cornwell, S. Beecher, A. Raja, D. D. C. Bradley, A. J. deMello, and J. C. deMello, "Monolithically integrated dye-doped PDMS long-pass filters for disposable on-chip fluorescence detection," *Lab Chip*, vol. 6, no. 8, pp. 981–987, Jul. 2006.

[30] A. M. Jorgensen, K. B. Mogensen, J. P. Kutter, and O. Geschke, "A biochemical microdevice with an integrated chemiluminescence detector," *Sensors and Actuators B: Chemical*, vol. 90, no. 1–3, pp. 15–21, Apr. 2003.

[31] H. Hosono, W. Satoh, J. Fukuda, and H. Suzuki, "On-chip handling of solutions and electrochemiluminescence detection of amino acids," *Sensors and Actuators B: Chemical*, vol. 122, no. 2, pp. 542–548, Mar. 2007.

[32] A. Chaubey and B. D. Malhotra, "Mediated biosensors," *Biosensors and Bioelectronics*, vol. 17, no. 6–7, pp. 441–456, Jun. 2002.

[33] E. Bakker and E. Pretsch, "Potentiometric sensors for trace-level analysis," *Trends Analyt Chem*, vol. 24, no. 3, pp. 199–207, Mar. 2005.

[34] A. Kueng, C. Kranz, and B. Mizaikoff, "Amperometric ATP biosensor based on polymer entrapped enzymes," *Biosensors and Bioelectronics*, vol. 19, no. 10, pp. 1301–1307, May 2004.

[35] T. V. Shishkanova, R. Volf, M. Krondak, and V. Král, "Functionalization of PVC membrane with ss oligonucleotides for a potentiometric biosensor," *Biosensors and Bioelectronics*, vol. 22, no. 11, pp. 2712–2717, May 2007.

[36] M. Galloway, W. Stryjewski, A. Henry, S. M. Ford, S. Llopis, R. L. McCarley, and S. A. Soper, "Contact Conductivity Detection in Poly(methyl methacylate)-Based Microfluidic Devices for Analysis of Mono- and Polyanionic Molecules," *Anal. Chem.*, vol. 74, no. 10, pp. 2407–2415, May 2002.

[37] L.-S. Bouchard, S. R. Burt, M. S. Anwar, K. V. Kovtunov, I. V. Koptyug, and A. Pines, "NMR Imaging of Catalytic Hydrogenation in Microreactors with the Use of para-Hydrogen," *Science*, vol. 319, no. 5862, pp. 442–445, Jan. 2008.

[38] M. S. Anwar, C. Hilty, C. Chu, L.-S. Bouchard, K. L. Pierce, and A. Pines, "Spin Coherence Transfer in Chemical Transformations Monitored by Remote Detection NMR," *Anal. Chem.*, vol. 79, no. 7, pp. 2806–2811, Apr. 2007.

[39] V.-V. Telkki, C. Hilty, S. Garcia, E. Harel, and A. Pines, "Quantifying the Diffusion of a Fluid through Membranes by Double Phase Encoded Remote Detection Magnetic Resonance Imaging," *J. Phys. Chem. B*, vol. 111, no. 50, pp. 13929–13936, Dec. 2007.

[40] M. Mujika, S. Arana, E. Castaño, M. Tijero, R. Vilares, J. M. Ruano-López, A. Cruz, L. Sainz, and J. Berganza, "Magnetoresistive immunosensor for the detection of

Escherichia coli O157:H7 including a microfluidic network," *Biosensors and Bioelectronics*, vol. 24, no. 5, pp. 1253–1258, Jan. 2009.

[41] J. Friend and L. Y. Yeo, "Microscale acoustofluidics: Microfluidics driven via acoustics and ultrasonics," *Rev. Mod. Phys.*, vol. 83, no. 2, pp. 647–704, Jun. 2011.

[42] P. L. Marston, X. Lurton, and D. R. Jackson, "An Introduction to Underwater Acoustics," *The Journal of the Acoustical Society of America*, vol. 115, no. 2, pp. 443–443, 2004.

[43] H. M. Author, C. S. C. Author, and T. K. Stanton, "Fundamentals of Acoustical Oceanography," *The Journal of the Acoustical Society of America*, vol. 105, no. 4, pp. 2065–2066, 1999.

[44] M. Long, *Architectural Acoustics*. Elsevier, 2006.

[45] S. M. Kuo and D. R. Morgan, "Active noise control: a tutorial review," *Proceedings of the IEEE*, vol. 87, no. 6, pp. 943 – 973, Jun. 1999.

[46] C. R. Hill, J. C. Bamber, and G. R. ter Haar, *Physical Principles of Medical Ultrasonics*. John Wiley & Sons, 2004.

[47] P. J. . Frinking, A. Bouakaz, J. Kirkhorn, F. J. Ten Cate, and N. de Jong, "Ultrasound contrast imaging: current and new potential methods," *Ultrasound in Medicine & Biology*, vol. 26, no. 6, pp. 965–975, Jul. 2000.

[48] A. L. Klibanov, "Microbubble contrast agents: targeted ultrasound imaging and ultrasound-assisted drug-delivery applications," *Invest Radiol*, vol. 41, no. 3, pp. 354–362, Mar. 2006.

[49] D. T. Blackstock, *Fundamentals of Physical Acoustics*. John Wiley & Sons, 2000.

[50] J. D. Maynard, E. G. Williams, and Y. Lee, "Nearfield acoustic holography: I. Theory of generalized holography and the development of NAH," *The Journal of the Acoustical Society of America*, vol. 78, no. 4, pp. 1395–1413, 1985.

[51] K. Länge, B. Rapp, and M. Rapp, "Surface acoustic wave biosensors: a review," *Analytical and Bioanalytical Chemistry*, vol. 391, no. 5, pp. 1509–1519, 2008.

[52] R. A. Lemons, "Acoustic microscope—scanning version," *Applied Physics Letters*, vol. 24, no. 4, p. 163, 1974.

[53] L. Biro, A. Das, A. Meunier, and J. L. Katz, "Digital ultrasonic imaging and its application to skeletal tissues," *Ultrason. Int. '83 Proc*, pp. 79–84, 1983.

[54] E. C. Weiss, P. Anastasiadis, G. Pilarczyk, R. M. Lernor, and P. V. Zinin, "Mechanical Properties of Single Cells by High-Frequency Time-Resolved Acoustic Microscopy," *IEEE Transactions on Ultrasonics, Ferroelectrics and Frequency Control*, vol. 54, no. 11, pp. 2257 –2271, Nov. 2007.

[55] T. Kundu, *Ultrasonic Nondestructive Evaluation: Engineering and Biological Material*

Characterization. CRC Press, 2004.

[56] J. D. N. Cheeke, *Fundamentals and Applications of Ultrasonic Waves*. CRC Press, 2002.

[57] R. M. Lemor, E. C. Weiss, G. Pilarczyk, and P. V. Zinin, "Measurements of elastic properties of cells using high-frequency time-resolved acoustic microscopy," in *2003 IEEE Symposium on Ultrasonics*, 2003, vol. 1, pp. 762 – 765 Vol.1.

[58] E. Drescher-Krasicka and J. R. Willis, "Mapping stress with ultrasound," *, Published online: 07 November 1996; | doi:10.1038/384052a0*, vol. 384, no. 6604, pp. 52–55, Nov. 1996.

[59] E. C. Weiss, R. M. Lemor, G. Pilarczyk, P. Anastasiadis, and P. V. Zinin, "Imaging of Focal Contacts of Chicken Heart Muscle Cells by High-Frequency Acoustic Microscopy," *Ultrasound in Medicine & Biology*, vol. 33, no. 8, pp. 1320–1326, Aug. 2007.

[60] Y. Saijo, M. Tanaka, H. Okawai, and F. Dunn, "The ultrasonic properties of gastric cancer tissues obtained with a scanning acoustic microscope system," *Ultrasound in Medicine & Biology*, vol. 17, no. 7, pp. 709–714, 1991.

[61] J. M. Cannata, J. A. Williams, Q. Zhou, T. A. Ritter, and K. K. Shung, "Development of a 35-MHz piezo-composite ultrasound array for medical imaging," *IEEE Transactions on Ultrasonics, Ferroelectrics and Frequency Control*, vol. 53, no. 1, pp. 224 –236, Jan. 2006.

[62] C. G. Liu, D. W. Wu, Q. F. Zhou, F. T. Djuth, and K. K. Shung, "High-frequency (50 #x2013;100MHz) medical ultrasound transducer arrays produced by micromachining bulk PZT materials," in *IEEE Ultrasonics Symposium, 2008. IUS 2008*, 2008, pp. 690 –693.

[63] R. Lucklum and P. Hauptmann, "Transduction mechanism of acoustic-wave based chemical and biochemical sensors," *Measurement Science and Technology*, vol. 14, no. 11, pp. 1854–1864, Nov. 2003.

[64] J. W. Grate, S. J. Martin, and R. M. White, "Acoustic Wave Microsensors," *Anal. Chem.*, vol. 65, no. 21, p. 940A–948A, Nov. 1993.

[65] *Piezoelectric Transducers and Applications*. .

[66] F. Herrmann, B. Jakoby, J. Rabe, and S. Büttgenbach, "Microacoustic Sensors for Liquid Monitoring," *Sensors Update*, vol. 9, no. 1, pp. 105–160, 2001.

[67] K. A. Marx, "Quartz Crystal Microbalance: A Useful Tool for Studying Thin Polymer Films and Complex Biomolecular Systems at the Solution−Surface Interface," *Biomacromolecules*, vol. 4, no. 5, pp. 1099–1120, Sep. 2003.

[68] A. Janshoff, H.-J. Galla, and C. Steinem, "Piezoelectric Mass-Sensing Devices as Biosensors—An Alternative to Optical Biosensors?," *Angewandte Chemie International Edition*, vol. 39, no. 22, pp. 4004–4032, 2000.

[69] F. Yin, Y. Zhang, Y. Wu, Y. Cai, Q. Xie, and S. Yao, “Study of bovine serum albumin adsorption onto a silicon dioxide surface using a ring-electrode piezoelectric sensor,” *Analytica Chimica Acta*, vol. 444, no. 2, pp. 271–277, Oct. 2001.

[70] D. S. Ballantine, *Acoustic Wave Sensors: Theory, Design, and Physico-Chemical Applications*. Academic Press, 1997.

[71] K. Nakanishi, H. Muguruma, and I. Karube, “A Novel Method of Immobilizing Antibodies on a Quartz Crystal Microbalance Using Plasma-Polymerized Films for Immunosensors,” *Anal. Chem.*, vol. 68, no. 10, pp. 1695–1700, Jan. 1996.

[72] J. . Abad, F. Pariente, L. Hernández, and E. Lorenzo, “A quartz crystal microbalance assay for detection of antibodies against the recombinant African swine fever virus attachment protein p12 in swine serum,” *Analytica Chimica Acta*, vol. 368, no. 3, pp. 183–189, Jul. 1998.

[73] J. Wegener, J. Seebach, A. Janshoff, and H.-J. Galla, “Analysis of the Composite Response of Shear Wave Resonators to the Attachment of Mammalian Cells,” *Biophysical Journal*, vol. 78, no. 6, pp. 2821–2833, Jun. 2000.

[74] F. Li, J. H.-C. Wang, and Q.-M. Wang, “Thickness shear mode acoustic wave sensors for characterizing the viscoelastic properties of cell monolayer,” *Sensors and Actuators B: Chemical*, vol. 128, no. 2, pp. 399–406, Jan. 2008.

[75] H. Wohltjen, “Mechanism of operation and design considerations for surface acoustic wave device vapour sensors,” *Sensors and Actuators*, vol. 5, no. 4, pp. 307–325, Jul. 1984.

[76] R. M. White and F. W. Voltmer, “DIRECT PIEZOELECTRIC COUPLING TO SURFACE ELASTIC WAVES,” *Applied Physics Letters*, vol. 7, no. 12, pp. 314–316, Dec. 1965.

[77] J. W. Grate and G. C. Frye, “Acoustic Wave Sensors,” *Sensors Update*, vol. 2, no. 1, pp. 37–83, 1996.

[78] K. Länge, B. Rapp, and M. Rapp, “Surface acoustic wave biosensors: a review,” *Analytical and Bioanalytical Chemistry*, vol. 391, no. 5, pp. 1509–1519, 2008.

[79] D. S. Lee, Y. Q. Fu, S. Maeng, X. Y. Du, S. C. Tan, J. K. Luo, A. J. Flewitt, S. H. Kim, N. M. Park, Y. J. Choi, H. C. Yoon, S. Y. Oh, and W. I. Milne, “Integrated ZnO Surface Acoustic Wave Microfluidic and Biosensor System,” in *Electron Devices Meeting, 2007. IEDM 2007. IEEE International*, 2007, pp. 851 –854.

[80] K. Kalantar-Zadeh, W. Wlodarski, Y. Y. Chen, B. N. Fry, and K. Galatsis, “Novel Love mode surface acoustic wave based immunosensors,” *Sensors and Actuators B: Chemical*, vol. 91, no. 1–3, pp. 143–147, Jun. 2003.

[81] H.-W. Chang and J.-S. Shih, “Surface acoustic wave immunosensors based on immobilized C60-proteins,” *Sensors and Actuators B: Chemical*, vol. 121, no. 2, pp. 522–529, Feb. 2007.

[82] O. Tamarin, S. Comeau, C. Déjous, D. Moynet, D. Rebière, J. Bezian, and J. Pistré, “Real time device for biosensing: design of a bacteriophage model using love acoustic waves,” *Biosensors and Bioelectronics*, vol. 18, no. 5–6, pp. 755–763, May 2003.

[83] C. Zimmermann, D. Rebière, C. Déjous, J. Pistré, E. Chastaing, and R. Planade, “A love-wave gas sensor coated with functionalized polysiloxane for sensing organophosphorus compounds,” *Sensors and Actuators B: Chemical*, vol. 76, no. 1–3, pp. 86–94, Jun. 2001.

[84] K. Zhang, L.-B. Zhao, S.-S. Guo, B.-X. Shi, T.-L. Lam, Y.-C. Leung, Y. Chen, X.-Z. Zhao, H. L. W. Chan, and Y. Wang, “A microfluidic system with surface modified piezoelectric sensor for trapping and detection of cancer cells,” *Biosensors and Bioelectronics*, vol. 26, no. 2, pp. 935–939, Oct. 2010.

[85] M. Yang and M. Thompson, “Multiple chemical information from the thickness shear mode acoustic wave sensor in the liquid phase,” *Anal. Chem.*, vol. 65, no. 9, pp. 1158–1168, May 1993.

[86] X. Zhang, W. Xu, A. Abbaspour-Tamijani, and J. Chae, “Thermal Analysis and Characterization of a High Q Film Bulk Acoustic Resonator (FBAR) as Biosensers in Liquids,” in *IEEE 22nd International Conference on Micro Electro Mechanical Systems, 2009. MEMS 2009*, 2009, pp. 939 –942.

[87] G. Wingqvist, J. Bjurström, L. Liljeholm, V. Yantchev, and I. Katardjiev, “Shear mode AlN thin film electro-acoustic resonant sensor operation in viscous media,” *Sensors and Actuators B: Chemical*, vol. 123, no. 1, pp. 466–473, Apr. 2007.

[88] M. R. Bringer, C. J. Gerdts, H. Song, J. D. Tice, and R. F. Ismagilov, “Microfluidic systems for chemical kinetics that rely on chaotic mixing in droplets,” *Philosophical Transactions of the Royal Society A: Mathematical, Physical and Engineering Sciences*, vol. 362, no. 1818, pp. 1087–1104, May 2004.

[89] D. N. Breslauer, P. J. Lee, and L. P. Lee, “Microfluidics-based systems biology,” *Mol Biosyst*, vol. 2, no. 2, pp. 97–112, Feb. 2006.

[90] J. Hong, J. B. Edel, and A. J. deMello, “Micro- and nanofluidic systems for high-throughput biological screening,” *Drug Discov. Today*, vol. 14, no. 3–4, pp. 134–146, Feb. 2009.

[91] K. Sato, K. Mawatari, and T. Kitamori, “Microchip-based cell analysis and clinical diagnosis system,” *Lab Chip*, vol. 8, no. 12, pp. 1992–1998, Dec. 2008.

[92] D. B. Weibel and G. M. Whitesides, “Applications of microfluidics in chemical biology,” *Curr Opin Chem Biol*, vol. 10, no. 6, pp. 584–591, Dec. 2006.

[93] A. Ashkin, J. M. Dziedzic, and T. Yamane, “Optical trapping and manipulation of single cells using infrared laser beams,” *Nature*, vol. 330, no. 6150, pp. 769–771, Dec. 1987.

[94] C. Gosse and V. Croquette, “Magnetic tweezers: micromanipulation and force

measurement at the molecular level.," *Biophys J*, vol. 82, no. 6, pp. 3314–3329, Jun. 2002.

[95] S. Rajaraman, H. (Moses) Noh, P. J. Hesketh, and D. S. Gottfried, "Rapid, low cost microfabrication technologies toward realization of devices for dielectrophoretic manipulation of particles and nanowires," *Sensors and Actuators B: Chemical*, vol. 114, no. 1, pp. 392–401, Mar. 2006.

[96] G. Schmera and L. B. Kish, "Surface diffusion enhanced chemical sensing by surface acoustic waves," *Sensors and Actuators B: Chemical*, vol. 93, no. 1–3, pp. 159–163, Aug. 2003.

[97] G. G. Yaralioglu, I. O. Wygant, T. C. Marentis, and B. T. Khuri-Yakub, "Ultrasonic Mixing in Microfluidic Channels Using Integrated Transducers," *Anal. Chem.*, vol. 76, no. 13, pp. 3694–3698, Jul. 2004.

[98] A. Neild, S. Oberti, and J. Dual, "Design, modeling and characterization of microfluidic devices for ultrasonic manipulation," *Sensors and Actuators B: Chemical*, vol. 121, no. 2, pp. 452–461, Feb. 2007.

[99] Y. Bourquin, R. Wilson, Y. Zhang, J. Reboud, and J. M. Cooper, "Phononic Crystals for Shaping Fluids," *Advanced Materials*, vol. 23, no. 12, pp. 1458–1462, 2011.

[100] S. S. Guo, L. B. Zhao, K. Zhang, K. H. Lam, S. T. Lau, X. Z. Zhao, Y. Wang, H. L. W. Chan, Y. Chen, and D. Baigl, "Ultrasonic particle trapping in microfluidic devices using soft lithography," *Applied Physics Letters*, vol. 92, no. 21, pp. 213901–213901–3, May 2008.

[101] O. Wagner, H. Schüler, P. Hofmann, D. Langer, P. Dancker, and J. Bereiter-Hahn, "Sound attenuation of polymerizing actin reflects supramolecular structures: viscoelastic properties of actin gels modified by cytochalasin D, profilin and alpha-actinin.," *Biochem J*, vol. 355, no. Pt 3, pp. 771–778, May 2001.

[102] A. Wixforth, C. Gauer, and J. Scriba, "Method and device for manipulating small quantities of liquid," U.S. Patent 2004007236615-Apr-2004.

[103] M. K. Tan, R. Tjeung, H. Ervin, L. Y. Yeo, and J. Friend, "Double aperture focusing transducer for controlling microparticle motions in trapezoidal microchannels with surface acoustic waves," *Applied Physics Letters*, vol. 95, no. 13, pp. 134101–134101–3, Sep. 2009.

[104] J. Reboud, R. Wilson, Y. Zhang, M. H. Ismail, Y. Bourquin, and J. M. Cooper, "Nebulisation on a disposable array structured with phononic lattices," *Lab on a Chip*, vol. 12, no. 7, p. 1268, 2012.

[105] R. Wilson, J. Reboud, Y. Bourquin, S. L. Neale, Y. Zhang, and J. M. Cooper, "Phononic crystal structures for acoustically driven microfluidic manipulations," *Lab on a Chip*, vol. 11, no. 2, p. 323, 2011.

[106] B. NONGAILLARD, P. CAMPISTRON, J. CARLIER, D. DEBAVELAERE-CALLENS, G. NASSAR, and F. LEFEBVRE, “DEVICE AND METHOD FOR STUDYING A STUDY AREA BY MEANS OF AN ACOUSTIC WAVE,” U.S. Patent WO2010072944.

[107] R. Daniel and D. Eugene, *Elastic Waves in Solids I Free and Guided Propagation*. Springer New York, 1996.

[108] R. E. Newnham, *Properties of Materials:Anisotropy, Symmetry, Structure: Anisotropy, Symmetry, Structure*. Oxford University Press, 2004.

[109] Y. Kumashiro, *Electric Refractory Materials*. CRC Press, 2000.

[110] J. Zhang, “MEMS -based High -Frequency (100-300 MHz) Ultrasonic Linear Phased Arrays,” thesis, Université de Valenciennes, 2011.

[111] H. F. Pollard, *Sound waves in solids*. Pion, 1977.

[112] S. Wang, J. Gao, J. Carlier, P. Campistron, A. NDieguene, S. Guo, O. B. Matar, D.-C. Dorothee, and B. Nongaillard, “Controlling the transmission of ultrahigh frequency bulk acoustic waves in silicon by 45° mirrors,” *Ultrasonics*, vol. 51, no. 5, pp. 532–538, Jul. 2011.

[113] A. NDIEGUENE, “CONTRIBUTION AU DEVELOPPEMENT DE MICROCOMPOSANTS POUR LA CARACTERISATION ULTRASONORE EN CANAL MICROFLUIDIQUE SUR SILICIUM: MODELISATION DE LA PROPAGATION,” Thesis, L’UNIVERSITE DE VALENCIENNES ET DU HAINAUT CAMBRESIS, 2011.

[114] J.-P. Berenger, “A perfectly matched layer for the absorption of electromagnetic waves,” *Journal of Computational Physics*, vol. 114, no. 2, pp. 185–200, Oct. 1994.

[115] J. Krautkrämer and H. Krautkrämer, *Ultrasonic testing of materials*. Springer-Verlag, 1977.

[116] M. J. Madou, *Fundamentals of Microfabrication: The Science of Miniaturization, Second Edition*, 2nd ed. CRC Press, 2002.

[117] M. Gad-el-Hak, Ed., *The MEMS Handbook*, 1st ed. CRC Press, 2001.

[118] S. Franssila, *Introduction to Microfabrication*. J. Wiley, 2004.

[119] P. Normand, K. Beltsios, A. Tserepi, K. Aidinis, D. Tsoukalas, and C. Cardinaud, “A new masking method for protecting silicon surfaces during anisotropic silicon wet etching,” *Microelectronic Engineering*, vol. 61–62, pp. 895–900, Jul. 2002.

[120] M. Hoffmann and E. Voges, “Bulk silicon micromachining for MEMS in optical communication systems,” *Journal of Micromechanics and Microengineering*, vol. 12, no. 4, pp. 349–360, Jul. 2002.

[121] K. Ishikawa, J. Zhang, A. Tuantranont, V. M. Bright, and Y.-C. Lee, “An integrated micro-optical system for VCSEL-to-fiber active alignment,” *Sensors and Actuators A: Physical*, vol. 103, no. 1–2, pp. 109–115, Jan. 2003.

[122] D. J. Sadler, M. J. Garter, C. H. Ahn, S. Koh, and A. L. Cook, “Optical reflectivity of micromachined {111}-oriented silicon mirrors for optical input - output couplers,” *Journal of Micromechanics and Microengineering*, vol. 7, no. 4, pp. 263–269, Dec. 1997.

[123] M. Elwenspoek and H. V. Jansen, “Silicon Micromachining,” *Silicon Micromachining, by Miko Elwenspoek and Henri V. Jansen, pp. 419. ISBN 0521607671. Cambridge, UK: Cambridge University Press, August 2004.*, vol. -1, Aug. 2004.

[124] S. hobha K. Lamichhane and M. R. Lamsal, “Etching of Crystalline Silicon in Thermal Environment,” *Himalayan Physics*, vol. vol 2, no. 2011, pp. 38–42.

[125] *Silicon Processing for the VLSI Era*. .

[126] O. Powell and H. B. Harrison, “Anisotropic etching of {100} and {110} planes in (100) silicon,” *Journal of Micromechanics and Microengineering*, vol. 11, no. 3, pp. 217–220, May 2001.

[127] D. Resnik, D. Vrtacnik, U. Aljancic, M. Mozek, and S. Amon, “The role of Triton surfactant in anisotropic etching of {1 1 0} reflective planes on (1 0 0) silicon,” *Journal of Micromechanics and Microengineering*, vol. 15, no. 6, pp. 1174–1183, Jun. 2005.

[128] I. Zubel and M. Kramkowska, “The effect of isopropyl alcohol on etching rate and roughness of (1 0 0) Si surface etched in KOH and TMAH solutions,” *Sensors and Actuators A: Physical*, vol. 93, no. 2, pp. 138–147, Sep. 2001.

[129] A. Merlos, M. Acero, M. H. Bao, J. Bausells, and J. Esteve, “TMAH/IPA anisotropic etching characteristics,” *Sensors and Actuators A: Physical*, vol. 37–38, pp. 737–743, Jun. 1993.

[130] E. H. Klaassen, R. J. Reay, C. Storment, and G. T. . Kovacs, “Micromachined thermally isolated circuits,” *Sensors and Actuators A: Physical*, vol. 58, no. 1, pp. 43–50, Jan. 1997.

[131] C.-R. Yang, C.-H. Yang, and P.-Y. Chen, “Study on anisotropic silicon etching characteristics in various surfactant-added tetramethyl ammonium hydroxide water solutions,” *Journal of Micromechanics and Microengineering*, vol. 15, no. 11, pp. 2028–2037, Nov. 2005.

[132] “Deep reactive-ion etching,” *Wikipedia, the free encyclopedia*. 27-Nov-2012.

[133] F. Laermer and A. Schilp, “Method of anisotropic etching of silicon,” U.S. Patent 653106811-Mar-2003.

[134] S. Tadigadapa and F. Lärmer, “Dry Etching for Micromachining Applications,” in *MEMS Materials and Processes Handbook*, R. Ghodssi and P. Lin, Eds. Springer US, 2011, pp. 403–456.

[135] H.-C. Liu, Y.-H. Lin, B. C. S. Chou, Y.-Y. Hsu, and W. Hsu, “Parameters study to improve sidewall roughness in advanced silicon etch process,” *Proceedings of SPIE*, vol. 4592,

no. 1, pp. 503–513, Nov. 2001.

[136] K. Jung, W. Song, H. W. Lim, and C. S. Lee, “Parameter study for silicon grass formation in Bosch process,” *Journal of Vacuum Science & Technology B: Microelectronics and Nanometer Structures*, vol. 28, no. 1, pp. 143–148, 2010.

[137] H.-C. Liu, Y.-H. Lin, B. C. S. Chou, Y.-Y. Hsu, and W. Hsu, “<title>Parameters study to improve sidewall roughness in advanced silicon etch process</title>,” 2001, pp. 503–513.

[138] IEMN, “Technical manuscript of STS machine.”

[139] L. Fu, J. . Miao, X. . Li, and R. . Lin, “Study of deep silicon etching for micro-gyroscope fabrication,” *Applied Surface Science*, vol. 177, no. 1–2, pp. 78–84, Jun. 2001.

[140] P. Dixit and J. Miao, “Effect of SF 6 flow rate on the etched surface profile and bottom grass formation in deep reactive ion etching process,” *Journal of Physics: Conference Series*, vol. 34, pp. 577–582, Apr. 2006.

[141] P. Dixit and J. Miao, “Effect of SF 6 flow rate on the etched surface profile and bottom grass formation in deep reactive ion etching process,” *Journal of Physics: Conference Series*, vol. 34, pp. 577–582, Apr. 2006.

[142] S. J. Pearton, D. P. Norton, K. Ip, Y. W. Heo, and T. Steiner, “Recent progress in processing and properties of ZnO,” *Progress in Materials Science*, vol. 50, no. 3, pp. 293–340, Mar. 2005.

[143] P. Muralt, “Recent progress in materials issues for piezoelectric MEMS,” *Journal of the American Ceramic Society*, vol. 91, no. 5, pp. 1385–1396, 2008.

[144] K. B. Sundaram and A. Khan, “Characterization and optimization of zinc oxide films by r.f. magnetron sputtering,” *Thin Solid Films*, vol. 295, no. 1–2, pp. 87–91, Feb. 1997.

[145] D. C. Look, D. C. Reynolds, C. W. Litton, R. L. Jones, D. B. Eason, and G. Cantwell, “Characterization of homoepitaxial p-type ZnO grown by molecular beam epitaxy,” *Applied Physics Letters*, vol. 81, no. 10, pp. 1830–1832, Sep. 2002.

[146] M. N. Kamalasanan and S. Chandra, “Sol-gel synthesis of ZnO thin films,” *Thin Solid Films*, vol. 288, no. 1–2, pp. 112–115, Nov. 1996.

[147] S. Goldsmith, “Filtered vacuum arc deposition of undoped and doped ZnO thin films: Electrical, optical, and structural properties,” *Surface and Coatings Technology*, vol. 201, no. 7, pp. 3993–3999, Dec. 2006.

[148] S. Zhang, Ed., *Biological and Biomedical Coatings Handbook, Two-Volume Set: Biological and Biomedical Coatings Handbook: Applications*, 1st ed. CRC Press, 2011.

[149] P. C. Jagadish and S. J. Pearton, *Zinc Oxide Bulk, Thin Films And Nanostructures: Processing, Properties And Applications*. Elsevier Science Ltd, 2006.

[150] W. L. Dang, Y. Q. Fu, J. K. Luo, A. J. Flewitt, and W. I. Milne, “Deposition and

characterization of sputtered ZnO films," *Superlattices and Microstructures*, vol. 42, no. 1–6, pp. 89–93, Jul. 2007.

[151] Ü. Özgür, Y. I. Alivov, C. Liu, A. Teke, M. A. Reshchikov, S. Doğan, V. Avrutin, S.-J. Cho, and H. Morkoç, "A comprehensive review of ZnO materials and devices," *Journal of Applied Physics*, vol. 98, no. 4, pp. 041301–041301–103, Aug. 2005.

[152] O. Kluth, G. Schöpe, J. Hüpkes, C. Agashe, J. Müller, and B. Rech, "Modified Thornton model for magnetron sputtered zinc oxide: film structure and etching behaviour," *Thin Solid Films*, vol. 442, no. 1–2, pp. 80–85, Oct. 2003.

[153] N. Fujimura, T. Nishihara, S. Goto, J. Xu, and T. Ito, "Control of preferred orientation for ZnOx films: control of self-texture," *Journal of Crystal Growth*, vol. 130, no. 1–2, pp. 269–279, May 1993.

[154] M. H. Koch, A. J. Hartmann, R. N. Lamb, M. Neuber, and M. Grunze, "Self-Texture in the Initial Stages of ZnO Film Growth," *J. Phys. Chem. B*, vol. 101, no. 41, pp. 8231–8236, 1997.

[155] M. Takeuchi, H. Yamada, Y. Yoshino, T. Makino, and S. Arai, "Effective electromechanical coupling coefficient (kt2) for fundamental mode of thickness extensional mode thin film bulk acoustic wave resonator fabricated by ZnO thin film," *Vacuum*, vol. 66, no. 3–4, pp. 463–466, Aug. 2002.

[156] W. Water and S.-Y. Chu, "Physical and structural properties of ZnO sputtered films," *Materials Letters*, vol. 55, no. 1–2, pp. 67–72, Jul. 2002.

[157] G. M. Whitesides, "The origins and the future of microfluidics," *Nature*, vol. 442, no. 7101, pp. 368–373, Jul. 2006.

[158] D. M.Pozar, *Microwave Engineering, 3Rd Ed*. Wiley India Pvt. Limited, 2009.

[159] J. Choma and W.-K. Chen, *Feedback Networks: Theory and Circuit Applications*. World Scientific, 2007.

[160] G. L. Matthaei, L. Young, and E. M. T. Jones, *Microwave filters, impedance-matching networks, and coupling structures*. McGraw-Hill, 1964.

[161] P. Campistron, J. Carlier, N. Saad, J. Gao, M. Toubal, L. Dupont, G. Nassar, and B. Nongaillard, "High Frequency Ultrasound, a Tool for Elastic Properties Measurement of Thin Films Fabricated on Silicon," *Advanced Materials Research*, vol. 324, pp. 277–281, Aug. 2011.

[162] S. Wang, P. Campistron, J. Carlier, D. Callens-Debavelaere, B. Nongaillard, A. NDieguene, G. Nassar, C. Soyer, and X. Zhao, "Su-8-based nanocomposites for acoustical matching layer," *IEEE Transactions on Ultrasonics, Ferroelectrics and Frequency Control*, vol. 56, no. 7, pp. 1483 –1489, Jul. 2009.

[163] J. M. M. Pinkerton, "The Absorption of Ultrasonic Waves in Liquids and its Relation to Molecular Constitution," *Proceedings of the Physical Society. Section B*, vol. 62, no. 2,

pp. 129–141, Feb. 1949.

Publications

1. **Jiaming GAO**, Julien CARLIER, Shengxiang WANG, Pierre CAMPISTRON, Dorothee CALLENS, Shishang GUO, Xingzhong ZHAO, Bertrand NONGAILLARD, Lab on a chip for high frequency acoustic characterization, sensors and actuates B-chemical, (in press)
2. N. Saad, R. Dufour, G. Nassar, M. Harnois, B. Merheb, R. Boukherroub, P.Campistron, V. Senez, J. Carlier, **J. Gao**, V. Thomy, M. Ajaka, and B. Nongaillard, Characterization of the state of a droplet on a micro-textured silicon wafer using ultrasound, Journal of applied physics, in press
3. WANG S., **GAO J**., CARLIER J., CAMPISTRON P., NDIEGUENE A., GUO S., BOU MATAR O., DEBAVELAERE-CALLENS D., NONGAILLARD B. Controlling the transmission of ultrahigh frequency bulk acoustic waves in silicon by 45 ° mirrors , Ultrasonics, **51**, 5 (2011) 532-538
4. CAMPISTRON P., CARLIER J., SAAD N., **GAO J**., TOUBAL M., DUPONT L., NASSAR G., NONGAILLARD B. High frequency ultrasound, a tool for elastic properties measurement of thin films fabricated on silicon, Adv. Mater. Res., **324** (2011) 277-281
5. XU W.J., JI X.M., **GAO J.M.**, CARLIER J., ZHANG J.Y., NONGAILLARD B., HUANG Y.P., PIWAKOWSKI B. A novel method for fabrication of high-frequency (>100 MHz) ZnO ultrasonic array transducers on silicon substrates, AIP Conf. Proc., **1433** (2011) 679-682, ISBN 978-0-7354-1019-0
6. **GAO J.**, CARLIER J., WANG S., CAMPISTRON P., CALLENS D., GUO S., ZHAO X., NONGAILLARD B. Integration of high frequency piezoelectric transducer for lab-on-chip, Actes du 11ème Congrès Français d'Acoustique et "2012 Annual IOA Meeting", Acoustics 2012, Nantes, France, 23-27 avril, 2012,papier 000480, 3323-3328, ISBN 978-2-919340-01-9

Laboratoire sur puce pour la caractérisation acoustique haute fréquence

Ce travail de thèse s'est porté sur le développement technologique d'un laboratoire sur puce permettant la caractérisation ultrasonore de milieux biologiques en canal microfluidique grâce à des transducteurs de ZnO fonctionnant à une fréquence centrale de 1 GHz. Ce système permet de caractériser, par la transmission d'ondes longitudinales de volume au travers de ce canal, les propriétés mécaniques du milieu sous investigation. Les ondes de volume sont guidées dans une direction parallèle à la surface du substrat grâce à l'introduction de miroirs à 45 °obtenus par gravures humides.

Cette thèse s'est portée plus particulièrement sur les développements technologiques des briques de base (transducteur ultrasonore en couche mince, miroirs acoustiques, canal microfluidique, lentille cylindrique) ainsi que leur intégration dans un laboratoire sur puce à base de silicium et PDMS. Ces élément ont été étudiés et optimisés afin de réussir le guidage d'ondes dans le substrat de silicium vers le canal microfluidique d'un transducteur émetteur vers un transducteur récepteur.

Ce système a permis de réaliser des essais de détection de particules, des mesures de concentration de milieu de référence et également de faire des premières mesures sur des liquides biologiques

Mots clés : transducteur ultrasonore haute fréquence, caractérisation acoustique, laboratoire su puce, microfluidique, ondes de volume.

Lab-on-a-chip for high frequency acoustic characterization

This thesis presents an acoustofluidics platform for elastic characterization of biological samples using ultra high frequency (~1GHz) ultrasonic bulk acoustic waves (BAW).

Passive 45 ° mirror planes obtained by wet chemical etching can be used to control bulk acoustic wave to transmit in the directions parallel to the surface of the silicon wafer. Zinc oxide (ZnO) thin film transducers were deposited by radio frequency sputtering on the other side of the wafer, which act as emitter/receiver after aligned with the mirrors.

A microchannel fabricated using ICP technology was inserted between 45 °mirror and vertical mirrors to realize the real time biosensing applications. To validate the design and technology of the silicon and PDMS-based platform, the propagation of bulk acoustic waves through the microfluidic channel was studied. This lab-on–a-chip platform was used to characterize different concentrations of chemical solutions in the microfluidic channel and detect latex particles passing through the channel.

Moreover, with this design, a confocal cylindrical lens using ICP technology was integrated in the microsystem. The confocal lens controls the phase of acoustic waves for focusing which is used to characterize and detect biosamples (e.g. blood cells), especially on-line to evaluate the concentration of red blood cells.

Key words: ultra high frequency transducer; acoustical characterization; Lab -on –a- chip; microfluidics; bulk acoustic wave